SANDIA REPORT

SAND2005-6994
Unlimited Release
Printed November 2005

Resistance of a Water Spark

Larry K. Warne, Roy E. Jorgenson, and Jane M. Lehr

Approved for public release; further dissemination unlimited.

ᚠ Sandia National Laboratories

Resistance of a Water Spark

Larry K. Warne and Roy E. Jorgenson
Electromagnetics and Plasma Physics Analysis Dept.

Jane M. Lehr
Advanced Pulsed Power Technologies Dept.

Sandia National Laboratories
P. O. Box 5800
Albuquerque, NM 87185-1152

Abstract

The later time phase of electrical breakdown in water is investigated for the purpose of improving understanding of the discharge characteristics. One dimensional simulations in addition to a zero dimensional lumped model are used to study the spark discharge. The goal is to provide better electrical models for water switches used in the pulse compression section of pulsed power systems. It is found that temperatures in the discharge channel under representative drive conditions, and assuming small initial radii from earlier phases of development, reach levels that are as much as an order of magnitude larger than those used to model discharges in atmospheric gases. This increased temperature coupled with a more rapidly rising conductivity with temperature than in air result in a decreased resistance characteristic compared to preceding models. A simple modification is proposed for the existing model to enable the approximate calculation of channel temperature and incorporate the resulting conductivity increase into the electrical circuit for the discharge channel. Comparisons are made between the theoretical predictions and recent experiments at Sandia. Although present and past experiments indicated that preceding late time channel models overestimated channel resistance, the calculations in this report seem to underestimate the resistance relative to recent experiments. Some possible reasons for this discrepancy are discussed.

Intentionally Left Blank

Contents

Figures

Resistance of a Water Spark

Larry K. Warne and Roy E. Jorgenson
Electromagnetics and Plasma Physics Analysis Dept.

Jane M. Lehr
Advanced Pulsed Power Technologies Dept.

Sandia National Laboratories
P. O. Box 5800
Albuquerque, NM 87185-1152

1 INTRODUCTION

The use of water insulated switches to transfer energy from one stage to another in large pulsed power drivers has led to a high degree of integration not possible with gas switches. This, coupled with the relatively high breakdown strength of fast charged water systems, allows for short gap lengths and correspondingly lower switch inductance. Though water switches have been used extensively in pulsed power drivers for many years, a predictive capability of their performance, and scaling with voltage, is lacking. Figure 1 shows such a switch in operation. There are several poles, each serving to initiate breakdown processes, which act as parallel current paths in the overall switch. This report focusses on a single breakdown channel.
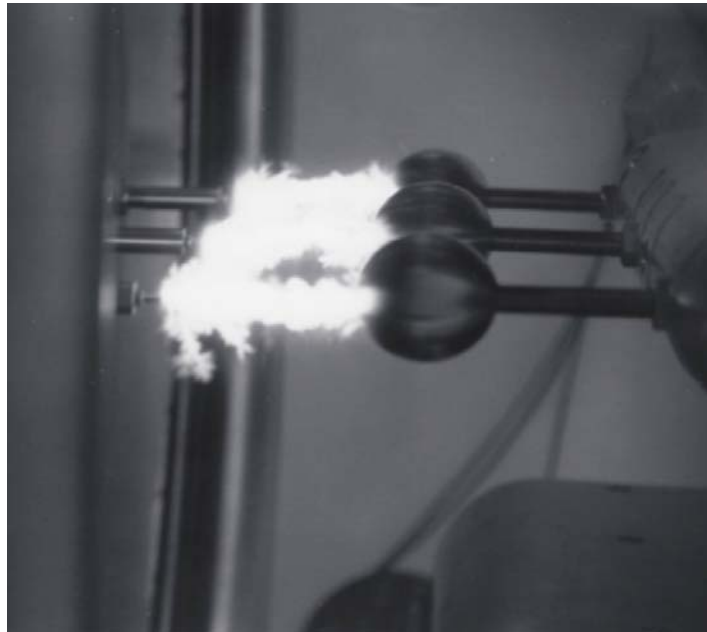
Figure 1. Three pole water switch.

The breakdown process in gases has several phases or time regimes. First there is an initiation and ionization phase where charge accumulates and a visible multibranched channel takes shape and propagates across the gap between the electrodes. Next there is a thermalization phase where a plasma forms,
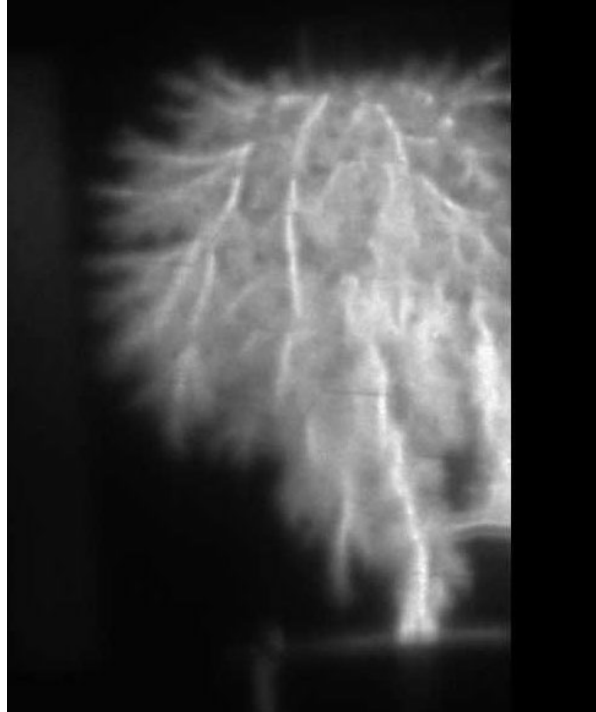
Figure 2. Framing camera photograph of a water spark (from [1]).

ionization levels become a sizable fraction of the neutral density, and appreciable current begins to flow. Finally, there is expansion of the plasma channel where the channel resistance drops and current levels rapidly increase to the point where the exterior drive circuit usually limits further increases. Although the early phases of water breakdown are less well understood one can still separate these from the final expansion phase. Of course, in doing so, information is lost on time delays associated with the early phases, as well as on initial conditions for the final expansion phase. These initial conditions may only affect the initial stages of the later time expansion phase, but will influence the channel length between electrodes. In this report we will focus on the later time expansion phase and consider the problem on a per unit length basis along the spark channel. Figure 2 shows a framing camera picture of a spark channel. Length increases of the order of twenty per cent over the electrode to electrode spacing seem quite plausible from these photographs.

Several models have been proposed for this final phase of the gas breakdown process. Some of these models have modeled the channel with a fixed average radius and varying channel conductivity [2], [3]. Another approach was taken by Braginskii [4], where the channel radius is allowed to grow through hydrodynamic expansion driven by the electric power delivered in Joule heating. Although many of the channel heat transfer processes and conductivity variations with temperature are examined in this paper [4], the final model makes use of a fixed channel conductivity. Discussion of these models versus experiments can be found in Meek and Craggs [5].

Some time ago Martin [6] applied the breakdown model developed for gases by Braginskii [4] to water. The results obtained have often overestimated the experimental resistances observed in recent pulsed power experiments. Because of the much larger density of water, versus typical gases, we felt that a reexamination of the assumptions in this model was appropriate; also the considerations of Fedorov [7] indicate that previously used temperatures and densities may not be accurate for high current drives of water breakdown. In particular, a goal of the present study was to examine whether higher temperatures are reached in water
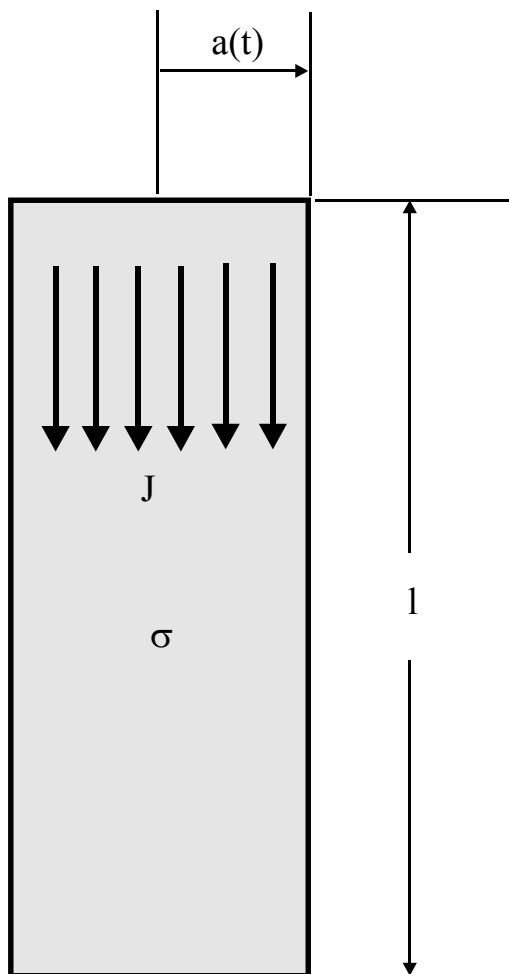
Figure 3. Side view of arc channel

breakdown experiments and how temperature variations of electrical conductivity might be incorporated into the model proposed by Martin. Another approach at incorporating conductivity variations in water breakdown has been taken by Krivitskii [8], [9], [10]. A practical reason for improving the fidelity of models for these switches is the desire to operate the switches at higher currents for future pulsed-power Z-pinch designs.

1.1 Braginskii-Martin Model

We now summarize the Braginskii-Martin model for the late time spark expansion. A side view of this geometry is shown in Figure 3. Current density $J_z(t)$ flows through the channel as indicated by the arrows. The channel radius is given by $a(t)$, which increases with respect to time. The electrical conductivity of the channel is given by σ. The length of the channel between the two electrodes is ℓ. A top view of the channel is shown in Figure 4. The arrows around the perimeter of the channel indicate that the channel is expanding.

The assumptions in this model are that the current flowing through a fixed conductivity gas expands the channel at supersonic velocity driving a cylindrical shock wave. It is thus the expansion of the channel
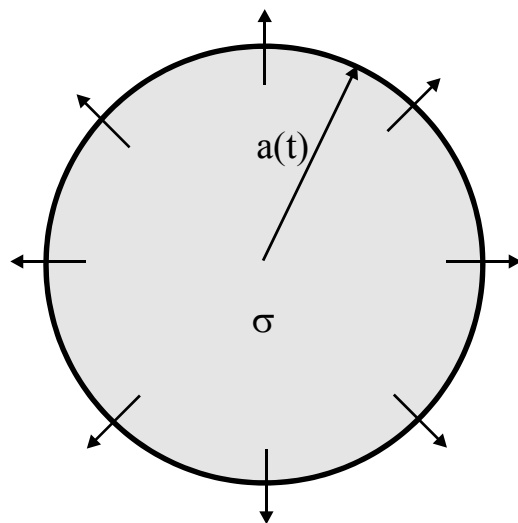
Figure 4. Top view of the arc channel

that reduces the resistance of the arc in this model. The channel radius $a(t)$ is obtained as [4], [6]

$$a^2(t) = \left(\frac{4}{\pi^2 \rho_0 \xi \sigma}\right)^{1/3} \int_0^t I^{2/3}(\tau)\, d\tau$$

where the undisturbed water density is taken as

$$\rho_0 \approx 1 \text{ g/cm}^3 = 10^3 \text{ kg/m}^3$$

the arc channel conductivity is taken as the fixed value,

$$\sigma \approx 600 \text{ S/cm} = 6 \times 10^4 \text{ S/m}$$

and a constant dependent on gas properties, and somewhat on current rise rate, is taken as

$$\xi \approx 4.5$$

The resistance of the arc channel is then

$$R = \frac{\ell}{\pi a^2 \sigma} \tag{1}$$

For a linear ramp

$$I(t) = I_0 \frac{t}{\tau}$$

with amplitude $I_0 = 300$ kA and duration $\tau = 100$ ns

$$a^2(t) = \frac{3}{5}\left(\frac{4 I_0^2 t^5}{\tau^2 \pi^2 \rho_0 \xi \sigma}\right)^{1/3} = (0.5548 \text{ mm})^2$$

where the final value results at $t = \tau$. Using this value with a channel length of $\ell = 12$ cm we find

$$R \approx 2 \text{ ohms}$$

In the next section we formulate the system of equations for the channel from the basic hydrodynamic equations and material constitutive relations. The following section examines the solution of this system. We then generalize the problem to a one dimensional radial model and apply ALEGRA_HEDP with the Lee-More-Desjarlais (LMD) conductivity model for water to perform the simulations. Next we discuss some modifications to the original simple Braginskii-Martin model for varying temperature and conductivity which allow simple calculations of channel resistance and inductance. Experiments in the Z20 test stand are discussed in detail and the results compared to model calculations. Finally some conclusions are given which discuss possible reasons for discrepancies between model calculations and experiments.

2 FORMULATION

We now set up the channel problem. Our goal here is to carefully examine channel conditions using approximate formulas to get a feel for the processes occurring there and to eventually make improvements to the model Braginskii used in gas breakdown. We are assuming here that the channel density is much

lower than liquid water. A more rigorous treatment is used in the section on one dimensional modeling using ALEGRA-HEDP [11], [12] with Sesame equation of state tables and LMD conductivity model [14].

2.1 Hydrodynamic Equations

We first ignore viscosity and thermal conduction. Continuity of mass gives [15]

$$\frac{\partial \rho}{\partial t} + \nabla \cdot (\rho \underline{u}) = 0$$

where ρ is the volume mass density of the fluid and $\underline{u}$ is the particle velocity. Next we have Euler's equation of motion [15], [13]

$$\rho \frac{\partial \underline{u}}{\partial t} + \rho \left(\underline{u} \cdot \nabla \right) \underline{u} = -\nabla p + \underline{F}$$

where p is the pressure and the electromagnetic force density is

$$\underline{F} = \underline{J} \times \underline{B} + \rho_q \underline{E}$$

where $\underline{B}$ is the magnetic induction, $\underline{E}$ is the electric field intensity, and ρ_q is the electric charge density. Finally we have the equation of energy transfer

$$\frac{\partial}{\partial t} \left(\rho \varepsilon + \frac{1}{2} \rho u^2 \right) + \nabla \cdot \left[\rho \underline{u} \left(h + \frac{1}{2} u^2 \right) \right] = -q$$

where the enthalpy is

$$h = \varepsilon + p/\rho$$

the internal energy per unit mass is ε and the power removed by nonmechanical losses (radiation) and the electric field is [15], [13]

$$q = \nabla \cdot \underline{S} + \rho_q \underline{u} \cdot \underline{E}$$

where S is the radiation flux. The contribution to q is negative for power per unit volume generated by external sources, for example by Joule heating

$$-q_s = \underline{J} \cdot \underline{E}$$

Ohm's law relates the two quantities

$$\underline{J} = \sigma \underline{E}$$

where σ is the electric conductivity. The quantity $\rho \underline{u} \left(h + u^2/2 \right)$ is the energy flux density vector [16].

In cylindrical coordinates, with one dimension r (assuming axisymmetry and uniformity in the axial direction z), these three equations become

$$\frac{\partial \rho}{\partial t} + \frac{\partial (r \rho u)}{r \partial r} = 0 \tag{2}$$

$$\rho \left(\frac{\partial u}{\partial t} + u \frac{\partial u}{\partial r} \right) = -\frac{\partial p}{\partial r} - J_z B_\varphi \tag{3}$$

$$\frac{\partial}{\partial t} \left(\rho\varepsilon + \frac{1}{2}\rho u^2 \right) + \frac{\partial}{r\partial r} \left[r\rho u \left(\varepsilon + p/\rho + \frac{1}{2}u^2 \right) + rS_r \right] = J_z E_z \tag{4}$$

where σ, the electric conductivity in the z direction, relates J_z and E_z, and we have neglected any radial electric field.

2.2 Channel Approximation

If we integrate the energy equation (4) from $r = 0$ to $r = a(t)$ over the channel area we have

$$2\pi \int_0^a \frac{\partial}{\partial t} \left(\rho\varepsilon + \frac{1}{2}\rho u^2 \right) r\,dr + 2\pi a \left[\rho u \left(\varepsilon + p/\rho + \frac{1}{2}u^2 \right) + S_r \right] = 2\pi \int_0^a J_z E_z r\,dr$$

Below we give an argument for neglecting the skin effect in the channel. In this case the current density will be distributed according to the conductivity (constant electric field). Thus interchanging the time derivative and the integral in the first term we can write

$$2\pi \frac{\partial}{\partial t} \int_0^a \left(\rho\varepsilon + \frac{1}{2}\rho u^2 \right) r\,dr + p\frac{d}{dt}\left(\pi a^2 \right) + 2\pi a \left[\rho \left(u - \frac{da}{dt} \right) \left(\varepsilon + p/\rho + \frac{1}{2}u^2 \right) + S_r \right] = E_z 2\pi \int_0^a J_z r\,dr = IE_z \tag{5}$$

where I is the total channel current.

The first term is the time derivative of the energy in the channel

$$U = 2\pi \int_0^a \left(\rho\varepsilon + \frac{1}{2}\rho u^2 \right) r\,dr$$

The second term is the work done in expanding the channel radius. The radiated power leaving the channel is

$$Q_R = 2\pi a S_r$$

The Joule heat deposited in the channel is

$$Q_J = IE_z = I^2 / \left[2\pi \int_0^a \sigma r\,dr \right]$$

The particle velocity relative to the channel boundary is $u - da/dt$. Thus the time derivative of the mass M in the channel is

$$\frac{dM}{dt} = -2\pi a \rho \left(u - \frac{da}{dt} \right)$$

If we integrate the energy equation to a point slightly beyond the radius a (to a point just ahead of the channel boundary, but behind the shock front where the temperature, internal energy, and enthalpy have fallen) so that little energy is escaping, then

$$2\pi \frac{\partial}{\partial t} \int_0^a \left(\rho\varepsilon + \frac{1}{2}\rho u^2 \right) r\,dr + p\frac{d}{dt}\left(\pi a^2 \right) = I E_z$$

Taking the difference of this and (5) gives

$$2\pi a \left[\rho \left(u - \frac{da}{dt} \right) \left(\varepsilon + p/\rho + \frac{1}{2}u^2 \right) + S_r \right] = 0$$

which means that energy radiated from the channel is returned by means of the energy flux density vector $\varepsilon + p/\rho + \frac{1}{2}u^2$ associated with mass returning. From these two equations we can thus write

$$\frac{dU}{dt} + p\frac{dA}{dt} = Q_J$$

$$\left(\varepsilon + p/\rho + \frac{1}{2}u^2 \right) \frac{dM}{dt} = Q_R$$

where

$$A = \pi a^2$$

Note that the pressure in the first equation arose from the channel boundary term and is thus related to the value at the wall. If thermal conduction is taking place at the channel boundary we approximately add

$$Q_T = -2\pi a\kappa \frac{\partial T}{\partial r}$$

to the radiation loss, where κ is the thermal conductivity. We approximate the thermal conductivity by the electron conductivity κ_e which we take as the Wiedemann-Franz law value [17], [7]

$$\kappa_e = \frac{\pi^2}{3} \frac{k}{e^2} \left(kT \right) \sigma$$

where $e = 1.6 \times 10^{-19}$ C is the electronic charge and Boltzman's constant is $k = 1.38 \times 10^{-23}$ J/K. Now if we neglect the kinetic energy terms $u^2/2$ in comparison to the internal energy ε and the enthalpy $\varepsilon + p/\rho$ we obtain the system of equations derived by Braginskii [4]

$$\frac{dU}{dt} + p\frac{dA}{dt} = Q_J$$

$$\left(\varepsilon + p/\rho \right) \frac{dM}{dt} \approx Q_R$$

$$U \approx 2\pi \int_0^a \rho\varepsilon r\,dr$$

2.3   Channel Equation of State

The equation of state in the channel is taken to be the ideal gas law

$$p = (1 + \overline{m})\, nkT = (1 + \overline{m})\, (\rho/m_a)\, kT$$

where n is the atomic density, the mass per "average atom" is set to one third the mass of the water molecule

$$3m_a = 18 \left(1.67 \times 10^{-27} \text{kg} \right)$$

and the mean ionization per average atom is taken as $\overline{m}$. An approximate method for the calculation of this quantity is found in [15], which replaces the set of ionization energies with a continuous function and assumes that the number density of one ionization level $n\,(m)$ is peaked and dominant. In our case we simplify the calculation by assuming complete dissociation (with dissociation energy $D_{H_2O} = 9.6$ eV per molecule [20]) and complete ionization of the hydrogen (with $I_H = 13.6$ eV per atom [18]) and write the approximate equation for the mean oxygen ionization number $\overline{m}_O$ as [15]

$$I \left(\overline{m}_O + \frac{1}{2} \right) = (kT) \ln \left[2 \left(\frac{2\pi m_e}{2\pi \hbar^2} \right)^{3/2} \frac{(kT)^{3/2}}{n\overline{m}} \right]$$

where the average ionization number is

$$\overline{m} = \frac{2}{3} + \frac{1}{3}\overline{m}_O$$

with $m_e = 9.11 \times 10^{-31}$ kg equal to the electron mass and $\hbar = 1.055 \times 10^{-34}$ J-s Planck's constant. Of course in the above formula we are assuming $1 \leq \overline{m}_O$ since we have taken the hydrogen to be fully ionized. The ionization function for oxygen is taken as a linear interpolation of the discrete values [15]

$$I\,(x) = (I_{m+1} - I_m)\, x + m\,, \ m + 1 > x > m$$

and the oxygen ionization levels are $I_0 = 0$, $I_1 = 13.6$ eV, $I_2 = 35.1$ eV, $I_3 = 54.9$ eV, $I_4 = 77.4$ eV, $I_5 = 113.9$ eV, $I_6 = 138.1$ eV, $I_7 = 739.3$ eV , $I_8 = 871.4$ eV [15], [18], [19]. This indicates that for temperatures between 5 eV and 60 eV and densities below 12% per cent of water the values of $\overline{m}$ approximately vary between 1 and 2.7 (the inner two K shell electrons are not removed to any appreciable extent, at least at lower densities). In fact between 25 eV and 60 eV and densities less than 4% of water (typical channel densities and temperature) it is a reasonable approximation to fix $\overline{m} \approx 8/3$.

It is also useful to define the effective adiabatic exponent as [15]

$$\frac{p}{\varepsilon \rho} = \gamma - 1$$

We write the internal energy per unit volume as [15]

$$\rho\varepsilon = \frac{3}{2} n\,(1 + \overline{m})\, kT + \frac{1}{3} n D_{H_2O} + \frac{2}{3} n I_H + \frac{1}{3} n Q\,(\overline{m}_O)$$

where the sum of the ionization energies is

$$Q\,(x) = (x - m)\,(I_{m+1} - I_m) + \sum_{p=0}^{m} I_p \ , \ m < x < m + 1$$

Noting that $Q\,(6) \approx 433$ eV we see that the effective adiabatic exponent in the channel is typically

$$\gamma \approx 1 + \frac{(1+2.66)\,kT}{\frac{3}{2}\,(1+2.66)\,kT + \frac{1}{3}9.6 \text{ eV} + \frac{2}{3}13.6 \text{ eV} + \frac{1}{3}433 \text{ eV}} \approx 1.31 - 1.45$$

in the range between 25 eV to 60 eV. It seems reasonable to select it at $\gamma \approx 1.35$ to capture the later time values of the channel temperature.

2.4   Channel Radiation

Braginskii [4] included channel radiation as "open" radiation in gas breakdown channels which were assumed to be nearly transparent. The formula used for radiation first involves the calculation of the mean free path [15]. There are several contributions to absorption; there are free - free transitions, free - bound transitions, and bound - bound transitions. Calculations [15] indicate that the presence of oxygen makes the bound - free component substantially larger than the free - free component. Thus we will focus on this component here. Generalization of the formulas [15] to a two component mixture of hydrogen and oxygen gives a mean free path based on the inverse of average absorption

$$\ell_A \approx \frac{(kT)^{9/2}}{\overline{m}\,(1+\overline{m})^2\,n^2 I\,(\overline{m}+1/2)}\left(1.13 \times 10^{113} \text{ J}^{-7/2}\text{m}^{-5}\right) \Rightarrow$$

$$\approx \frac{(kT)^{9/2}}{n\overline{m}\left\{\frac{2}{3}n\,(2)^2\,I_H + \frac{1}{3}n\,(\overline{m}_O+1)^2\,I\,(\overline{m}_O+1/2)\right\}}\left(1.13 \times 10^{113} \text{ J}^{-7/2}\text{m}^{-5}\right) \approx 1/\left(5.3 \times 10^4 \text{ m}^{-1}\right)$$

and the Rosseland average mean free path

$$\ell_R \approx \frac{(kT)^{7/2}}{\overline{m}\,(\overline{m}+1)^2\,n^2}\left(4.5 \times 10^{112} \text{ J}^{-7/2}\text{m}^{-5}\right) \Rightarrow$$

$$\approx \frac{(kT)^{7/2}}{n\overline{m}\left\{\frac{2}{3}n\,(2)^2 + \frac{1}{3}n\,(\overline{m}_O+1)^2\right\}}\left(4.5 \times 10^{112} \text{ J}^{-7/2}\text{m}^{-5}\right) \approx 1/\left(3.1 \times 10^4 \text{ m}^{-1}\right)$$

where the final values result from the example $T = 322,000^o$ K (28 eV), $n = 2.5 \times 10^{27}$ m^{-3} (2.5% water density). In the open radiation limit $a << \ell_P$ we expect the total radiation to be proportional to the channel area and it is given by [15]

$$Q_R = \pi a^2 4\sigma_S T^4/\ell_A \,,\ a << \ell_A$$

where $\sigma_S = 5.67 \times 10^{-8}$ W/$\left(\text{m}^2\text{K}^4\right)$ is the Stefan-Boltzman constant. Thermal heat conduction at the boundary of the channel would also have to be accounted for in this open limit [4]. In the black body limit $a >> \ell_R$ we expect the total radiation to be proportional to the channel perimeter and given by

$$Q_R = 2\pi a\sigma_S T^4 \,,\ a >> \ell_R$$

In this limit it seems reasonable to assume that heat conduction with enhancements from radiation $16\sigma_s T^3\ell_R/3$ [15], operates inside the channel to maintain an approximate isothermal region; because of the steep discontinuity in temperature at the channel boundary, the black body power is lost to the wall. Note that for $a = 20$ μm in the above example we have

$$a/\ell_R = 0.62$$

and that for this channel radius the channel resistance is typically large compared to other drive circuit impedance elements. Note also that $2a/\ell_A = 1$ (corresponding to the transition between the two formulas) at $a = 10\ \mu$m in this example. Thus we will assume that black body radiation is a reasonable approximation as the channel expands to radii for which there is substantial resistive fall in the spark circuit model. This is in contrast to what is assumed in the low density gas breakdown channels [4]. At early times, when the temperature is rising, we expect the radiation to be unimportant.

2.5   Channel Conductivity

The channel conductivity model is taken as the Spitzer form [21], [22]

$$\sigma = \frac{8}{\pi} \frac{(4\pi\varepsilon_0)^2}{\sqrt{2\pi m_e}} \frac{(kT)^{3/2}}{\overline{Z} e^2 \ln\Lambda} \tag{6}$$

The Coulomb logarithm is taken from the nondegenerate limit of [23] as

$$\ln\Lambda = \ln\sqrt{1 + b_{\max}^2/b_{\min}^2}$$

where the maximum impact parameter is taken as the Debye screening value [24],[23]

$$b_{\max} = \sqrt{\frac{\varepsilon_0 kT}{ne^2\overline{m}\left(1 + \overline{Z}\right)}}$$

and the minimum impact parameter is taken, for example, as the larger of the classical value or by the value obtained from the uncertainty principle [23]

$$b_{\min} = \max\left[\left(\frac{\overline{Z}e^2}{12\pi\varepsilon_0 kT}\right), \frac{\pi\hbar}{(3m_e k)^{1/2}}\right]$$

When the Coulomb logarithm $\ln\Lambda$ is less than 2 it is set equal to this value [23]. For a mixture of gases we use the average value [15]

$$\overline{Z} = \left(\frac{2}{3} + \frac{1}{3}\overline{m}_O^2\right)/\overline{m}$$

To get a feel for the behavior of the conductivity we have plotted the results from this formula with fixed $\overline{m} = 8/3$ and $\overline{m}_O = 6$, versus results from the Lee-Moore-Desjarlais (LMD) model [14] used in the ALEGRA-HEDP simulations [11], [12]. The Spitzer formula (6) with fixed ionization number and the saturation value for the Coulomb logarithm can be written as

$$\sigma = (kT)^{3/2}\ 5.4 \times 10^{31}\ \mathrm{S}/\left(\mathrm{m\text{-}J}^{3/2}\right) \tag{7}$$

is shown as the green curve in the figure.

Also shown as the red curve is the linear approximation [7]

$$\sigma = (kT)\,\sigma_0\,,\ \sigma_0 = 1.6 \times 10^{23}\ \mathrm{S}/\left(\mathrm{J\text{-}m}\right) \tag{8}$$
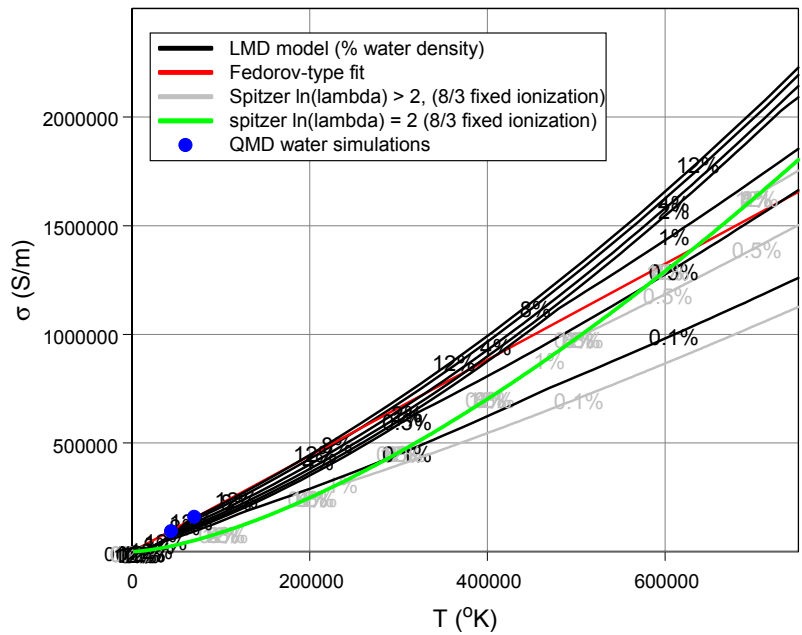
Figure 5. Comparison of Spitzer formula (grey curves) and LMD model [14], [11] (black curves) for various densities from 0.1% of water to 12% of water. Also shown is a linear Fedorov-type fit (red curve) and Spitzer's model with fixed Coulomb logarithm (green curve). The blue dots are QMD calculations (from [25]).

The coefficient σ_0 was estimated previously [7] as 0.8×10^{23} S/(J-m), however this has been modified in the plot to fit the behavior with several percent water density to about 40 eV (which bounds the typical channel temperature except at very early times). These two formulas will be used in the zero dimensional lumped model calculations.

2.5.1 influence of magnetic field

The magnetic field influence on the conductivity is now estimated. The electron relaxation time is estimated from the formula (using $T = 42$ eV, $\ln \Lambda = 2$, $n_i = 80 \left(10^{26}\right)/\text{m}^3$, $\overline{Z} = 4.7$) [23]

$$\tau_e = \frac{3}{4}\sqrt{\frac{m_e}{2\pi}} \frac{(4\pi\varepsilon_0)^2 (kT)^{3/2}}{\overline{Z}^2 n_i e^4 \ln \Lambda} = \frac{3\pi}{32} \frac{m_e \sigma}{e^2 \overline{Z} n} \approx 2.7 \times 10^{-16} \text{ s}$$

This value could be increased by as much as a factor of 4 for densities approaching 2% of water, giving 1.1×10^{-15} s. The electron gyro frequency is

$$\omega_e = \frac{eB}{m_e} = \frac{e\mu_0 I}{m_e 2\pi a}$$

where $\mu_0 = 4\pi \times 10^{-7}$ H/m is the permeability of free space. If we use the Martin formula for the ramp current we have

$$a^2(t) = \frac{3}{5}\left(\frac{4I_0^2 t^5}{\tau^2 \pi^2 \rho_0 \xi \sigma}\right)^{1/3}$$

and setting $t^{1/6} = \tau_e^{1/6}$, to maximize the result ($\sigma = 1.25 \times 10^6$ S/m, $I_0 = 300$ kA, $\rho_0 = 10^3$ kg/m^3, $\tau = 15$ ns), gives

$$\omega_e = \frac{eB}{m_e} = \frac{5^{1/2} e\mu_0 \sigma^{1/6} \xi^{1/6} \rho_0^{1/6} I_0^{2/3}}{2^{4/3} 3^{1/2} \pi^{2/3} m_e \tau^{1/2}} \approx 8.1 \times 10^{13} \text{ radians}/s$$

The typical value is then $\omega_e \tau_e = 0.022$ and $\omega_e \tau_e/(1 + \omega_e \tau_e) < 0.02$. But in the worst case it could be as much as $\omega_e \tau_e = 0.09$ and $\omega_e \tau_e/(1 + \omega_e \tau_e) < 0.08$. The table in [23] indicates that the magnetic field would result in less than a 10% reduction in conductivity. Thus we will ignore this effect. The small nature of the change is consistent with ALEGRA-HEDP simulations where almost no difference was exhibited by the two components of electrical conductivity.

2.5.2 skin effect

From Maxwell's equations (without displacement current)

$$\nabla \times \underline{E} = -\mu_0 \frac{\partial}{\partial t}\underline{H}$$

$$\nabla \times \underline{H} = \sigma \underline{E}$$

and the continuity equation (with no electric charge)

$$\nabla \cdot \underline{J} = \nabla \cdot (\sigma \underline{E}) = \nabla \sigma \cdot \underline{E} + \sigma \nabla \cdot \underline{E} = 0$$

we find

$$\nabla \times \nabla \times \underline{E} = \nabla \left(\nabla \cdot \underline{E} \right) - \nabla^2 \underline{E} = -\nabla \left(\frac{1}{\sigma} \nabla \sigma \cdot \underline{E} \right) - \nabla^2 \underline{E} = -\mu_0 \frac{\partial}{\partial t} \left(\sigma \underline{E} \right)$$

or

$$\nabla^2 E_z = \left(\frac{\partial^2}{\partial r^2} + \frac{1}{r} \frac{\partial}{\partial r} \right) E_z = \mu_0 \frac{\partial}{\partial t} \left(\sigma E_z \right)$$

where $\underline{H}$ is the magnetic field intensity. Now if we take σ to be a constant, as far as the electromagnetic problem is concerned, we have

$$\left(\frac{\partial^2}{\partial r^2} + \frac{1}{r} \frac{\partial}{\partial r} \right) E_z = \mu_0 \sigma \frac{\partial}{\partial t} E_z$$

Letting $\zeta = r \sqrt{\mu_0 \sigma / (4t)}$ and $E_z = t^\alpha F(\zeta)$ gives the ordinary differential equation

$$F'' + (2\zeta + 1/\zeta) F' - 4\alpha F = 0$$

If we instead consider a planar approximation

$$\frac{\partial^2}{\partial r^2} E_z = \mu_0 \sigma \frac{\partial}{\partial t} E_z$$

Letting $\zeta = (a - r) \sqrt{\mu_0 \sigma / (4t)}$ and $E_z = t^\alpha F(\zeta)$ gives the ordinary differential equation

$$F'' + 2\zeta F' - 4\alpha F = 0$$

For a step voltage $\alpha = 0$

$$E_z = E_0 \text{erfc} (\zeta)$$

At the center (really a distance a away from the surface, since this is a planar approximation) $\zeta_0 = a / \sqrt{4t / (\mu_0 \sigma)}$ and we can write

$$E_z / E_0 \sim 1 - \frac{2}{\sqrt{\pi}} \zeta_0 = 1 - a/\delta = 1 - a / \sqrt{\pi t / (\mu_0 \sigma)}, \ \zeta_0 << 1$$

$$\sim \frac{1}{\sqrt{\pi} \zeta_0} e^{-\zeta_0^2} = \frac{1}{a} \sqrt{4t / (\pi \mu_0 \sigma)} \exp \left[-\frac{a^2}{4t / (\mu_0 \sigma)} \right], \ \zeta_0 >> 1 \quad (9)$$

If $\sigma = 10^6$ S/m and $t = 100$ ns, $\sqrt{\pi t / (\mu_0 \sigma)} = 500 \ \mu$m, which seems to justify neglecting the skin effect in the channel (particularly at early time, because the channel is expanding). Braginskii [4] indicates that when the penetration depth is larger than the radius we can also neglect magnetic forces in the channel (the $J_z B_\varphi$ term in (3) above). We will say more on this approximation in the next subsection.

2.5.3 losses on metallic poles

The skin effect losses on the metallic poles at the ends of the gap are now estimated. First the surface electric field E_0 created by an electric surface current or surface magnetic field H_0 can be written for an infinitely deep linear metal as the Riemann-Liouville fractional derivative [26], [27]

$$E_0 = \sqrt{\mu_0/\sigma} \frac{d^{1/2}}{dt^{1/2}} H_0$$

provided $H_0(t) = o(t^{-1/2})$ as $t \to 0$. When $H_0(t)$ is proportional to t^r we use the result $\frac{d^{1/2}}{dt^{1/2}} t^\beta = \frac{\Gamma(\beta+1)}{\Gamma(\beta+1/2)} t^{\beta-1/2}$, where $\Gamma(x)$ is the gamma function. For a step excitation $\beta = 0$

$$E_0/H_0 = \sqrt{\frac{\mu_0}{\pi t \sigma}}$$

For 304 stainless steel with $\sigma = 1.4 \times 10^6$ S/m, and taking $t = 50$ ns, this gives a surface impedance of 2.4 mohms. The contribution from the rod is then

$$Z_r \approx \frac{1}{2\pi} \left[\frac{\ell_r}{b_r} + \ln(b_r/a) \right] E_0/H_0$$

If we set $\ell_r/b_r \approx 8$ and $b_r/a \approx 25$ we find $Z_r \approx 4.2$ mohms. The other side with the spherical rods gives roughly 2 mohms. These values are small and can be neglected.

2.6   Shock Approximation

Integrating the equations of conservation of mass (2) and motion (3) across the shock front at $r = a_c(t)$ gives

$$\rho u = \rho_0 u_0 = \rho_0 \frac{da_c}{dt}$$

$$\rho_0 u_0^2 - \rho u^2 = \rho_0 \left(\frac{da_c}{dt} \right)^2 - \rho u^2 = p - p_0$$

where we have replaced the particle velocity ahead of the shock (relative to the shock front) by the shock velocity. The equation of state for water is well studied. A simple form for pressures that are not too high is

$$p = c_1 (\rho/\rho_0)^{\gamma_1} - c_2$$

where $c_1 = 3001$ bar $= 3.001 \times 10^8$ Pa, $c_2 = 3000$ bar $= 3 \times 10^8$ Pa, $\gamma_1 = 7$ [28], [15]. Thus from the equations of mass and of motion, assuming $p >> p_0$, we find

$$\rho_0 \left(\frac{da_c}{dt} \right)^2 \left[1 - \frac{1}{(p/c_1 + c_2/c_1)^{1/\gamma_1}} \right] = p$$

The coefficient in brackets is slowly varying and has a value near 0.5 for pressures in the $2 - 3$ megabar range. However we must connect the pressure with the velocity of the channel wall. Braginskii [4] modified this coefficient to approximate the pressure as

$$p = K_p \rho_0 \left(\frac{da}{dt} \right)^2 \tag{10}$$

This is probably a point where improvements can be introduced by keeping track of the two front locations a and a_c. At the present time we will stick with Braginskii's approximation but modify the value of the coefficient K_p to better represent the pressures observed in the one dimensional simulations. The value of K_p seems to range from $2 - 3$. It seems reasonable to select it as $K_p \approx 2$ [10] since this value was most

often observed in both voltage and current drives.

If we examine the contribution to the pressure from the magnetic term in (3) by integration in r

$$p = p_0 + \int_r^a J_z B_\varphi dr' \approx p_0 + \frac{\mu_0 I^2}{4\pi^2 a^2} \left(1 - r^2/a^2\right) \tag{11}$$

where we have assumed that p_0 is nearly uniform over the channel (and represents the approximate pressure at the channel wall) and we have assumed that the electric current density is uniformly distributed in the channel with $B_\varphi = \mu_0 I r / \left(2\pi a^2\right)$. The average is

$$\langle p \rangle = \frac{2\pi}{\pi a^2} \int_0^a pr dr \approx p_0 + \frac{\mu_0 I^2}{8\pi^2 a^2}$$

Thus if we take p to be p_0 in the relation (10) we can replace the relation by

$$\langle p \rangle = K_p \rho_0 \left(\frac{da}{dt}\right)^2 + \frac{\mu_0 I^2}{8\pi^2 a^2}$$

This takes account of the effect of the magnetic force on the pressure average. Note that the magnetic term is not necessarily small in this application despite that fact that skin effect is not observed in the current. If the magnetic term is included then the value of K_p is reduced. The relation above (10) increased the value of K_p to approximately account for this extra term and this was used in the lumped model simulations. Over the time regime examined, the predictions for channel temperature, pressure, density, radius, and resistance per unit length are similar for the two models and agree reasonably well with the one-dimensional simulations.

3   ZERO DIMENSIONAL LUMPED MODEL

This section discusses solutions to the zero dimensional lumped model. First we summarize the system of equations.

3.1   Equations for Lumped Model

We now consider the channel temperature, density, and pressure to be replaced by average quantities over the channel area

$$U = \rho \varepsilon A$$

$$M = \rho A$$

For definiteness in comparing to one dimensional simulations we consider each of these quantities to be slowly varying over the channel and take the average by means of

$$\langle X \rangle = \frac{1}{A} 2\pi \int_0^a X\left(r\right) r dr$$

If we expand the slowly varying function $X = T, \rho, p$ in a power series about some internal point r_0

$$X(r) = X(r_0) + X'(r_0)(r - r_0) + \cdots$$

and insert this into the average integral

$$\langle X \rangle = X(r_0) + X'(r_0)\frac{1}{A}2\pi\int_0^a (r - r_0)\, r\, dr + \cdots$$

we see that the first order term vanishes if we choose

$$r_0 = \frac{2}{3}a$$

This radial point will be used to pick off values of the one dimensional simulations of the next section to compare to the zero dimensional results. This approximate approach could be made more precise by using integration of the one dimensional results, but the preceding simple approximation is thought to be reasonably accurate. The one exception is the channel resistance value in the one dimensional simulations, which will be found from the integral definition

$$\ell/R = 2\pi\int_0^b \sigma r\, dr \tag{12}$$

where b is the outer radial boundary of the simulation.

The system can thus be written as

$$\frac{d}{dt}\left(\frac{p}{\gamma - 1}A\right) + p\frac{dA}{dt} = \frac{I^2}{A\sigma} \tag{13}$$

$$\frac{\gamma}{\gamma - 1}\frac{p}{\rho}\frac{d}{dt}(\rho A) = Q_R = \sqrt{4\pi A}\sigma_S T^4 \tag{14}$$

$$p = K_p\rho_0\frac{1}{4\pi A}\left(\frac{dA}{dt}\right)^2 \tag{15}$$

The unknowns are A, p, T; the average density ρ can be eliminated by use of the gas law (in terms of the average pressure and temperature)

$$p = (1 + \overline{m})(\rho/m_a)kT \tag{16}$$

and the average ionization number can be found from

$$I\left(3\overline{m} - \frac{3}{2}\right) = (kT)\ln\left[2\left(\frac{2\pi m_e}{2\pi\hbar^2}\right)^{3/2}\frac{(kT)^{3/2}}{(\rho/m_a)\overline{m}}\right]$$

For channel conditions prevailing after the initial rise in temperature it is reasonable to fix $\overline{m} \approx 8/3$, the effective adiabatic exponent $\gamma \approx 1.35$, and the coefficient $K_p \approx 2$. The conductivity is taken as the power law

$$\sigma = \sigma_0(kT)^v \tag{17}$$

where the linear Fedorov approximation $v = 1$ uses $\sigma_0 \approx 1.6 \times 10^{23}$ S/(m-J) and the Spitzer case uses $v = 1.5$ and $\sigma_0 \approx 5.4 \times 10^{31}$ S/$\left(\text{m-J}^{3/2}\right)$.

3.1.1 voltage and circuit drives

The above system is complete for known current drives $I(t)$. However if a circuit drive is desired we must add an additional circuit equation. In the case of a voltage source V_0, drive circuit resistance R_0, switch inductance L, and switch resistance R, the extra equation is

$$V_0 = R_0 I + \frac{d}{dt}(LI) + RI \tag{18}$$

The switch resistance is

$$R = \frac{\ell}{\sigma A} \tag{19}$$

and the switch inductance for a coaxial return at distance b is

$$L = \frac{\mu_0 \ell}{2\pi}\left[\frac{1}{4} + \ln\left(\frac{b}{a(t)}\right)\right] \tag{20}$$

where the first term is the internal inductance of the channel and the second term is the external inductance. The coaxial return distance in the ALEGRA-HEDP simulations was taken to be $b = 1$ mm. Because the logarithm is slowly varying we can include its effect as a perturbation to the switch voltage; the equation can be solved first without it and then its contribution can be added using the previously determined current waveform. Note that to compare simulation results to experiments a correction inductance must be added to conform with the experimental geometry.

3.2 Behavior of Solution

We now examine behaviors of the solution using similarity analysis of the equations, including only parts of the channel losses in each subsubsection.

3.2.1 early time exact differential solution

The growth of the temperature at early time can be captured by ignoring the radiation term (and the thermal conduction term) and writing

$$\frac{d}{dt}\left(\frac{p}{\gamma - 1}A\right) + p\frac{dA}{dt} = \frac{I^2}{A\sigma}$$

$$\frac{d}{dt}(\rho A) = 0$$

$$p = K_p \rho_0 \frac{1}{4\pi A}\left(\frac{dA}{dt}\right)^2$$

The second equation implies constant channel mass and density inversely proportional to the channel area

$$\rho = \rho_0 A_0 / A$$

36

$$pA/A_0 = (1 + \overline{m})(\rho_0/m_a)kT$$

$$\sigma = (kT)^v \sigma_0 = \frac{(pA)^v / A_0^v}{(1 + \overline{m})^v (\rho_0/m_a)^v} \sigma_0$$

Thus

$$A(Ap)^v \left[\frac{d}{dt}\left(\frac{p}{\gamma - 1}A\right) + p\frac{dA}{dt} \right] = (1 + \overline{m})^v (\rho_0/m_a)^v (A_0^v/\sigma_0) I^2$$

or

$$\left(\frac{dA}{dt}\right)^{2v} \left[\frac{1}{(\gamma - 1)}A\frac{d}{dt}\left(\frac{dA}{dt}\right)^2 + \left(\frac{dA}{dt}\right)^3 \right] = \left(\frac{4\pi}{K_p\rho_0}\right)^{1+v} (1 + \overline{m})^v (\rho_0/m_a)^v (A_0^v/\sigma_0) I^2$$

$$\frac{d}{dt}\left[A\left(\frac{dA}{dt}\right)^{2+2v} \right] + A\left(\frac{dA}{dt}\right)^{2v} \left[\frac{1}{(\gamma - 1)} - (1 + v) \right] \frac{d}{dt}\left(\frac{dA}{dt}\right)^2 = \left(\frac{4\pi}{K_p\rho_0}\right)^{1+v} (1 + \overline{m})^v (\rho_0/m_a)^v (A_0^v/\sigma_0) I^2$$

Now if we take $\gamma \approx 1.4$ then the second term vanishes if $v = 1.5$ (this exact differential approach has been used before [29]). Thus for the Spitzer-type conductivity function and this value of the adiabatic exponent

$$A\left(\frac{dA}{dt}\right)^5 = \left(\frac{4\pi}{K_p\rho_0}\right)^{5/2} (1 + \overline{m})^{3/2} (\rho_0/m_a)^{3/2} \left(A_0^{3/2}/\sigma_0\right) \int_0^t I^2(\tau)\,d\tau$$

$$\frac{5}{6}A^{6/5}(t) = \left(\frac{4\pi}{K_p\rho_0}\right)^{1/2} (1 + \overline{m})^{3/10} (\rho_0/m_a)^{3/10} \left(A_0^{3/10}/\sigma_0^{1/5}\right) \int_0^t \left[\int_0^{t'} I^2(\tau)\,d\tau \right]^{1/5} dt'$$

3.2.2 similarity solutions for early time expansion

A power law solution for linear current rise

$$I(t) = I_0 t^j$$

using

$$A(t) = A_0 t^\alpha$$

is

$$A_0^{2v+3} \alpha^{2v+3} t^{(2v+3)(\alpha-1)} \left[\frac{1}{(\gamma - 1)} 2(1 - 1/\alpha) + 1 \right] = \left(\frac{4\pi}{K_p\rho_0}\right)^{1+v} (1 + \overline{m})^v (\rho_0/m_a)^v (A_0^v/\sigma_0) I_0^2 t^{2j}$$

Thus

$$\alpha = 1 + \frac{j}{v + 3/2}$$

If $j = 1$ and $v = 1$ then $\alpha = 7/5$ and the radius expansion rate is $O\left(t^{0.7}\right)$. If $j = 1$ and $v = 3/2$ then $\alpha = 4/3$ and the radius expansion rate is $O\left(t^{2/3}\right)$. If $j = 0$ then $\alpha = 1$ and the radius expansion rate is $O\left(t^{1/2}\right)$.

3.2.3 heat conduction and similarity solution

If heat conduction is added

$$\frac{\gamma}{\gamma - 1}\frac{p}{\rho}\frac{d}{dt}\left(\rho A\right) = Q_T = -2\pi a \kappa\left(T\right)\frac{\partial T}{\partial r}$$

If use the approximation used by Braginskii [4] for the thermal gradient $-\partial T/\partial r \approx 1.3\left(T/a\right)$, and using electronic heat conduction with the electrical conductivity law $\sigma = \sigma_0 T^v$, we then have the system

$$\frac{d}{dt}\left(\frac{p}{\gamma - 1}A\right) + p\frac{dA}{dt} = \frac{I^2}{A\sigma_0 T^v}$$

$$\frac{\gamma}{\gamma - 1}\frac{p}{\rho}\frac{d}{dt}\left(p\frac{\rho}{p}A\right) = 1.3\frac{2}{3}\frac{\pi^3}{e^2}\sigma_0\left(kT\right)^{v+2}$$

$$p = K_p\rho_0\frac{1}{4\pi A}\left(\frac{dA}{dt}\right)^2$$

$$p/\rho = \left(\frac{1 + \overline{m}}{m_a}\right)kT$$

which can be reduced to a system for A and T alone

$$\frac{d}{dt}\left[\frac{1}{\gamma - 1}\left(\frac{dA}{dt}\right)^2\right] + \frac{1}{A}\left(\frac{dA}{dt}\right)^3 = \frac{4\pi}{K_p\rho_0}\frac{I^2}{A\sigma_0 T^v}$$

$$\frac{\gamma}{\gamma - 1}\left(\frac{1 + \overline{m}}{m_a}\right)kT\frac{d}{dt}\left[\left(\frac{m_a}{1 + \overline{m}}\right)\frac{1}{kT}\left(\frac{dA}{dt}\right)^2\right] = 1.3\frac{2}{3}\frac{4\pi}{K_p\rho_0}\frac{\pi^3}{e^2}k^{v+2}\sigma_0 T^{v+2}$$

If we take $\overline{m}$ to be fixed (or slowly varying) and substitute

$$I\left(t\right) = I_0 t^j$$

$$A\left(t\right) = A_0 t^\alpha$$

$$T\left(t\right) = T_0 r^\tau$$

we find

$$\left[\frac{2}{\gamma - 1}\left(1 - 1/\alpha\right) + 1\right]A_0^2\alpha^3 t^{2\alpha - 3} = \frac{4\pi}{K_p\rho_0}\frac{I_0^2}{A_0\sigma_0 T_0^v}t^{2j - v\tau - \alpha}$$

$$\frac{\gamma}{\gamma-1}A_0^2\alpha^2\left(2\alpha-2-\tau\right)t^{2\alpha-3}=1.3\frac{2}{3}\frac{4\pi}{K_p\rho_0}\frac{\pi^3}{e^2}k^{2+v}\sigma_0T_0^{v+2}t^{v\tau+2\tau}$$

and thus

$$2j-v\tau-\alpha=2\alpha-3=\tau v+2\tau$$

$$3\alpha=2j+3-v\tau$$

$$\tau=\frac{4j-3}{6+5v}$$

$$\alpha=1+\frac{2}{3}j+\frac{v}{3}\frac{3-4j}{6+5v}$$

First we take a ramp $j=1$

$$\tau=1/\left(6+5v\right)$$

$$\alpha=\frac{10+8v}{6+5v}$$

For $v=1$ this gives $\tau=1/11\approx0.0909$ and $\alpha=18/11\approx2\,(0.818)$. For $v=5/4$ this gives $\tau=4/49\approx0.0816$ and $\alpha=80/49\approx2\,(0.816)$. For $v=3/2$ this gives $\tau=2/27\approx0.0741$ and $\alpha=44/27\approx2\,(0.815)$. We thus see with thermal diffusion present the temperature is nearly constant in time and the radius grows like $O\left(t^{0.8}\right)$. The pressure is $O\left(t^{\alpha-2}\right)$ and the density is $O\left(t^{\alpha-2-\tau}\right)$.

Next we examine a constant current $j=0$

$$\tau=-\frac{3}{6+5v}$$

$$\alpha=1+\frac{v}{6+5v}$$

For $v=1$ this gives $\tau=-3/11\approx-0.273$ and $\alpha=12/11\approx2\,(0.545)$. For $v=5/4$ this gives $\tau=-12/49\approx-0.245$ and $\alpha=54/49\approx2\,(0.551)$. For $v=3/2$ this gives $\tau=-6/27\approx-0.222$ and $\alpha=30/27\approx2\,(0.555)$. We thus see with thermal diffusion present and the current constant, the temperature decreases as the quarter root of time $O\left(t^{-0.25}\right)$ and and the radius grows like $O\left(t^{0.55}\right)$. The pressure is $O\left(t^{\alpha-2}\right)$ and the density is $O\left(t^{\alpha-2-\tau}\right)$.

The approximation $-\partial T/\partial r\approx1.3\left(T/a\right)$ used by Braginskii and given above can also be viewed from the typical temperature profiles produced in nonlinear heat conduction [15]. With electron thermal conductivity $\kappa_e=O\left(T^{1+v}\right)$, for an impulsive plane source [15] the temperature profile is similar to that in the cylindrical problem

$$T\approx T_0\left(1-r^2/a^2\right)^{1/(v+1)} \tag{21}$$

The actual distributed, time-dependent, source may cause changes to this profile (for example, an increasing

ramp at late time, causes changes that can be observed in the no radiation one-dimensional example below). The average temperature for this profile is

$$\langle T \rangle = T_0 \frac{2\pi}{\pi a^2} \int_0^a \left(1 - r^2/a^2\right)^{1/(v+1)} r\,dr = \frac{v+1}{v+2} T_0$$

Taking the mean value of the heat conduction term for this profile (of course this is weighted toward the largest radius) gives

$$-\left\langle T^{1+v} \frac{\partial T}{\partial r} \right\rangle = T_0^{1+v}\left(T_0/a\right) \frac{2\pi}{\pi a^2} \frac{2}{v+1} \int_0^a \left(r^2/a\right)\left(1 - r^2/a^2\right)^{1/(v+1)} dr$$

$$= \langle T \rangle^{v+1}\left(\langle T \rangle / a\right) \frac{2}{v+1} \frac{\Gamma\left(3/2\right)\Gamma\left\{1 + 1/\left(v+1\right)\right\}}{\Gamma\left\{5/2 + 1/\left(v+1\right)\right\}} \left(\frac{v+2}{v+1}\right)^{v+2}$$

which for $v = 1$ gives

$$-\left\langle T^2 \frac{\partial T}{\partial r} \right\rangle = \left(\langle T \rangle^{v+2}/a\right) \frac{\pi}{8}\left(\frac{3}{2}\right)^3 = \langle T \rangle^{v+1} 1.3\left(\langle T \rangle / a\right)$$

It is of interest to determine where the radiation and electron heat conduction terms are equivalent

$$\sqrt{4\pi A}\sigma_S T^4 = 2\pi\left(1.3\right)\kappa_e T = 1.3 \frac{2}{3}\frac{\pi^3}{e^2} k^{2+v}\sigma_0 T^{v+2}$$

The case $v = 1$ yields

$$T = 1.3\frac{1}{3}\frac{\pi^2}{e^2}\frac{k^{2+1}}{a}\sigma_0/\sigma_S = 1.24\ \text{K-m}/a = 1.24 \times 10^5\ \text{K (10.7 eV) for } a = 10\ \mu\text{m}$$

Therefore for the later time phase of the expansion the black body radiation is larger than the electron diffusion alone.

3.2.4 radiation and similarity solution

If black body radiation is used

$$\frac{\gamma}{\gamma - 1}\frac{p}{\rho}\frac{d}{dt}\left(\rho A\right) = Q_R = 2\pi a\sigma_S T^4 = \sqrt{4\pi A}\sigma_S T^4$$

we then have the system

$$\frac{d}{dt}\left(\frac{p}{\gamma - 1}A\right) + p\frac{dA}{dt} = \frac{I^2}{A\sigma_0 T^v}$$

$$\frac{\gamma}{\gamma - 1}\frac{p}{\rho}\frac{d}{dt}\left(p\frac{\rho}{p}A\right) = \sqrt{4\pi A}\sigma_S T^4$$

$$p = K_p\rho_0\frac{1}{4\pi A}\left(\frac{dA}{dt}\right)^2$$

$$p/\rho = \left(\frac{1+\overline{m}}{m_a}\right) kT$$

which can be reduced to a system for A and T alone

$$\frac{d}{dt}\left[\frac{1}{\gamma-1}\left(\frac{dA}{dt}\right)^2\right] + \frac{1}{A}\left(\frac{dA}{dt}\right)^3 = \frac{4\pi}{K_p\rho_0}\frac{I^2}{A\sigma_0 T^v}$$

$$\frac{\gamma}{\gamma-1}\left(\frac{1+\overline{m}}{m_a}\right) kT \frac{d}{dt}\left[\left(\frac{m_a}{1+\overline{m}}\right)\frac{1}{kT}\left(\frac{dA}{dt}\right)^2\right] = \frac{\sigma_S\left(4\pi\right)^{3/2}}{K_p\rho_0}\sqrt{A}T^4$$

If we take $\overline{m}$ to be fixed (or slowly varying) and substitute

$$I\left(t\right) = I_0 t^j$$

$$A\left(t\right) = A_0 t^\alpha$$

$$T\left(t\right) = T_0 r^\tau$$

we find

$$\left[\frac{2}{\gamma-1}\left(1-1/\alpha\right)+1\right] A_0^2\alpha^3 t^{2\alpha-3} = \frac{4\pi}{K_p\rho_0}\frac{I_0^2}{A_0\sigma_0 T_0^v}t^{2j-v\tau-\alpha}$$

$$\frac{\gamma}{\gamma-1}A_0^2\alpha^2\left(2\alpha-2-\tau\right)t^{2\alpha-3} = \frac{\sigma_S\left(4\pi\right)^{3/2}}{K_p\rho_0}A_0^{1/2}T_0^4 t^{4\tau+\alpha/2}$$

and thus

$$2j - v\tau - \alpha = 2\alpha - 3 = 4\tau + \alpha/2$$

or

$$\tau = \frac{2j-3}{8+v}$$

$$\alpha = 1 + \frac{2}{3}j - \frac{v}{3}\frac{2j-3}{8+v}$$

For a linear ramp $j = 1$

$$\tau = -1/\left(8+v\right)$$

$$\alpha = 2 - \frac{8/3}{8+v}$$

For $v = 1$ this gives $\tau = -1/9 \approx -0.111$ and $\alpha = 46/27 \approx 2\left(0.852\right)$. For $v = 5/4$ this gives

$\tau = -4/37 \approx -0.1081$ and $\alpha \approx 2\,(0.856)$. For $v = 3/2$ this gives $\tau = -2/19 \approx -0.105$ and $\alpha \approx 2\,(0.860)$. We thus see with radiation present that the temperature is nearly constant in time and the radius grows like $O\left(t^{0.85}\right)$.

For a constant current $j = 0$

$$\tau = -\frac{3}{8+v}$$

$$\alpha = 1 + \frac{v}{8+v}$$

For $v = 1$ this gives $\tau = -1/3 \approx -0.333$ and $\alpha = 10/9 \approx 2\,(0.555)$. For $v = 5/4$ this gives $\tau = -12/37 \approx -0.324$ and $\alpha \approx 2\,(0.568)$. For $v = 3/2$ this gives $\tau = -6/19 \approx -0.316$ and $\alpha \approx 2\,(0.579)$. We thus see with radiation present and constant current, that the temperature decreases with the cube root of time and the radius grows like $O\left(t^{0.57}\right)$.

3.3 Lumped Model Solution

The first order system is

$$\frac{dA}{dt} = \sqrt{\frac{4\pi}{K_p \rho_0}} A p$$

$$A\frac{dp}{dt} = -\gamma p \frac{dA}{dt} + (\gamma - 1)\frac{I^2}{A\sigma_0 T^v} \tag{22}$$

$$\frac{Ap}{T}\frac{dT}{dt} = A\frac{dp}{dt} + p\frac{dA}{dt} - \frac{\gamma - 1}{\gamma}Q_R$$

We have ignored the time derivative of γ and of the average ionization number $\overline{m}$. It is possible to approximate $\overline{m}$ by an explicit function of temperature alone and then simply include both time derivatives. However for high temperatures the variations are small. The unknowns are A, p, T. In the case where radiation is omitted and thermal diffusion is included we replace $Q_R = \sqrt{4\pi A}\sigma_S T^4$ by $Q_T \approx 1.3\left(\frac{2}{3}\pi^3/e^2\right)\sigma_0\,(kT)^{v+2}$.

3.3.1 initial conditions

The initial conditions on the later time channel expansion result from the preceding phases of the breakdown process, which are not completely known. We therefore decided to select undisturbed water density for the initial condition for the smaller starting radii and one tenth water density for the largest starting radii (since standard water density leads to too large an initial channel conductance)

$$\rho = \rho_0 = 0.1, 1 \text{ g/cm}^3$$

The initial channel was made somewhat conductive so that the heating and expansion process at late can get started, by taking the initial temperature to be one electron volt

$$T = 1 \text{ eV}$$

The radius was varied over a range similar to that used in air breakdown simulations [30], but a final larger
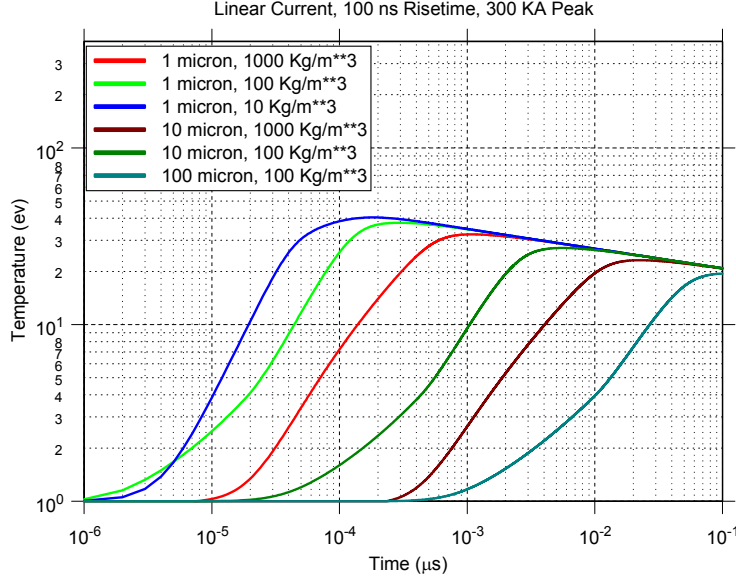
42

Figure 6. Temperature 0D results for various starting conditions of initial radius and initial density.

value was introduced to observe the effect on final resistance values

$$a = 1, 10, 100 \ \mu\text{m}$$

Values of starting radius in the tens of microns are consistent with previous work in both oil [31] and water [32].

Using these initial conditions the preceding system (22) was integrated in time (the circuit equation (18) was included for voltage drives). The first and second equations in the system (22) are substituted in the third to obtain a single first derivative in each equation as given in the Appendix A.

For the 0.1 g/cm^3 starting cases we used some interpolation of the electrical conductivities at early time from quantum mechanical dynamics simulations [25].

3.3.2 lumped model results

Some results are now discussed for a slow rise time linear ramp current drive. The current rises from zero to 300 kA in 100 ns (the time range of the plots).

The final resistance per unit length values seem fairly independent of the initial conditions explored in this slow current drive case. Note that the initial Fedorov fit conductivities in the 10 kg/m^3 initial density cases are not accurate [25]; there is also a question about the initial use of the black body radiation formula in these cases. Further comparisons of the lumped model with one-dimensional simulations will be given later in the report.
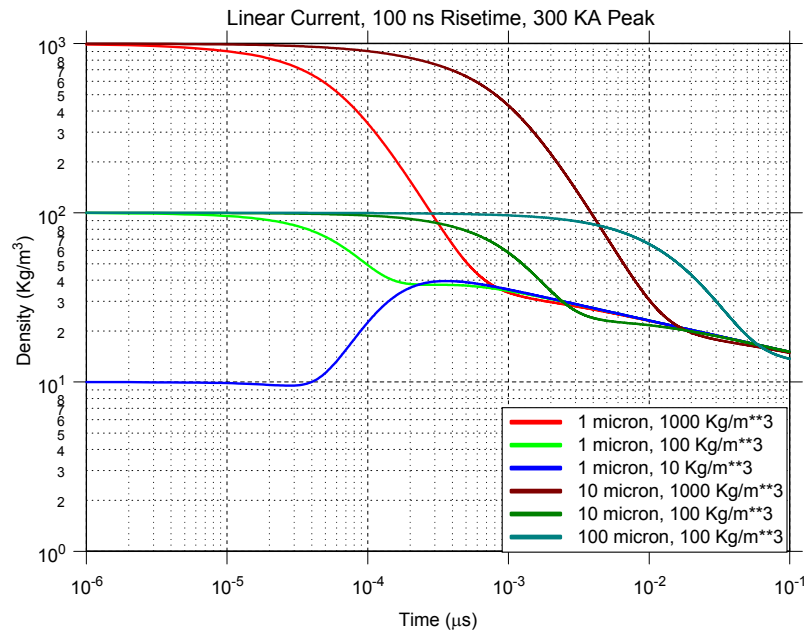
Figure 7. Density 0D results for various starting conditions of initial radius and initial density.
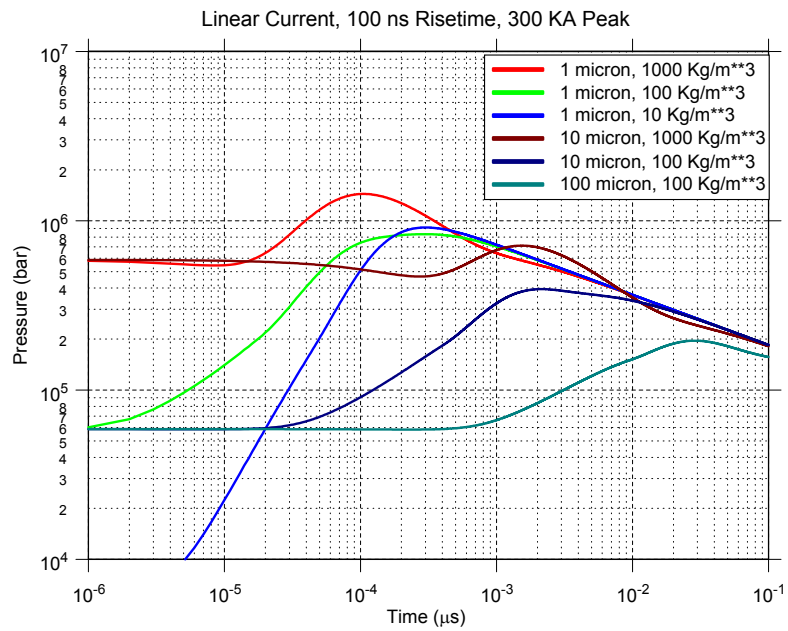
Figure 8. Pressure 0D results for various starting conditions of initial radius and initial density.

44
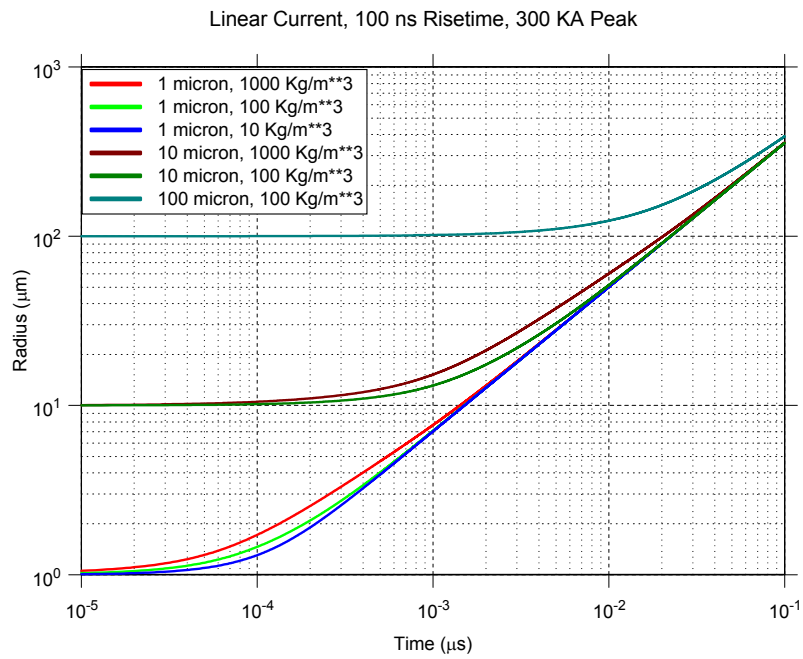
Figure 9. Channel radius 0D results for various starting conditions of initial radius and initial density.
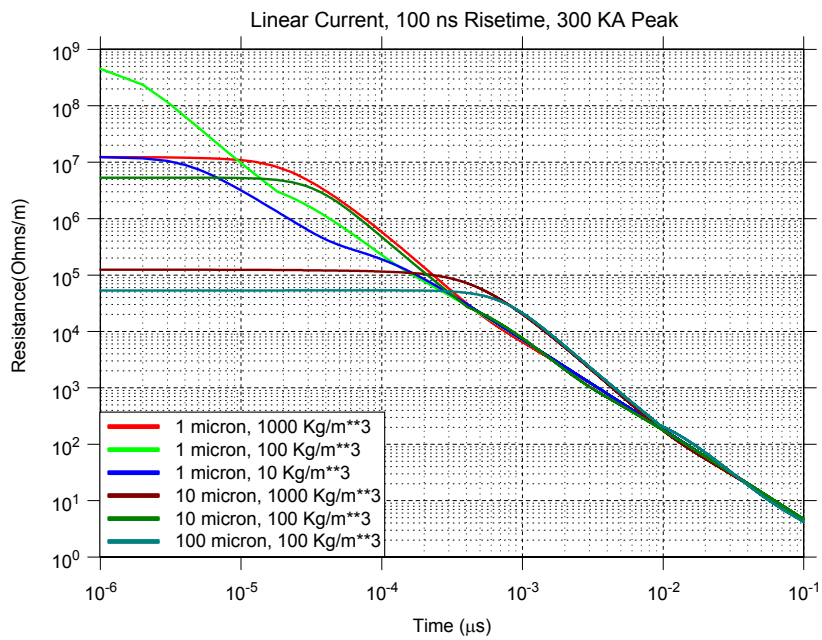
Figure 10. Resistance per unit length 0D results for various starting conditions of initial radius and initial density.

4 ONE DIMENSIONAL SIMULATIONS

The one dimensional simulations using ALEGRA-HEDP [12] are now discussed. The first set resides in this section and the remaining sets reside in the Appendix C. The first two sets correspond to a linear ramp current drive rising to $I_0 = 300$ kA in $\tau = 100$ ns. The first set has initial channel conditions of $a = 1$ μm, initial temperature $T = 1$ eV, and initial channel density $\rho = 1$ g/cm^3. The second set is the same except that radiation has been turned off to explore the importance of the different loss mechanisms. The third has radiation turned on but uses an initial channel radius $a = 10$ μm to explore the effect of this initial condition. The fourth set uses the same starting parameters as the first set but has a current rise time of 15 ns, beyond which the current remains fixed at 300 kA to explore the effect of fast transients mimicking voltage drive turn on times. The fifth set has a current rise time of 30 ns to 600 kA to explore higher current levels that might be of interest on future higher power machines. The sixth set has a voltage step drive (actually rising in 1 ns), which, if scaled to a gap length of 10 cm, corresponded to a source $V_0 = 4.5$ MV with a load resistance of $R_0 = 16$ ohms; the current was thus limited to $I_0 = 280$ kA. The final set has the same voltage level and load but the voltage rises in 50 ns to better represent experimental voltage excitations.

The simulation graphs are ordered as temperature (2-3 time scales), density (some have expanded vertical scales to show channel values), pressure, electric conductivity, thermal conductivity, average opacity (again some have expanded vertical scales to see the channel), Rosseland opacity (some have expanded vertical scales to see the channel), total radiation (if available), internal energy, average ionization degree, and axial current density (if available).

4.1 Slow Rise Current Drive

The first set, for a slow 100 ns ramp current drive, now follows.
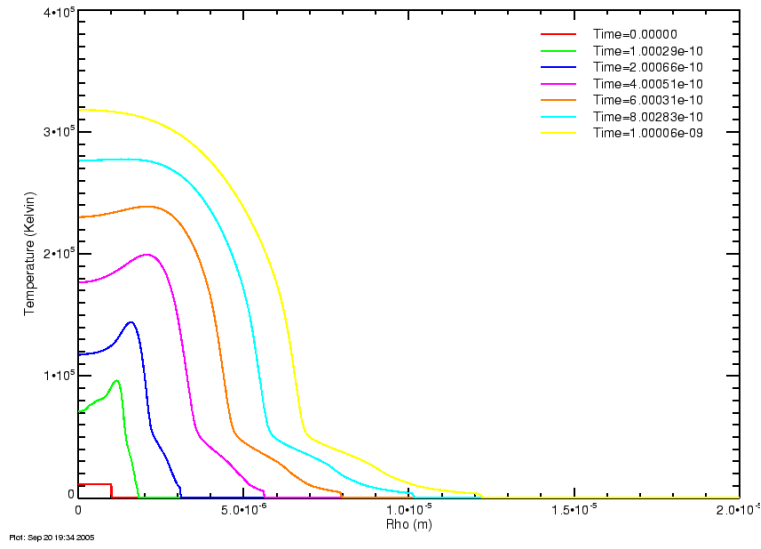
Figure 11. Early time temperature profiles for slow ramp current drive.
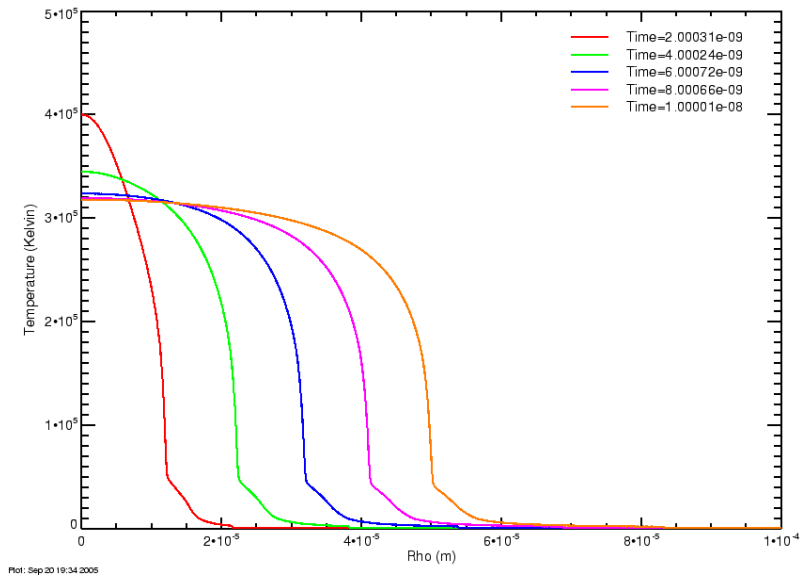
Figure 12. Intermediate time temperature profiles for slow current drive.

48
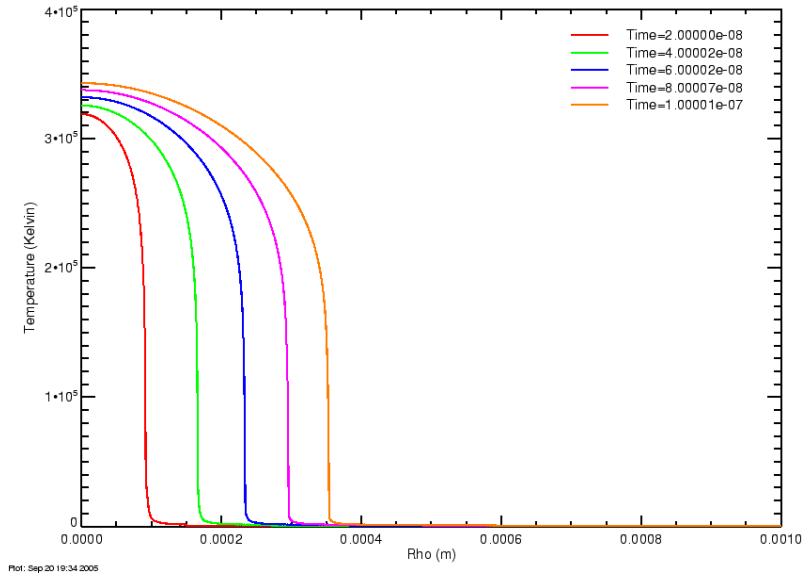
Figure 13. Late time temperature profiles for slow current drive.
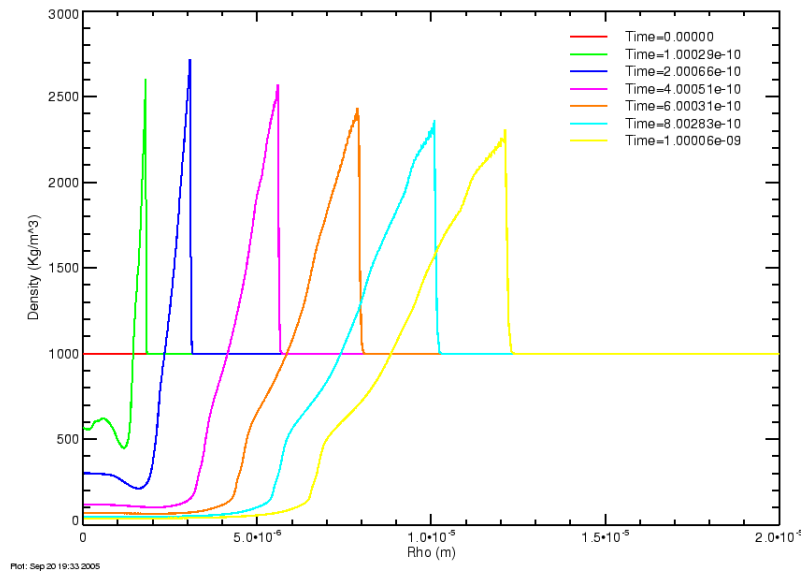
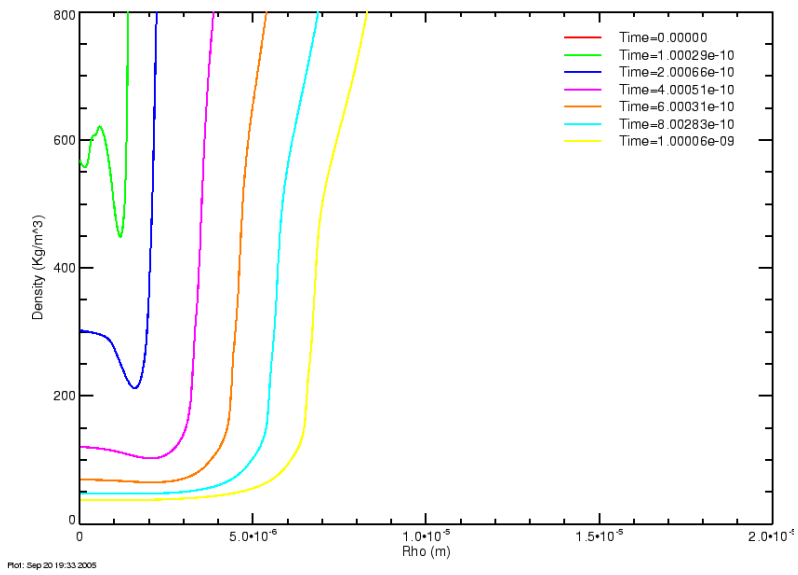Figure 14. Early time density profiles for slow current drive.

49

Figure 15. Expanded channel densities at early time for slow current drive.
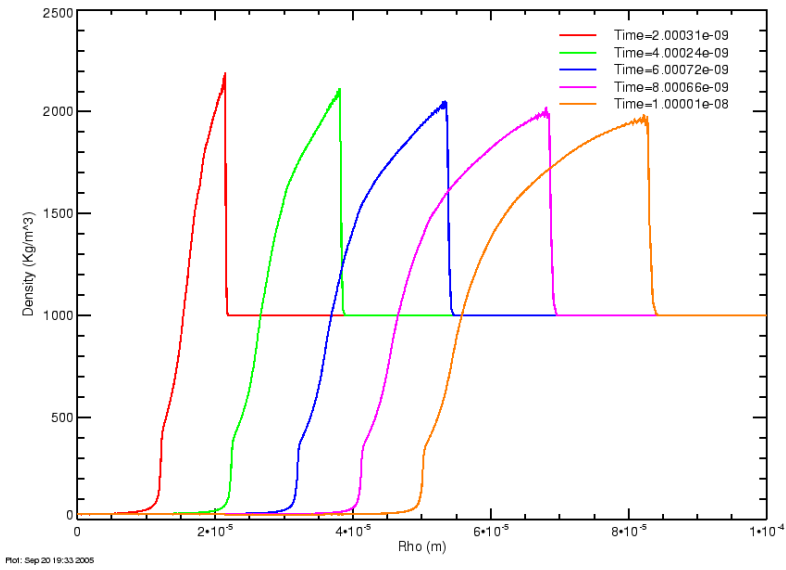
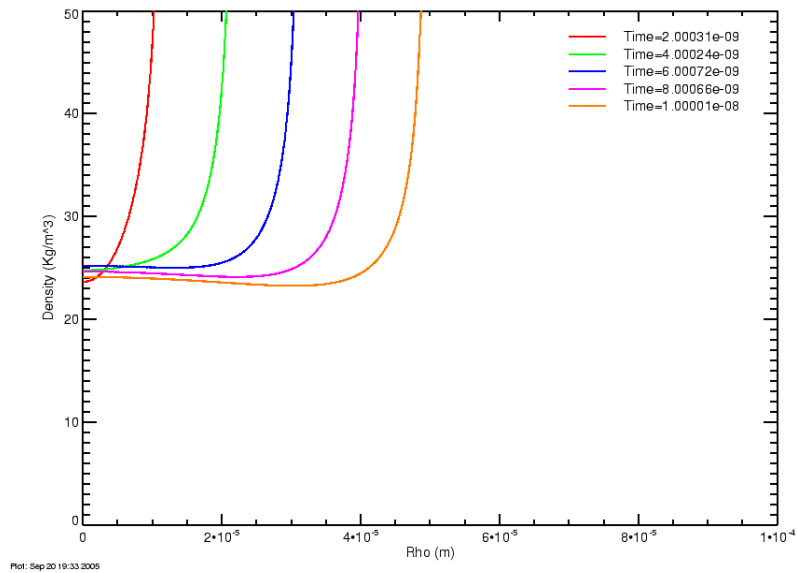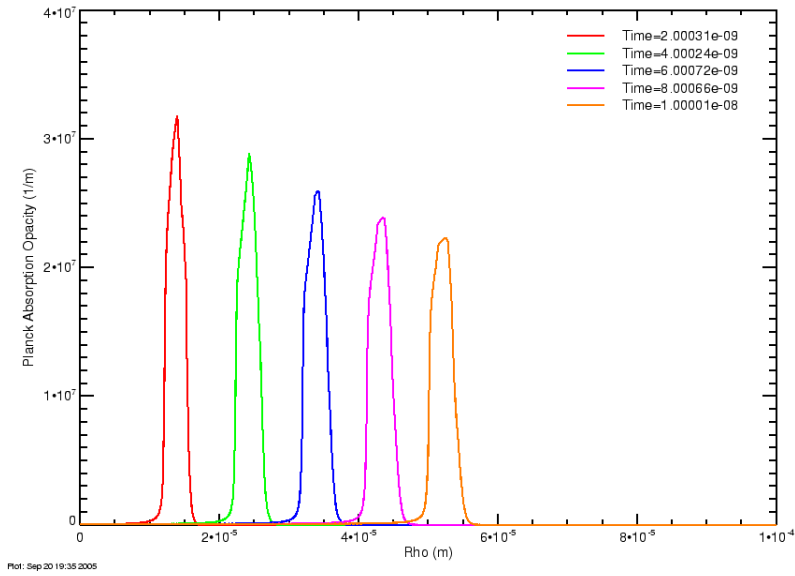Figure 16. Intermediate time density profiles for slow current drive.
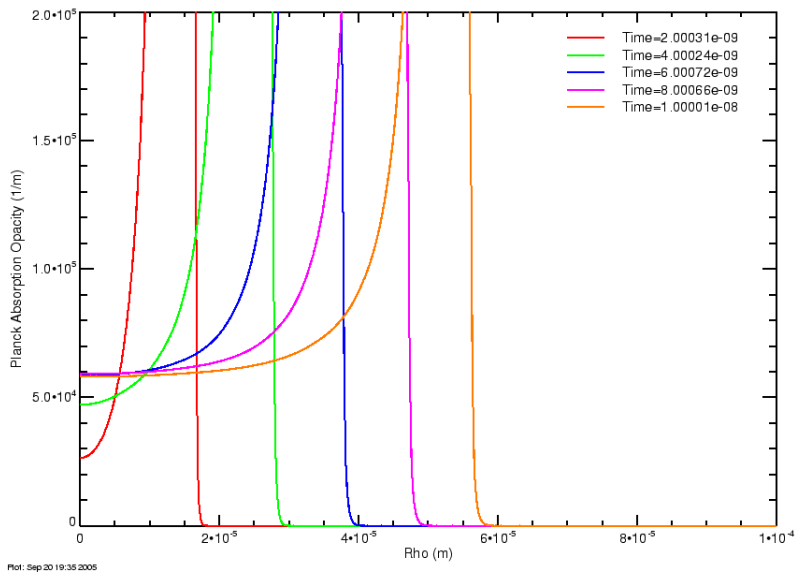

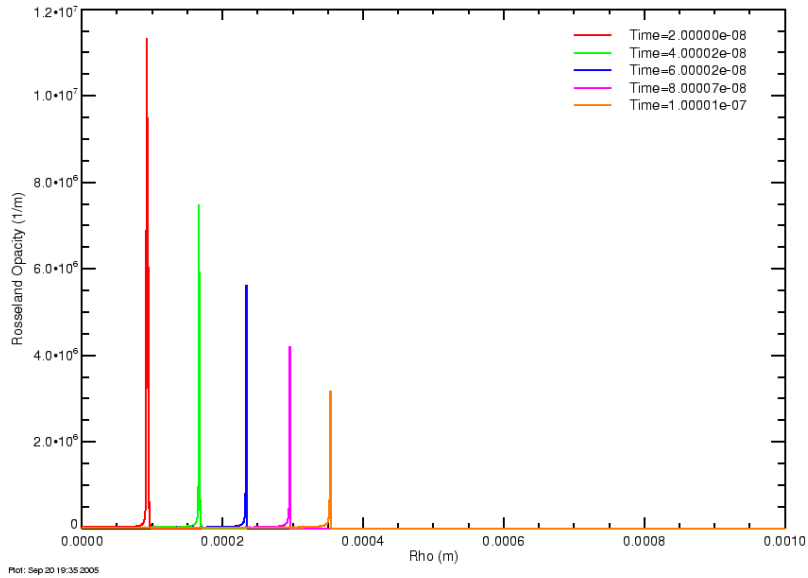Figure 17. Expanded channel densities for intermediate times and slow current drive.
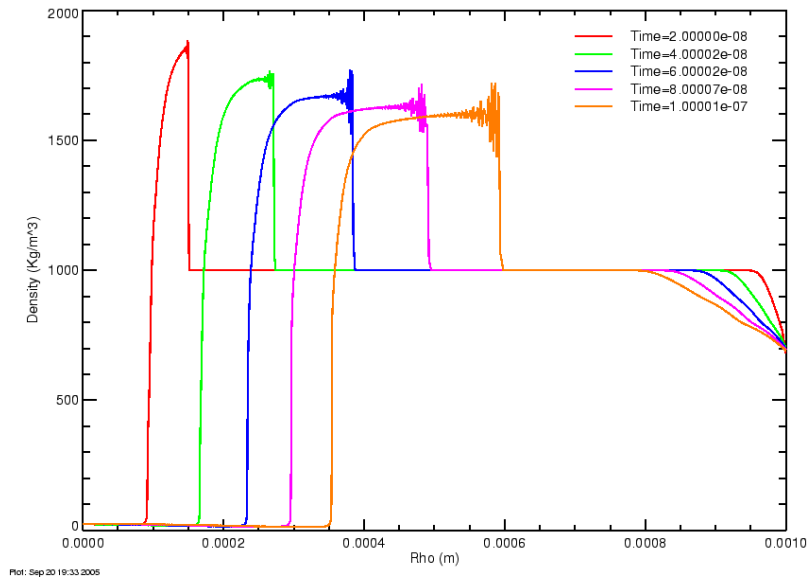
Figure 18. Late time densities for slow current drive.
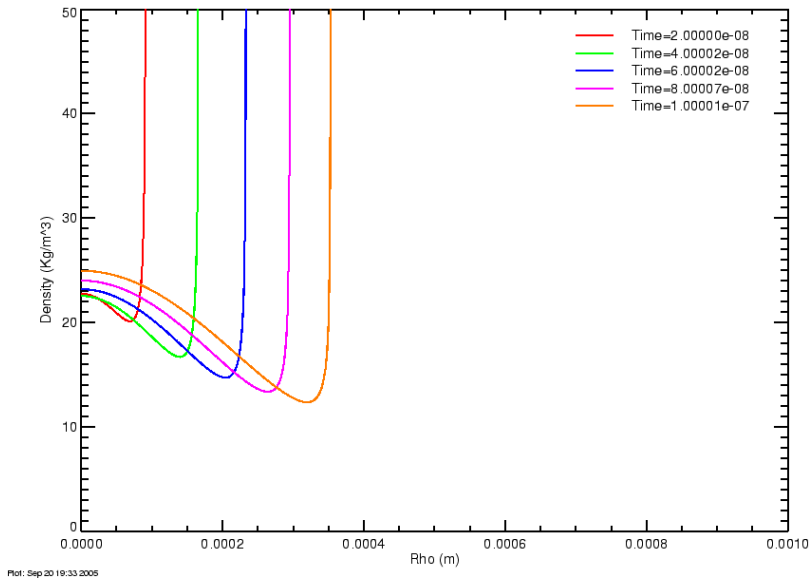
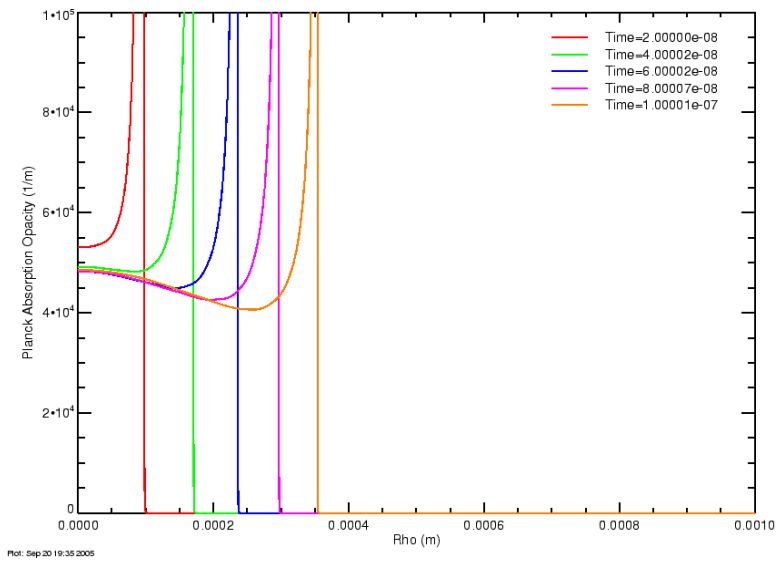Figure 19. Expanded channel densities for late times and slow current drive.
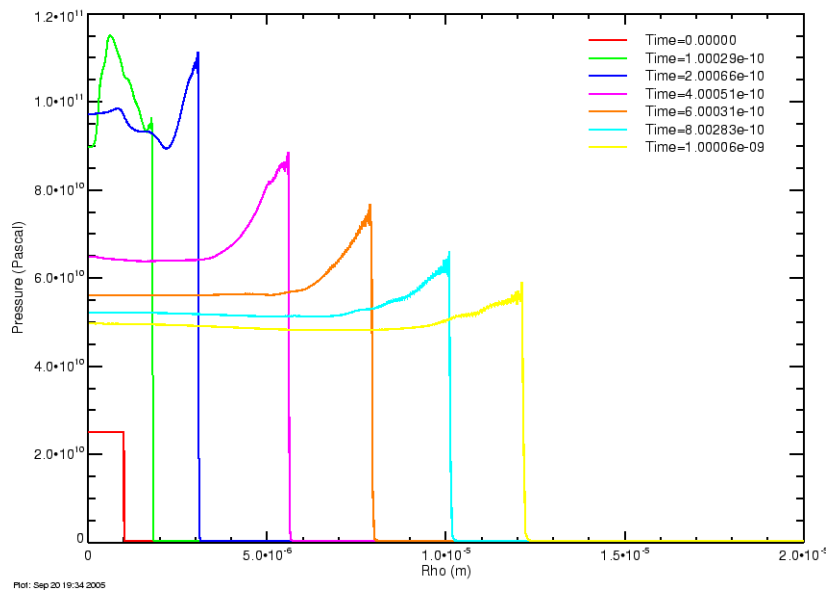
Figure 20. Early time pressures for slow current drive.
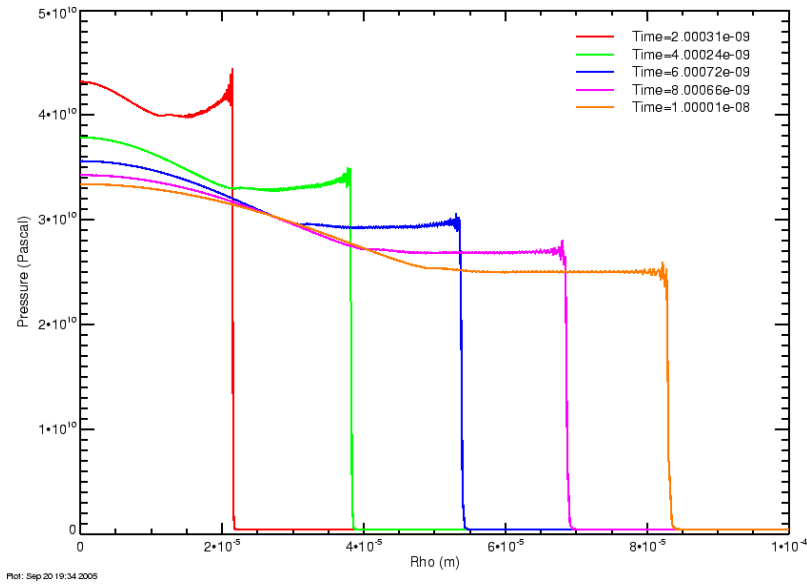
Figure 21. Intermediate pressures for slow current drive.
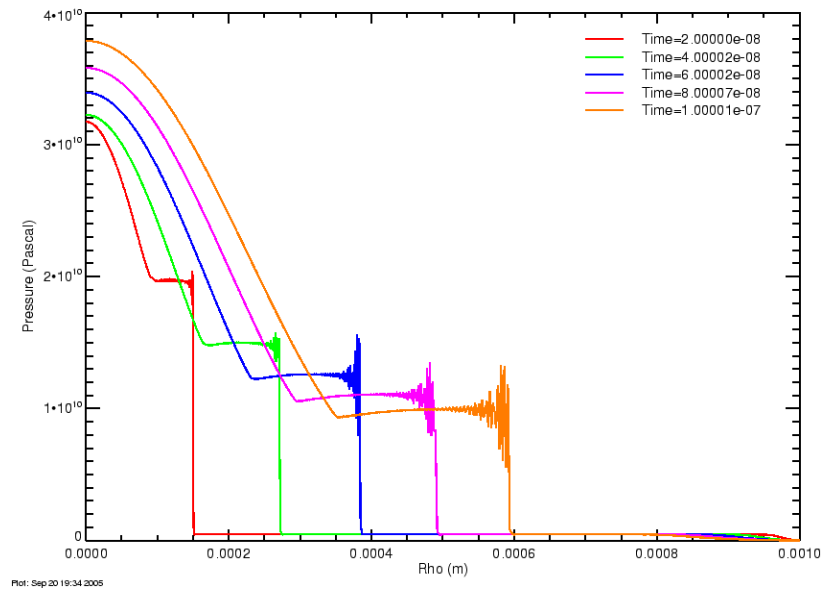
Figure 22. Late time pressures for slow current drive.
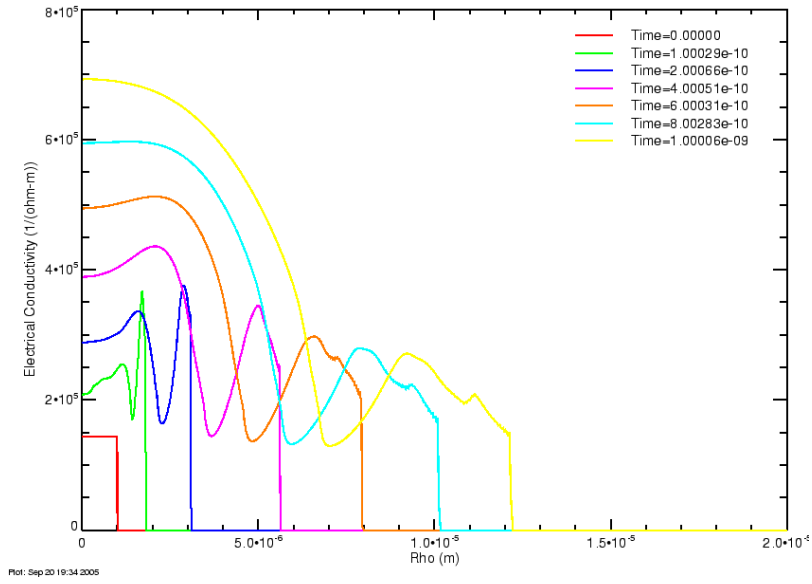
Figure 23. Early time electrical conductivity profiles for slow current drive.
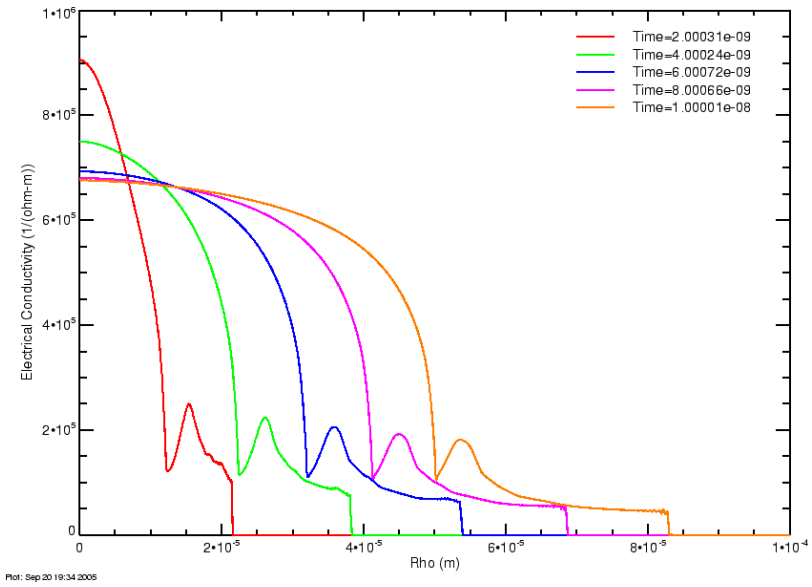
Figure 24. Intermediate time electrical conductivities for slow current drive.
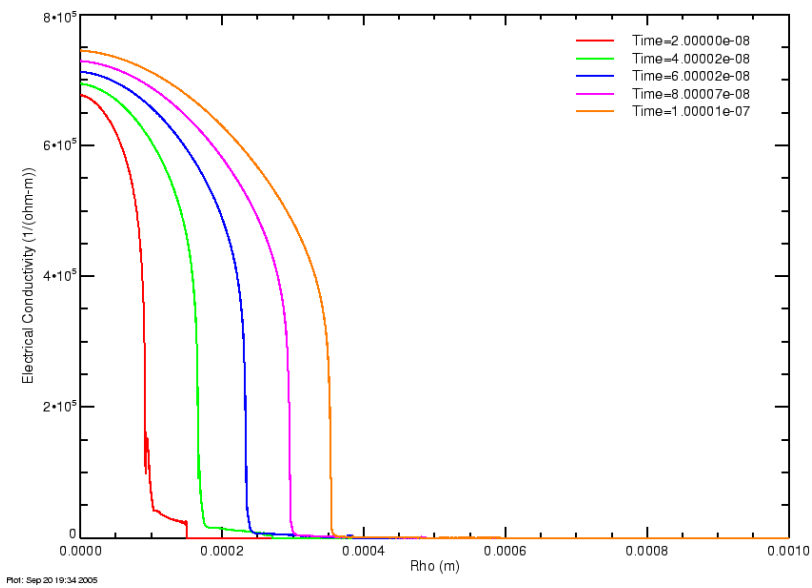
Figure 25. Late time electrical conductivies for slow current drive.
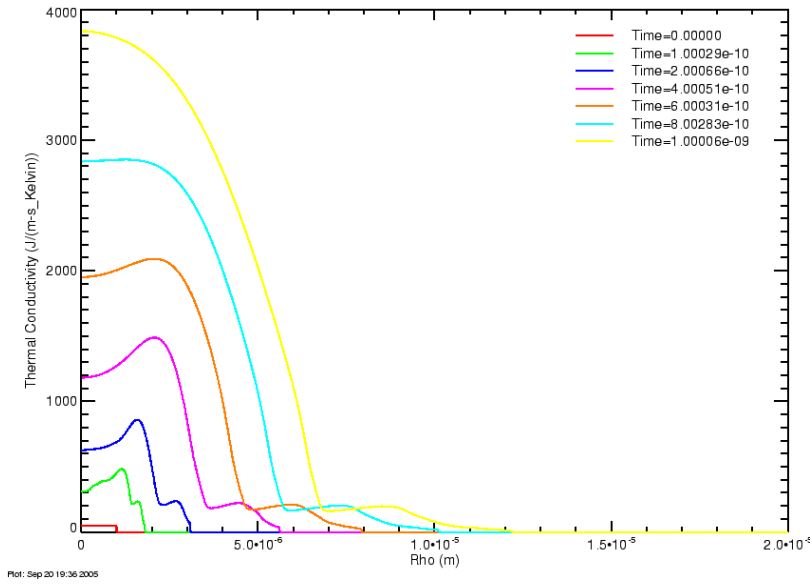
Figure 26. Early time thermal conductivies for slow current drive.
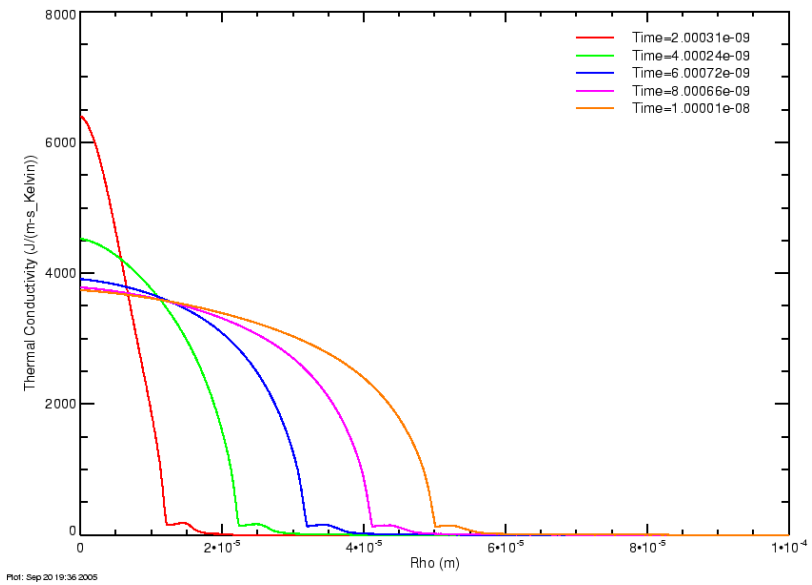
Figure 27. Intermediate time thermal conductivities for slow current drive.
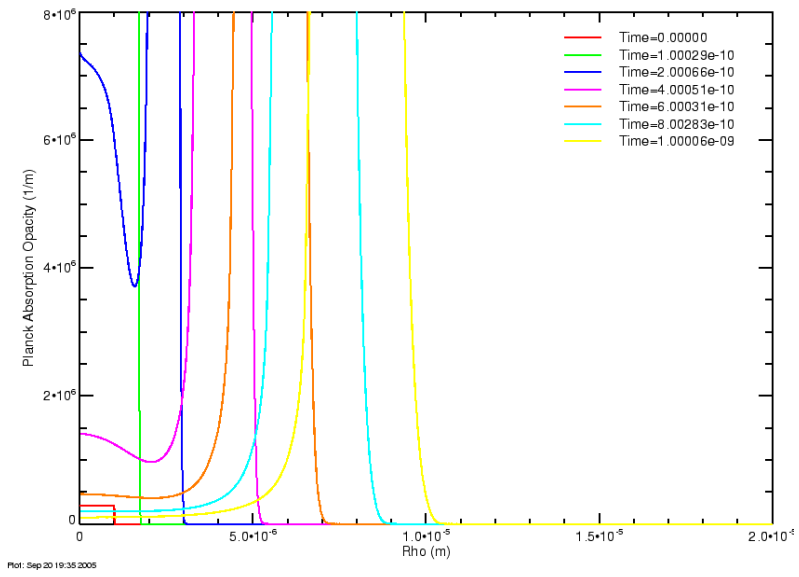
Figure 30. Expanded average channel opacities for early time and slow current drive.

Figure 31. Intermediate time average opacities for slow current drive.

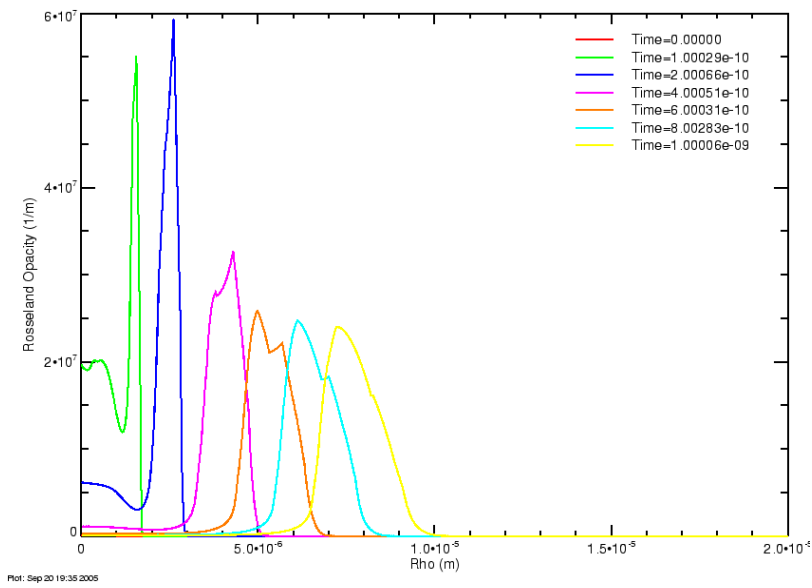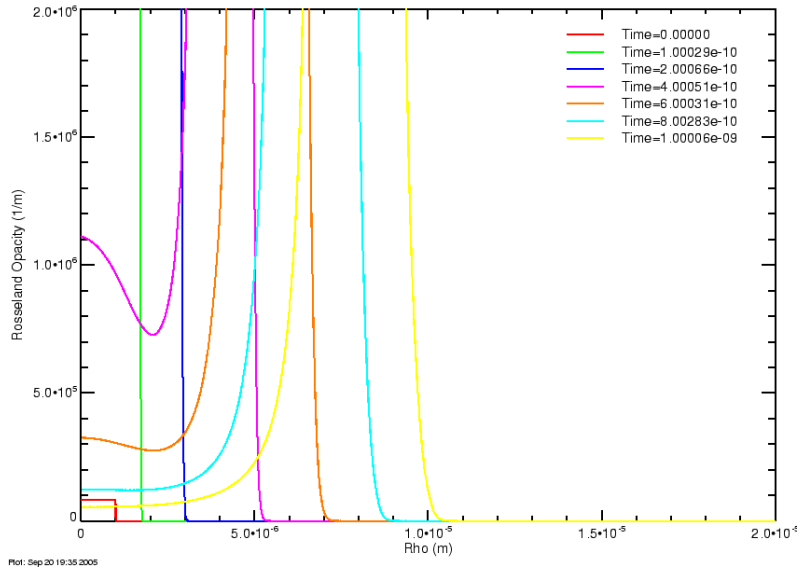Figure 32. Expanded average channel opacities for intermediate times and slow current drive.

60

Figure 33. Late time average opacities for slow current drive.

Figure 34. Expanded average channel opacities for late times and slow current drive.

Figure 35. Early time Rosseland opacities for slow current drive.

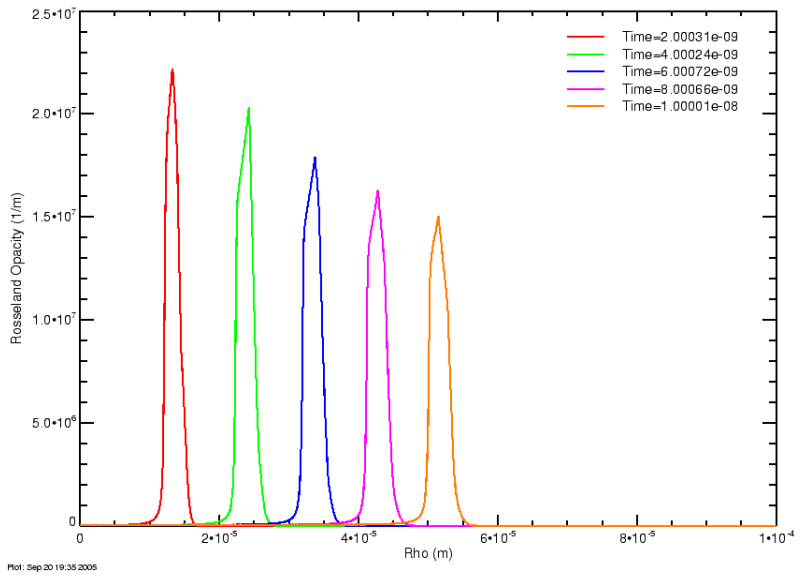Figure 36. Expanded Rosseland channel opacities for early time and slow current drive.

Figure 37. Intermediate time Rosseland opacities for slow current drive.
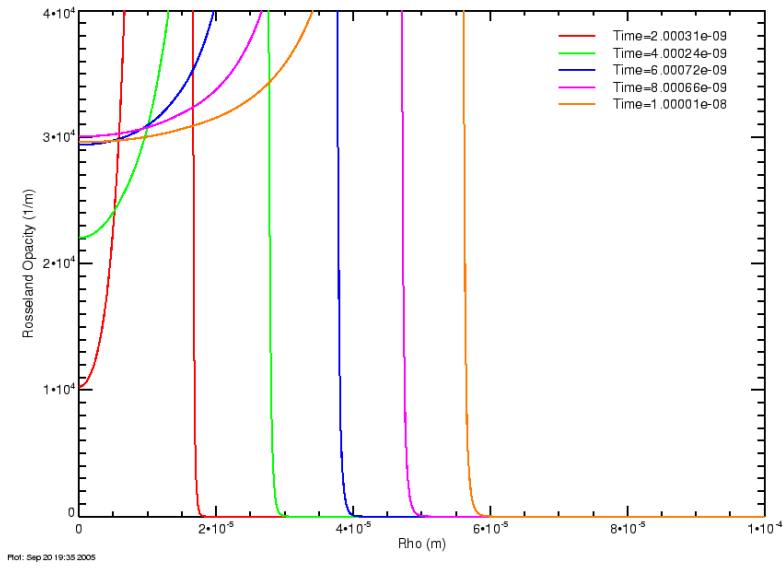
Figure 38. Expanded Rosseland channel opacities for intermediate times and slow current drive.
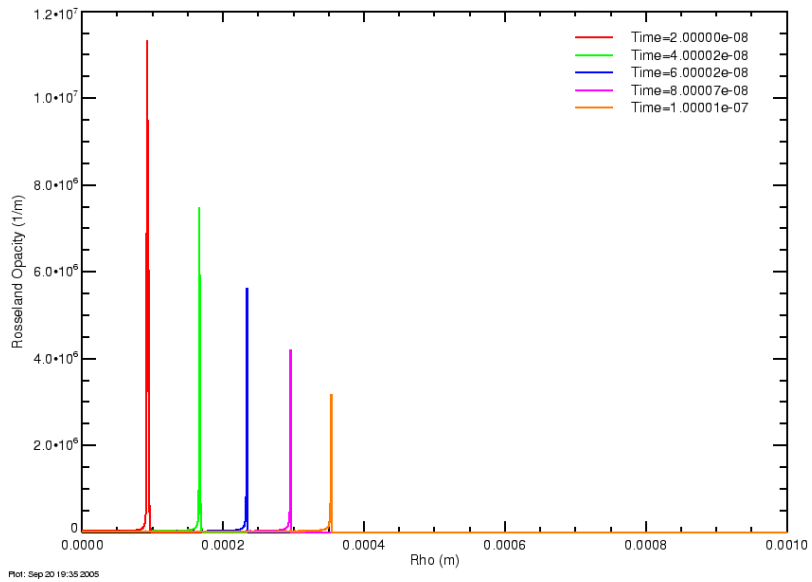

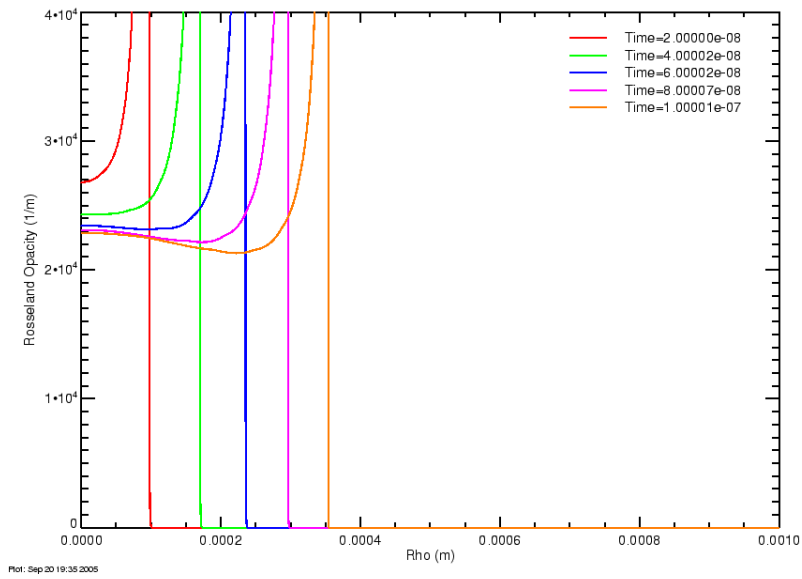Figure 39. Late time Rosseland channel opacities for slow current drive.

Figure 40. Expanded Rosseland channel opacities for late time and slow current drive.
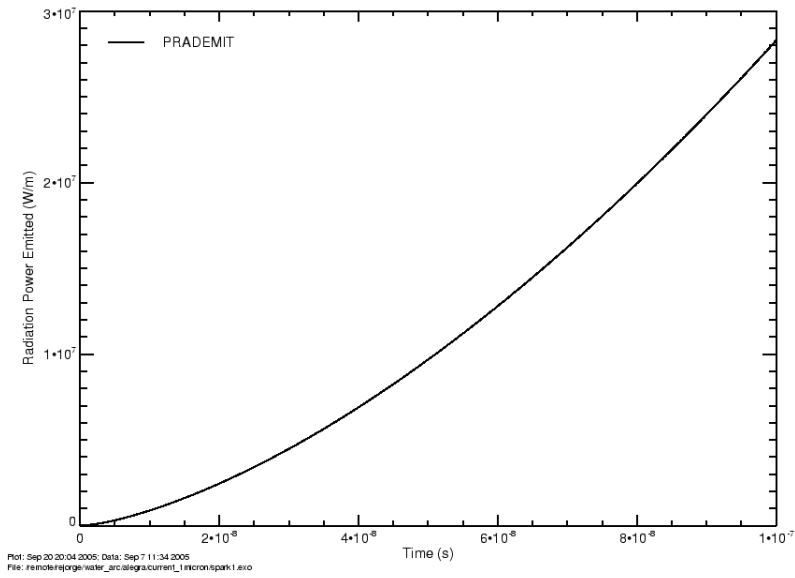
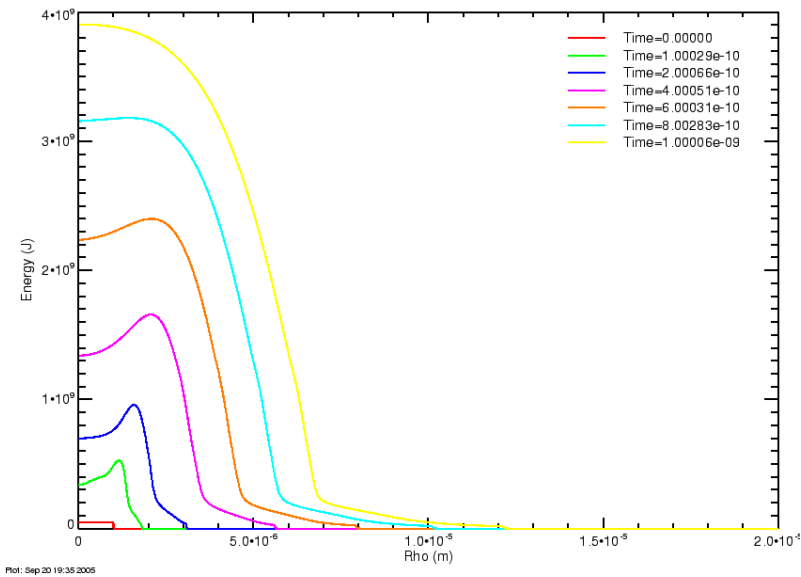Figure 41. Total problem radiation for slow current drive.

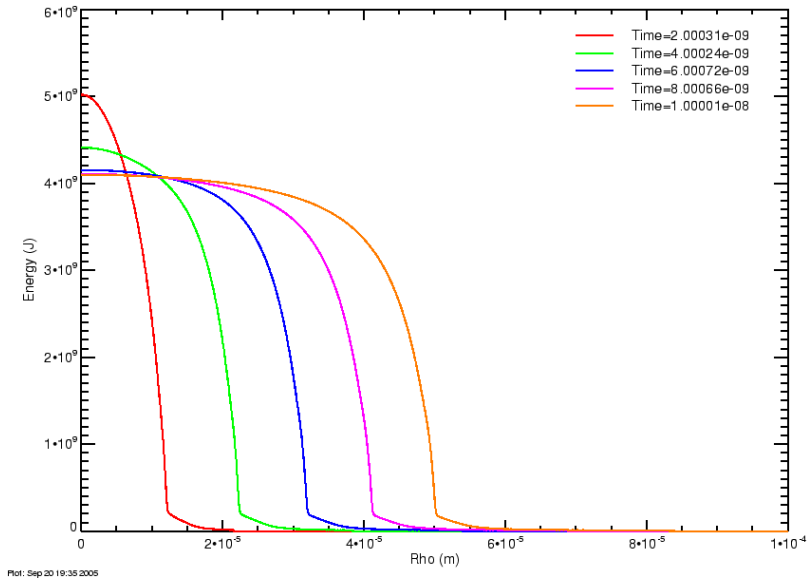Figure 42. Internal energies for early time and slow current drive.

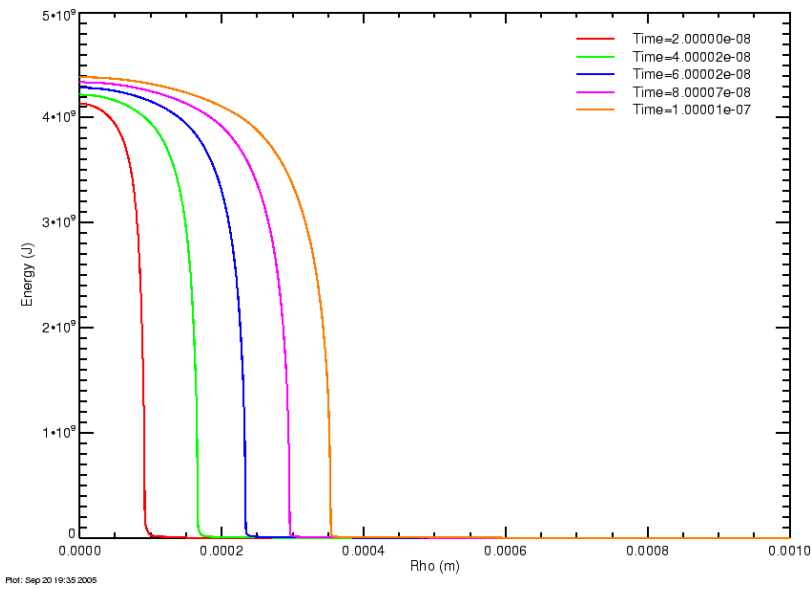Figure 43. Internal energies for intermediate times and slow current drive.

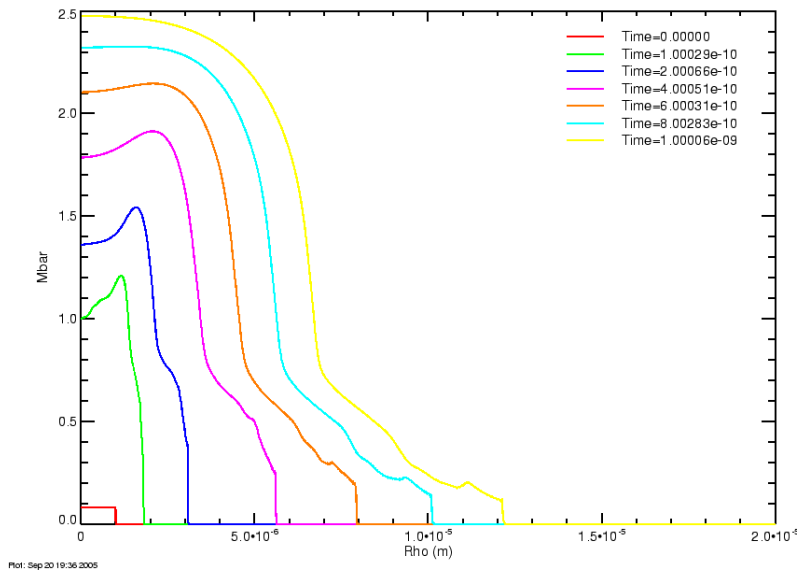Figure 44. Late time internal energies for slow current drive.

67

Figure 45. Average ionization number for early times and slow current drive.
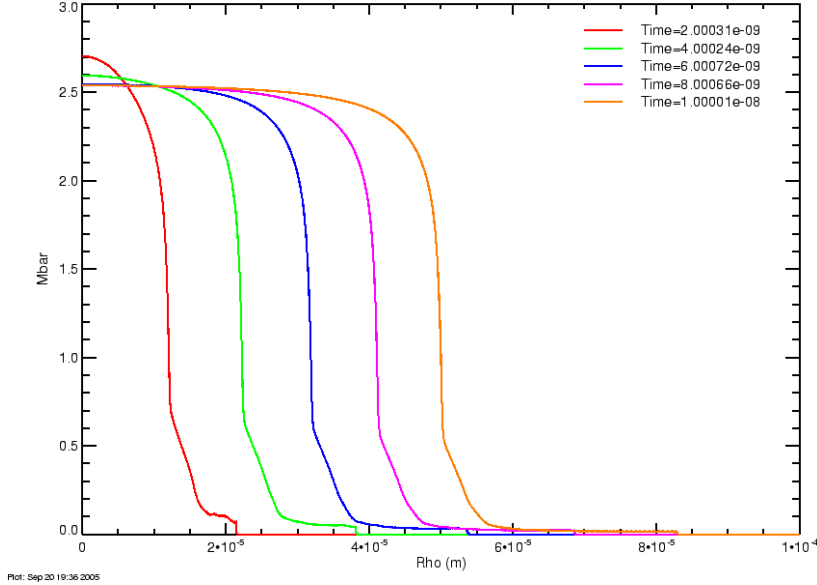
Figure 46. Average ionization number for intermediate times and slow current drive.

The preceding results give justification for a lumped channel model, especially the temperature distribution with radiation turned on. Furthermore the current density seems to follow the conductivity distribution even in the fast rise case. Also, the varying pressure profile in the channel (particularly at late time) appears to be explained by magnetic forces in the channel (11), and similarly for the varying density profile in the channel (by use of the ideal gas law).

The preceding simulations used only a single temperature model for the radiation transport, which may underestimate the depth of photon penetration into the channel wall. A two temperature simulation, to check the effects of this approximation, is planned for the future.

5   IMPROVEMENTS TO LATE TIME CIRCUIT MODEL

To further simplify the zero dimensional lumped model we now approximate the system of equations by means of a Braginskii-Martin approach, but using black body radiation to determine the temperature and conductivity. The starting system is

$$\frac{dU}{dt} + p\frac{dA}{dt} = \frac{I^2}{A\sigma\left(T\right)} \tag{23}$$

$$\left(\varepsilon + p/\rho\right)\frac{dM}{dt} = 2\pi a\sigma_S T^4 = \sqrt{4\pi A}\sigma_S T^4 \tag{24}$$

$$p = K_p\rho_0\left(\frac{da}{dt}\right)^2 = \frac{K_p\rho_0}{4\pi}\frac{1}{A}\left(\frac{dA}{dt}\right)^2 \tag{25}$$
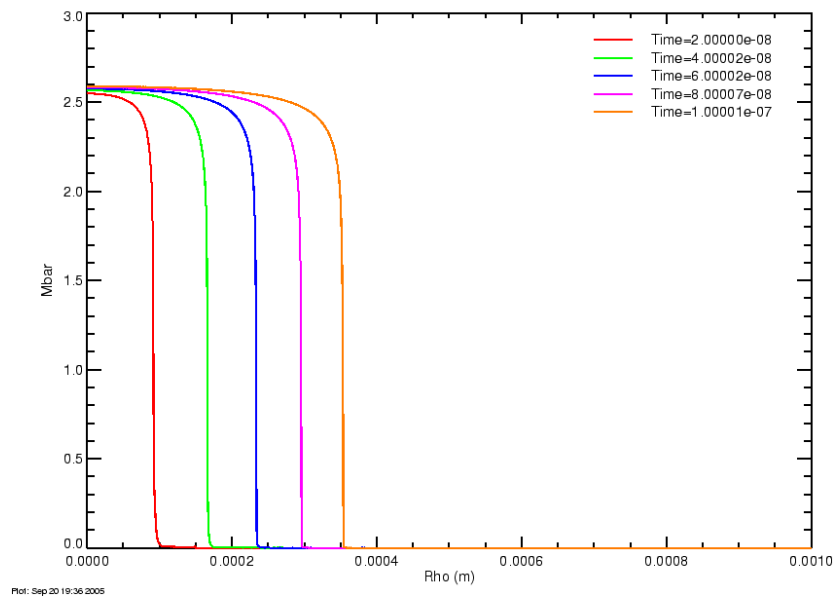
where

69

Figure 47. Average ionization number for late time and slow current drive.

$$p = (1 + \overline{m}) \frac{\rho}{m_a} kT$$

$$U = A\rho\varepsilon$$

$$\gamma - 1 = \frac{p}{\rho\varepsilon}$$

$$A = \pi a^2$$

$$M = \rho A$$

and we use the linear conductivity in this section

$$\sigma(T) = \sigma_0(kT)$$

Now for later times the temperature, internal energy, and enthalpy are nearly constant in time. Thus in the first equation (23) we write

$$\varepsilon \frac{dM}{dt} + p \frac{dA}{dt} = \frac{I^2}{A\sigma_0 kT}$$

In the second equation (24) we write

$$\gamma \varepsilon \frac{dM}{dt} = \sqrt{4\pi A} \sigma_S T^4$$

Let us also treat the density as slowly varying at later times. Then the first equation (23) becomes

$$\gamma \varepsilon \rho \frac{dA}{dt} = \frac{\gamma}{\gamma - 1} p \frac{dA}{dt} = \frac{I^2}{A\sigma_0 kT}$$

and from the third equation (25)

$$\left(\frac{dA}{dt} \right)^3 = \frac{4\pi (\gamma - 1)}{K_p \rho_0 \gamma \sigma_0 k} \frac{I^2}{T} \tag{26}$$

Note that this equation corresponds to Braginskii's choice [4] $\xi_{Braginskii} = K_p \gamma / (\gamma - 1) \approx 7.7$ which agrees with the radial growth with time $a = a_0 t^{\alpha/2}$ and the value $\alpha/2 = 1$ (the difference in value has arisen solely due to differences in the values of K_p and in γ). The second equation (24) is then

$$\varepsilon \rho \frac{dA}{dt} = \frac{1}{\gamma - 1} p \frac{dA}{dt} = \frac{1}{\gamma} \sqrt{4\pi A} \sigma_S T^4$$

and using the third equation (25)

$$\frac{1}{A^{3/2}} \left(\frac{dA}{dt} \right)^3 = \frac{(\gamma - 1)(4\pi)^{3/2}}{\gamma K_p \rho_0} \sigma_S T^4 \tag{27}$$

5.1 Solution with Variable Temperature

If we solve for T in the preceding equation and substitute it into the first equation (26) we find

$$A^{-1/10}\frac{dA}{dt} = \left[\frac{4\pi(\gamma-1)}{K_p\rho_0\gamma}\right]^{1/3}\left[\frac{(4\pi)^{1/2}\sigma_S}{(\sigma_0 k)^4}\right]^{1/15}I^{8/15}$$

Integration yields

$$A(t) = \left\{\frac{9(4\pi)^{1/30}\sigma_S^{1/15}}{10\sigma_0^{4/15}k^{4/15}}\left[\frac{4\pi(\gamma-1)}{K_p\rho_0\gamma}\right]^{1/3}\int_0^t I^{8/15}(\tau)\,d\tau\right\}^{10/9}$$

The corresponding temperature is

$$T = \left(\frac{10}{9}\right)^{1/3}\left[\frac{K_p\rho_0\gamma}{16\pi^2\sigma_0 k\sigma_S^2(\gamma-1)}\right]^{1/9}\frac{I^{2/5}(t)}{\left[\int_0^t I^{8/15}(\tau)\,d\tau\right]^{1/3}}$$

and the resistance is

$$R = \frac{\ell}{\sigma A} = \frac{\ell}{\sigma_0(kT)A}$$

Alternatively if we have a circuit drive then from the preceding equations we write the circuit equation as

$$V_0 = R_0 I + \frac{d}{dt}(LI) + RI = R_0 I + \frac{d}{dt}(LI) + R_1\frac{I^{3/5}(t)}{\left[\int_0^t I^{8/15}(\tau)\,d\tau\right]^{7/9}}$$

where the constant is

$$R_1 = \frac{\ell/(\sigma_0 k)}{\left(\frac{10}{9}\right)^{1/3}\left[\frac{K_p\rho_0\gamma}{16\pi^2\sigma_0 k\sigma_S^2(\gamma-1)}\right]^{1/9}\left\{\frac{9(4\pi)^{1/30}\sigma_S^{1/15}}{10\sigma_0^{4/15}k^{4/15}}\left[\frac{4\pi(\gamma-1)}{K_p\rho_0\gamma}\right]^{1/3}\right\}^{10/9}}$$

5.2 Solution with Slowly Varying Temperature

Alternatively we can use (26) to eliminate $\left(\frac{dA}{dt}\right)^3$ in (27) and obtain the set

$$\left(\frac{dA}{dt}\right)^3 = \frac{4\pi(\gamma-1)}{K_p\rho_0\gamma\sigma_0 k}\frac{I^2}{T}$$

$$\frac{I^2}{A^{3/2}} = (4\pi)^{1/2}\sigma_0 k\sigma_S T^5$$

If we integrate the first equation, treating the temperature as approximately constant, we find

$$A = \left[\frac{4\pi (\gamma - 1)}{K_p \rho_0 \gamma \sigma_0 k}\right]^{1/3} \frac{1}{T^{1/3}} \int_0^t I^{2/3}(\tau)\, d\tau$$

Inserting this into the preceding equation gives

$$\frac{I^{4/9}}{(4\pi\sigma_S)^{2/9} \left[\int_0^t I^{2/3}(\tau)\, d\tau\right]^{1/3}} \left[\frac{K_p \rho_0 \gamma}{\sigma_0 k (\gamma - 1)}\right]^{1/9} = T$$

For a linear current $I = I_0 t/\tau$

$$T = \frac{I_0^{2/9} t^{-1/9} \tau^{-2/9}}{(4\pi\sigma_S)^{2/9} (3/5)^{1/3}} \left[\frac{K_p \rho_0 \gamma}{\sigma_0 k (\gamma - 1)}\right]^{1/9}$$

$$A = \left[\frac{4\pi (\gamma - 1) I_0^2}{K_p \rho_0 \gamma \sigma_0 k}\right]^{1/3} \frac{1}{T^{1/3}} \frac{3}{5} \left(t^{5/3}/\tau^{2/3}\right)$$

and at $t = \tau = 100$ ns, $I_0 = 300$ kA, $\gamma = 1.35$, $K_p = 2$, $\rho_0 = 10^3$ kg/m^3, $\sigma_0 = 1.6 \times 10^{23}$ S/ (m-J), $\ell = 12$ cm

$$T = \left(\frac{5}{3\tau}\right)^{1/3} \left[\frac{I_0^2 K_p \rho_0 \gamma}{16\pi^2 \sigma_S^2 \sigma_0 k (\gamma - 1)}\right]^{1/9} \approx 2.42 \times 10^5 \text{ K } (21 \text{ eV})$$

$$A = \left[\frac{4\pi (\gamma - 1) I_0^2}{K_p \rho_0 \gamma \sigma_0 k}\right]^{1/3} \frac{1}{T^{1/3}} \frac{3}{5} \tau \approx 3.9 \times 10^{-7} \text{ m}^2$$

$$R = \frac{\ell}{A\sigma_0 kT} \approx 0.58 \text{ ohms}$$

The case of a circuit drive requires the equation

$$V_0 = R_0 I + \frac{d}{dt}(LI) + RI = R_0 I + \frac{d}{dt}(LI) + R_1 \frac{I^{19/27}(t)}{\left[\int_0^t I^{2/3}(\tau)\, d\tau\right]^{7/9}}$$

where the constant is

$$R_1 = \frac{\ell/(\sigma_0 k)}{\left[\frac{K_p \rho_0 \gamma}{(4\pi\sigma_S)^2 \sigma_0 k (\gamma - 1)}\right]^{2/27} \left[\frac{4\pi(\gamma - 1)}{K_p \rho_0 \gamma \sigma_0 k}\right]^{1/3}}$$

This second simple approach is used as the final simplified model in the following comparisons. It is denoted as "Braginskii-Martin BB" (black body) model.

6 COMPARISON OF MODEL RESULTS

The figures in this section show comparisons of the 0D results, the 1D results obtained from ALEGRA-HEDP, and the Braginskii-Martin BB results for temperature, density, pressure, radius, and resistance per unit length of the spark channel.

6.1 Slow Rise Current Drive

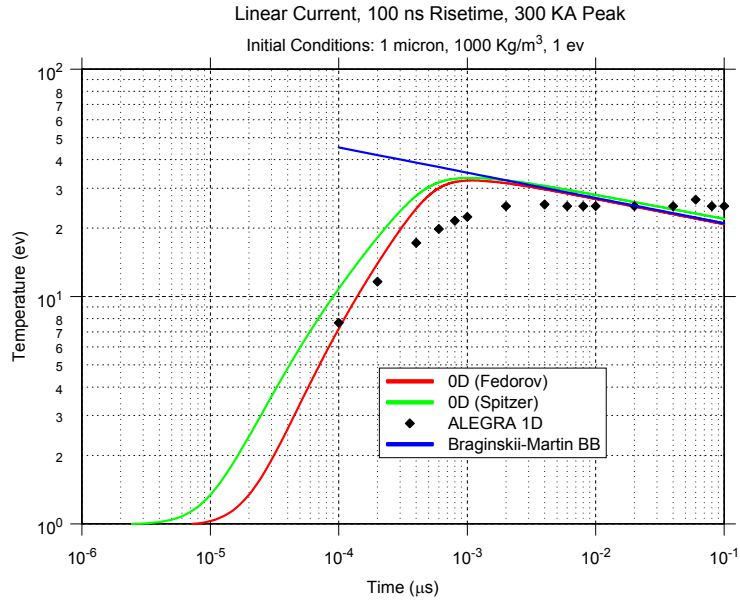The first case is the linear current rise to 300 kA in 100 ns.

Figure 48. Comparison of 0D, ALEGRA_HEDP 1D simulations, and simple Braginskii-Martin Black Body models for temperature with a slow current drive.
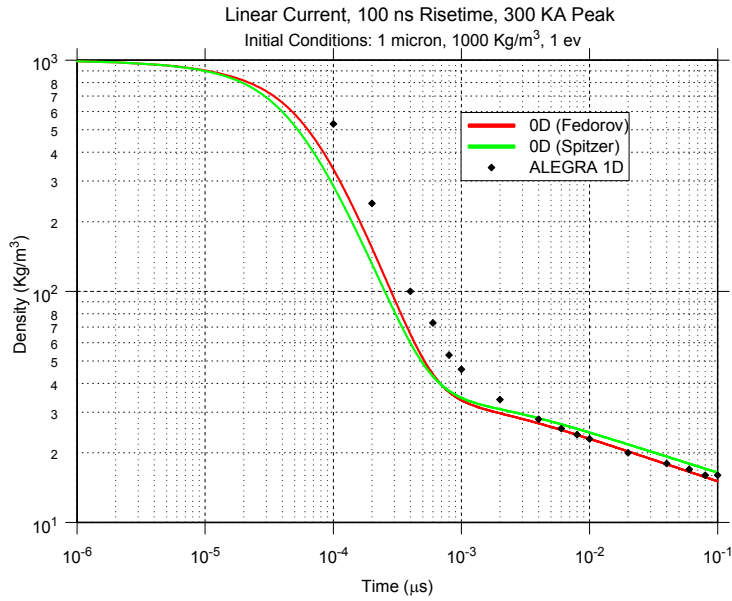
Figure 49. Comparison of 0D, ALEGRA_HEDP 1D simulations, and simple Braginskii-Martin Black Body models for density with a slow current drive.
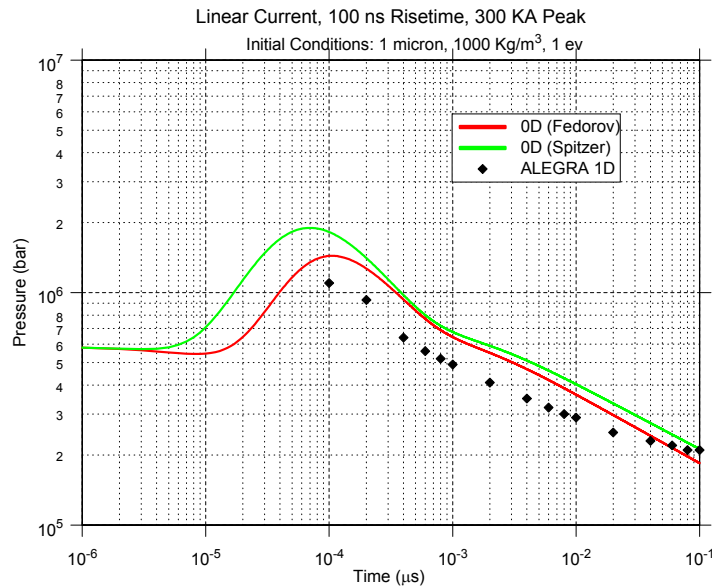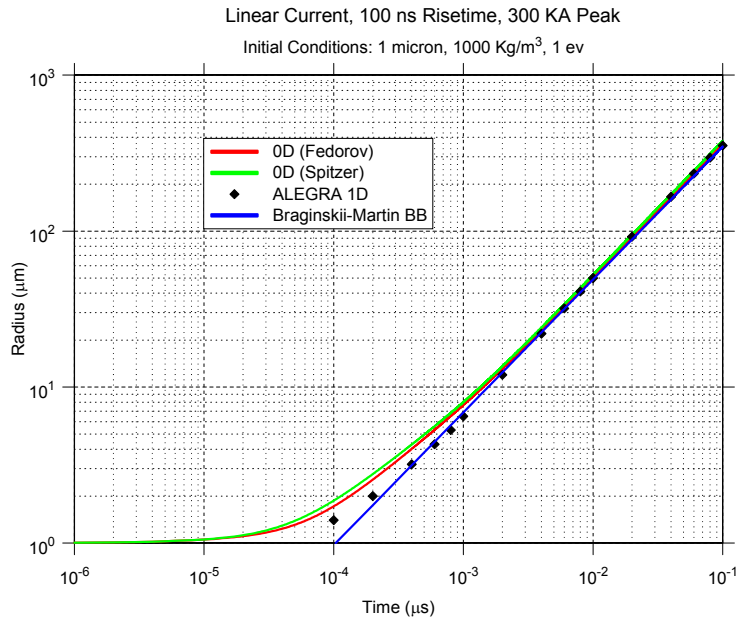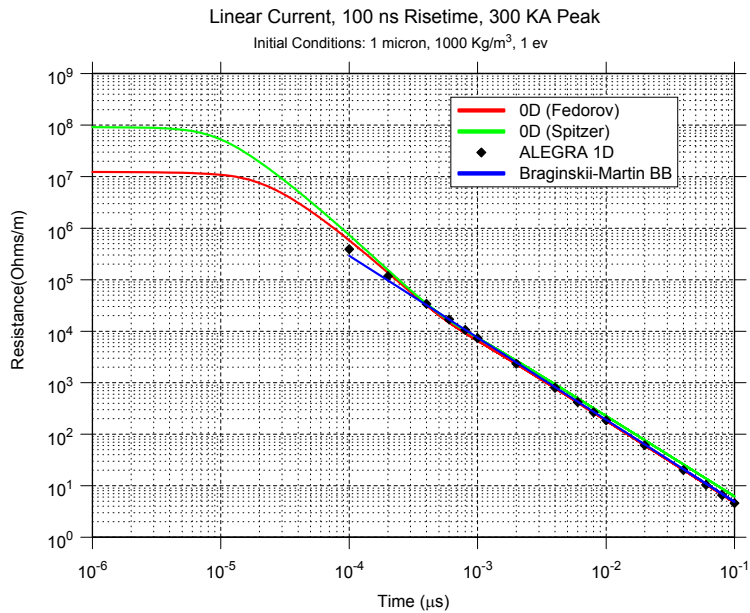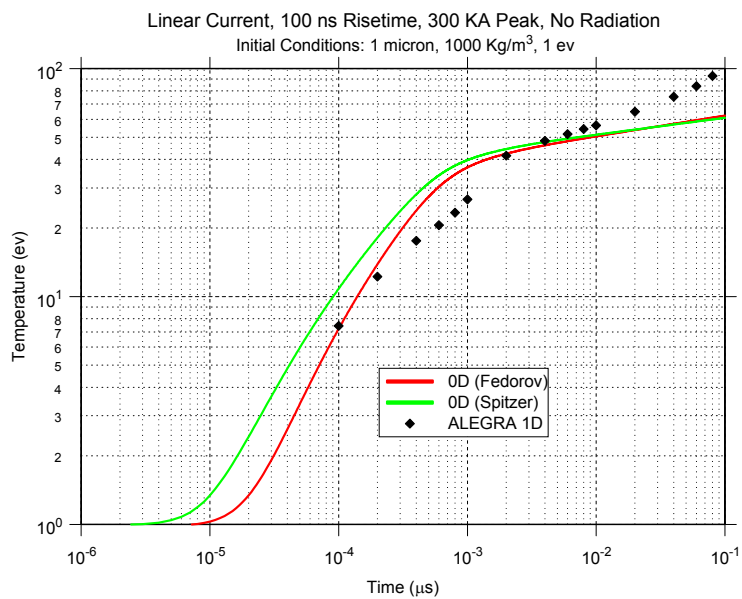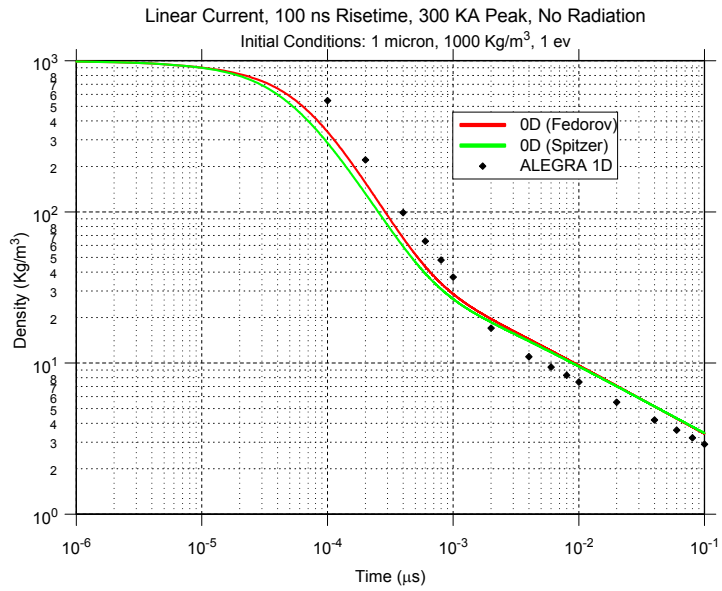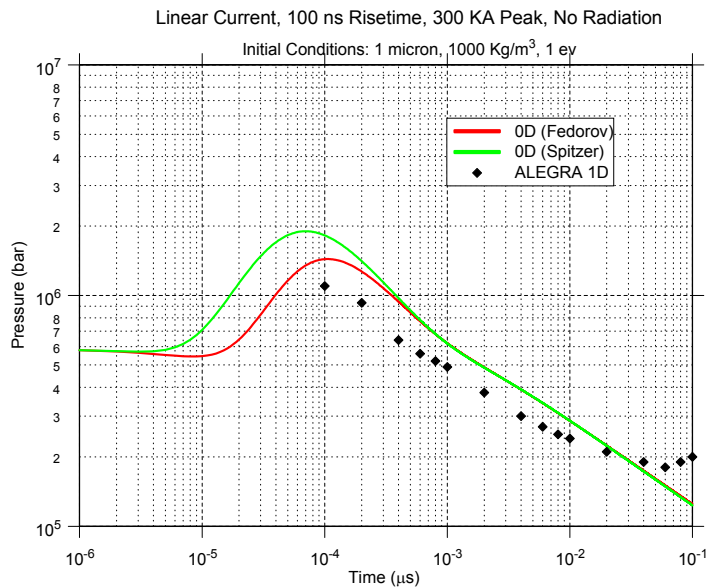

Figure 50. Comparison of 0D, ALEGRA_HEDP 1D simulations, and simple Braginskii-Martin Black Body models for pressure with a slow current drive.
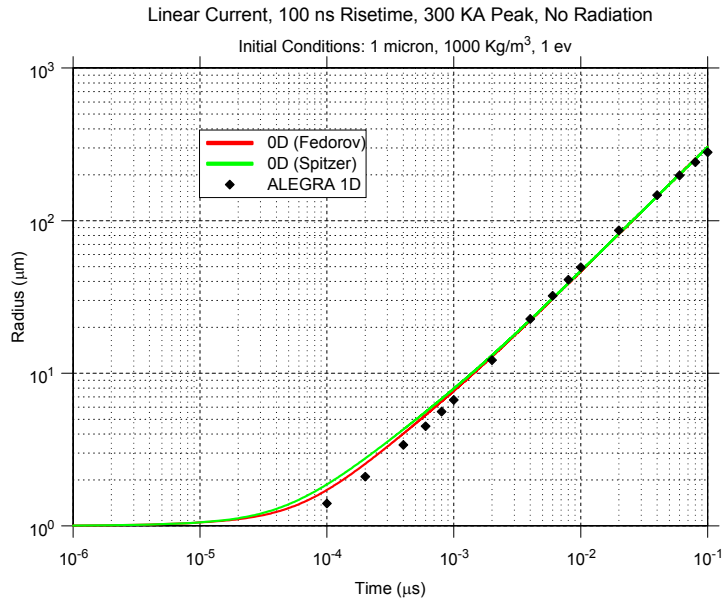
Figure 51. Comparison of 0D, ALEGRA_HEDP 1D simulations, and simple Braginskii-Martin Black Body models for channel radius with a slow current drive.
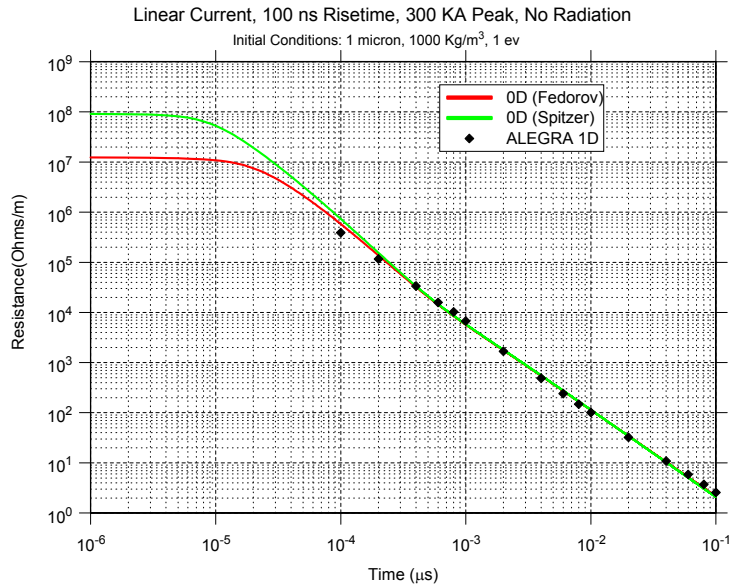

Figure 52. Comparison of 0D, ALEGRA_HEDP 1D simulations, and simple Braginskii-Martin Black Body models for resistance per unit length with a slow current drive.

6.2 Radiation Off

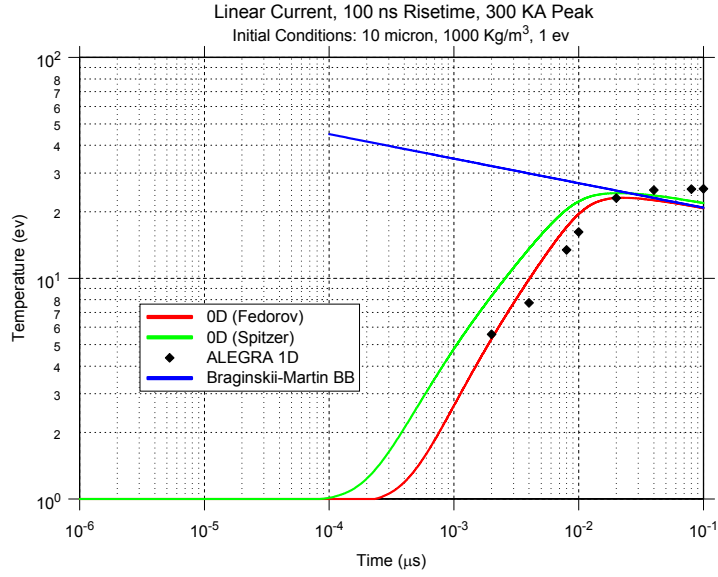Next the case with radiation turned off.

Figure 53. Comparison of 0D, ALEGRA_HEDP 1D simulations, and simple Braginskii-Martin Black Body models for temperature with a slow current drive and no radiation.

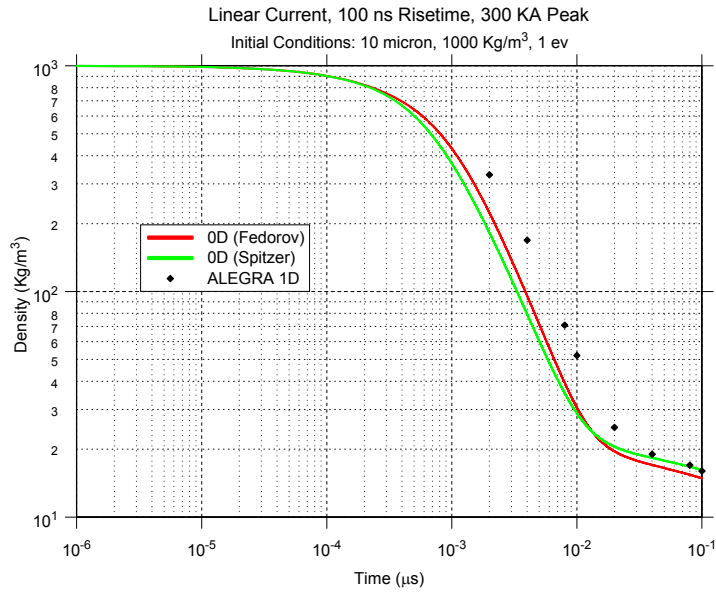Figure 54. Comparison of 0D, ALEGRA_HEDP 1D simulations, and simple Braginskii-Martin Black Body models for density with a slow current drive and no radiation.
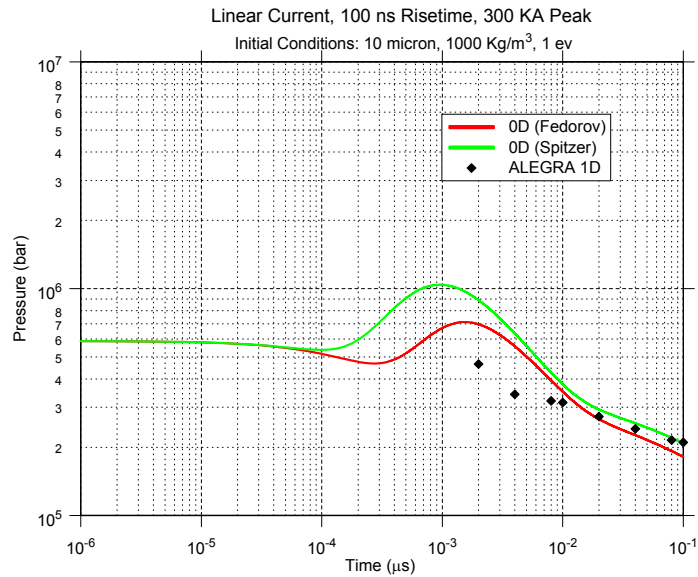

Figure 55. Comparison of 0D, ALEGRA_HEDP 1D simulations, and simple Braginskii-Martin Black Body models for pressure with a slow current drive and no radiation.
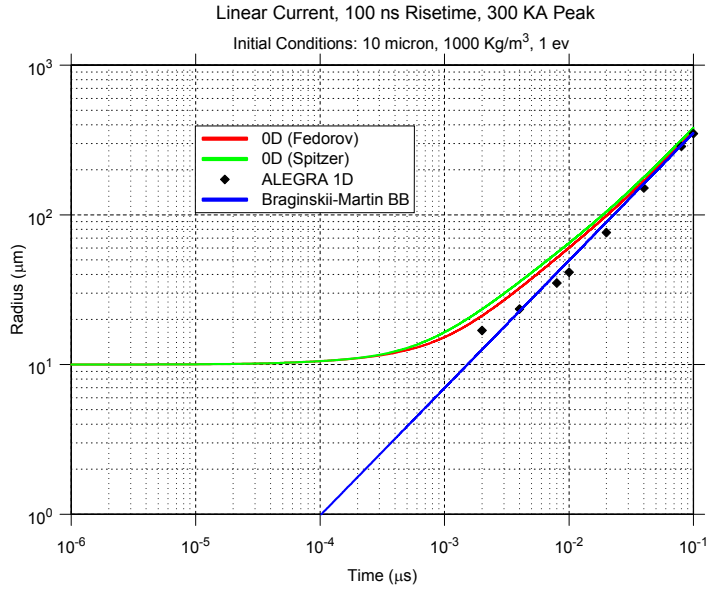
Figure 56. Comparison of 0D, ALEGRA_HEDP 1D simulations, and simple Braginskii-Martin Black Body models for channel radius with a slow current drive and no radiation.
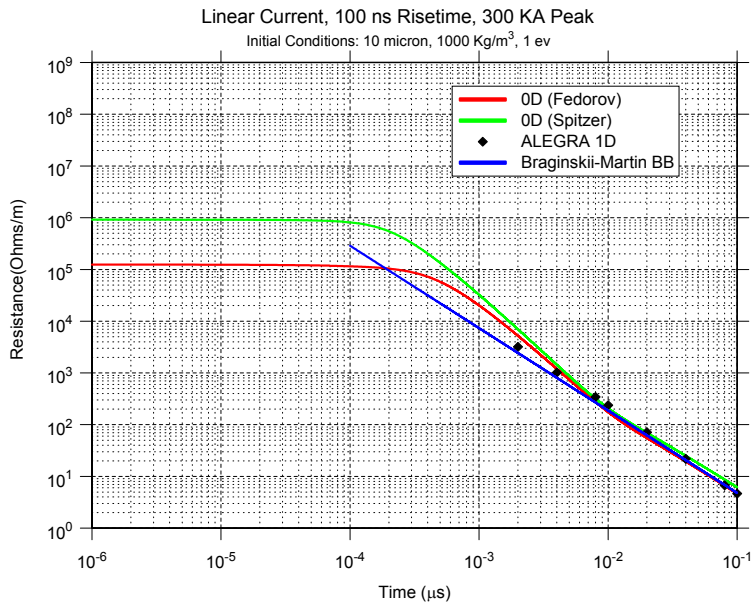

Figure 57. Comparison of 0D, ALEGRA_HEDP 1D simulations, and simple Braginskii-Martin Black Body models for channel resistance per unit length with a slow current drive and no radiation.

6.3 Larger Starting Radius

Next the case with a 10 μm starting radius.

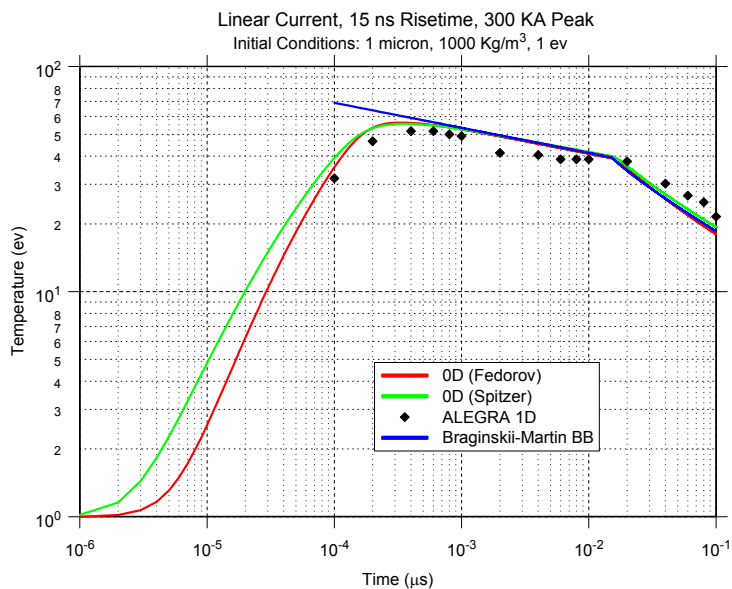
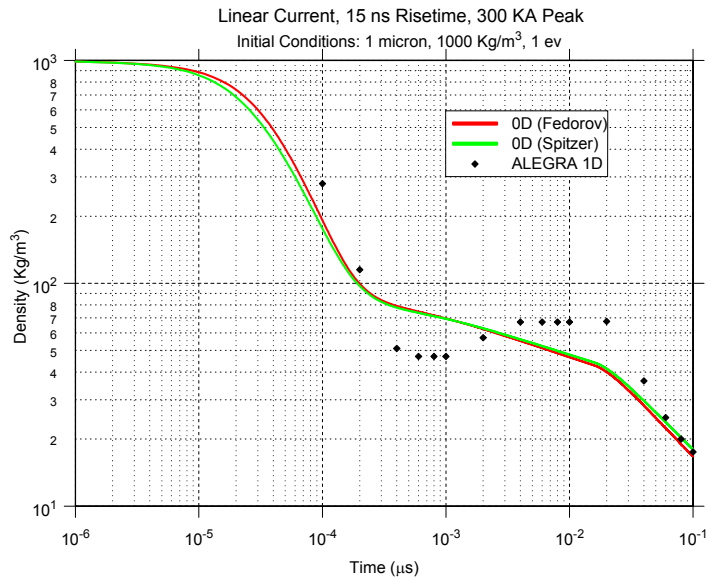Figure 58. Comparison of 0D, ALEGRA_HEDP 1D simulations, and simple Braginskii-Martin Black Body models for temperature with a slow current drive and 10μm initial channel radius.

Figure 59. Comparison of 0D, ALEGRA_HEDP 1D simulations, and simple Braginskii-Martin Black Body models for density with a slow current drive and 10μm initial channel radius.
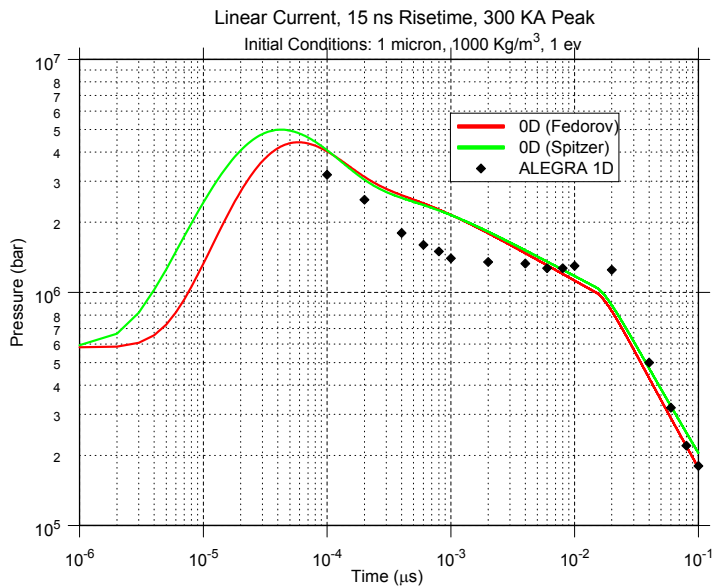

Figure 60. Comparison of 0D, ALEGRA_HEDP 1D simulations, and simple Braginskii-Martin Black Body models for pressure with a slow current drive and 10μm initial channel radius.

Figure 61. Comparison of 0D, ALEGRA_HEDP 1D simulations, and simple Braginskii-Martin Black Body models for channel radius with a slow current drive and 10μm initial channel radius.

Figure 62. Comparison of 0D, ALEGRA_HEDP 1D simulations, and simple Braginskii-Martin Black Body models for channel resistance per unit length with a slow current drive and 10μm initial channel radius.

6.4 Fast Current Drive

Next the case with current rising linearly to 300 kA in 15 ns remaining constant after this time.

Figure 63. Comparison of 0D, ALEGRA_HEDP 1D simulations, and simple Braginskii-Martin Black Body models for temperature with a fast rise time current drive.
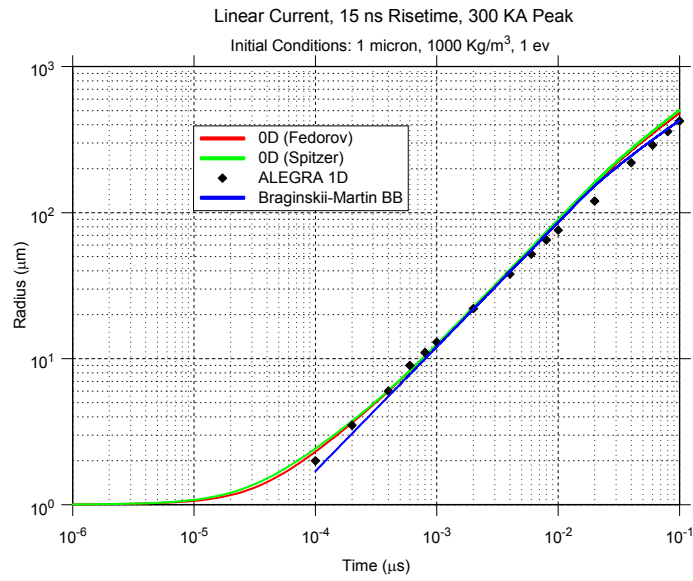
Figure 64. Comparison of 0D, ALEGRA_HEDP 1D simulations, and simple Braginskii-Martin Black Body models for density with a fast rise time current drive.
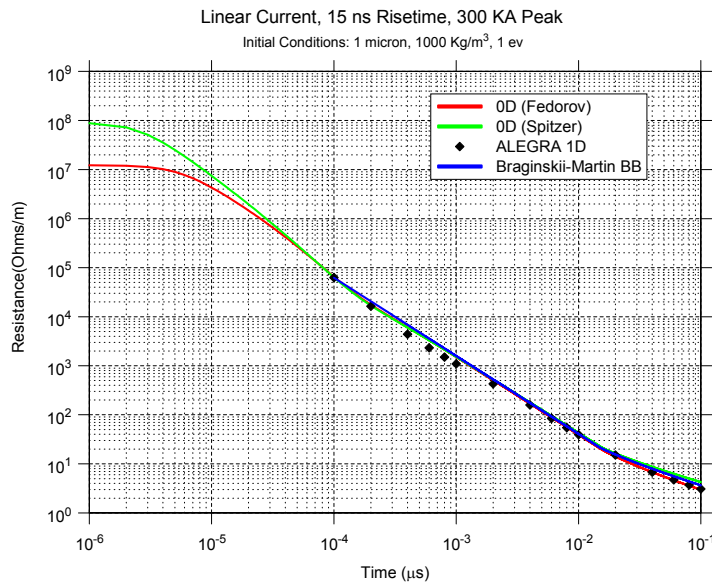

Figure 65. Comparison of 0D, ALEGRA_HEDP 1D simulations, and simple Braginskii-Martin Black Body models for pressure with a fast rise time current drive.

Figure 66. Comparison of 0D, ALEGRA_HEDP 1D simulations, and simple Braginskii-Martin Black Body models for channel radius with a fast rise time current drive.

Figure 67. Comparison of 0D, ALEGRA_HEDP 1D simulations, and simple Braginskii-Martin Black Body models for resistance per unit length with a fast rise time current drive.

6.5 Larger Current Drive

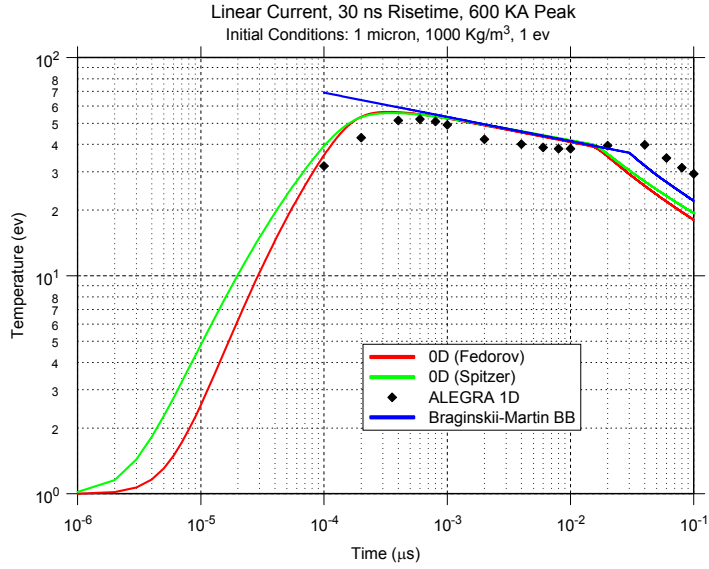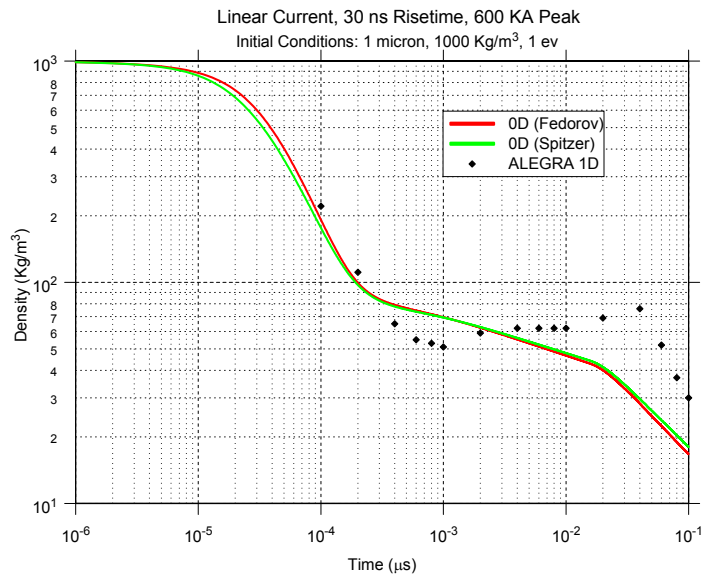Next the case with currents rising to 600 kA in 30 ns.

Linear Current, 30 ns Risetime, 600 KA Peak
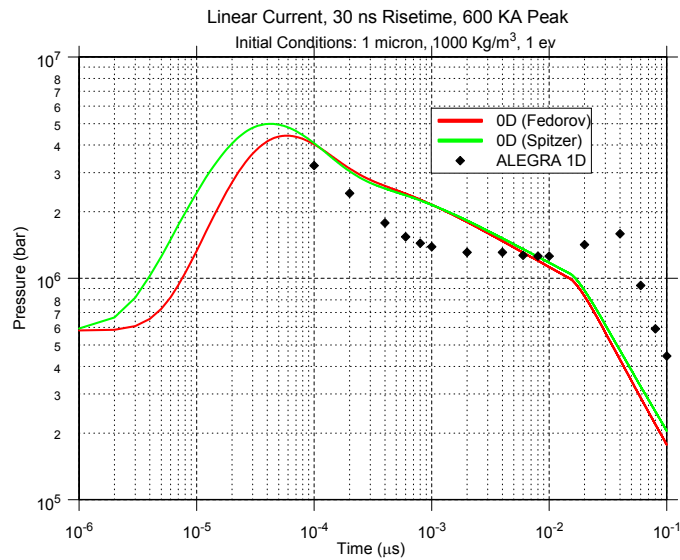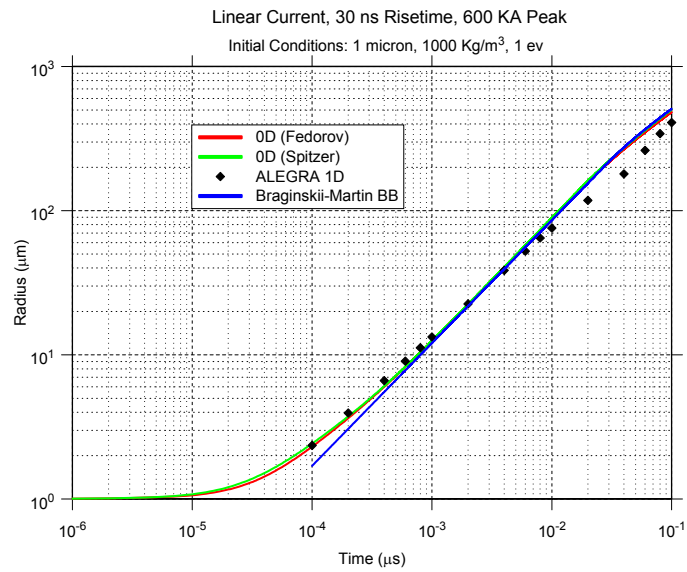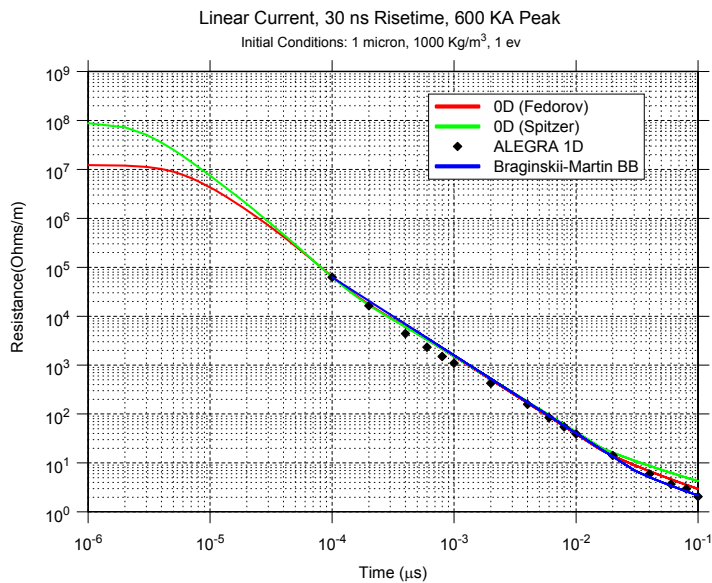Initial Conditions: 1 micron, 1000 Kg/m³, 1 ev

Figure 68. Comparison of 0D, ALEGRA_HEDP 1D simulations, and simple Braginskii-Martin Black Body models for temperature with a fast rise time high current drive.

Figure 69. Comparison of 0D, ALEGRA_HEDP 1D simulations, and simple Braginskii-Martin Black Body models for density with a fast rise time high current drive.

Figure 70. Comparison of 0D, ALEGRA_HEDP 1D simulations, and simple Braginskii-Martin Black Body models for pressure with a fast rise time high current drive.

Figure 71. Comparison of 0D, ALEGRA_HEDP 1D simulations, and simple Braginskii-Martin Black Body models for channel radius with a fast rise time high current drive.

Figure 72. Comparison of 0D, ALEGRA_HEDP 1D simulations, and simple Braginskii-Martin Black Body models for channel resistance per unit length with a fast rise time high current drive.

6.6 Step Voltage Drive

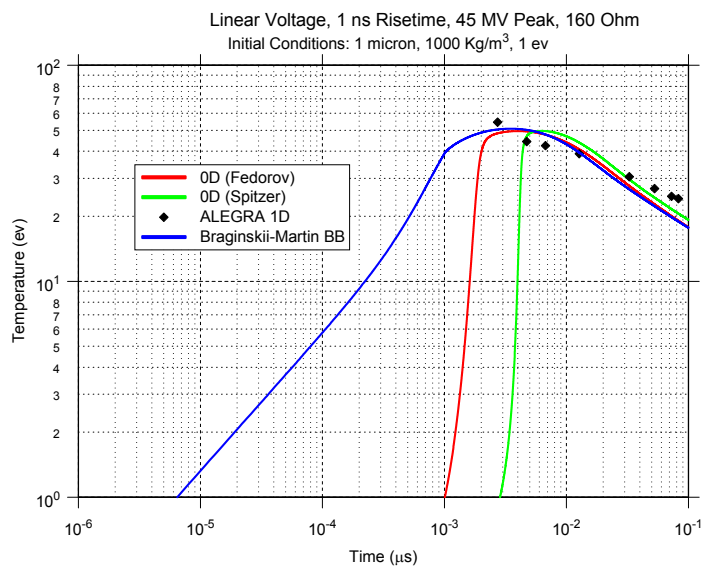The next case has a step voltage drive (1 ns rise time).

Figure 73. Comparison of 0D, ALEGRA_HEDP 1D simulations, and simple Braginskii-Martin Black Body models for temperature with a fast rise time or step voltage drive.
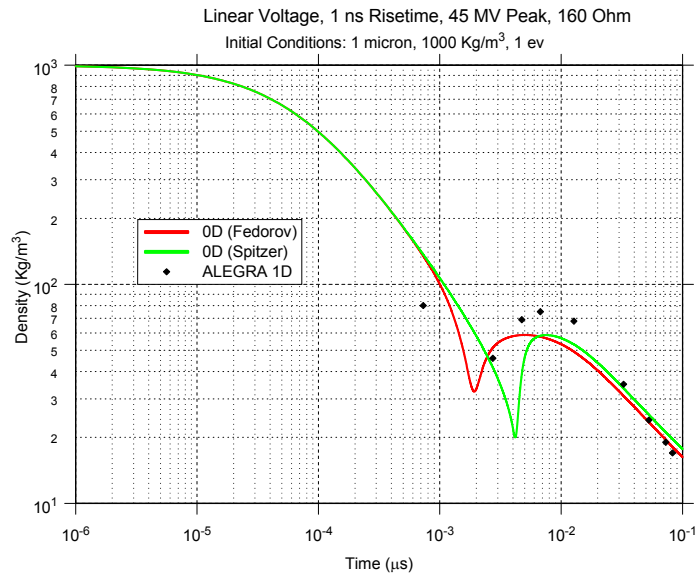
Figure 74. Comparison of 0D, ALEGRA_HEDP 1D simulations, and simple Braginskii-Martin Black Body models for density with a fast rise time or step voltage drive.
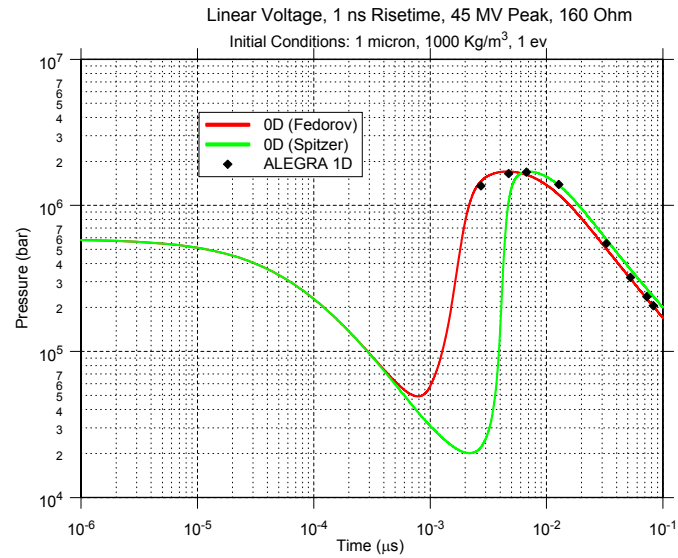

Figure 75. Comparison of 0D, ALEGRA_HEDP 1D simulations, and simple Braginskii-Martin Black Body models for pressure with a fast rise time or step voltage drive.
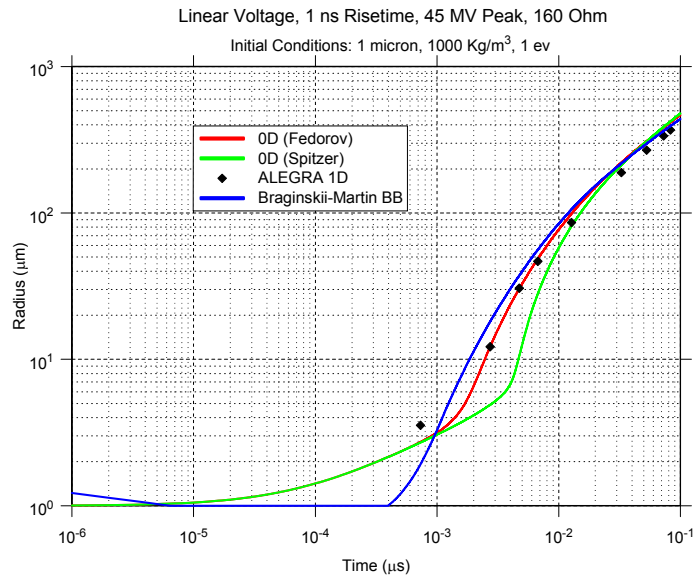
Figure 76. Comparison of 0D, ALEGRA_HEDP 1D simulations, and simple Braginskii-Martin Black Body models for channel radius with a fast rise time or step voltage drive.
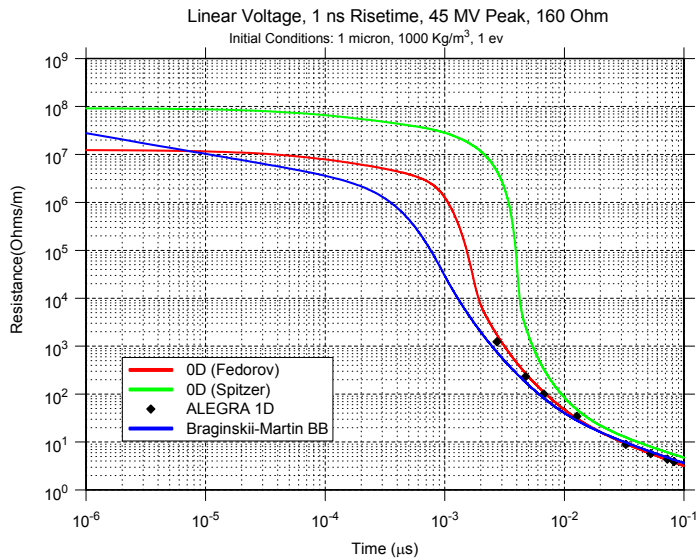

Figure 77. Comparison of 0D, ALEGRA_HEDP 1D simulations, and simple Braginskii-Martin Black Body models for channel resistance per unit length with a fast rise time or step voltage drive.

The agreement between the 0D model, the ALEGRA-HEDP 1D model, and the simple Braginskii-Martin BB model is reasonably good. There are discrepancies at early time in the Braginskii-Martin BB model, but these are not too important since the channel resistance is typically quite high in this region.

7   SWITCH IMPEDANCE

We now briefly consider other terms in the switch impedance besides the resistance term.

7.1   Low Frequency Inductance

In the experiment we actually have several poles on the switch. With three poles the inductance of the arcs is approximately [33]

$$L = \frac{\mu_0 \ell}{2\pi} \left[\frac{1}{3}\frac{1}{4} + \ln\left(b_{eff}\right) - \frac{\ln^2\left(w\right) - \ln\left(a\right)\ln\left(\sqrt{2aw}\right)}{2\ln\left(w\right) - \ln\left(a\right) - \ln\left(\sqrt{2aw}\right)} \right] \tag{28}$$

where the first term is the internal inductance of the three arcs in parallel, the arc radius is $a\left(t\right)$ (to get an idea of the inductance at later times we can take roughly $a = 0.5$ mm), the spacing between poles is $w = 15$ in, $\ell = 10.5$ cm, and in two dimensions the effective return current radius is $b_{eff} = 50$ in. The formula (28), without the internal first term, can also be used to estimate the metallic rod inductance, using a different fixed value of the radius $a \to b_r \approx 0.5$ in, and rod length $\ell_r \approx 4$ in; the other side of the gap we can take $b_r \approx 1.5$ in. We are after the difference inductance due to the transition from triplate strip center conductor to three cylinders (arc or electrodes). To correct for the change from the center conductor being a thick strip to three rods we take the difference of (28) and the inductance of a strip conductor (of width $2w_1$ and thickness $2\Delta_1$) [33]

$$L_{strip} = \frac{\mu_0 \ell}{2\pi} \left[\ln\left(b_{eff}\right) - \ln\left(a_{eq}\right) \right]$$

where the inner equivalent radius of the strip is

$$a_{eq} \approx \frac{w_1}{2} \left[1 + \frac{\Delta_1}{\pi w_1} \left\{ \ln\left(4\pi w_1 / \Delta_1\right) + 1 \right\} \right], \ w_1 \geq \Delta_1$$

Thus the difference inductance is

$$\Delta L = \frac{\mu_0 \ell}{2\pi} \left[\frac{1}{3}\frac{1}{4} + \ln\left(a_{eq}\right) - \frac{\ln^2\left(w\right) - \ln\left(a\right)\ln\left(\sqrt{2aw}\right)}{2\ln\left(w\right) - \ln\left(a\right) - \ln\left(\sqrt{2aw}\right)} \right]$$

If we take the strip thickness to be $2\Delta_1 \approx 6$ in strip width to be $2w_1 \approx 50$ in, to approximate the triplate region, then $\Delta L \approx 33$ nH $+ 45$ nH ≈ 78 nH, where we did not include the internal inductance in the first term which is associated with the electrodes.

The time derivative of the arc inductance is found by differentiation of (28)

$$\frac{dL}{dt} = \frac{dL}{da}\frac{da}{dt} \approx -\frac{1}{3}\left(\frac{\mu_0 \ell}{2\pi a}\frac{da}{dt} \right) \tag{29}$$

The experimental circuit models frequently include a transmission line representing the nominal three

electrode characteristic impedance values. In this case the difference inductance would be modified to be the difference between this nominal value and the arc inductance

$$\Delta L = \frac{\mu_0 \ell}{2\pi} \left[\frac{1}{4} + \ln \left(b_r / a \right) \right] \frac{1}{3}$$

where in this case b_r is a nominal electrode radius.

7.2   Switch Capacitance

Note that because of transient effects (propagation time delays in the switch region) there may be corrections to this impedance term which should be taken into account [34]. At late time this contribution physically results from the shunt capacitance $C = O \left(1 \text{ nF} \right)$ across the switch, which is sizable due to the presence of the water dielectric, in addition to propagation delays (accounted for by transmission line sections in the experiment).

8   EXPERIMENT

The experiments done on the Z20 test stand are now summarized and compared.

8.1   Introduction

There is a long history of using untriggered water dielectric spark gap switches in schemes to generate terawatt peak power levels for high energy density physics applications. At Sandia, these machines are known as Ripple, Proto II, Hermes III, Saturn, PBFA II, RITS (Radiographic Integrated Test Stand) and now Z. Other accelerators in the United States using water switches are Gamble and Mercury at the Naval Research Laboratory in Washington DC and PITHON, Double Eagle at Titan, Pulse Sciences Division. While untriggered water switching has been used successfully on these machines, the energy losses in the water spark gap switch are always a concern, particularly at very high voltages. A machine at Harry Diamond Laboratories, the Aurora Modification Project (AMP), was eventually dismantled because excessive losses in the water switches prevented the performance specification from being met. Presently, an increasing concern is the lack of a predictive model for high power water switches where risetime effects and energy losses are known apriori.

The experimental data for this analysis has been obtained from the ongoing module testing, a continuation of the System Assessment Test Program (SATPro) for the ZR project. The pulsed power for Z20 is based on technology previously developed at Sandia of Marx generators, water insulated pulse forming and transmission lines. Z20 is one module of the latest design of the full 36 module ZR [35], [36], [37]. The goal of Z20/SATPro testing is to assess this design for meeting the performance specification for ZR and to identify areas for improvements for ZR and beyond present capabilities to the next generation machine.

8.2   Experimental Setup

The SATPro module is comprised of a 60-stage, 100 kV, 43 nF Marx generator charging a 26 nF, 100 ns Intermediate Storage Water Capacitor (ISC) to a peak voltage of approximately 5.5 MV in about 1.2 μs. See Figures 78 and 79. A Laser Triggered Rimfire Gas Switch (LTS) switches the ISC into a 2.6 Ω, 45 ns long coaxial Pulse forming Line (PFL) in approximately 200 ns. The negatively charged PFL is switched
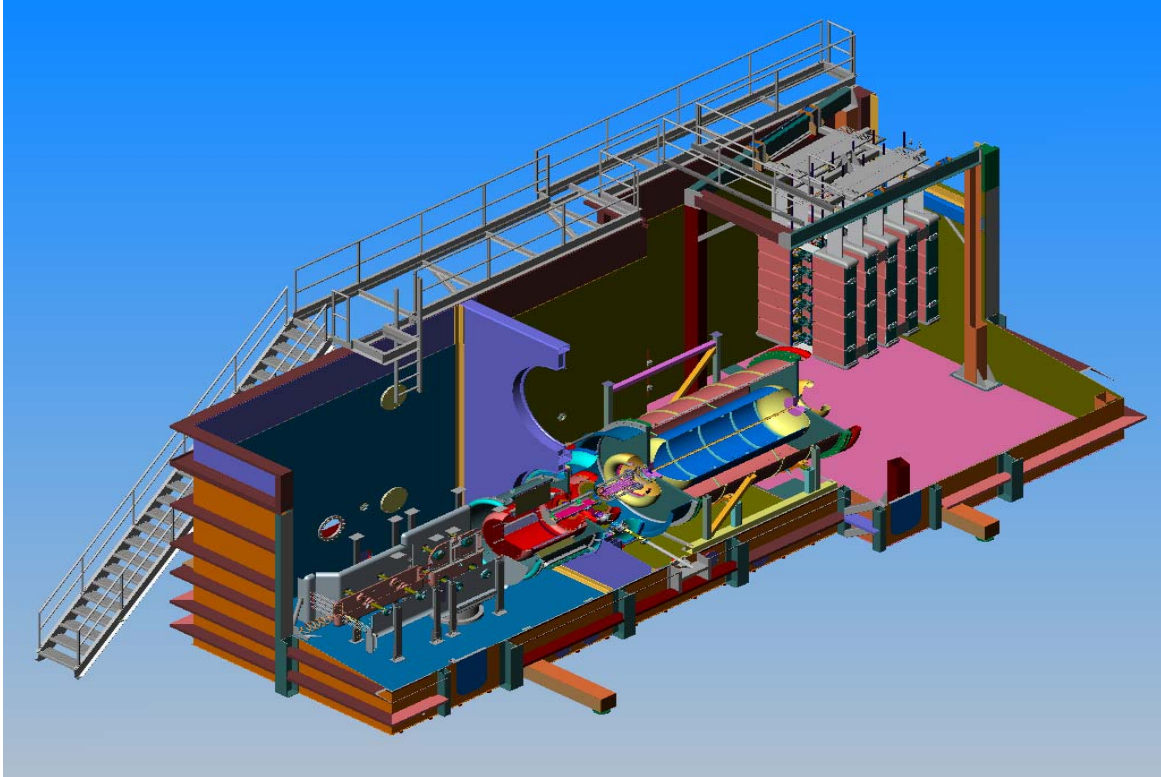
Figure 78. The Z20/SatPro module at Sandia National Laboratories.

via water switches into a 4.2 Ω, 35 ns tri-plate transmission line (OTL1). Pre-pulse/peaking switches are located between the output of OTL1 and a 6.4 Ω, 50 ns transmission line (OTL2). For the purpose of assessing the system, OTL2 is terminated in eight parallel liquid resistors made of a Sodium Thiosulfate water solution. Initially the load was intended to be matched to the impedance of OTL2. However, the voltage across the load was too high, resulting in electrical breakdowns. Subsequently, the resistance was lowered to 2.5 ohms resulting in a decreased voltage at the load.

To correctly and efficiently assess the system, extensive diagnostics are featured. Current and voltage monitors are co-located in the input and output positions on the Marx Bank, ISC and PFL, as well as numerous positions on the output transmission lines. Current viewing resistors (CVRs) measured the current through each of the eight liquid resistors constituting the resistive dummy load for the system, allowing for an assessment of current uniformity along the OTL2.

94
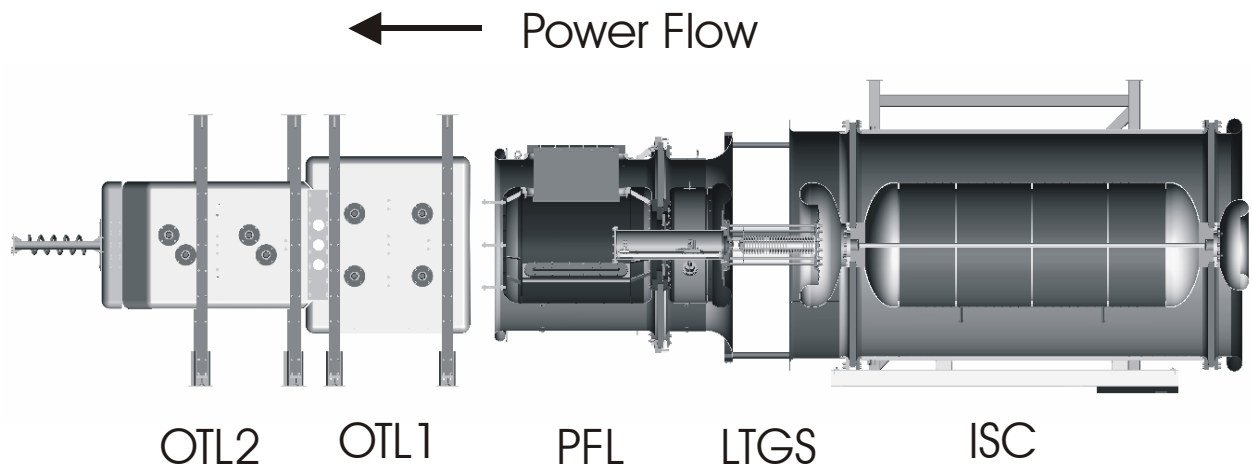
Figure 79. The SATPro experimental setup consists of a Marx (not shown) firing into the pulse forming section. The main water switches are between the PFL and OTL1 and prepulse/peaking switches are between OTL1 and OTL2.

8.3 Comparisons of Experimental Data and Circuit Models

Circuit models have been extensively used in the evaluation of the Z20/SATPro performance assessment for ZR and the experimental data has been used to refine the ZR circuit model, since accurate and precise modeling of pulsed power components is an increasingly important critical mission area. This model has been used extensively in the data analysis for this effort. For a circuit code to be valid, the match to data must be very good throughout the system. Since the present effort relies heavily on the Z20 SCREAMER model, a thorough depth match between data and circuit code is presented.

The circuit code used in the modeling is called SCREAMER [38]. SCREAMER is a lumped element circuit code developed at Sandia National Laboratories. Among its features is a library of components unique to pulsed power and a quick run time. The existing switch models available in SCREAMER will be discussed later in this report. The Z20 SCREAMER model is arranged such that code outputs occur in the same electrical length as the physical monitors in the experiment. This allows relative timing between signals to be accounted for. Also the monitors in the experiment are all set to a common start time allowing for a full agreement between the circuit model and the experiment.

8.3.1 the energy storage system

The circuit characterization of the Marx Bank was obtained in the first phase of the SATPro program. The series resistance and inductance were obtained by doing short circuit shots using ringing frequency and decay. These measured values of 1.4 Ω for the series resistance and 11 μH for the inductance are largely independent of voltage. The measurement of these internal circuit elements are important because the complicated hanging hardware, shown in Figure 80, can add significantly to the equivalent circuit element and be very difficult to estimate. In the circuit code, the Marx Bank is represented by an RC parallel combination, charged to the full (actual) charge voltage and discharged through its internal series resistance and inductance. The Marx discharge current is measured by a CVR both in the experiment and its equivalent in the circuit code. Comparison of the Screamer circuit code and the experimental data, shown in Figure 81, indicates an excellent match.

8.3.2 the pulse forming section

While the Intermediate Storage Capacitor (ISC) is conceptually simple, the details of the design make its modeling a several step process. As shown in Figure 82, the contours of the ISC connections are intricate to control the electric fields. The ISC is insulated with water between its inner and outer conductors and immersed in the same transformer oil bath as the Marx Bank. The ISC circuit component model is developed by first computing the capacitance of the various connection components using a commercial electrostatic code then representing it in the circuit code by transmission lines of the calculated capacitance and correct electrical length. The input cones, fluid separation barrier and the tank head inner are all modeled this way. Additionally, stray capacitances at the connections are treated as lumped elements. Comparisons between experiment and circuit models are shown in Figure 83. Note some deviations are seen in late time but it is well past the waveform peak.

The ISC energy is switched to the PFL, Figure 84, though a laser triggered gas switch. While laser triggered gas switches are complicated and expensive, their modeling is fairly straightforward. Variations in the shot-to-shot run time, as well as issues with the laser trigger timing are used as an input to the circuit code. With this input, the transit time between actual physical monitors is defined and very reliable from shot-to-shot.
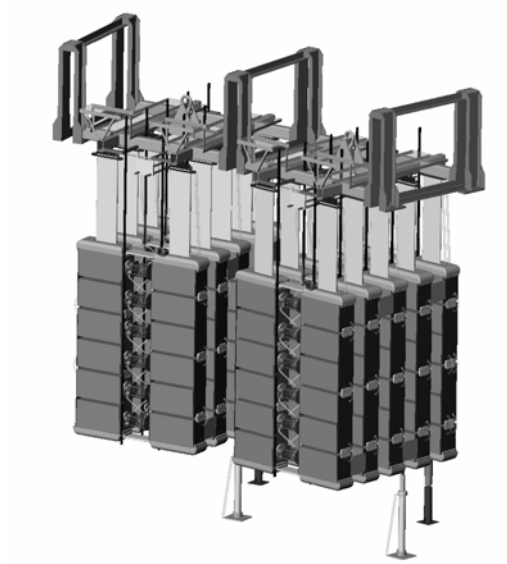
Figure 80. The physical layout of the Marx Bank showing the hanging hardware for structural support.
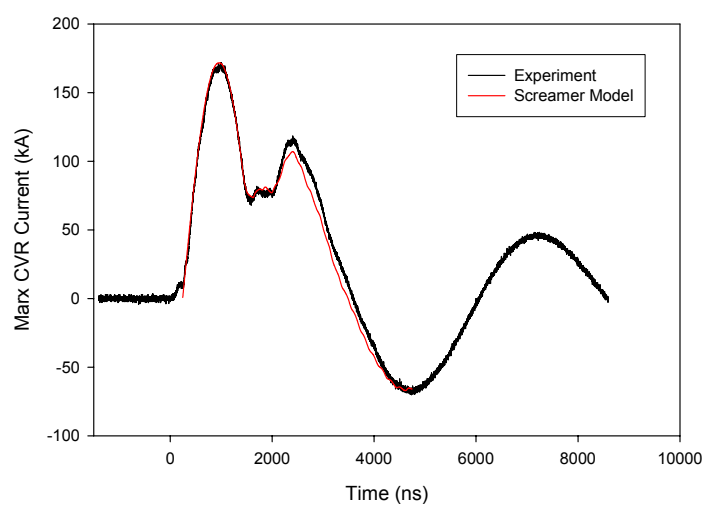

Figure 81. The match between the circuit model and experimental data. The agreement is such that it is difficult to discern between experiment and model.
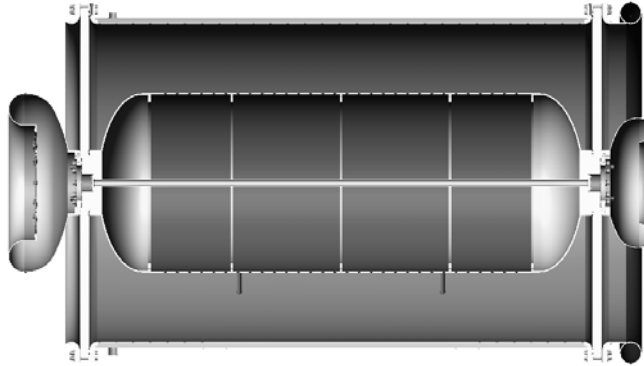
Figure 82. The physical layout of the ISC. Each transition on the inner conductor has a transit time and capacitance associated with it.

As with the ISC the implementation of the PFL is rather complicated by the necessity of field grading requirements around the laser triggered gas switch. The modeling is further complicated because the output of the PFL is governed by a set of water spark gap switches and a geometry conversion from coaxial PFL geometry to the parallel plate geometry of the output transmission lines. As shown in Figure 85, the circuit modeling captures the changing voltage waveform of the PFL and is in reasonable agreement even late in the waveform.
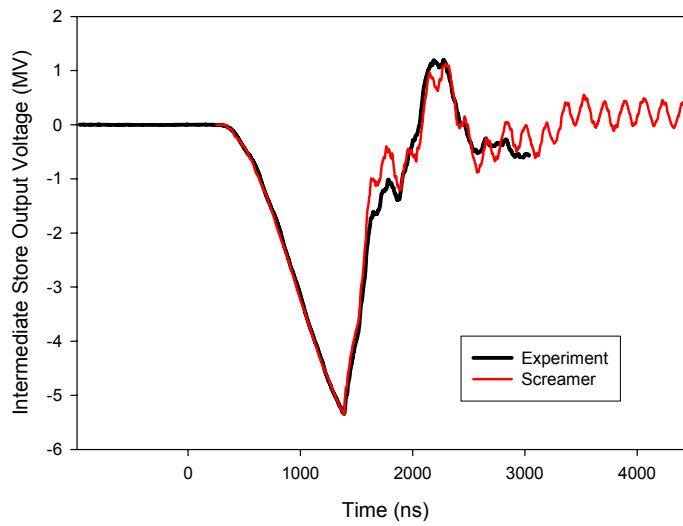
Figure 83. The match between experimental data and the circuit modeling is excellent until many 100s of ns past the peak voltage.

Figure 84. The physical layout of the PFL with a view of the water spark gap switch shown.

8.3.3 the water switches

A detailed water switch study on basic ZR-like switches had been performed just prior to SATPro to address concerns regarding water switch losses at the voltage levels required for ZR as well as abrupt geometry changes and multi-moding of the output transmission lines [39], [40]. In that experiment, the number of water switches could be varied between 1 and 5 with various electrode enhancements possible. It was shown that (1) three water switches operated independently from each other and carried roughly equal peak currents, (2) water switch jitter showed unexpectedly small dependence electrode enhancement but one configuration did result in minimum jitter, and (3) an abrupt coaxial-to-tri-plate geometry change was adequate and the tri-plate transmission line does not multi-mode with the frequency content of interest.

The water switch region in Z20/SATPro is asymmetrical. As shown in Figure 86 and 87, electrodes are attached (a) to the faceplate of the PFL and (b) the center conductor of the tri-plate. Z20 has electrode mounting hardware for between one and four switch sites, equally spaced along the tri-plate center conductor. The baseline water switch configuration was chosen to minimize jitter and consists of 3 water switches with a 3 inch diameter cathode attached to the PFL and a 1 inch anode on the tri-plate, with a nominal inter-electrode gap spacing of 12.7 cm. Later in the testing both the electrode profile as well as the gap spacing were changed. These changes are noted. For this modeling effort, the resistance of the water switches, $R(t)$ is represented by a semi-empirical expression referred to as the "Exponential Decay Model". The success of the water switch modeling is established by comparing the match of waveforms on the output transmission line, OTL1, between modeling and experimental data, shown in Figure 89.
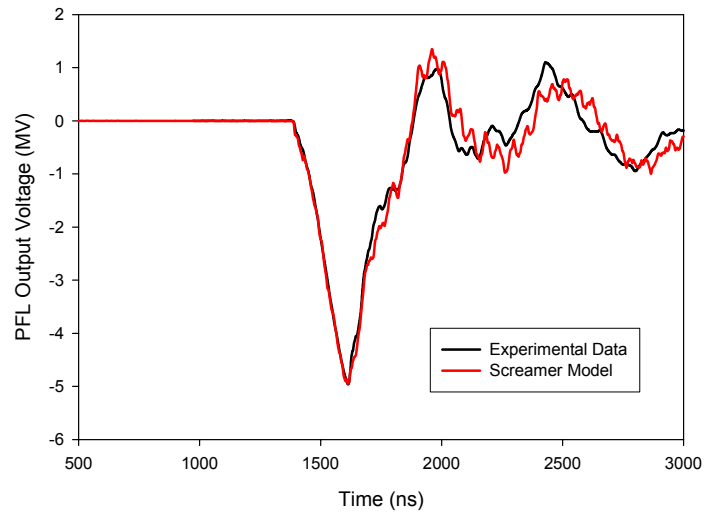
Figure 85. The circuit modeling even captures some of the structure of the waveform though deviations occur late in time.
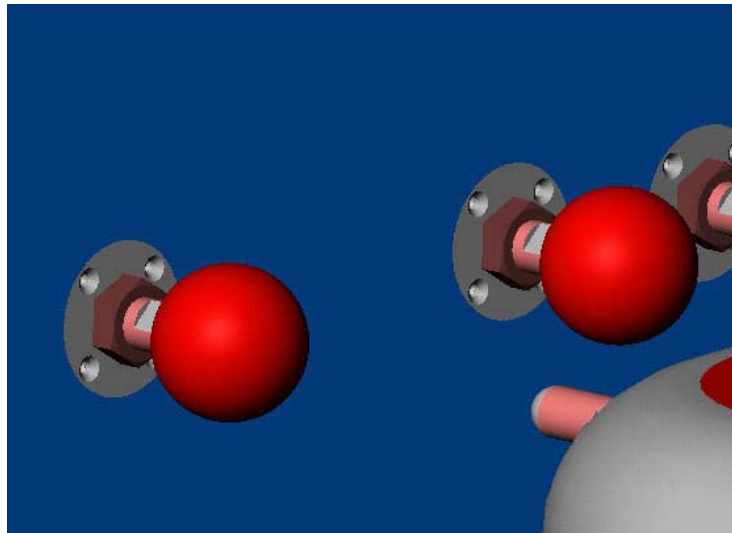
Figure 86. The details of the water switches. The cathodes are attached to the PFL and have the larger electrode diameter.
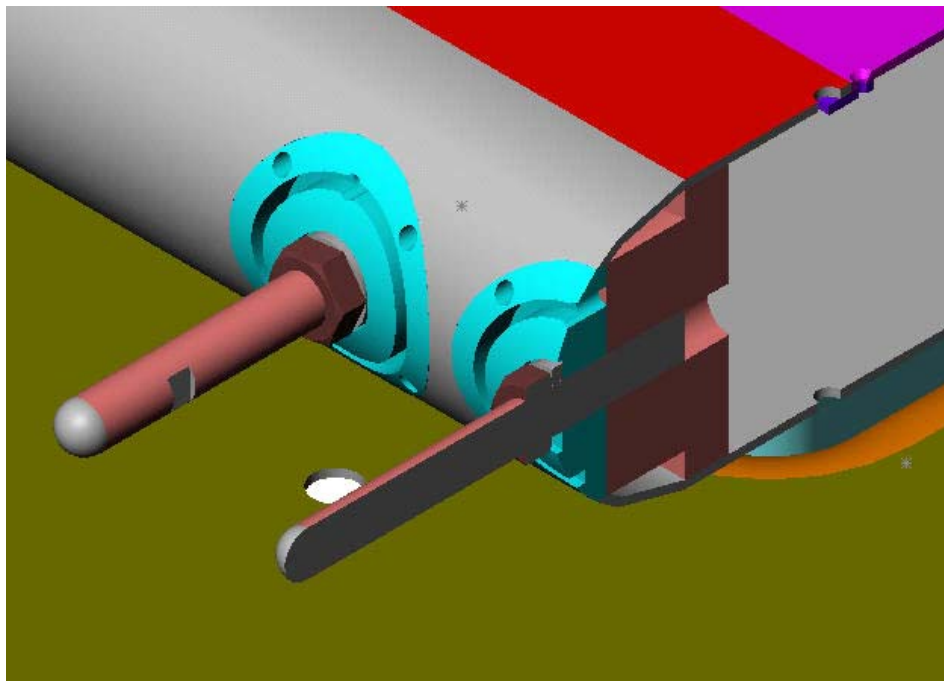
Figure 87. The details of the water switches. The anodes, attached to the tri-plate, are shown with 1 inch diameter hemispheres on a 1 inch rod.

8.3.4 output transmission lines

The output transmission lines in Z20 are a tri-plate design, chosen for its resistance to multiple mode propagation. The design consists of 2 output lines, oriented vertically, as shown in Figure 88. The two lines, designated OTL1 and OTL2, have different characteristic impedances, and are separated by the prepulse suppression switches. The prepulse switches are closed for the shots in this analysis. OTL2 is terminated in an undermatched resistive load.

Careful consideration was given to the placement of diagnostics in the OTLs. Each OTL has three probes normal to the direction of propagation in two locations. One location is near the water switches on (main water switches on OTL1 and prepulse water switches on OTL2) and another near the midpoint of the OTL. Each probe location has co-located ports for current and voltage measurements. The voltages are measured with capacitive electric field probes and are calibrated in-situ to insure accurate calibrations. The currents are measured with derivative magnetic field probes (B-dot probes) and calibrated to the total current in the transmission line. The monitors of interest for the calculation of the dynamic spark resistance $R(t)$ are located in the middle position as shown in Figure 88, and is denoted OTL1_M. Probes are located in each ground plane of the triplate transmission line. The agreement between the SCREAMER circuit modeling code and the experimental data is excellent and is shown in Figure 89.

The intentional impedance mismatch between OTL1 and OTL2 increases the current of the output pulse. To further increase the efficiency of the machine, the electrical length of OTL1 is short compared to the pulse risetime. This results in multiple reflections along the line, and the effect is seen in the pulse shape, shown in Figure 90. Two changes in the slope of the voltage rise occur in the voltage waveforms measured at OTL1_M position. Since the pulse risetime is longer than the electrical length of the transmission line, it is expected that the portion of the wave reflected from the OTL2 will interfere with the measured waveform. The influence of the impedance mismatch is shown by using the co-located current and voltage monitors to construct the forward-going voltage waveform, $V_{for}(t)$ and the reflected voltage waveform, $V_{ref}(t)$ at the midplane monitor location, OTL1_M, from the relations

$$V_{for}(t) = \frac{V(t) + Z_0 I(t)}{2}$$

and

$$V(t) = V_{for}(t) + V_{ref}(t)$$

The relationship between the measured voltage, the forward going voltage, and the reflected voltage on OTL1 is shown in Figure 91. The first inflection point in the measured waveform is the result of the wave reflected from the impedance mismatch between OTL1 and OTL2. This has been checked by transit time calculations between the monitors and the reflection points.

The second point of inflection is quite pronounced in the measured voltage waveform at OTL1_M. The second inflection point has been identified with the aid of the SatPro SCREAMER circuit model. In SCREAMER, additional components are easily added. To determine the effect of a reflection from the water switches on the measured waveform, 30 ns of transmission line was added to OTL1 between the water switches and the OTL1_M monitor position. An overlay of the forward going voltage waveform on OTL1 derived from the measurements, $V_{for}(t)$, and the simulated forward going voltage, V_{for}^{sim}, is shown in Figure 92. The addition of 30 ns of transmission line yields a forward going voltage, V_{for}^{sim} with a much reduced peak voltage than the actual $V_{for}(t)$ and the deviations in the waveform occur at the same time as the second inflection point. This implies the reflected voltage wave is again reflected from the water switches providing a contribution to the forward going wave. For our purpose of identifying the voltage across the

water spark gap as a function of time, the last 40 ns before the peak of the derived voltage $V_{for}(t)$ is not valid for the calculation of the dynamic impedances.
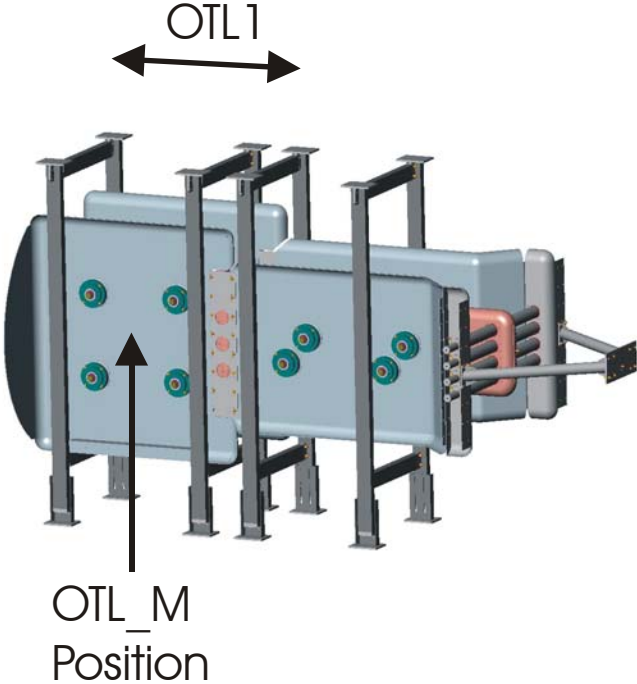
Figure 88. The output transmission line structure showing the location of the monitors in the ground planes of the triplate transmission line, OTL1.
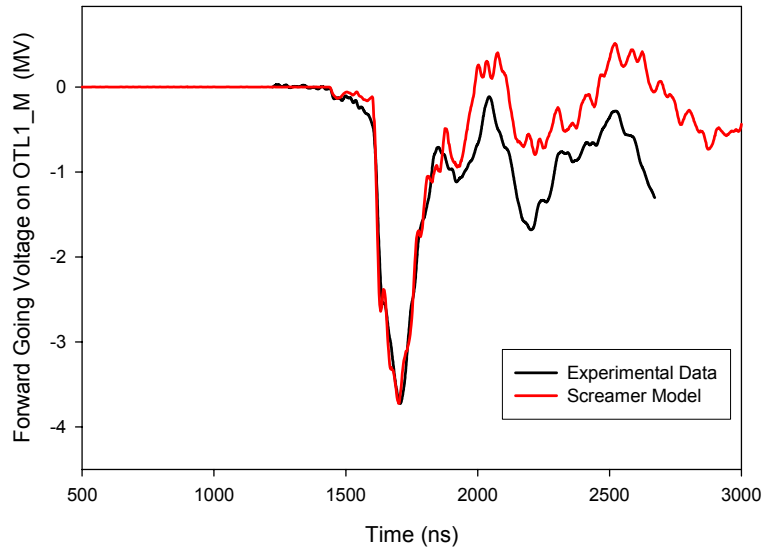
Figure 89. The agreement between the SCREAMER model and the experimental data is shown for the forward going voltage on OTL1_M. The forward going voltage is constructed from co-located current and voltage monitors.
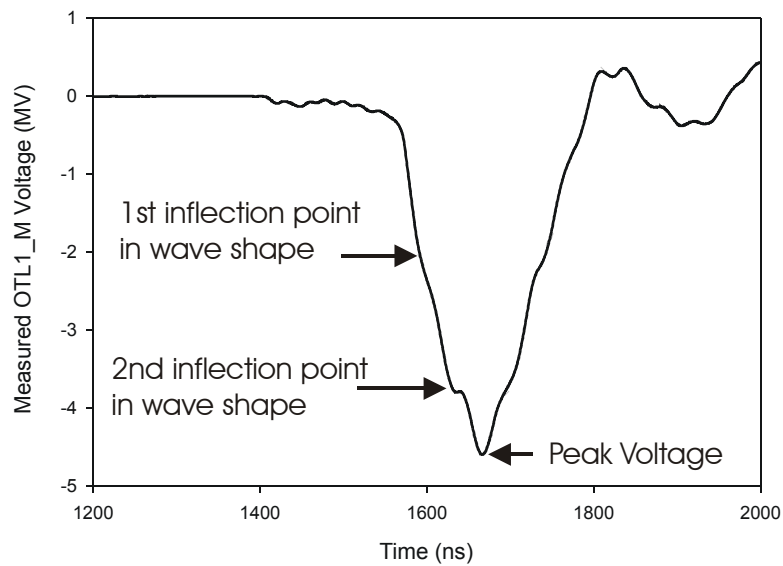
Figure 90. The voltage waveform measured on OTL1 at the Mid position. Two changes in the slope of the voltage are shown.
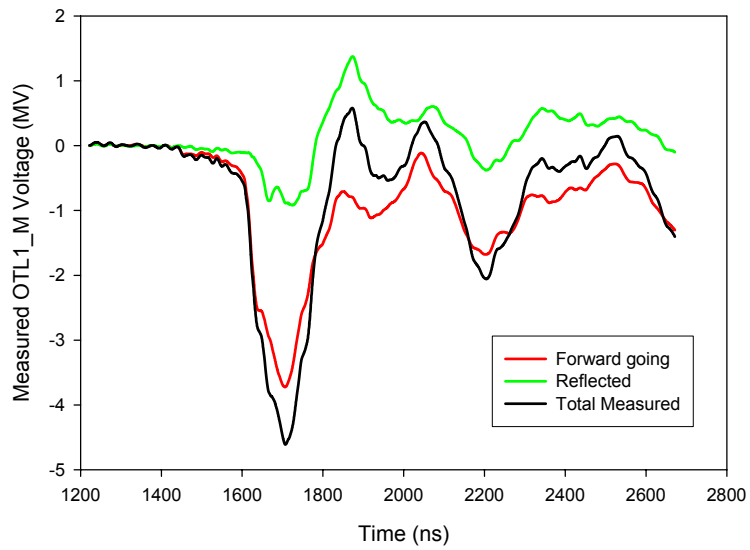
Figure 91. The relationship between the measured voltage (black), the forward going voltage (red) and the reflected voltage (green). The first inflection point in the measured voltage is caused by the voltage reflected from the impedance mismatch at OTL2.
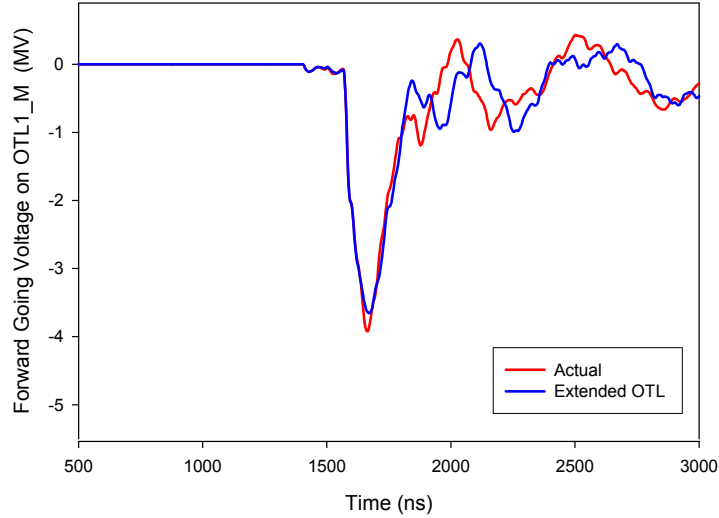
Figure 92. The origin of the second point of inflection is identified by adding an additional 30 ns of electrical length to OTL1 between the OTL1_M monitor location and the water switch location. The second point of inflection is caused by the short electrical length of OTL1 which produces a reflection from the water switches of the reflected wave, resulting in a forward going wave again.

8.4 Calculation of the Impedance

The difficulties of directly measuring the voltage drop across an arc channel and the resistance of the arc, even at moderate voltages, are well known [41], [42], [43], [44]. In addition to the very large dynamic range of such a measurement, in a machine with charging voltages on the order of 5 MV with low impedances, the difficulties in making precise measurements are enormous. Yet, in spite of these difficulties, notable contributions to the literature on the resistance of water arc channels for high power accelerators have been made [45], [46], [47].

8.4.1 the model

Prior to the time to switch closure, t_{switch}, the water spark gap is modeled as a parallel combination of a capacitor and resistor. For long gaps, the capacitor is variable to account for the time varying capacitance of the advancing streamer [48], [49]. For times greater than the switch closure time, the model is represented by the circuit shown in Figure 93. The circuit equations are

$$I(t) = I_C(t) + I_R(t) + I_a(t)$$

and

$$V_{out}(t) = V_{in}(t) - I_a(t) R_a(t) - \frac{d}{dt}[L(t) I_a(t)]$$

where the inductance, $L(t)$ is

107
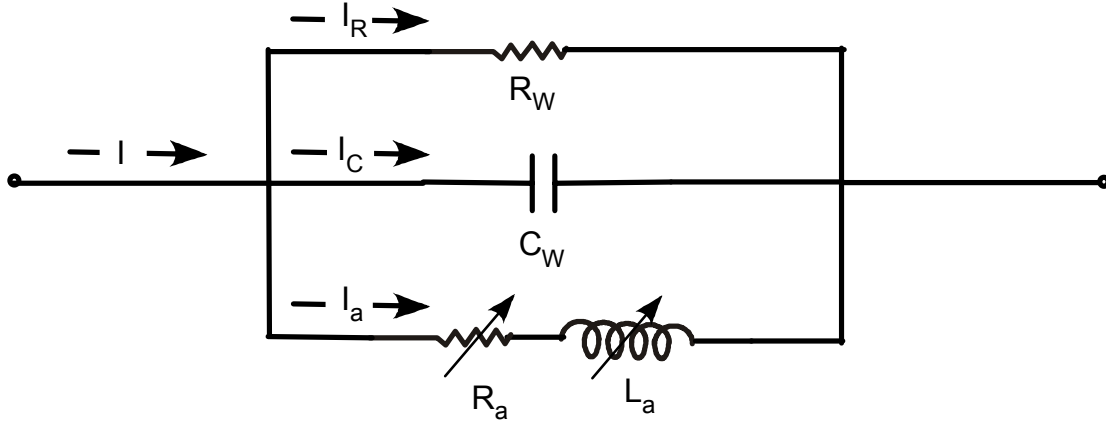
Figure 93. The circuit representation of the water spark gap for times, $t > t_{switch}$.

$$L(t) = L_a(t) + L_e$$

and L_e is the inductance of the electrodes and $L_a(t)$ is the arc inductance.

The dynamic resistance of the arc, $R_a(t)$, is calculated from the circuit equation

$$R_a(t) = \frac{V_{in}(t) - V_{out}(t) - L(t)\, dI_a(t)/dt - I_a(t)\, dL_a(t)/dt}{I_a(t)}$$

In our regime of interest, once the current magnitude starts to rise and becomes circuit limited, the change in radius with time is small

$$I_a(t)\frac{d}{dt}L_a(t) << V_{in}(t) - V_{out}(t) - L(t)\frac{d}{dt}I_a(t)$$

and

$$R_a(t) \approx \frac{V_{in}(t) - V_{out}(t) - L(t)\, dI_a(t)/dt}{I_a(t)}$$

At peak current, when $t = t_p$, the dynamic arc impedance reaches its minimum value, $R_{\min}$, given as,

$$R_{\min} = R_a(t_p) = \frac{V_{in}(t_p) - V_{out}(t_p)}{I_a(t_p)}$$

The minimum value is a powerful check on the calculation of the dynamic resistance, because in a circuit code which is well matched throughout the system, the minimum resistance can be easily matched with experimental data at peak current.

8.4.2 the dynamic arc impedance

With the long gaps in the high power water switches, a significant inductance is expected. As an intermediate step, a treatment similar to that used by Ristic and Sorensen [50], where the inductive term is neglected, is used. This intermediate quantity will be referred to as the "dynamic arc impedance", $Z_a(t)$, defined as

$$Z_a\left(t\right) = V_a\left(t\right)/I_a\left(t\right)$$

where $V_a\left(t\right)$ is the voltage across the water arc given by

$$V_a\left(t\right) = V_{in}\left(t\right) - V_{out}\left(t\right)$$

For times significantly greater than the switch time, t_{switch},

$$I_a\left(t\right) >> I_C\left(t\right),\ I_R\left(t\right)$$

yielding

$$I_a\left(t\right) \approx I\left(t\right)$$

The difficulties of contracting a large three dimensional problem into a zero dimensional circuit code are considerable. The computation of the arc voltage, $V_a\left(t\right)$, from the physical monitors is complicated by the electrical size of the system and the development of the water arc. The baseline gap spacing in the water switch is 12.7 cm. Since the wave propagation in water is 1.3 inch/ns, the electromagnetic wave takes approximately 4 ns to reach the other electrode. In this analysis, that transit time is preserved. The entire data acquisition system on Z20 is relative to a single starting time, allowing for discrimination between relative timing of signals.

The first approximately 180 ns of the forward going voltage on OTL1_M is the well-understood capacitive prepulse. The prepulse voltage, V_{pp}, is given by

$$V_{pp} = Z_{OTL1}\frac{d}{dt}\left[C\left(t\right)V_{PFL}\left(t\right)\right]$$

and is valid for $t < t_{switch}$. The voltage prepulse is evident in Figure 94 and ends at approximately $t = 1550$ ns. The prepulse voltage is disregarded from the calculation of the dynamic impedance and the dynamic resistance, since the arc channel is not yet established [49].

The timing of the two voltages is verified by overlaying the time-shifted PFL voltage and the forward going voltage at OTL1_M, as shown in Figure 95, observing that the prepulse voltage starts several nanoseconds after the start of the PFL voltage. The dynamic impedance begins at the start of switch closure.

8.4.3 calculation of dynamic impedance

The experimental parameters are related to those of the dynamic resistance calculation by

$$V_{in}\left(t\right) = V_{PFL}\left(t\right)$$

and

$$V_{out}\left(t\right) = V_{for1}\left(t\right)$$

where the forward going voltage on OTL1, V_{for1}, is the switch output voltage, in order to disregard the effects of reflected waves on the short transmission line, OTL1. The arc voltage, $V_a\left(t\right)$, current through the switch, $I_a\left(t\right)$, are given for times prior to the arrival of the reflected waveform at the switch by
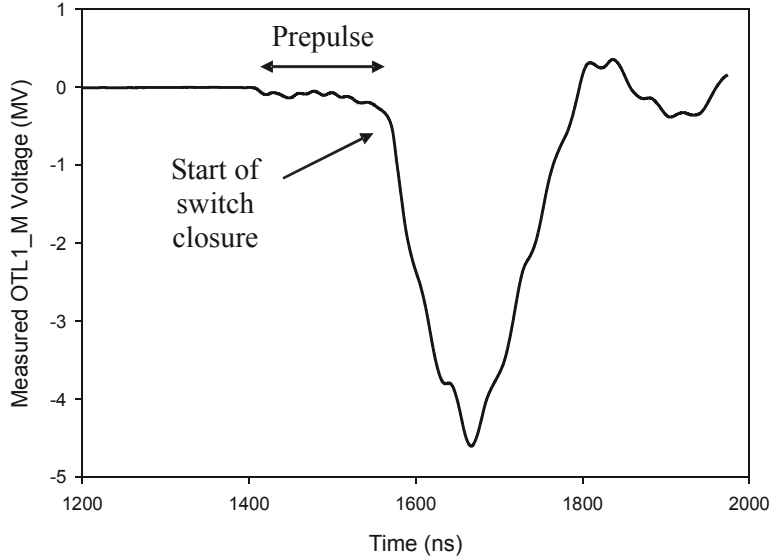
Figure 94. The output voltage on the first output transmission line. The switch prepulse is a result of the displacement currents through the capacitance of the switch prior to breakdown. The prepulse current of the Z20 water switches is typically on the order of 30 kA.

$$V_a\left(t\right) = V_{PFL}\left(t\right) - V_{for1}\left(t\right)$$

and

$$I_a\left(t\right) = I_{for1}\left(t\right) = V_{for1}\left(t\right)/Z_{OTL1}$$

Substitution yields

$$Z_a\left(t\right) = \frac{V_a\left(t\right)}{I_a\left(t\right)} = Z_{OTL1}\left[\frac{V_{PFL}\left(t\right)}{V_{for1}} - 1\right]$$

The experimental data is easily exported into an ASCI file, which allows this computation to be done point-by-point in a spreadsheet, provided the timebases have equal intervals. The results are shown in Figure 96 for an early data shot. The dynamic impedance calculated from the above expression, is plotted alongside the resistance calculated using the exponential decay switch model in SCREAMER. This overlay indicates the experimental dynamic impedance is consistent with a dynamic resistance model which is a good match to experimental data. As previously established, the SCREAMER circuit model is well matched to the experimental data. Because of the multiple reflections on OTL1 and their contribution to the forward going wave, the calculation of the dynamic impedance is terminated approximately 40 ns before the peak current is reached. The minimum values of dynamic resistance are obtained from the SCREAMER model.

110
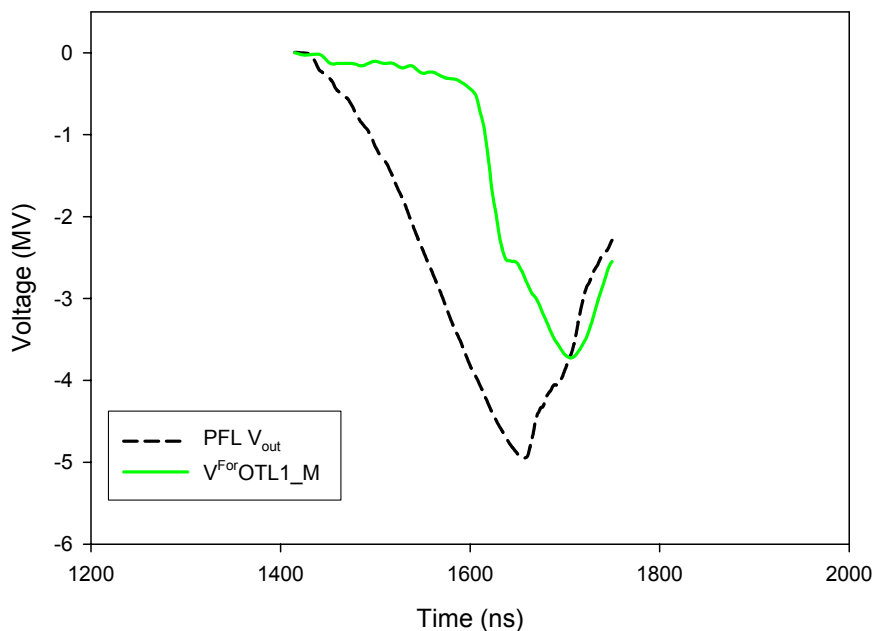
Figure 95. The relative timing for Shot 868 between the timeshifted output voltage on the PFL and the forward going voltage on OTL1_M for calculation of the dynamic arc impedance. The PFL voltage time shift is verified with the SCREAMER code.

8.4.4 the screamer water switch models

SCREAMER is a circuit simulation code custom-developed by Sandia to incorporate models of pulsed power components not available in commercial circuit codes (and run quickly). Currently, SCREAMER has models of basic components such as gas and water spark gap switches as well as advanced power flow components such as magnetically insulated transmission lines and the Z-pinch load. SCREAMER contains 3 models for high power spark gap switches which are used for both gas and liquid spark gaps. The first is a simple decay model. The second model is a more sophisticated, but still semi-empirical, expression, known as the "Exponential Decay Model". The last is the formulation of the Braginskii - Martin Model, known in SCREAMER as the "The Tom Martin Lossy Switch Model".

EXPONENTIAL DECAY MODEL

The dynamic resistance, $R(t)$, in the Exponential Decay Model is given by

$$R\left(t\right) = R_{close} + \frac{Z_{switch}e^{-\alpha}}{1 - e^{-\alpha} + Z_{switch}/10^6 \text{ ohms}}$$

where Z_{switch} is the sum of the source and load impedances being switched, R_{close} is the switch plateau resistance, and

$$\alpha = \frac{t - t_{switch}}{\tau_R}$$
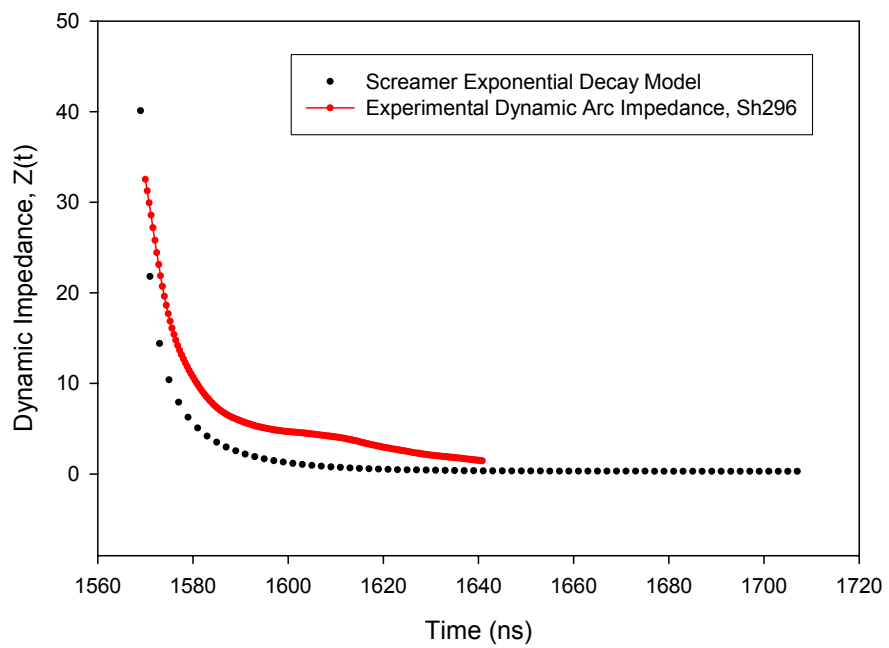
Figure 96. The dynamic arc impedance derived from the experimental voltage signals for SATPro Shot 296. The water switch gap length is 12.7 cm. The dynamic resistance from the SCREAMER code matched to experimental data is shown for comparison. The experimental $Z_a(t)$ is terminated prior to reaching its minimum value because of the multiple reflections on OTL1.

where τ_R is the JCM resistive phase constant given by

$$\tau_R = \frac{5 \text{ ns}}{Z_{switch}^{1/3} E^{4/3}}$$

and E is the mean electric field in the switch gap in MV/cm and Z_{switch} is in ohms.

In practice, the Exponential Decay water switch model has two parameters which largely determine the shape and amplitude of the transmitted pulse: α, the decay constant and the final (minimum) resistance value, R_{final}. This model is relatively insensitive to values of the other input parameters of the switch, the switchtime and the switch impedance, Z_{switch}. The decay constant, α, is largely determined by matching the risetime of the output pulse. The minimum resistance value, R_{final}, is determined by the peak of the output pulse, when $dI/dt = 0$. For matching experimental data in a circuit code, the Exponential Decay model has a great advantage in its simplicity.

TOM MARTIN'S LOSSY SWITCH MODEL

The Tom Martin Lossy Switch Model is the implementation of a treatise on losses in spark gap switches encompassing a wide variety of materials commonly used in pulsed power [6]. In SCREAMER, the dynamic resistance is given by

$$R(t) = \frac{\ell}{\sigma \pi a^2}$$

with

$$a^2 = \left(\frac{K}{\rho_0 \sigma}\right)^{1/3} \int_0^t I^{2/3}(\tau)\, d\tau$$

In the Tom Martin Lossy Switch model, a is the radius of the channel, ℓ is the length of the gap, K is a constant, σ is the conductivity of the channel in S/cm, ρ_0 is the density of the outer medium, and I is the current through the water channel. The external inputs to the model are the dielectric (water, oil, gas), switchtime, gap length, pressure, number of switches, and number of channels per switch.

8.4.5 comparison of the two SCREAMER models

A comparison of the two models was done using the same SCREAMER code with as similar input data as possible. The inputs to both models were the "as calculated" and not tweaked to produce the best match to data. For instance, the exponential decay model requires the JCM resistive time constant, which calculates to be 8.3 ns and the input to the Lossy Switch model is the material, which is water. The switchtime is an input for both models and the same value was used. The effect of the water switch model on the output pulse is shown in Figure 97. While the Lossy Switch model is forced to start at the same time, the risetime of the output pulse is significantly slower than that of the exponential decay model. The dynamic resistance of each of the models is compared in Figure 98, 99. The Lossy Switch model appears to decay more slowly than the exponential decay model and the minimum values differ significantly. The value chosen in the exponential decay model to fit the peak of the experimental data is 0.32 Ω and the Lossy Switch value at peak is 0.566 Ω. The comparison with experimental data is shown in Figure 100.
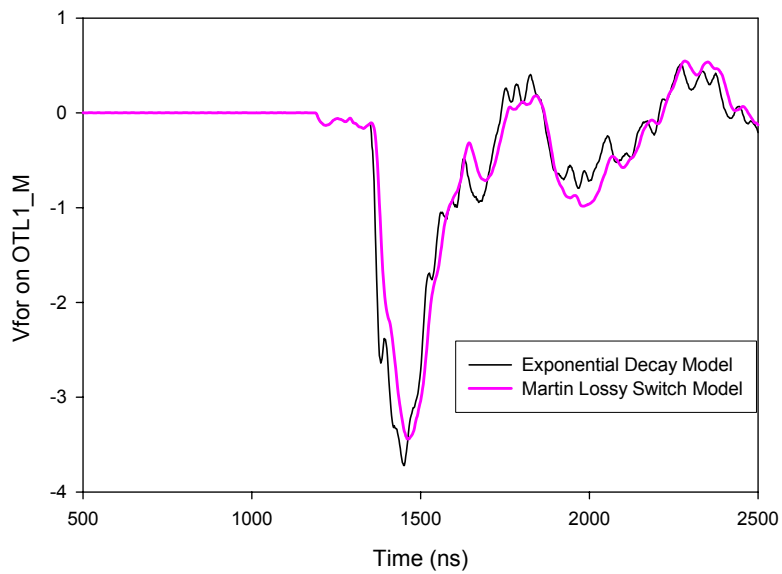
Figure 97. A comparison of the forward going voltage on OTL1_M of the SCREAMER circuit models of

Z20 using different switch models. Both switch models initiate simultaneously, but the Martin Lossy Switch model rises more slowly and indicates a smaller peak voltage. Both models were given the "best guess" at their required input: the Exponential Decay model used its calculated JCM τ_R of 8.3 ns and the Martin Lossy Switch model used 3 switches and one channel per switch.
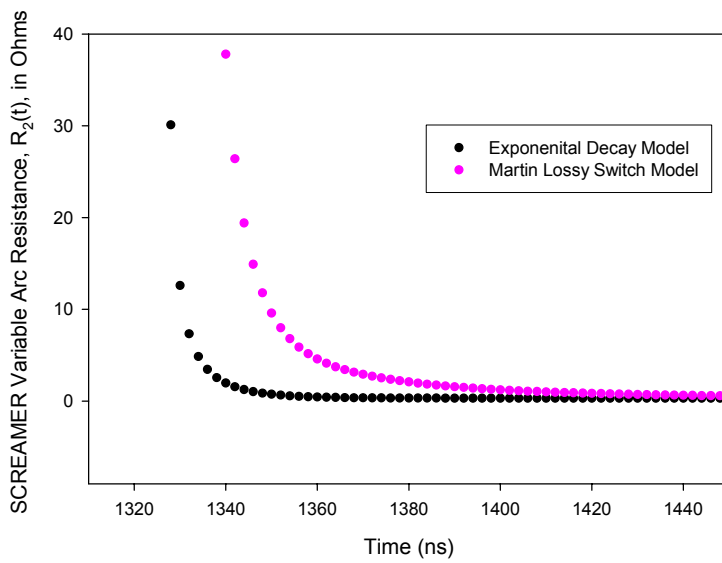
Figure 98. The dynamic arc impedance, $R_a(t)$, from the Martin Lossy Switch Model and the Exponential Decay Model on a linear scale. The models both begin the decay from its open circuit resistance to its minimum resistance at the same time. The values of Rmin are significantly different: the Exponential Decay model is minimum at 0.32 ohms and the Martin Lossy Switch Model is 0.5660 ohms.
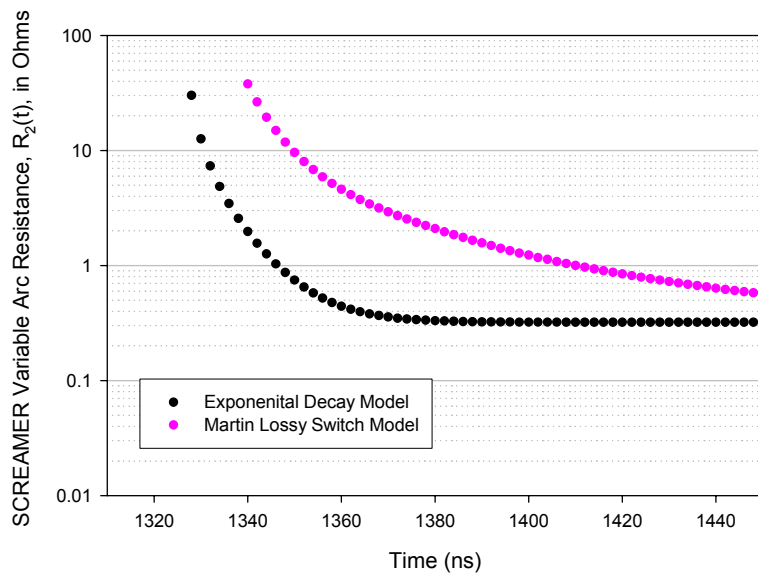
Figure 99. The dynamic arc impedance, $R_a(t)$, from the Martin Lossy Switch Model and the Exponential Decay Model on a logarithmic scale.
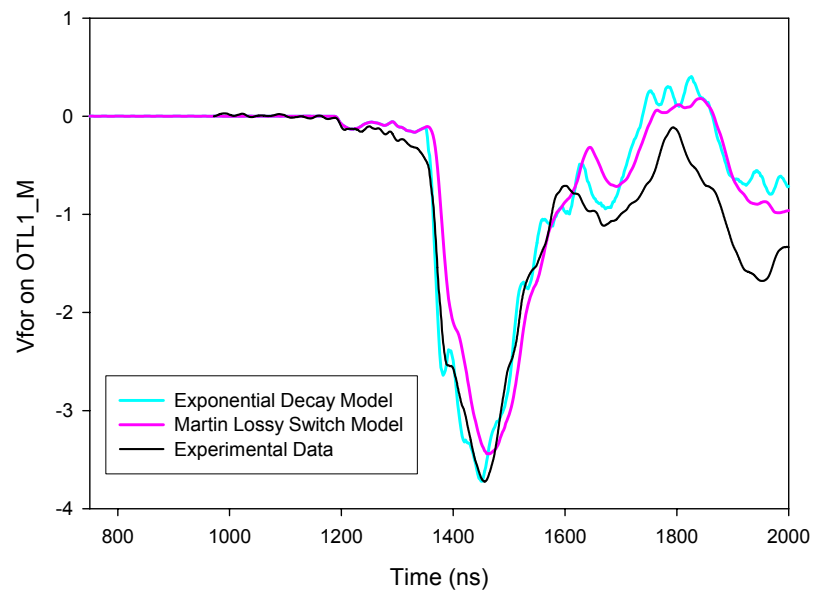
Figure 100. A comparison of the SCREAMER models using the two different water switch models with experimental data. The SCREAMER run using the Exponential Decay water switch model is a better match with the experimental data, even showing the structure in the waveform at the correct times. The Martin Lossy Switch model is derived from theory and gets the approximate waveshape and peak correct, indicating a solid foundation.

8.4.6 the dynamic resistance

The commonly accepted model for a water arc requires the inductive contribution to be subtracted from the arc voltage to yield the voltage drop across the dynamic resistance. The dynamic resistance is calculated by

$$R_a(t) = \frac{V_{PFL}(t) - V_{for1}(t) - LdI_a(t)/dt}{I_a(t)}$$

The inductance with 3 switches in the system is given by (28). For the present shot, with $\ell = 10.5$ cm, $b = 50$ in, $w = 15$ in, and taking $a = 0.5$ mm, the arc inductance is about $L = 70$ nH. Using this value (just to get a feel for the size of the inductive contribution), the inductive drop can be calculated from the derivative of the forward going current.

To evaluate the relative magnitude of the inductive drop, the arc voltage, $V_{PFL} - V_{for1}$ and the resistive arc voltage are computed and compared in Figure 101. Rapid changes in the derivative term result in a choppy waveform for the resistive arc voltage. The comparison shows the inductive term is not too large in the early time calculation of $R(t)$. A large dip in the resistive arc voltage is clearly attributable to the inductive term and the time derivative of current. It can be shown that this dip occurs at the second point of inflection on the forward going voltage, and it is attributable to the effects of multiple reflections along the OTL1. Thus, the dip will be ignored and the inductive contribution will be calculated later in the waveform, where the two curves intersect again. This is summarized in Figure 102, where the dynamic resistance, $R_a(t)$, is shown with the dynamic arc impedance, $Z_a(t)$, and the dynamic resistance from the SCREAMER model. The minimum resistance, at the time of peak current, is also shown for reference. The curves have similar shapes and indicate the minimum resistance value from the circuit model is an appropriate value.
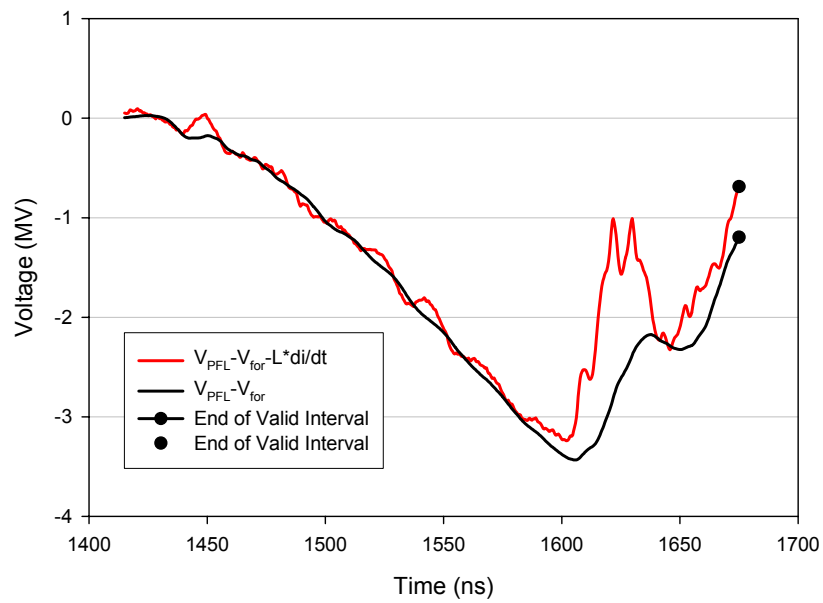
Figure 101. A comparison of the arc voltage (V_{PFL}-V_{for}_OTL1_M) and the resistive arc voltage ((V_{PFL}-V_{for}_OTL1_M- LdI/dt). The arc inductance used in this calculation is 30 nH and electrode inductance of 40 nH. The large drop in voltage due to the inductive term is known to occur where the plateau occurs in the forward going voltage and is likely due to imprecise calibration in the current monitors. The inductive drop term is significant as the peak current is approached.
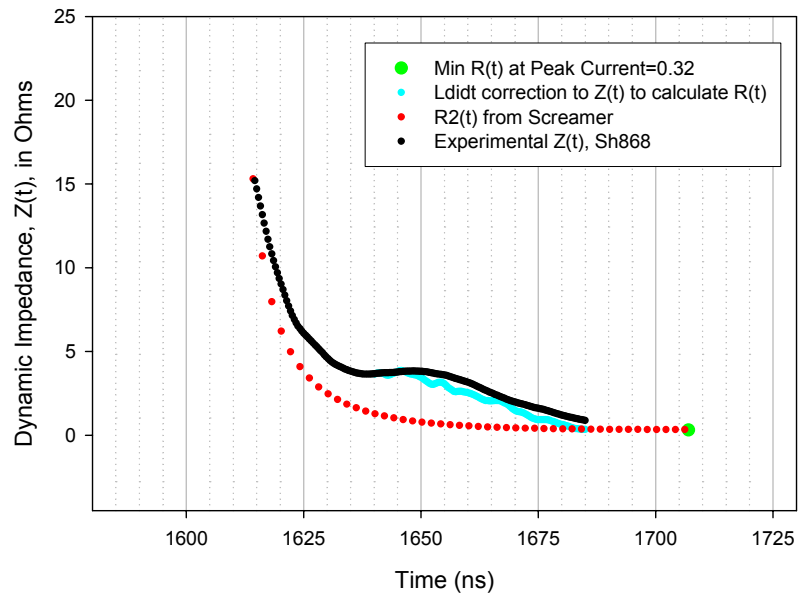
Figure 102. The correction to the dynamic impedance, $Z_a(t)$, gives the dynamic resistance, $R_a(t)$. The corrective term is $(L/I_a)\, dI_a/dt$. The minimum value, where $dI_a/dt = 0$, is 0.32 ohms.

8.4.7 scaling with current: comparison of the number of switches

An analysis of a single switch site shot on Z20 is interesting because it is a way to scale with current without changing the baseline characteristics of the shot, such as switch delay time or gap length. This allows the current per switch to be varied while keeping other parameters fixed. The switch geometry is the baseline configuration: a 3 inch diameter negative electrode, 1 inch diameter positive electrode with a 12.7 cm gap. The advantage of using the number of switch sites to scale with current is the charge time remains the same.

The match to experimental data for the SCREAMER model for the single switch shots is not nearly as good as for the 3 switch sites. This may be because of the increased generation of multiple modes by the single switch launched onto OTL1 [39], which cannot be captured in a single circuit code. Multi-moding can be described in a 0D circuit code by implementing a circuit code for each propagating mode. It is not useful to do this for SATPro data.

The dynamic impedance for the single channel switch is shown in Figure 103. The fit with the SCREAMER variable resistance, $R_2(t)$, is not particularly close. The resistive fall derived from experiment appears to indicate that it may converge with the minimum resistance value of 0.36 Ω, but with such a discrepancy in the SCREAMER PFL voltage, this value may not be very accurate.

It is also interesting to plot the dynamic impedances derived from experimental data for different number of switches under identical conditions, as in Figures 104, 105. From previous tests, it is known that under these experimental conditions, the current is shared nearly equally between the switches. The rate of impedance collapse is slower in the higher current cases.

8.5 One Dimensional Simulation With Experimental Current

A one-dimensional simulation was run with ALEGRA-HEDP using the experimental current waveform in Figure 106.

The results are given in the following sequence.
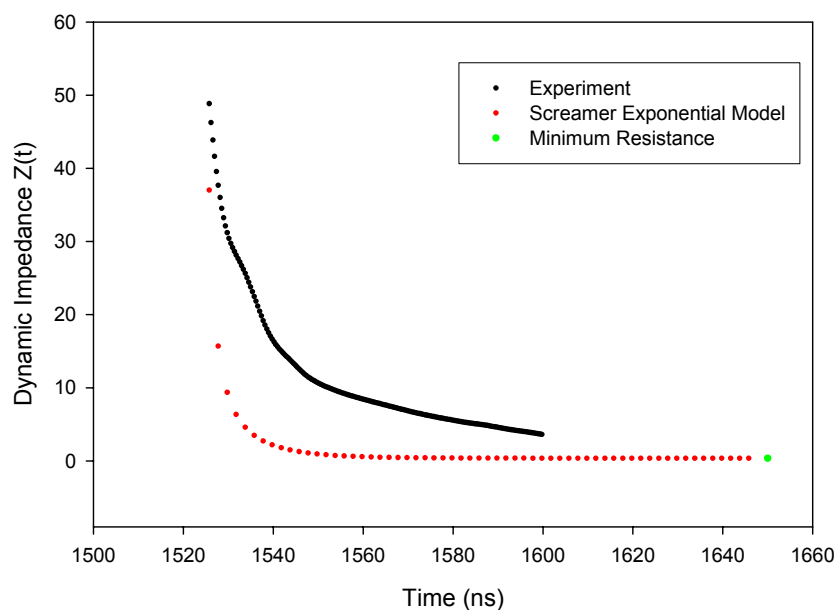
Figure 103. The dynamic impedance of a single water spark gap derived from experimental data taken in

Z20. The peak current through the spark channel is 730 kA. The minimum resistance of the arc is 0.36 ohm as determined by a match-to-peak in the SCREAMER circuit code. It is difficult to match the circuit code to the experimental data, which is evidenced by the rough fit in this graph, and the minimum resistance value may not be very accurate.
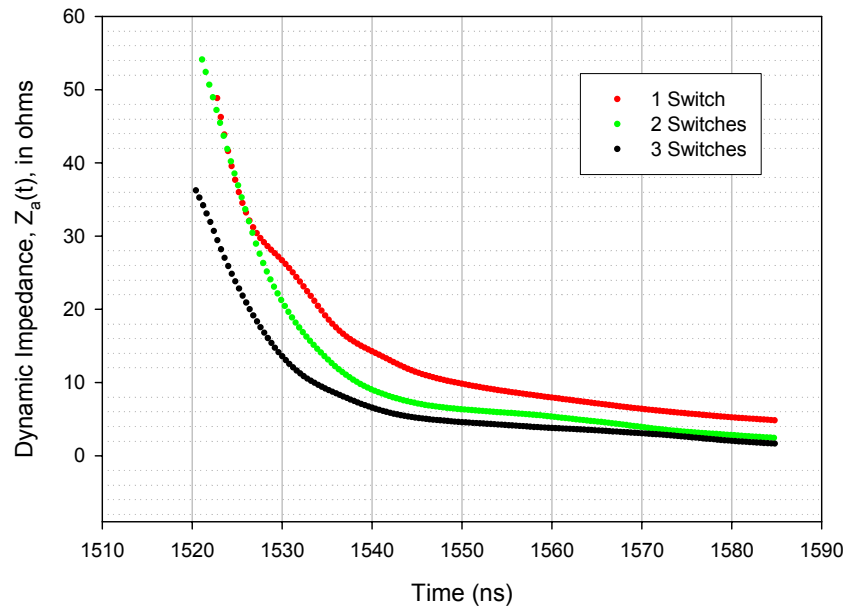
Figure 104. The dynamic arc impedance for one, two and three switches under identical experimental conditions.
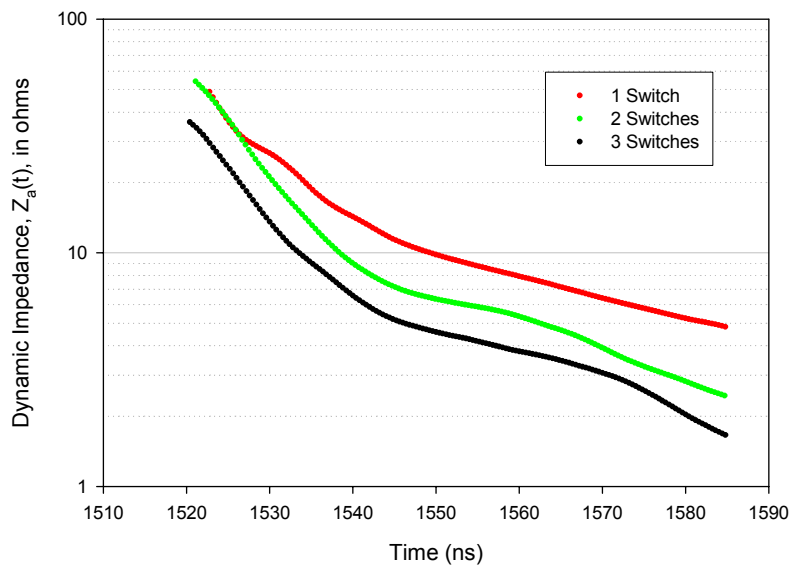
Figure 105. The dynamic arc impedance for one, two and three switches under identical experimental conditions on a logarithmic scale.
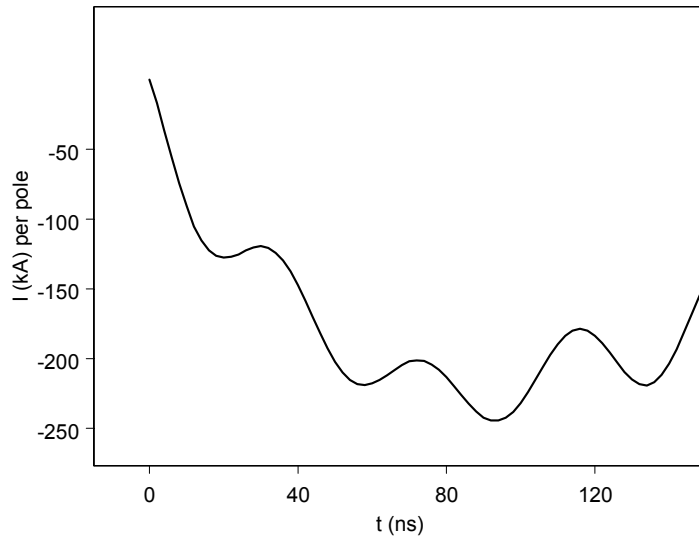
Figure 106. One third of total switch current in experiment (actually from the SCREAMER circuit simulation of the experiment at the water switch) is taken as the current per switch pole or channel. This was used to drive the model calculations.
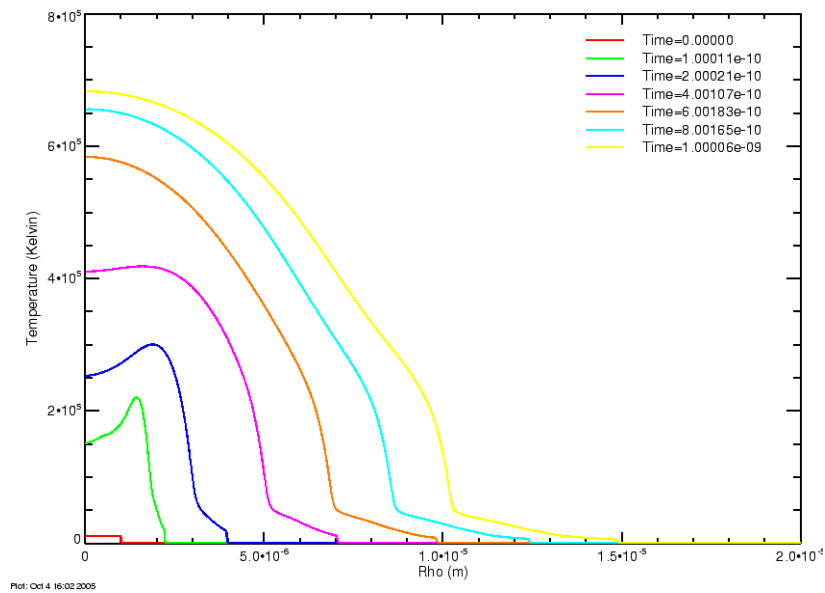
Figure 107. Early time temperature profile for experimental current drive.

124
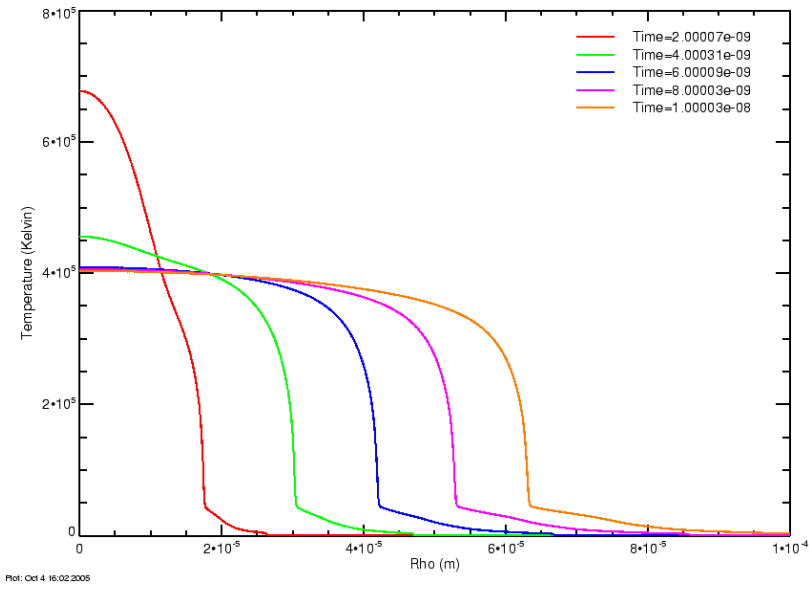
Figure 108. Intermediate time temperature profile for experimental current drive.
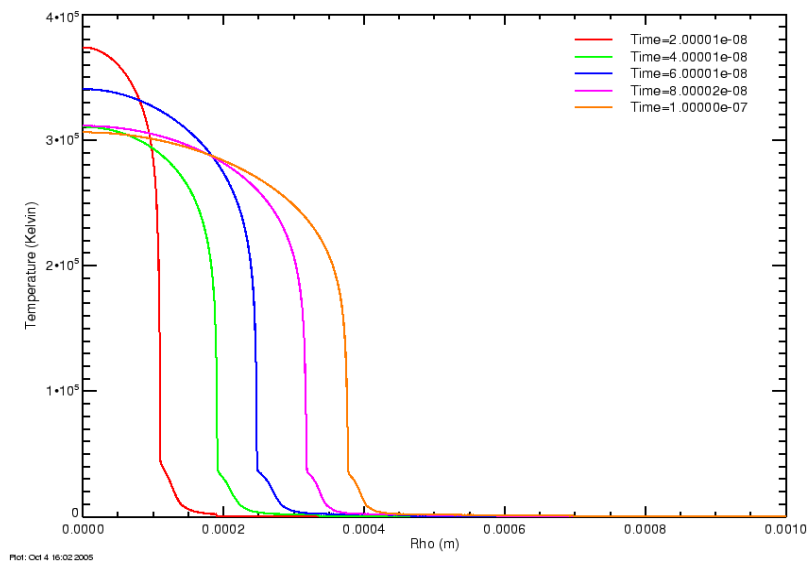
Figure 109. Late time temperature profile for experimental current drive.

125
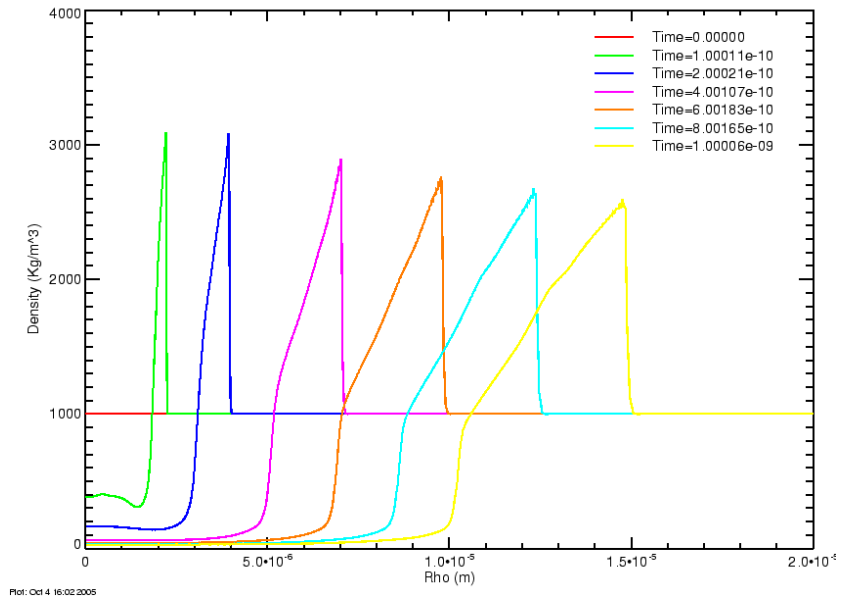
Figure 110. Early time density profile for experimental current drive.
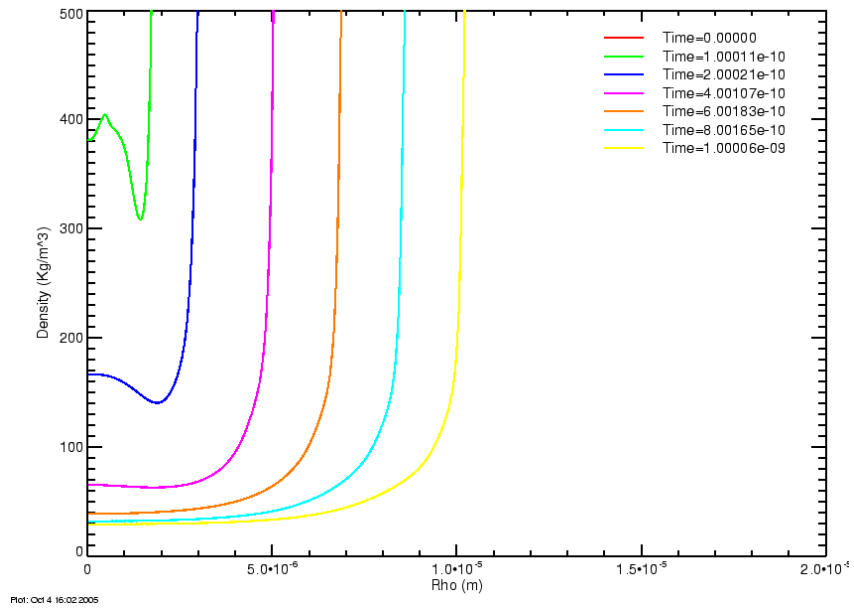
Figure 111. Early time expanded channel density for experimental current drive.

126
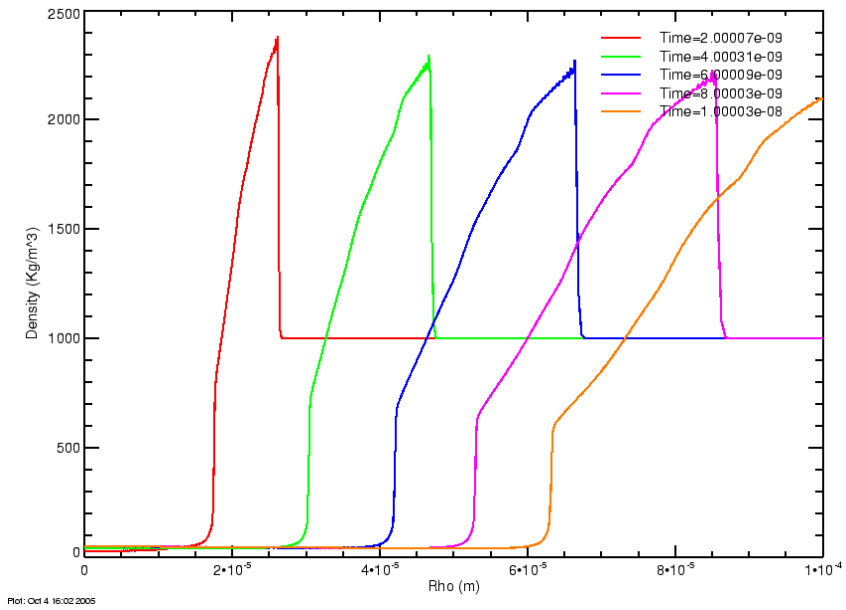
Figure 112. Intermediate time density profile for experimental current drive.
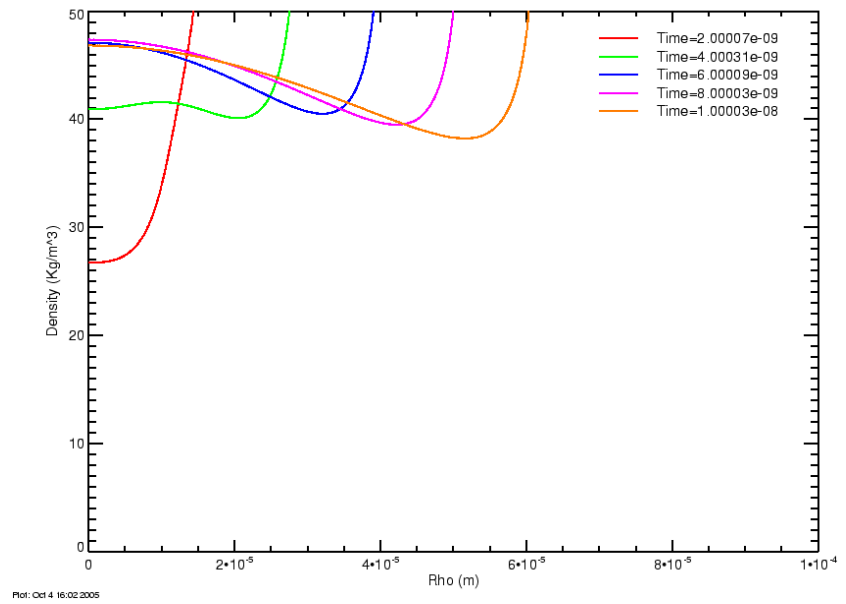
Figure 113. Intermediate time expanded channel density for experimental current drive.

127
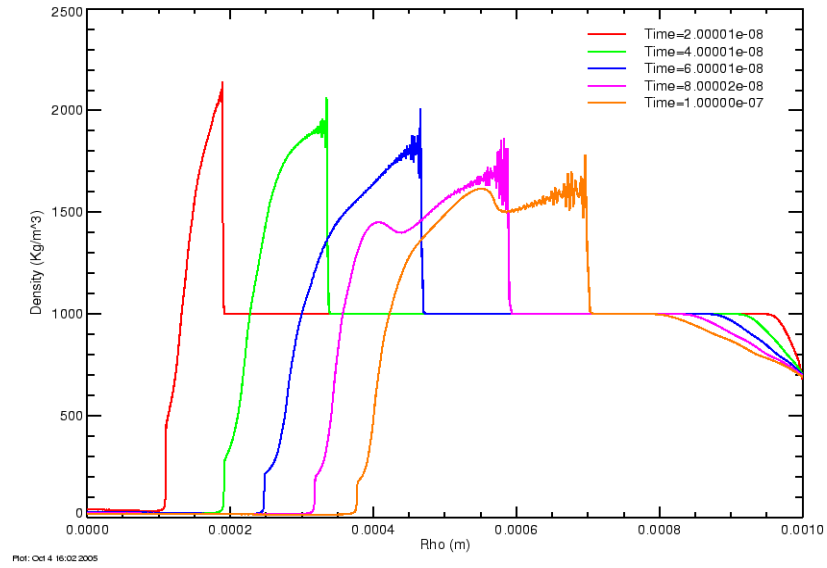
Figure 114. Late time density profile for experimental current drive.
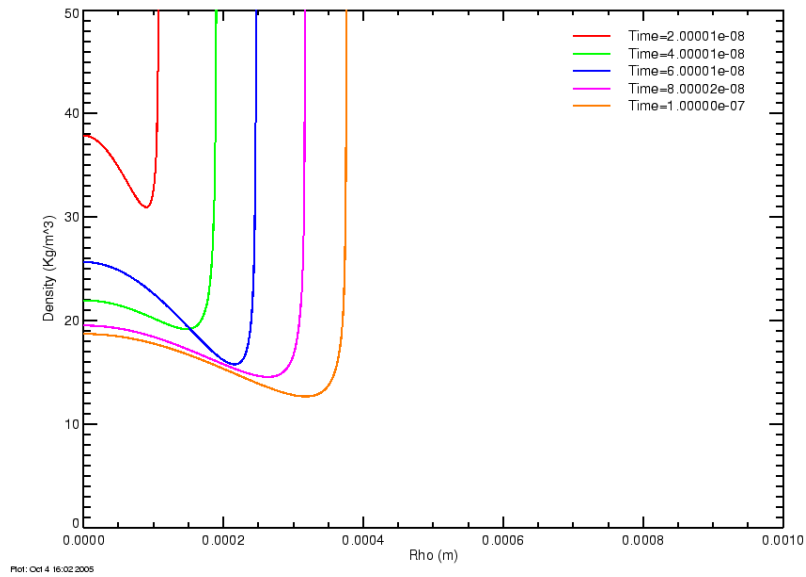
Figure 115. Late time expanded channel density for experimental current drive.
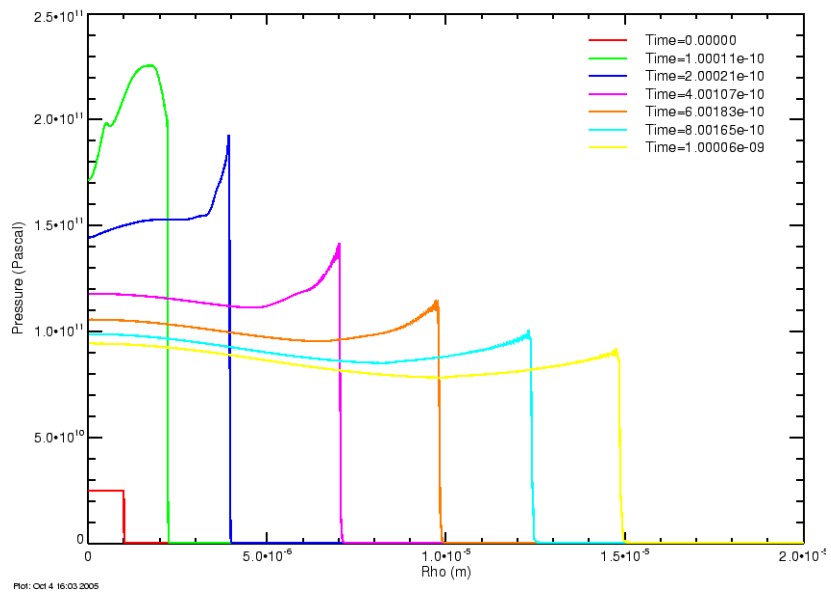
Figure 116. Early time pressure profile for experimental current drive.
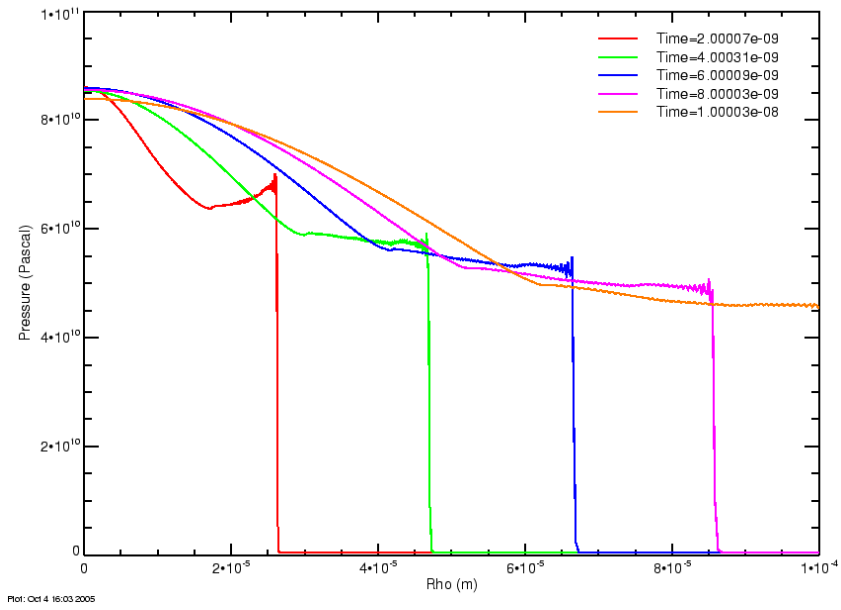
Figure 117. Intermediate time pressure profile for experimental current drive.
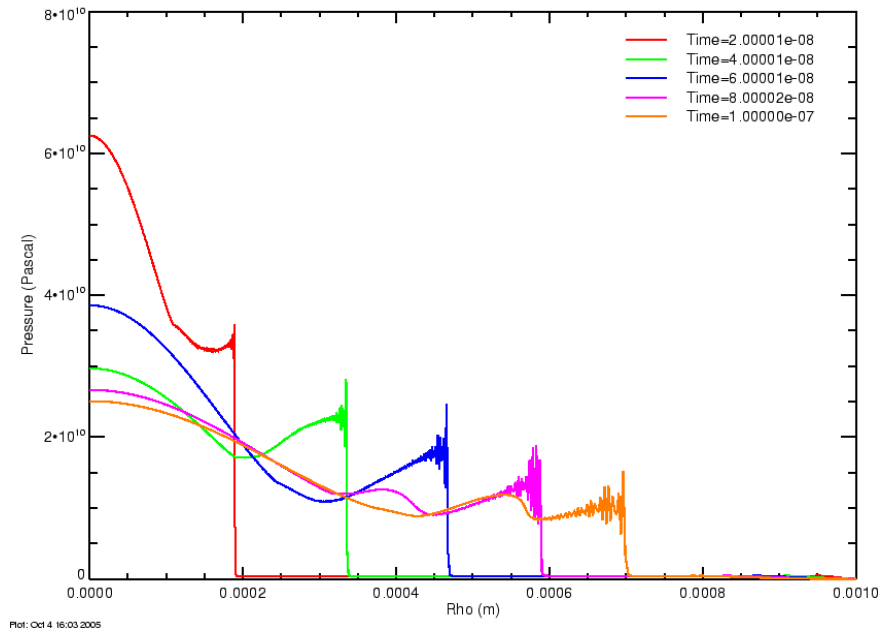
Figure 118. Late time pressure profile for experimental current drive.

130
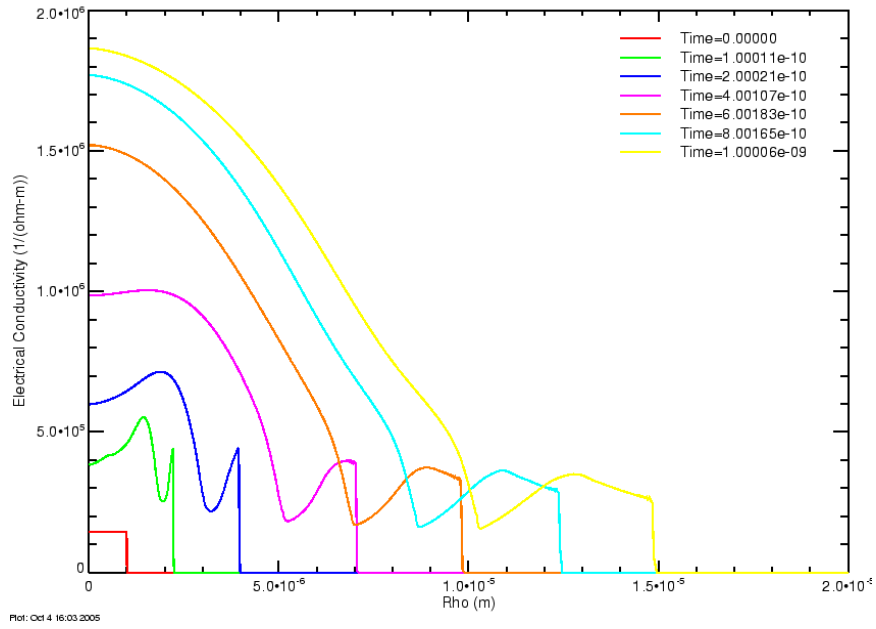
Figure 119. Early time electrical conductivity profile for experimental current drive.
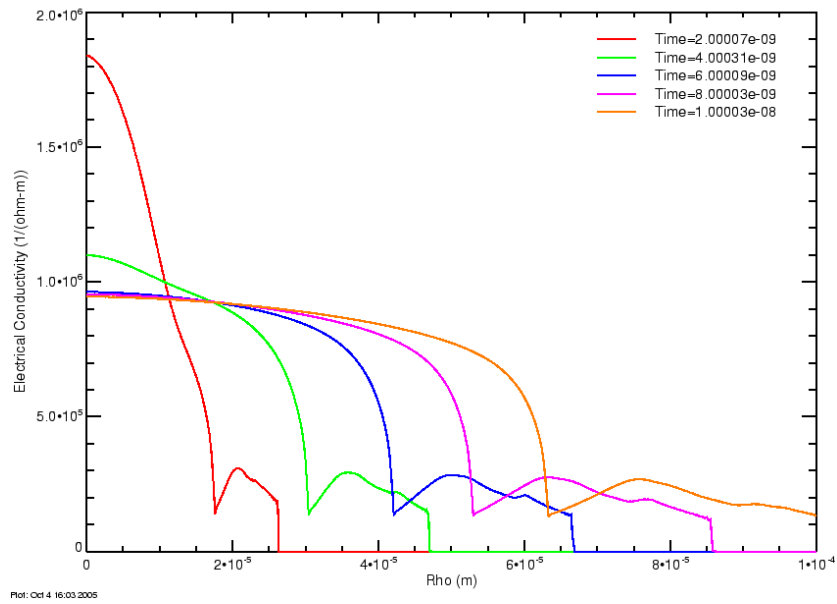
Figure 120. Intermediate time electrical conductivity profile for experimental current drive.
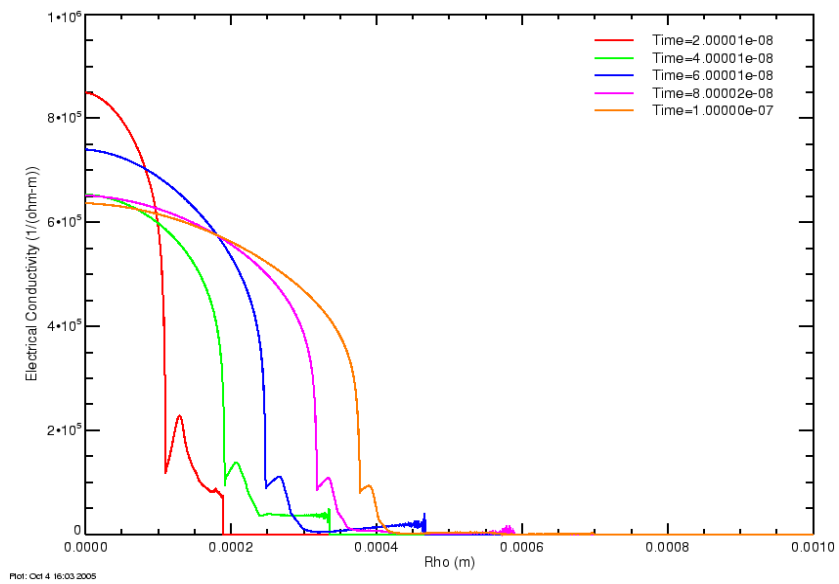
Figure 121. Late time electrical conductivity profile for experimental current drive.
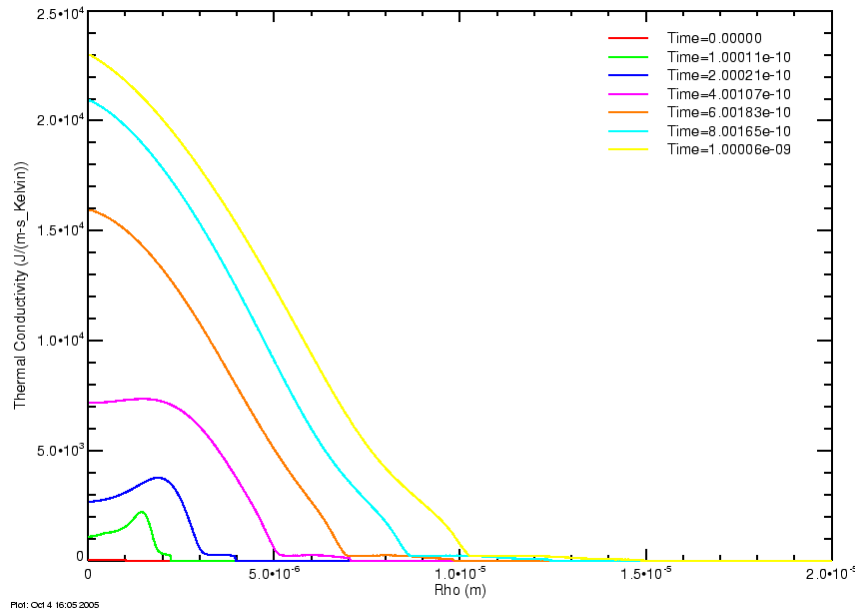
Figure 122. Early time thermal conductivity profile for experimental current drive.
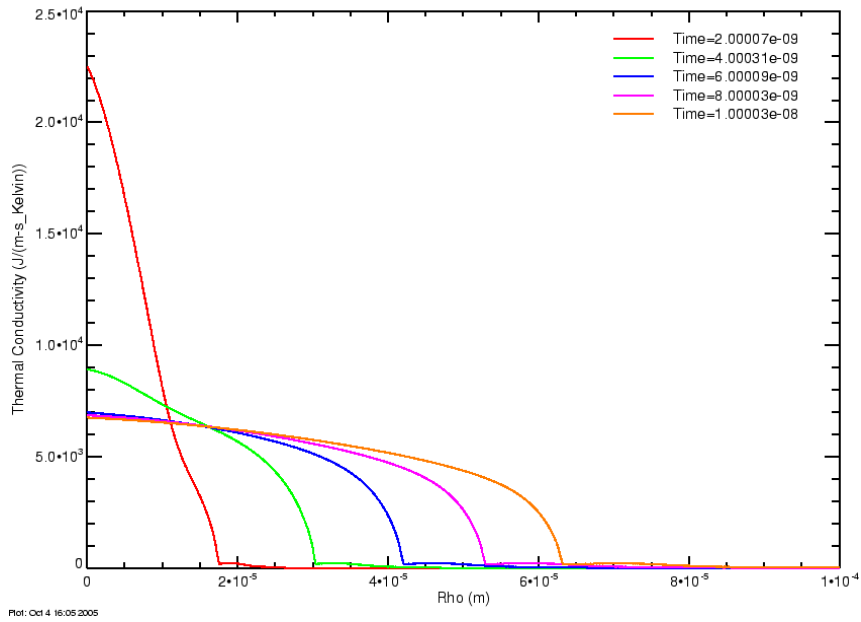
Figure 123. Intermediate time thermal conductivity profile for experimental current drive.
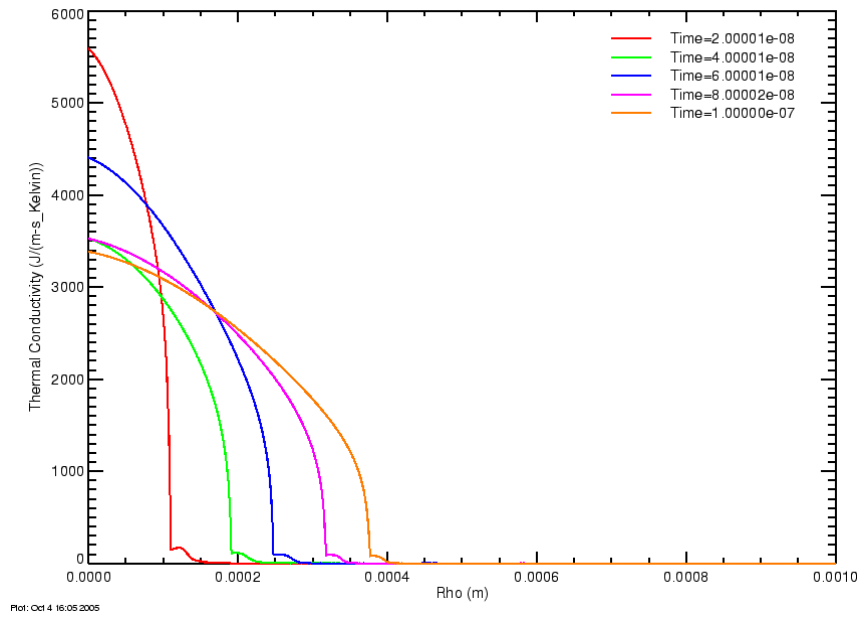
Figure 124. Late time thermal conductivity profile for experimental current drive.
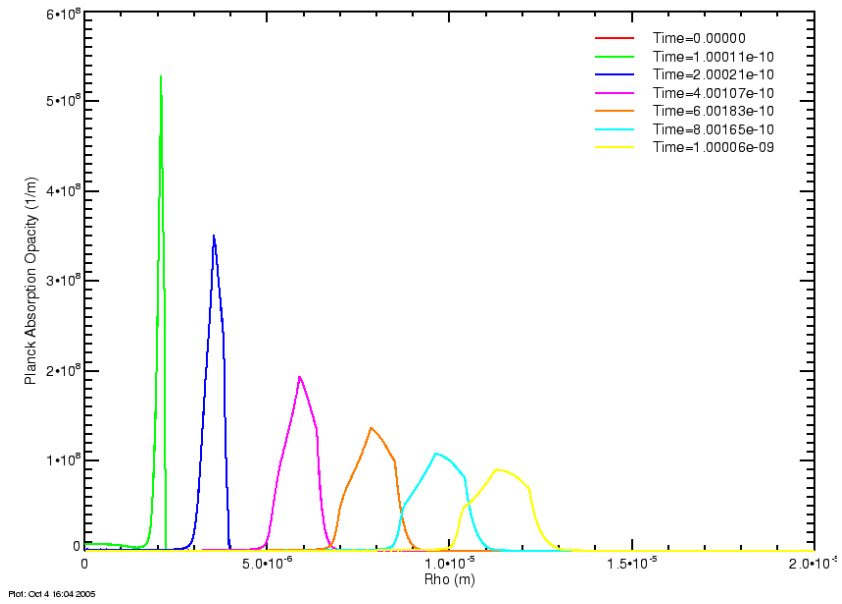
Figure 125. Early time average opacity for experimental current drive.
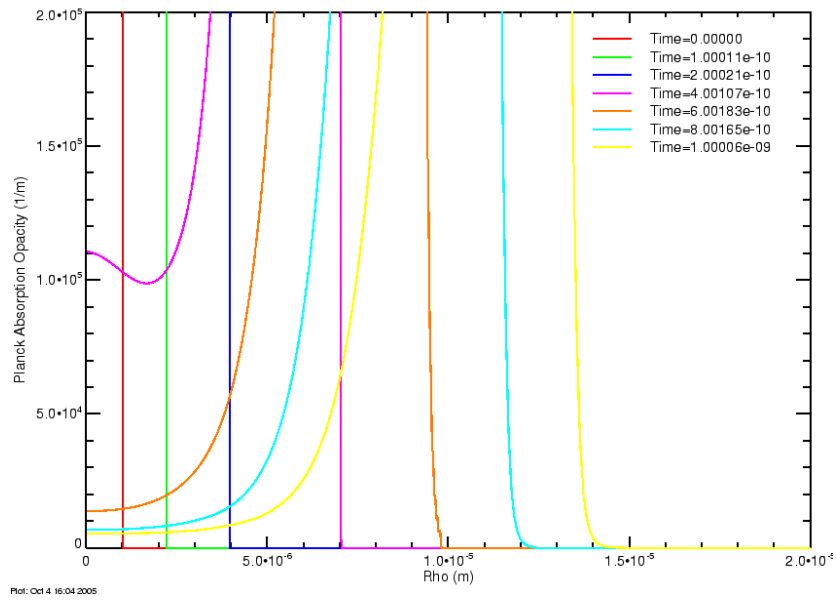
Figure 126. Early time expanded average channel opacity for experimental current drive.
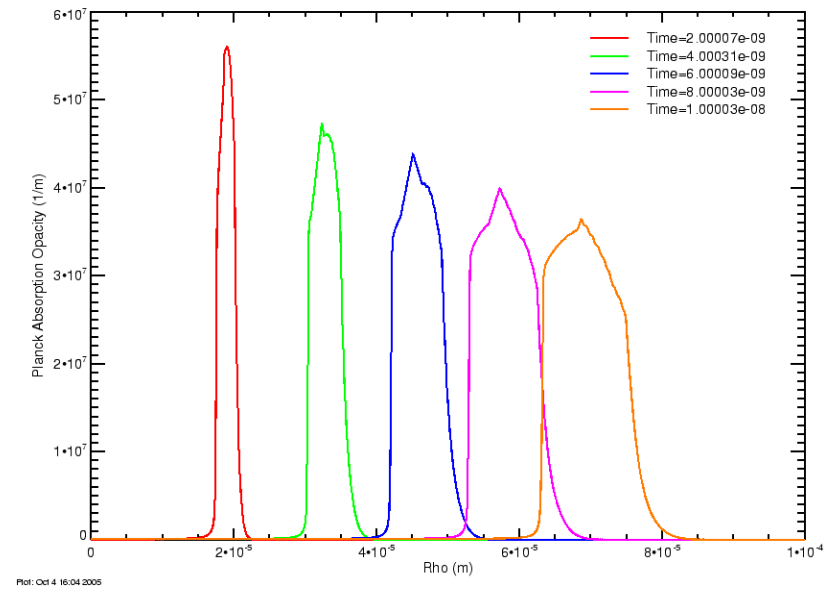
Figure 127. Intermediate time average opacity for experimental current drive.

135
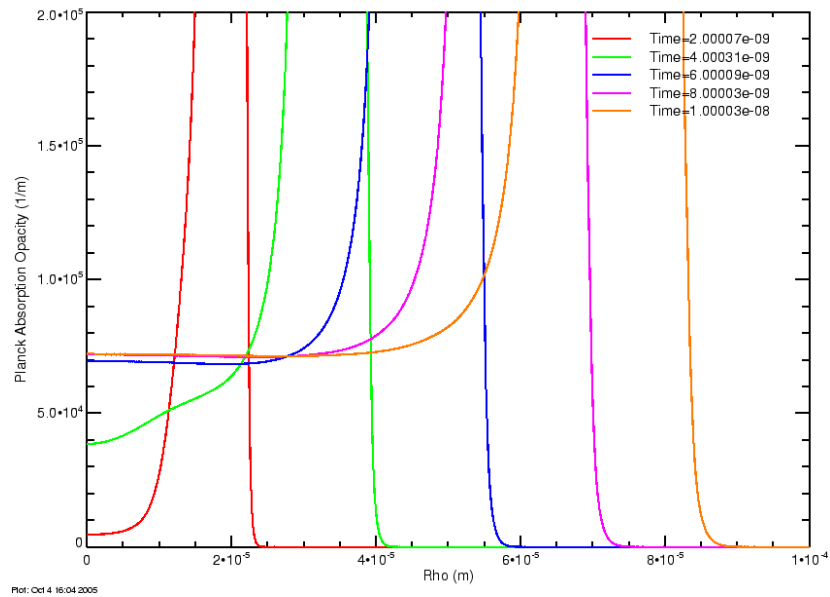
Figure 128. Intermediate time expanded average channel opacity for experimental current drive.
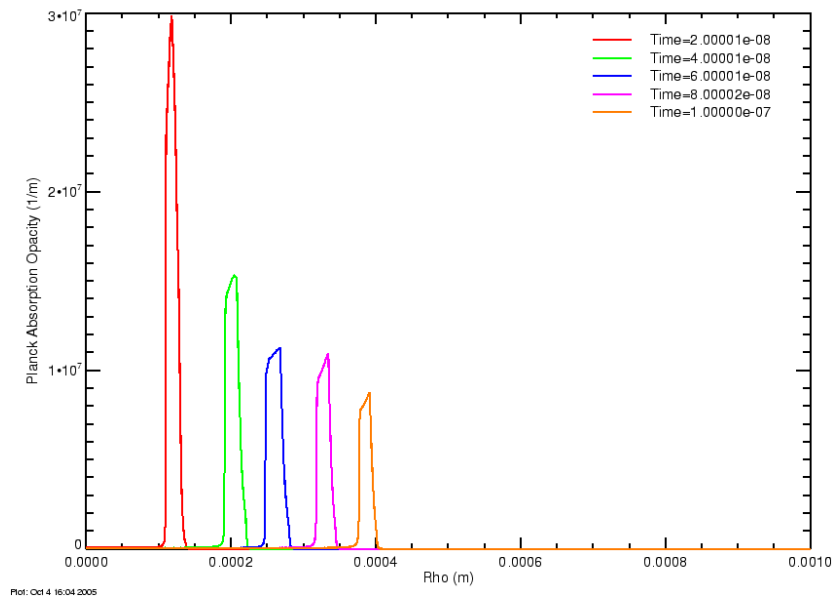
Figure 129. Late time average opacity for experimental current drive.
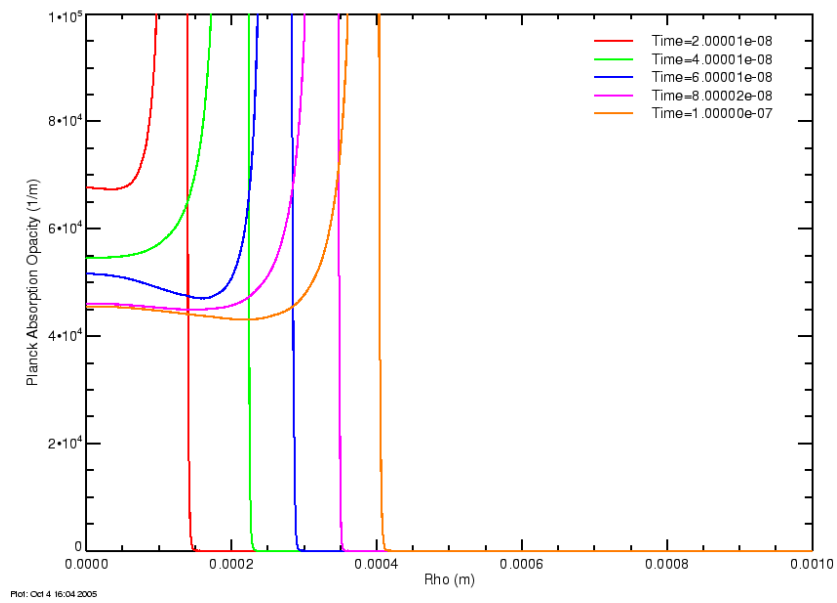
Figure 130. Late time expanded average channel opacity for experimental current drive.
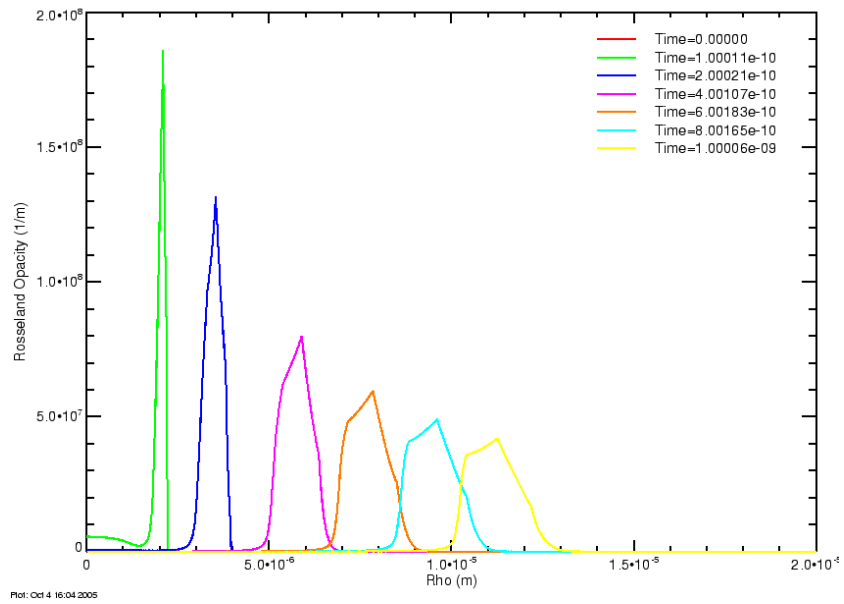
Figure 131. Early time Rosseland opacity for experimental current drive.
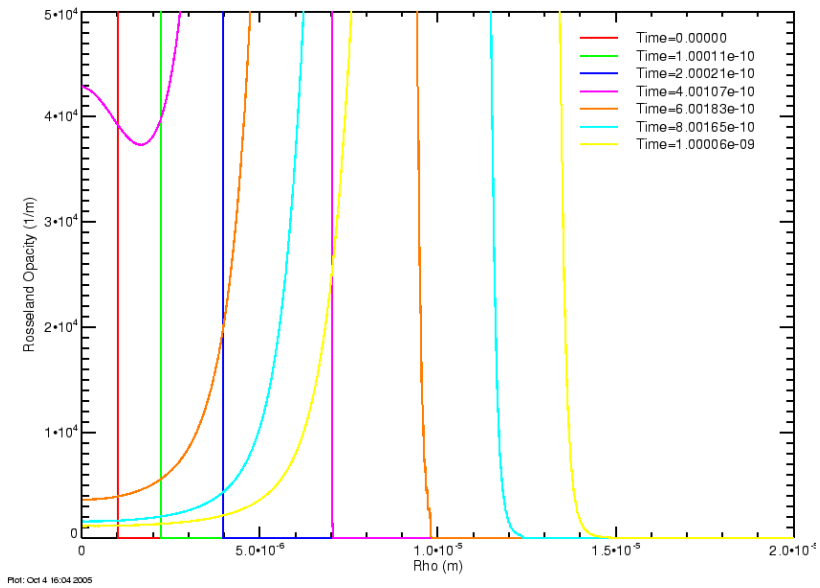
Figure 132. Early time expanded Rosseland channel opacity for experimental current drive.

138
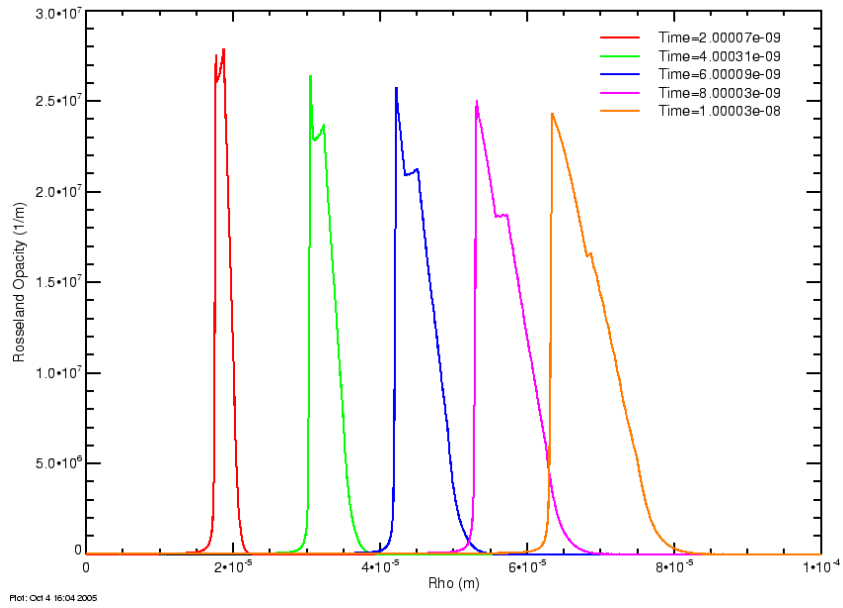
Figure 133. Intermediate time Rosseland opacity for experimental current drive.
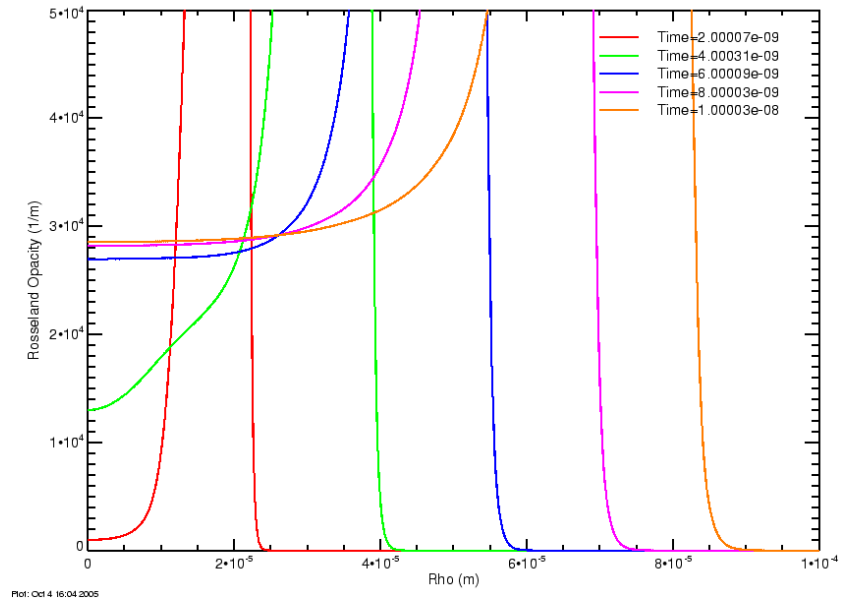
Figure 134. Intermediate time expanded Rosseland channel opacity for experimental current drive.
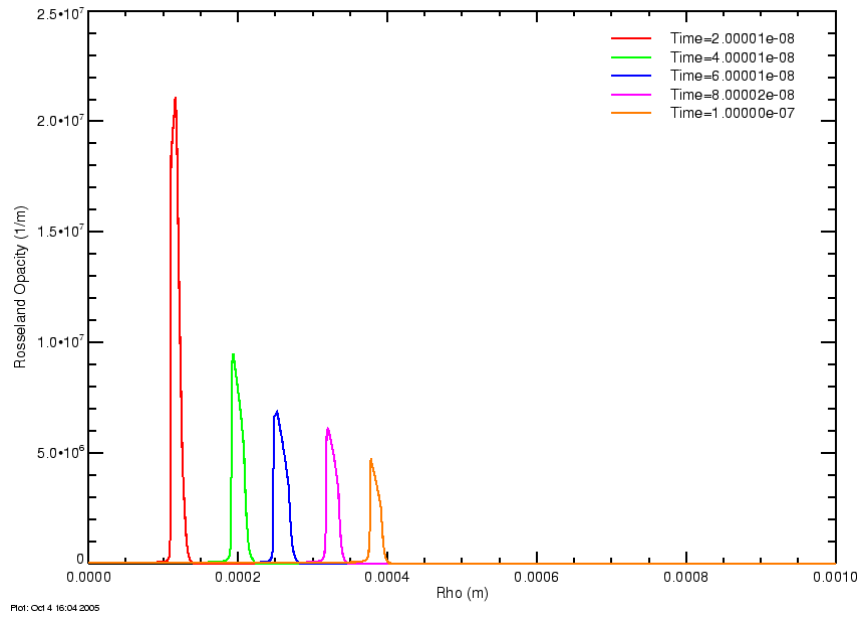
Figure 135. Late time Rosseland opacity for experimental current drive.
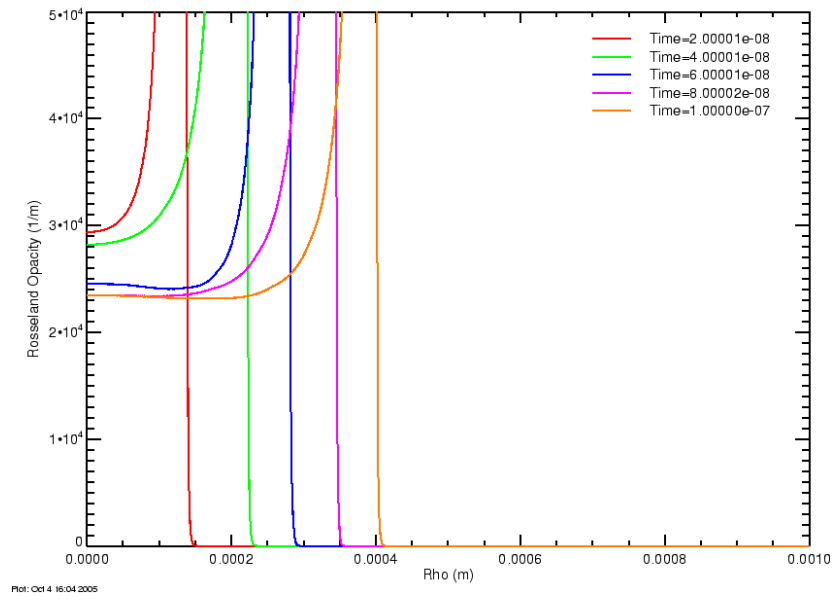
Figure 136. Late time expanded Rosseland channel opacity for experimental current drive.

140
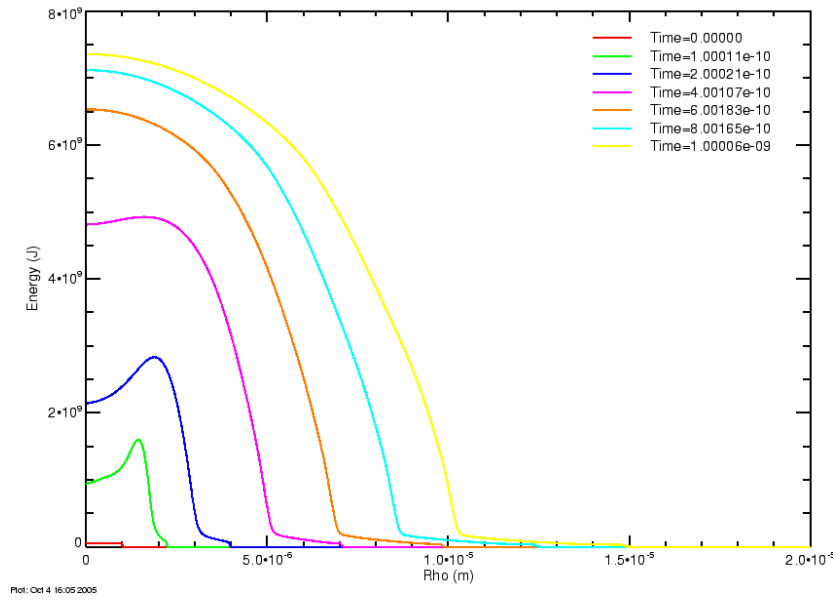
Figure 137. Early time internal energy for experimental current drive.
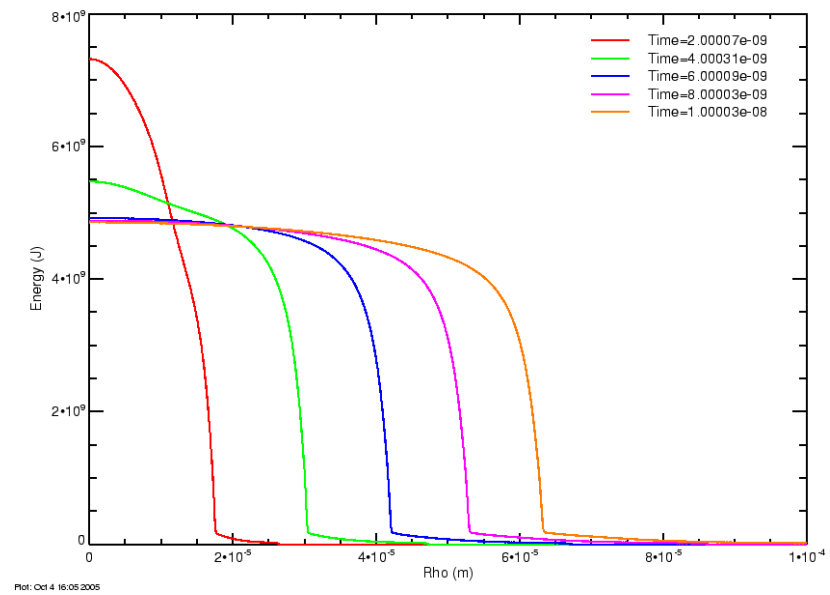
Figure 138. Intermediate time internal energy for experimental current drive.
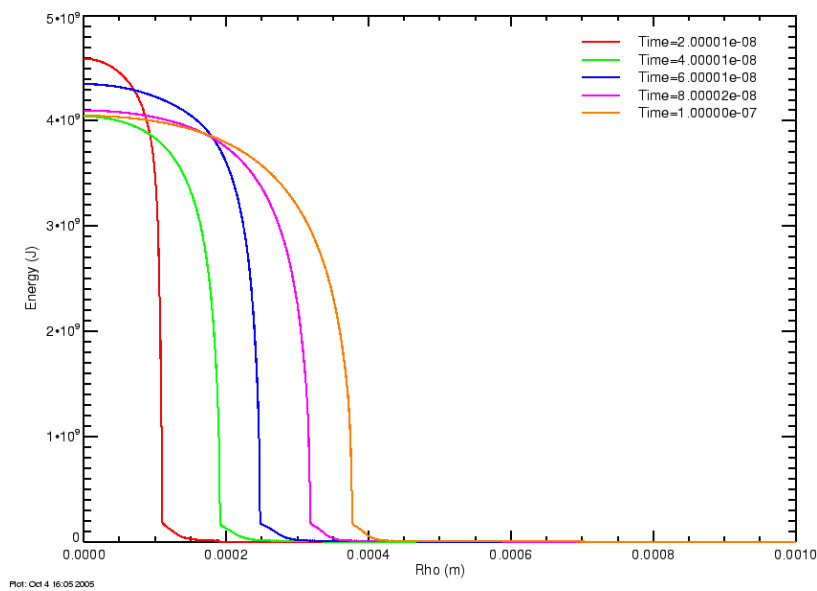
Figure 139. Late time internal energy for experimental current drive.
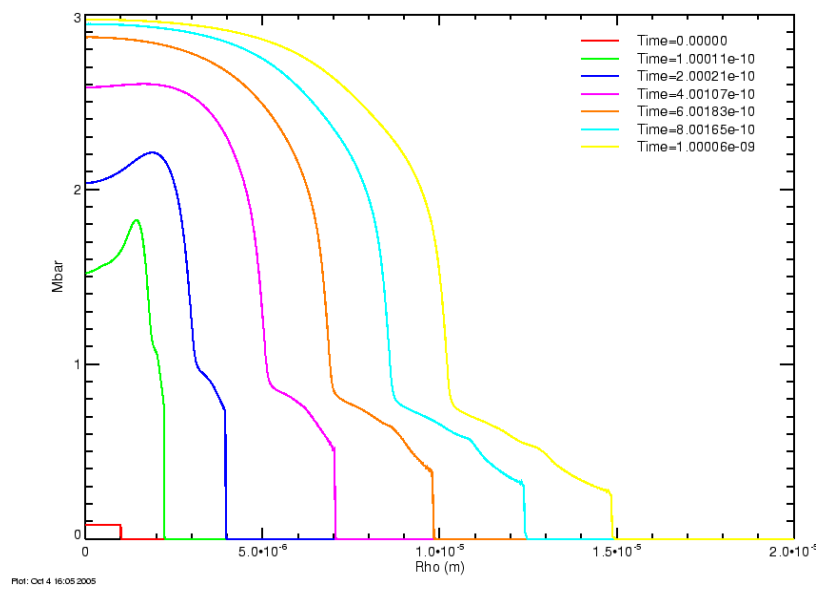
Figure 140. Early time average ionization number for experimental current drive.
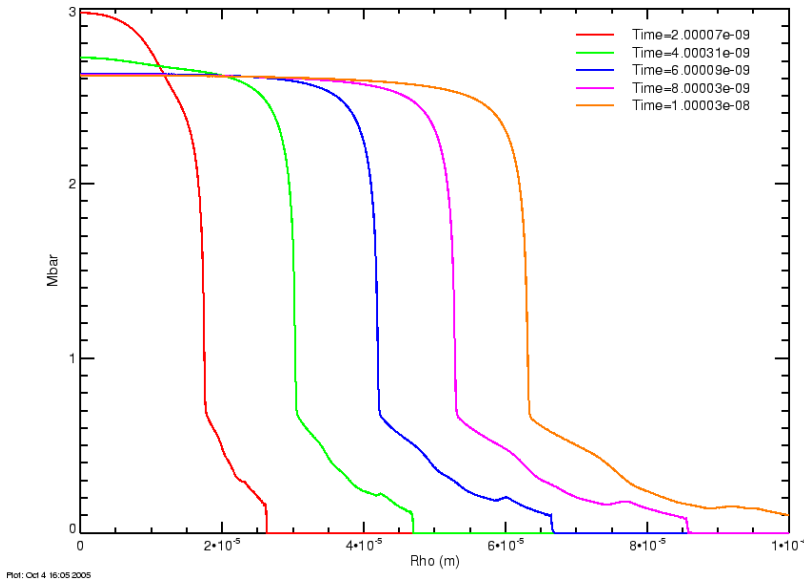
Figure 141. Intermediate time average ionization number for experimental current drive.

The resistance per unit length is shown in Figure 143

If we take the value 4.6 ohms/m at 95 ns from the start of the fall, and scale with a length of $\ell \approx 10.5$ cm and three channels in parallel, we find 0.16 ohms. This value seems to be about half the experimental plateau values discussed above. Note that we have used a length ℓ of the electrode to electrode spacing and not taken account of any increase resulting from a varying channel path. From the characteristics of the channel length observed in framing camera photographs, the channel length is certainly longer than the pole to pole spacing used here but it is unlikely that a factor of two increase will be reached. It is curious that if we had used Fedorov's coefficient 0.81 S/(m-J) in the linear conductivity formula we would have obtained approximately 7.2 ohms/m at 95 ns, and after scaling, a total resistance for three channels of 0.25 ohms (about 20% below the experimental level). The scaling of the model with channel number, for a fixed current, is similar to the Braginskii-Martin model $1/N^{1/3}$ and seems consistent with the experimental plateau levels exhibited by the SCREAMER exponential model fit to the experimental data for one and three poles.

The final figure shows the inductive part of the switch voltage divided by the current (green), the switch resistance (red), and the sum or total voltage to current ratio (black). The size of the inductive contribution indicates that it is difficult to extract the resistive part from the total. Note also that the $d\Delta L/dt$ term is small but not zero (about one third of the resistive term and negative in value). Note that the SCREAMER current used in the model is the total current and includes reflections (responsible for the oscillations in the current and inductive voltage).
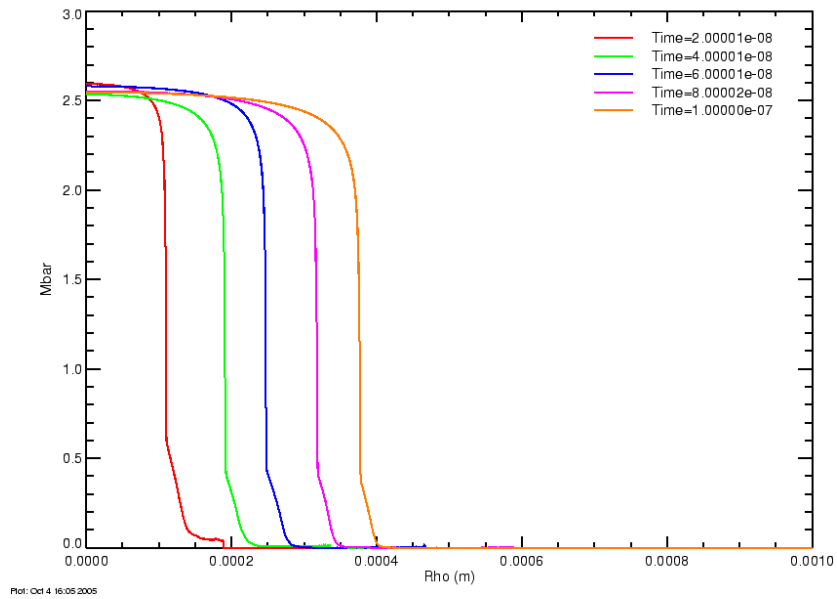
Figure 142. Late time average ionization number for experimental current drive.
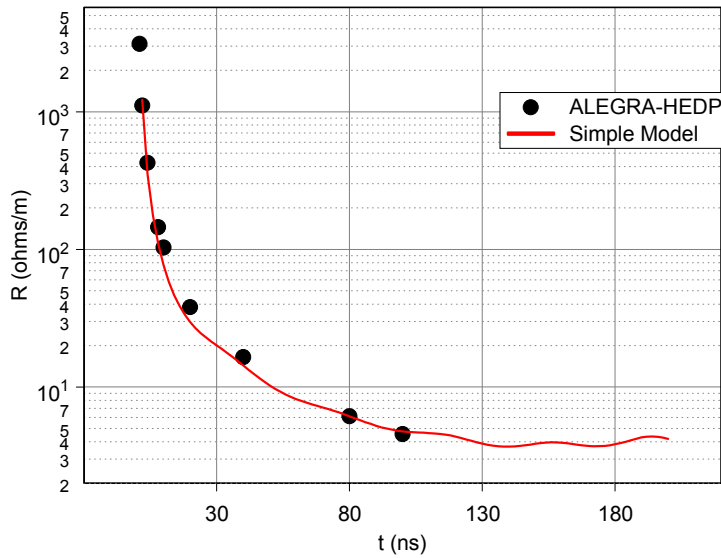
Figure 143. Resistance per unit length from ALEGRA_HEDP one dimensional simulation and from simple Braginskii-Martin Black Body model for experimental current excitation.

144
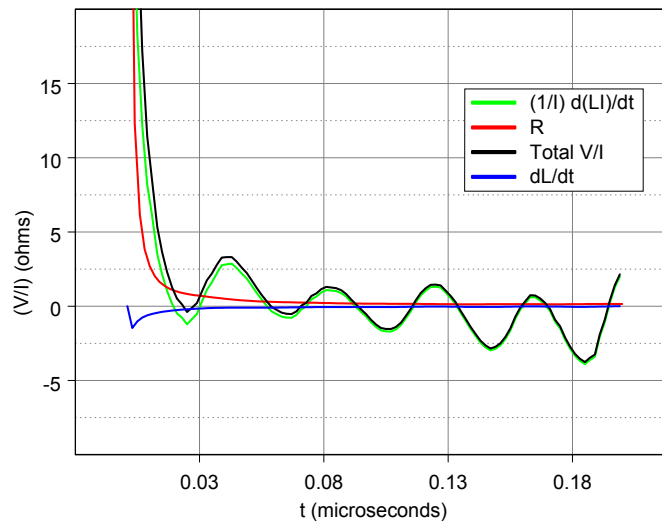
Figure 144. Total switch voltage divided by current from simple Braginskii-Martin Black Body model.

Inductive and resistive contributions are broken out of the total for comparison. The inductance used here is actually the difference inductance $\Delta L \approx 78$ nH.

9 CONCLUSIONS

The late time expansion phase of water breakdown was examined without making an initial assumption about final channel conductivity as was done in many previous efforts. Although starting conditions of radius, initial temperature, and initial density were varied, the late time values seemed to be independent of these choices. Nevertheless, all the starting conditions examined still assumed that the channel initiated from a relatively small size compared to the final values attained during the late time expansion phase. Once this underlying assumption is made, the temperatures (and densities) reached, and the resulting conductivities attained, are determined from the physical system. Both one-dimensional simulations, using ALEGRA_HEDP, and zero-dimensional calculations using a lumped model of the channel, were included, and agreed in late time values.

It was found that radiation damping resulted in relatively constant channel temperature at later times. The channel densities and opacities were large enough that the character of the radiation approached black body at later times in the expansion, unlike the open radiation used in gas breakdown [4]. Consequently this simple radiation model was primarily used in the zero-dimensional calculations.

The latest available information on channel conductivities in water were used in the calculations. The channel temperatures reached (20-40 eV) are higher than those assumed previously in breakdown channels. The characteristics of water (the hydrogen component) results in an increased growth of conductivity with temperature than in air (from a few eV to tens of eV). Thus channel resistances were considerably reduced compared to those typically used in Braginskii's and Martin's models.

Experiments in the Z20 test stand were discussed in detail and experimental data from the current and voltage monitors were presented. Values of channel resistance are typically inferred by using the circuit model for the test setup and examining the plateau resistance value in the exponential switch model, required to match the experimental voltage and current monitors. The inferred values are lower than that predicted by the Braginskii-Martin model, but higher than those predicted by the calculations in this report, using the pole to pole spacing in the switch (without any further increases in arc path length introduced due to wander of the initial channel). There are several possible reasons for this underestimate, which include: the effects of initial conditions (channel length and initial radius and density) changing the channel properties at late time, monitor displacement from the water switch with limited clear times in the experiment (limiting accuracy), the neglect of transient effects such as capacitances in the late time switch circuit model (they have been included in the experiment), and questions remaining about the model (depth of radiation penetration into the channel wall). Future investigations are now listed to address these.

1. The channel length may be longer than the electrode spacing. This is an initialization problem, which we may better understand by statistically examining more of the early time framing camera photographs, although it is a challenge to trace the brightest channel through the streamer bush.

2. The initial conditions for radius, channel density, and temperature are not well known and could have an influence on later expansion, particularly if initial radii exceed 100 microns. Some further simulations using large initial radii could be useful in determining when these initial conditions persist into the later time expansion and influence the final resistance values.

3. The single temperature 1D simulations in ALEGRA_HEDP should be checked with a two-temperature simulation to estimate the accuracy of this approximation.

4. The conductivity of the material in the channel is of critical importance to get the resistance correct. The LMD model is currently being updated to incorporate new information from the QMD simulations of water.

146

5. To reduce length and radius uncertainties of the initial channel, examination of the laser-triggered water breakdown data would be useful, even though the initial channel characteristics may be influenced by the laser triggering (and these are short gap data). Examination of any thin wire triggered water breakdown data would also be useful although we would have to consider the metallic products in the gas channel.

6. It might be instructive to examine data from RITS which has a longer clear time and thus allows more direct examination of the minimum resistance. Other data such as PITHON would be useful to re-examine.

7. Implement the simplified Braginskii-Martin Black Body model in SCREAMER to further examine comparisons between it and the experimental data (and include transmission line time delays and capacitance consistently).

8. Implement magnetic effects more rigorously in the lumped model.

10 ACKNOWLEDGEMENTS

11 REFERENCES

[1]   J. R. Woodworth, J. M. Lehr, J. Elizondo-Decanini, P. A. Miller, P. Wakeland, M. Kincy, J. Garde, B. Aragon, W. Fowler, G. Mowrer, J. E. Maenchen, G. S. Sarkisov, J. Corley, K. Hodge, S. Drennan, D. Guthrie, M. Navarro, D. L. Johnson, H. C. Ives, M. J. Slattery and D. A. Muirhead, "Optical and Pressure Diagnostics of a 4MV Water Switches in the Z20 Test Facility," IEEE Transactions on Plasma Science, Vol 32, No. 5, pp. 1778-1789, October 2004.

[2]   R. Rompe and W. Weizel, "On the Toepler Spark Law," Zeitschrift fur Physik. 122, pp. 636-639, 1944.

[3]   A. E. Vlastos, "The Resistance of Sparks," J. Appl. Phys., Vol 43, No. 4, pp. 1987-1989, April 1972.

[4]   S. I. Braginskii, "Theory of the development of a spark channel, Sov. Physics - JEPT, vol. 34(7), pp. 1068-1074, Dec. 1958.

[5]   J. M. Meek and J. D. Craggs (editors), **Electrical Breakdown of Gases**, New York: John Wiley & Sons, Chapter 10, 1978.

[6]   T. H. Martin, J. F. Seaman, and D. O. Jobe, "Energy Losses in Switches," Proceedings of the 9th Int. Pulsed Power Conference, pp.463-470, 1993.

[7]   V. M. Fedorov, "High Power Nanosecond Discharge Channel in Water," in Megagauss Fields and Pulsed Power Systems, V.M. Titov and G. A. Shvetsov, Eds., Nova Science Publishers, pp. 319-326, 1990.

[8]   E. V. Krivitskii, "Resistance of an Underwater Spark," Soviet Physics - Technical Physics, Vol. 17, No. 11, pp. 1839-1841, May 1973.

[9]   E. V. Krivitskii and V. V. Shamko, "Similarity of Underwater Spark Discharges," Soviet Physics -

Technical Physics, Vol. 17, No. 1, pp. 62-65, July 1972.

[10] V. V. Shamko and E. V. Krivitskii, "Characteristics of an underwater spark," Soviet Physics - Technical Physics, Vol. 22, No. 1, pp. 52-57, Jan. 1977.

[11] T. A. Brunner, "A Uses Guide to Radiation Transport in ALEGRA," Sandia Laboratories report, to be published.

[12] T. A. Brunner, K. R. Cochrane, C. J. Garasi, T. A. Haill, T. A. Mehlhorn, A. C. Robinson, and R. M. Summers, "ALEGRA-HEDP: Version 4.6," SAND2004-5996, Dec. 2004.

[13] T. A. Haill, K. R. Cochrane, C. J. Garasi, T. A. Mehlhorn, A. C. Robinson, and R. M. Summers, "ALEGRA-MHD: Version 4.6," SAND2004-5997, December 2004.

[14] M. P. Desjarlais, "Practical Improvements to the Lee-More Conductivity Near the Metal-Insulator Transition," Contributions to Plasma Physics, Vol. 41, No. 2-3, pp. 267-270, 2001.

[15] Ya. B. Zel'dovich and Yu P. Raizer, **Physics of Shock Waves and High-Temperature Hydrodynamic Phenomena**, Vol. 1 and 2, New York: Academic Press, 1966.

[16] L. D. Landau and E. M. Lifshitz, **Fluid Mechanics**, Oxford: Pergamon Press, 1959.

[17] J. M. Ziman, **Principles of the Theory of Solids**, Cambridge: University of Cambridge Press, 1972, p. 232.

[18] W. Benenson, J. W. Harris, H. Stocker, H. Lutz (editors), **Handbook of Physics**, New York: Springer-Verlag, Inc., 2002, p. 1072.

[19] G. W. C. Kaye and T. H. Laby, **Tables of Physical and Chemical Constants**, New York: John Wiley & Sons, 1986.

[20] L. Pauling, **General Chemistry**, Dover Pub., Inc., 1970, pp. 914-915.

[21] L. Spitzer, Jr., **Physics of Fully Ionized Gases**, New York: John Wiley & Sons, 1962, pp. 136-143.

[22] R. J. Goldston and P. H. Rutherford, **Introduction to Plasma Physics**, Bristol: Institute of Physics Pub., 1995, Chapter 13.

[23] Y. T. Lee and R. M. More, "An electron conductivity model for dense plasmas," Physics of Fluids, Vol. 27, No. 5, May 1984, pp. 1273-1286.

[24] L. D. Landau and E. M. Lifshitz, **Statistical Physics**, Oxford: Pergamon Press, 1958, pp. 225-228.

[25] T. R. Mattsson and M. P. Desjarlais, "Electrical conductivity of water from density functional theory," to be published.

[26] L. K. Warne, W. A. Johnson, K. C. Chen, and K. O. Merewether, "Joint Voltages Resulting From Lightning Currents," to be published.

[27] K. S. Miller and B. Ross, **An Introduction to the Fractional Calculus and Fractional Differential Equations**, New York: John Wiley & Sons, Inc., pp. 44-125.

[28] R. Courant and K. O. Friedrichs, **Supersonic Flow and Shock Waves**, New York: Springer-Verlag, p. 8.

[29] T. G. Engel, A. L. Donaldson, and M. Kristiansen, "The Pulsed Discharge Arc Resistance and Its Functional Behavior," IEEE Transactions on Plasma Science, Vol. 17, No. 2, 1989.

[30] T. W. Hussey, K. J. Davis, J. M. Lehr, N. F. Roderick, R. C. Pate, and E. Kunhardt, "Dynamics of Nanosecond Spark-Gap Channels," 1999 Pulsed Power Conference Digest, pp. 1171-1174.

[31] M. Zahn, E. O. Forster, E. F. Kelley, and R. E. Hebner, Jr., "Hydrodynamic Shock Wave Propagation After Electrical Breakdown," Journal of Electrostatics, Vol. 12, pp. 535-546, 1982.

[32] I. V. Lisitsyn, H. Nomiyama, S. Karsuki, and H. Akiyama, "Thermal Processes in a Streamer Discharge in Water," IEEE Transactions on Dielectrics and Electrical Insulation, Vol. 6, No. 3, pp. 351-356, June 1999.

[33] L. K. Warne and W. A. Johnson, "Inductance of Switch Region," Sandia Laboratories internal memorandum, May 9, 2003.

[34] K. R. Prestwich, Private Communication, 2003.

[35] D. H. McDaniel, M. G. Mazarakis, D. E. Bliss, J. M. Elizondo, H. C. Harjes, H. C. Ives, D. L. Kitterman, J. E. Maenchen, T. D. Pointon, S. E. Rosenthal, D. L. Smith, K. W. Struve, W. A. Stygar, E. A. Weinbrect, D. L. Johnson, and J. P. Corley, "The ZR Refurbishment Project," Conf. Record of the 25th Int. Power Modulator Symposium, H.C. Kirbie and D. Goebel Eds., 2002.

[36] E. A. Weinbrect, D. H. McDaniel and D. D. Bloomquist, "The Z Refurbishment Project at Sandia National Laboratories," Proc. Int. Pulsed Power Conference, M. Giesselmann and A. Nueber, Eds., pp 157-162, 2003.

[37] J. M. Lehr, D. D. Bloomquist, J. P. Corley, S. A. Drennan, D. W. Guthrie, H. C. Harjes, K. C. Hodge, D. L. Johnson, J. E. Maenchen, D. H. McDaniel, K. W. Struve, "SATPro: The System Assessment Test Program for ZR," Proc. Of the 26th Int. Power Modulator Symposium, pp 106-110.

[38] M. L. Kiefer, K. L. Fugelso, K. W. Struve, M. M. Widner, "SCREAMER, a Pulsed Power Design Tool, Users Guide for VERsion 2.0," August 25, 1995.

[39] W. A. Johnson, R. S. Coats, R. E. Jorgenson, J. D. Kotulski, J. M. Lehr, M. F. Pasik, S. E. Rosenthal, C. D. Turner and L. K. Warne, "Electromagnetic Analysis and Modeling of the Coax-to Triplate Transition for the Pulse Compression Section of the ZR Accelerator," Proc. of the 14th Int. Pulsed Power Conf., M. Giesselman and A. Nueber, Eds, pp. 630-633, 2003.

[40] J. M. Lehr, J. E. Maenchen, J. R. Woodworth, W. A. Johnson, R. S. Coates, L. K. Warne, L. P. Mix, D. L. Johnson, I. D. Smith, J. P. Corley, S. A. Drennan, K. C. Hodge, D.W. Guthrie, M. J. Navarro and G. S. Sarkisov, "Multi-megavolt Water Breakdown Experiments," Proc. of the Int. Pulsed Power Conf., M. Giesselman and A. Nueber, Eds, pp. 609-614, 2003.

[41] M. J. Kushner, W. D. Kimura and S. R. Bryon, "Arc resistance of laser-triggered spark gaps," J. Appl. Phys. Vol. 58, No. 5, pp. 1744-1751, September 1985.

[42] H. Akiyama, M. Kristiansen, H. Krompholz, and B. Maas, "Current-Voltage Characteristics of a High Current Pulsed Discharge in Air," IEEE Trans. Plas. Sci. Vol. 16 No.2, April, 1988.

[43] K. Takaki and H. Akiyama, "Resistance of Pulsed Arc Discharge in Air and SF6," Proc. of the Pulsed Power Conference, R. Reinovsky and M. Newton, Eds., 2001.

[44] J. M. Elizondo, J. P. Corley, K. W. Struve, D. L. Johnson, P. Corcoran, K. R. Prestwich, "Water Switches Impedance from SCREAMER Circuit Model and Experimental Waveform Match," Proceedings of the 14th Int. Pulsed Power Conference, pp 171-174, 2003.

[45] J. P. Vandevender, "The Resistive Phase of a High Voltage Water Spark," J. Appl. Phy. 49 (5) May 1978.

[46] P. W. Spence, Y. G. Chen, G. Frazier, and H. Calvin, "Inductance and Resistance Characteristics of Single Site Untriggered Water Switches in Water Transfer Capacitor Circuits," Proc. Int. Pulsed Power Conf., A. Guenther and M. Kristiansen, Eds., pp. 359-362, 1979.

[47] J. C. Martin, "Duration of the Resistive Phase and Inductance of Spark Channels," SSWA/JCM/1065/25 Atomic Weapons Research Establishment Paper.

[48] G. M. Wilkinson, "Time Dependent Capacitance Effects in Water Dielectric Switching," pp 323-326, Proceedings of the International Pulsed Power Conference, 1983.

[49] J. M. Lehr, J. E. Maenchen, J. P. Corley, J. R. Woodworth, D. L. Johnson, "Correlations between Optical and Electrical Diagnostics in High Power Water Switches," IEEE ICOPS, 2004.

[50] T. P. Sorensen and V. M. Ristic, "Risetime and Time-dependent Spark Gap Resistance in Nitrogen and Helium," J. Appl. Phys. Vol. 48, No.1, Jan 1977.

Appendix A. PROGRAM DETAILS

For a current drive I we solve the three differential equations (Equation (19)) using a Runge-Kutta-Fehlberg method to determine the channel area (A), pressure (p) and temperature (T). Because of numerical difficulties we had to scale A, p and T. We let A represent square microns so A is in units of 10^{-12}. We let p represent Mbars so we multiplied all instances of p by 10^{+11}. We let T represent units of 10^{-19} Joules. The three equations become

$$\frac{dA}{dt} = \sqrt{\frac{4\pi}{K_p \rho_0}} Ap \left[10^{11} \sqrt{10} \right]$$

$$\frac{dp}{dt} = \frac{(\gamma - 1) I^2}{\sigma A^2} \left[10^{13} \right] - \gamma \frac{p}{A} \frac{dA}{dt}$$

where σ is the channel conductivity in $(\Omega - m)^{-1}$ as obtained from either Spitzer or Fedorov.

$$\frac{dT}{dt} = \left[-\frac{Ap}{(1+m) T^2} \right]^{-1} \left[\frac{(\gamma - 1)}{\gamma} \frac{\sqrt{4\pi A} \sigma_S T^3}{k^4 (1+m)} 10^{-81} - \frac{A}{T(1+m)} \frac{dp}{dt} - \frac{p}{T(1+m)} \frac{dA}{dt} \right]$$

For a voltage drive V_{oc} we solve five differential equations numerically to determine A, p, T, the current in the channel (I), and inductance of the channel (L). In addition to the three equations above we add

$$\frac{dL}{dt} = -\frac{\mu_0}{2\pi} \frac{1}{2A} \frac{dA}{dt}$$

$$\frac{dI}{dt} = \frac{V_{oc}}{L} - \frac{(R_0 + R_{arc})}{L} I - \frac{1}{L} \frac{dL}{dt} I$$

where

$$R_{arc} = \frac{1}{A\sigma} \left[10^{12} \right]$$

and R_0 is the external resistance of the circuit.

For the Braginskii-Martin Black Body model with a voltage drive, we solve three differential equations numerically to determine H, I, and L.

$$\frac{dH}{dt} = I^{2/3}$$

$$\frac{dL}{dt} = -\frac{\mu_0}{2\pi} \frac{1}{2A} \frac{dA}{dt}$$

$$\frac{dI}{dt} = \frac{V_{oc}}{L} - \frac{R_0}{L} I - \frac{R_1}{L} \frac{I^{19/27}}{H^{7/9}} - \frac{1}{L} \frac{dL}{dt} I$$

Appendix B. INPUT FILES

This appendix describes the input files used in the ALEGRA-HEDP one-dimensional simulations shown in Section 5 (linear ramp current rising to $I_0 = 300$ kA, in $\tau = 100$ ns). The geometry shown in Figure B-1 is generated by the CUBIT input file given below. The boundary conditions and initial condition shown in Figure B-2 are generated by the Alegra input file in Section B.2.
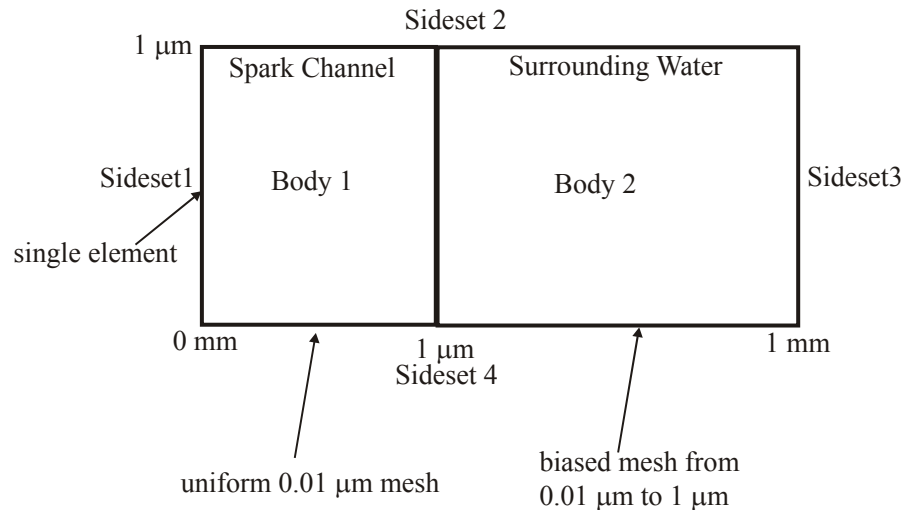
Figure B-1. Geometry generated by CUBIT input

B.1 Cubit Input File

```
journal off
label curve on
#### Defining variables
# r1 = {r1 = 1.0}  ### Channel dimension
# r2 = {r2 = 1000.0}  ### Outer boundary dimension
# z1 = {z1 = 1.0}  ### Try to maintain square cells
# d3 = {d3 = 1.0}   ### Length of channel
# scalefactor = { scalefactor = 1.0e-6}  ### Scale to microns

#### Create two rectangles
create brick x {r1} y {z1} z {d3}   ### Channel
body 1 move x {r1/2.} y {z1/2.}
create brick x {r2} y {z1} z {d3}  ### Surrounding water
body 2 move x {r1+r2/2.} y {z1/2.}
imprint all
merge all  ### Boundaries are connected

#### Define mesh density
curve 3 interval 1  ### Channel length
curve 2 4 interval 100  ### Channel top and bottom
# small = {small = r1/100.}
# large = {large = r1}
```

curve 14 scheme bias fine {small} coarse {large} start vertex 2 ### Surrounding water top
curve 16 scheme bias fine {small} coarse {large} start vertex 1 ### Surrounding water bottom

####Mesh the channel and surrounding water
mesh surface 1
block 1 surface 1
mesh surface 7
block 2 surface 7
block all Element Type quad4
transform mesh output scale {scalefactor} ### rescale to meters

Define sidesets and nodesets for boundary conditions
sideset 1 curve 3 ### on axis
sideset 2 curve 2 14 ### top
sideset 3 curve 13 ### right axis
sideset 4 curve 4 16 ### bottom
nodeset 1 curve 3 ### on axis
nodeset 2 curve 2 14 ### top
nodeset 3 curve 13 ### right axis
nodeset 4 curve 4 16 ### bottom

Name of genesis file
export genesis "spark2.gen"
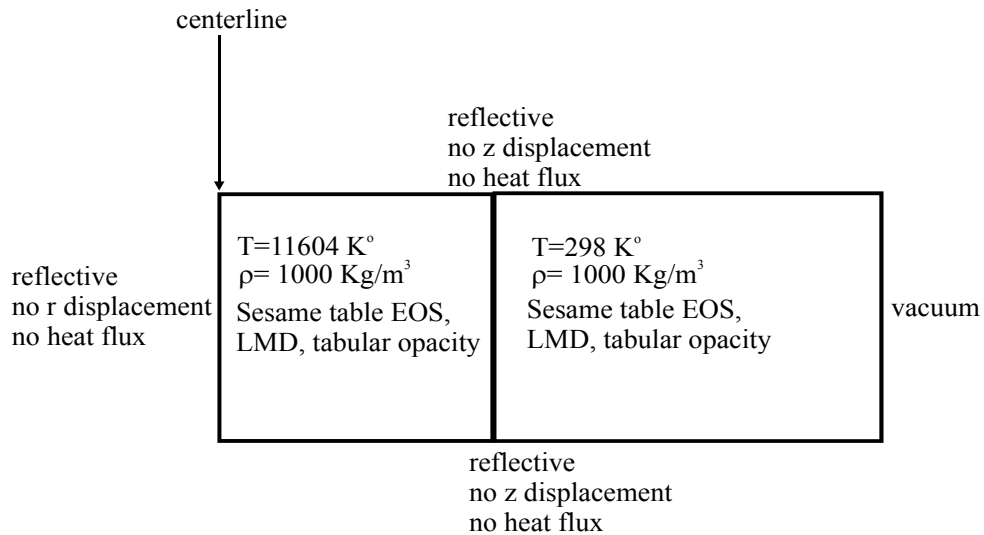
Figure B-2. Boundary conditions and initial conditions in the Alegra input

B.2   Alegra Input File

title
Water Spark Problem, Slow Risetime Current
Units, SI $ Units definition

$$$ physics options
radiation magnetohydrodynamics conduction

cylindrical
maximum initial time step = 1.0e-15
void compression = off
maximum time step limit = 1.0e-11
transient magnetics
void conductivity = 1.0e-6
rz cyl radial slot bc, sideset 3, function 1, scale 1.0,
r 0., z 0., -2., -1., 1., 2.
centerline bc, sideset 1
material fraction force limiter = 0.001, power = 1.0
joule heat, maxsigma
aztec set, 1
end

function 1 $ 3kA/ns
0.0 0.0
1.0 3.0e12
end

hydrodynamics
no displacement, nodeset 1, r
no displacement, nodeset 2, z
no displacement, nodeset 4, z
end

thermal conduction
no heat flux, sideset 1
no heat flux, sideset 2
no heat flux, sideset 4
end

linearized diffusion
max energy density change = 0.04
flux limiter = simplified levermore pomraning
initial conditions, uniform temperature 298.15
aztec set, 1
group bounds
log 0.01 [eV] to 100. [eV] by 1
end

reflective boundary, sideset 1
reflective boundary, sideset 2
vacuum boundary, sideset 3
reflective boundary, sideset 4
end

block 1
lagrangian mesh
material 1
end

block 2

lagrangian mesh
material 2
end
end

$$$$$$$$$$$$$$$$$$$$$$$$$$$$$ algorithm control $$$$$$$$$$$$$$$$$$$$$$$$$$$$$$$
aztec 0 $ thermal cond. control
solver = CG
scaling = sym_row_sum
conv norm = rhs
precond = jacobi
output = none
max iter = 5000
tol = 1.0e-14
end

aztec 1
solver, lu
output, none
end
CRT = OFF $ output stuff to screen off if running in batch

$$$$$$$$$$$$$$$$$$$$$$$$$$$$$ execution control $$$$$$$$$$$$$$$$$$$$$$$$$$$$$$$
start time= 0.0
Termination time = 1.0e-7
Emit plot, time interval=1.0e-10 from 0.0 to 1.0
Emit restart, time interval=1.0e-9 from 0.0 to 1.0

Plot variable $ Variables written to exodus file
coordinates
velocity
btheta
j
e
psi $ actually rBtheta
density : avg
energy : avg
temperature : avg
pressure : avg
sound speed : avg
specific heat vol : avg
econ : avg
econ_par : avg
econ_perp : avg
thermal_con : avg, as 'tcon'
thermal_con_par : avg
thermal_con_perp : avg
zbar : avg
opacity_a : avg
opacity_r : avg
end

154

$$$$$$$$$$$$$$$$$$$$$$$$$$$$$ material models $$$$$$$$$$$$$$$$$$$$$$$$$$$$$$$$$$$
material 1 H2O
density = 1.0e3 $kg/m^3
temperature = 11604.5 $ Degrees Kelvin
model 1
model 2
model 3
number of elements 1
element 3, mass 6.0053, fraction 1.0
end
end

material 2 H2O
density 1.0e3 $ kg/m^3
temperature 297.97 $ Degrees Kelvin
model 1
model 2
model 3
number of elements 1
element 3, mass 6.0053, fraction 1.0
end
end

model 1 lanl sesame
nmat = 7150
table = 301
clip = 250.0
end

model 2 lmd
z = 3.3333
a = 6.0053
rho solid = 1.0e3
tmelt = 273.0
XIEV = 14.0
G0 = 5.05
G1 = 7.95
LOG LAMBDA MIN = 2.0
P1 = 1.
P2a = 0.2
P2b = 0.0
P2c = 25000.
P2d = 2.0e22
P2e = 2.0
P3a = 0.01
P3b = 0.33
P4a = 1.0
P4b = 0.33
P5 = 0.0
PRESSURE IONIZATION PREFACTOR = 0.98
PRESSURE IONIZATION EXPONENT = 1.05
DIPOLE ALPHA = 11.5353

```
end

model 3 tabular opacity
dynamic integration
material = 'water'
end
exit
```

Appendix C. ONE DIMENSIONAL SIMULATIONS

This appendix contains the five remaining one-dimensional simulations from Section 4.

C.1 Radiation Off

The second set has radiation turned off. The current drive is a linear ramp rising to $I_0 = 300$ kA with a risetime of 100 ns. The channel initial conditions are radius of 1 μm, temperature of 1 eV and density of 1000 kg/m^3.
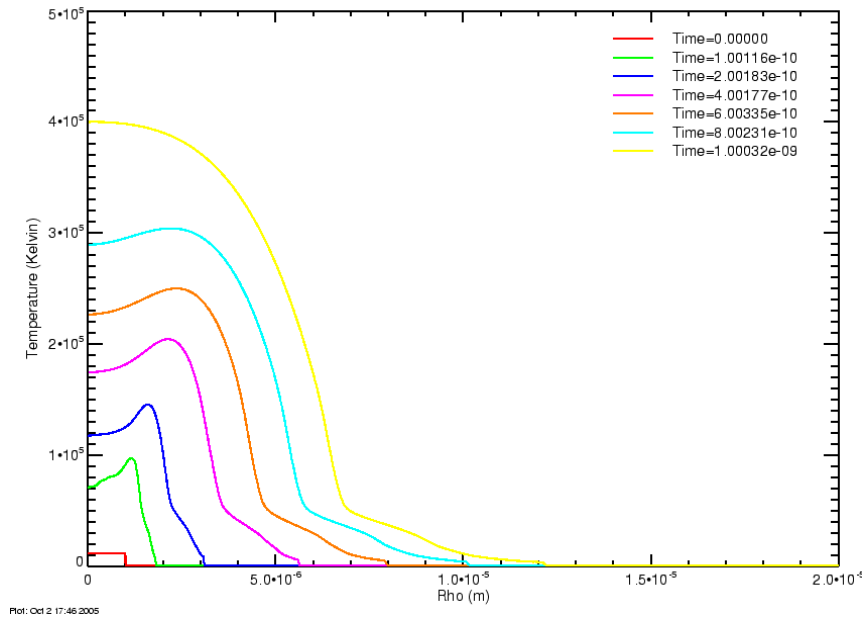
Figure C-1. Early time temperature profiles for slow ramp current, radiation off
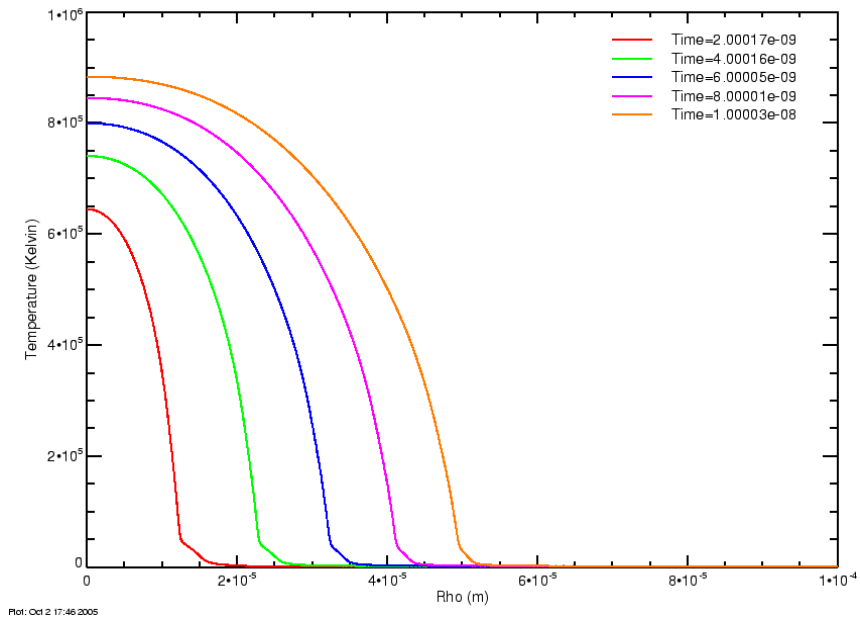
Figure C-2. Intermediate time temperature profiles for slow ramp current, radiation off
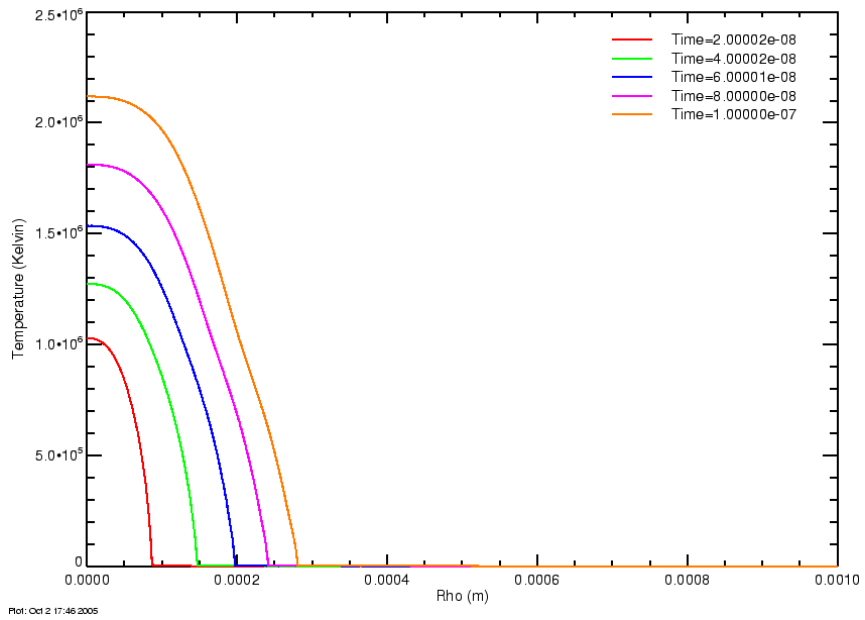
Figure C-3. Late time temperature profiles for slow ramp current, radiation off

158
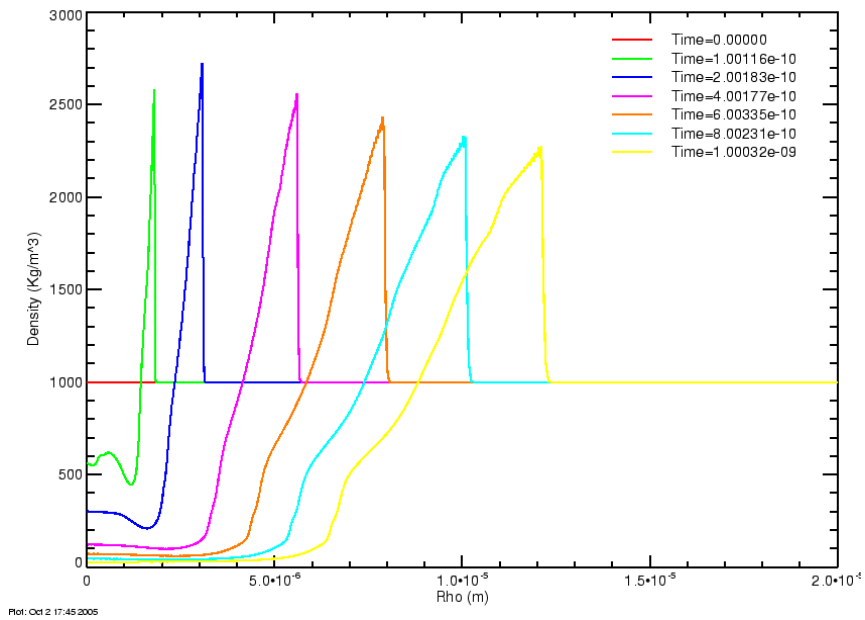
Figure C-4. Early time density profiles for slow ramp current, radiation off
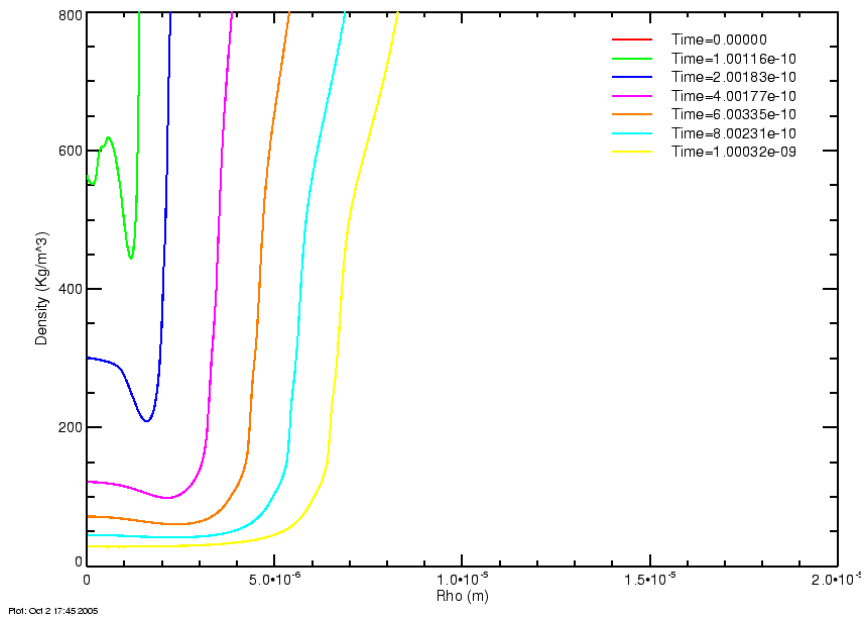
Figure C-5. Detail of early time temperature profiles for slow ramp current, radiation off
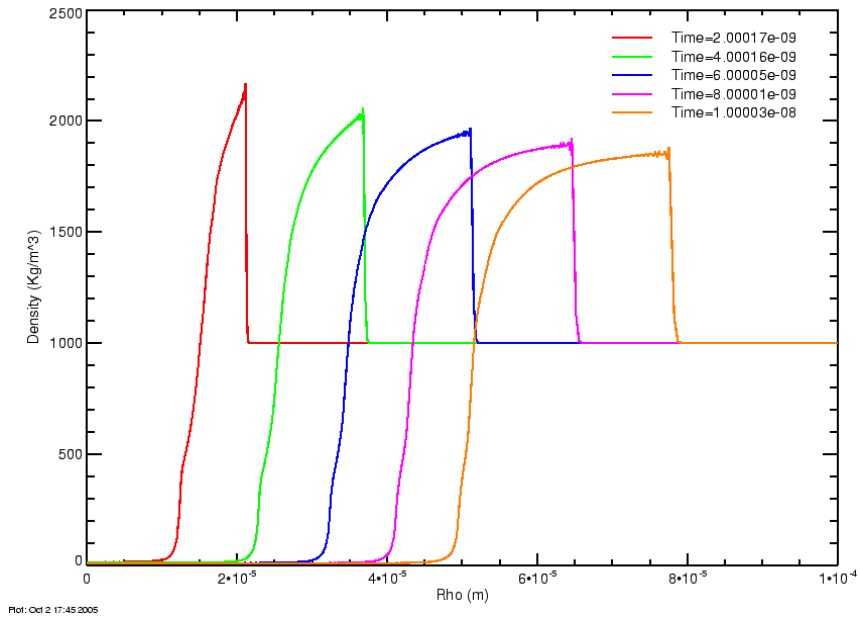
Figure C-6. Intermediate time density profiles for slow ramp current, radiation off
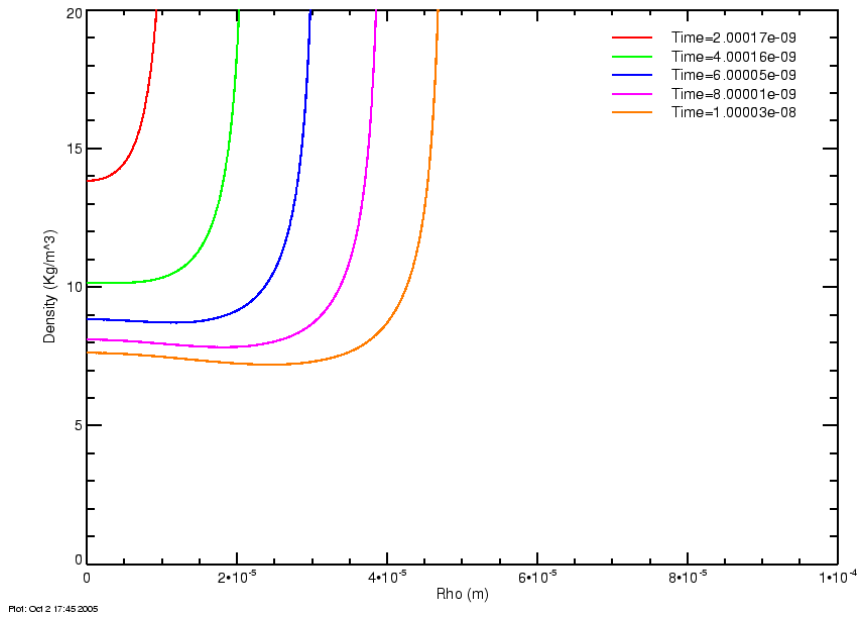
Figure C-7. Detail of intermediate time density profiles for slow ramp current, radiation off
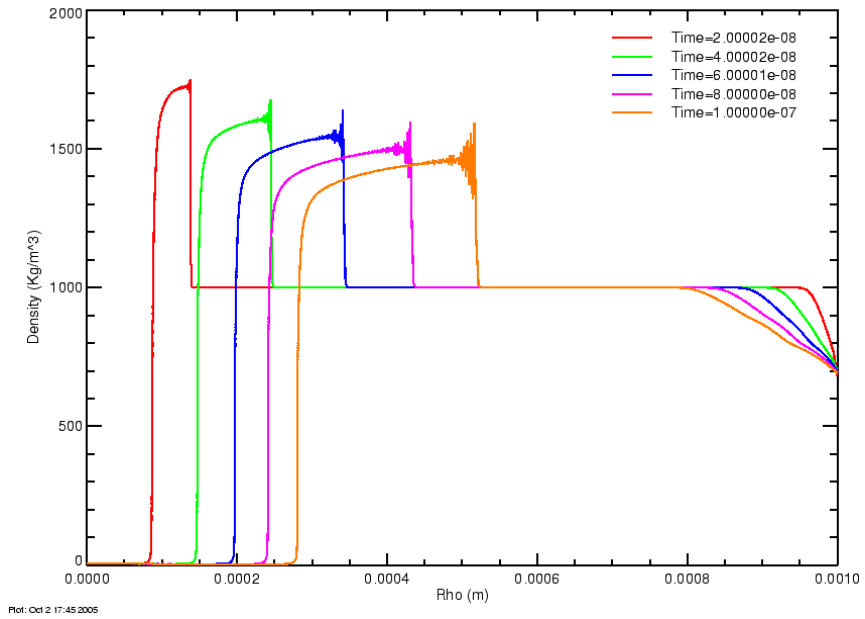
Figure C-8. Late time density profiles for slow ramp current, radiation off
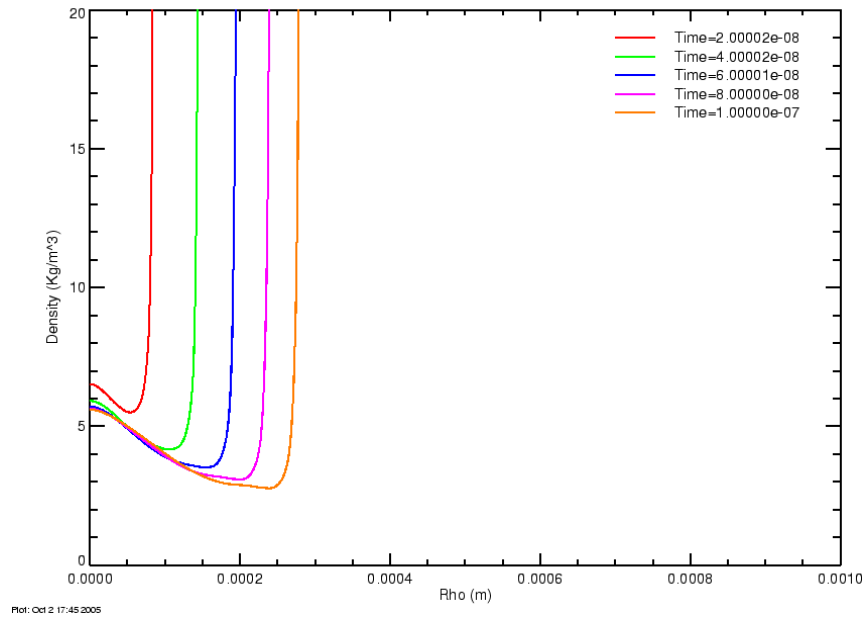
Figure C-9. Detail of late time density profiles for slow ramp current, radiation off
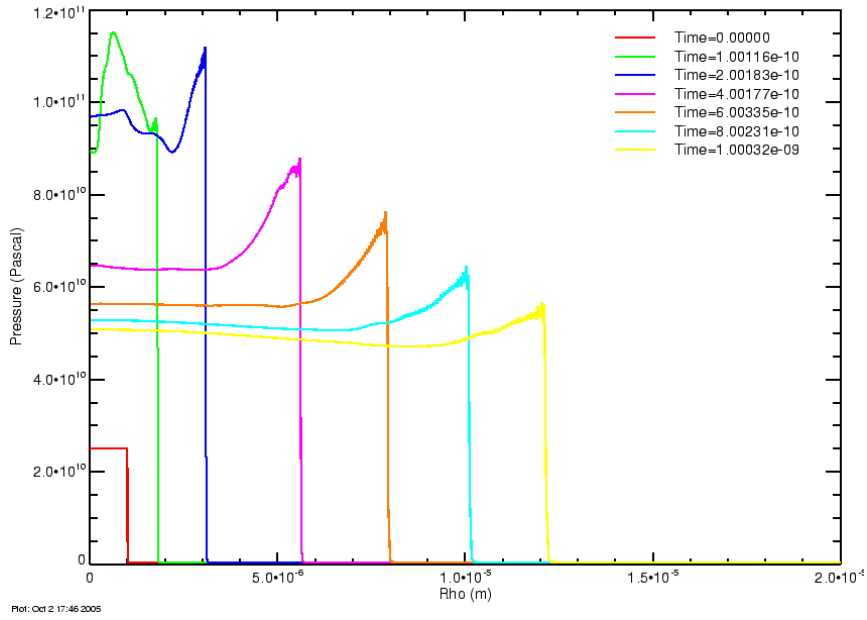
Figure C-10. Early time pressure profiles for slow ramp current, radiation off

162
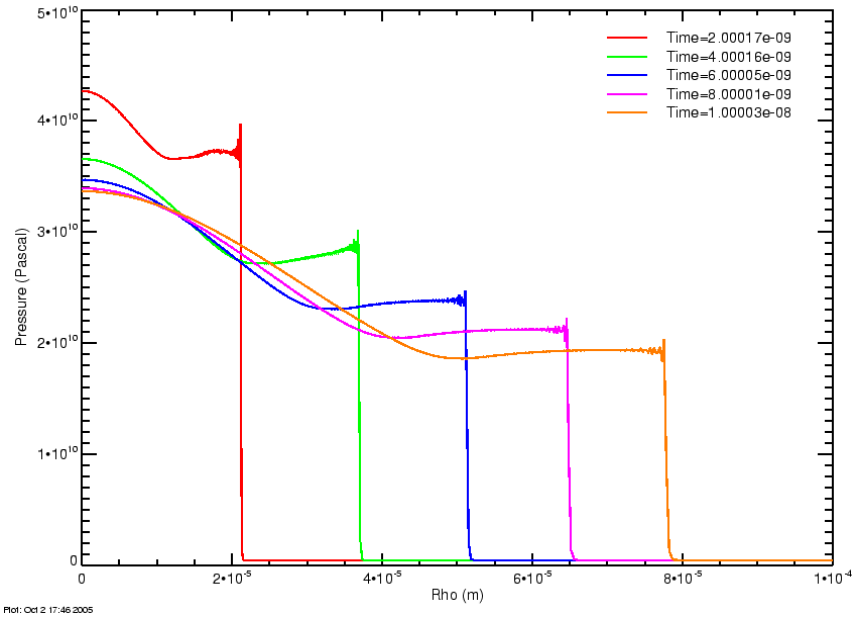
Figure C-11. Intermediate time pressure profiles for slow ramp current, radiation off
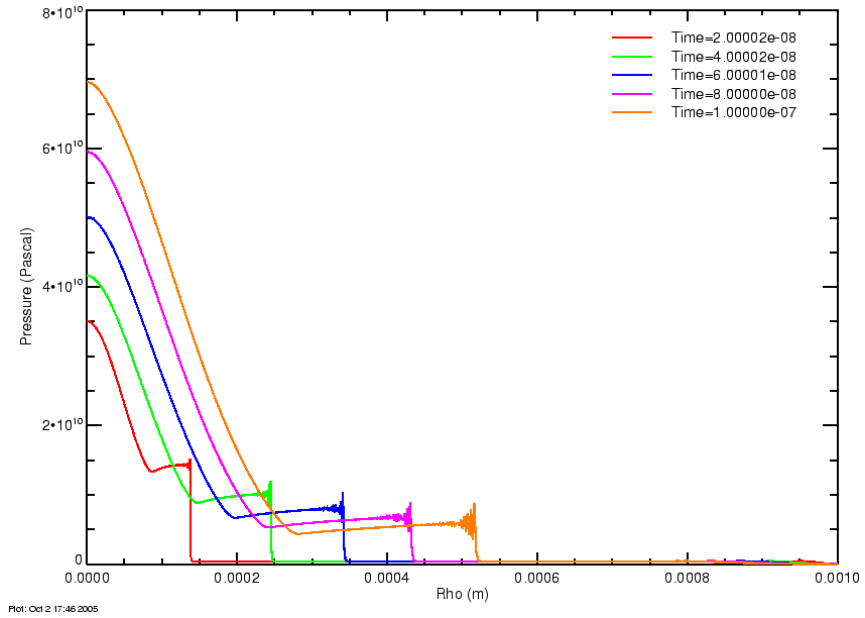
Figure C-12. Late time pressure profiles for slow ramp current, radiation off

163
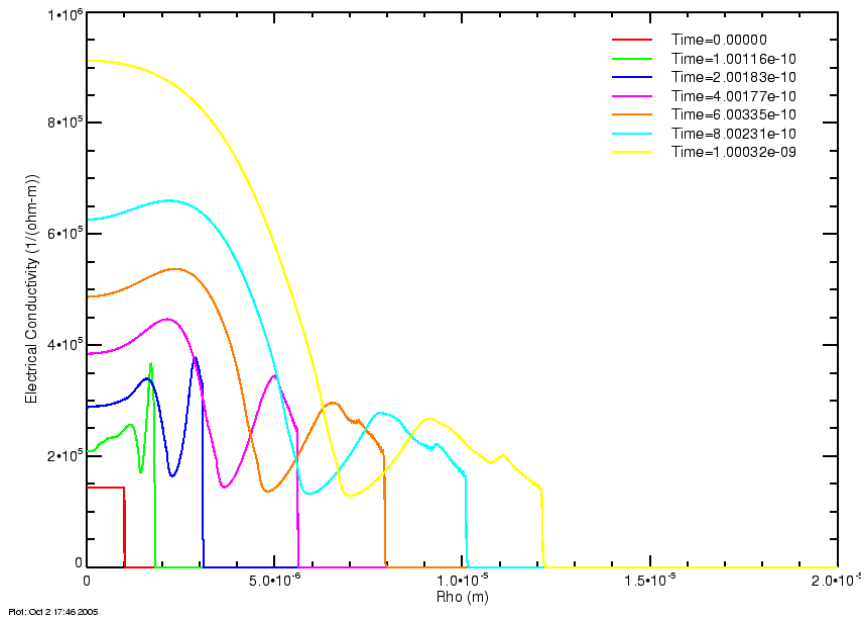
Figure C-13. Early time electric conductivity profiles for slow ramp current, radiation off
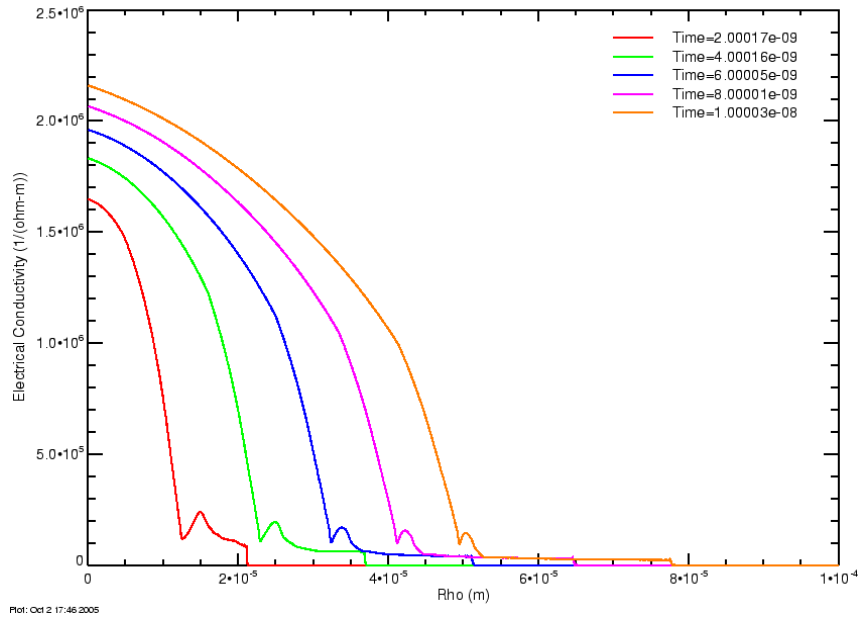
Figure C-14. Intermediate time electric conductivity profiles for slow ramp current, radiation off
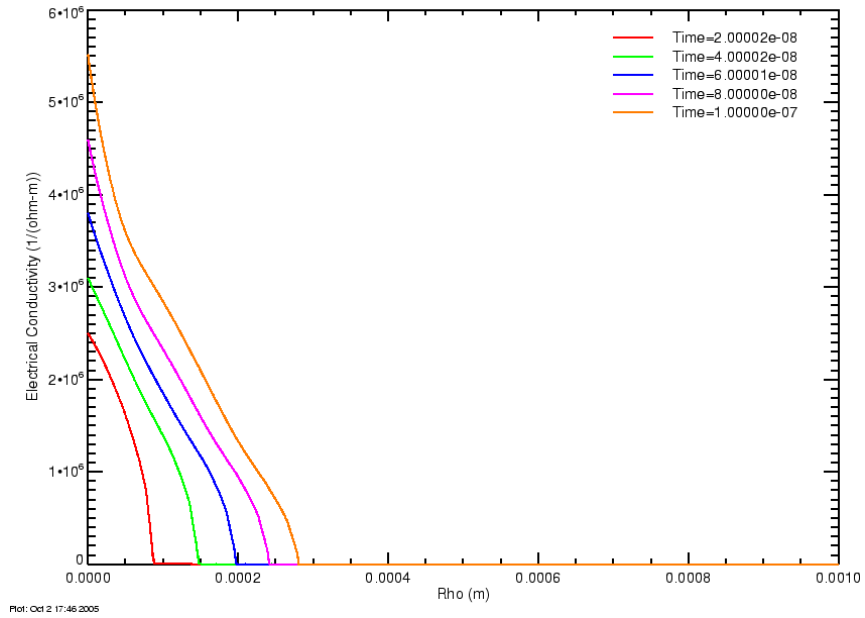
Figure C-15. Late time electric conductivity profiles for slow ramp current, radiation off
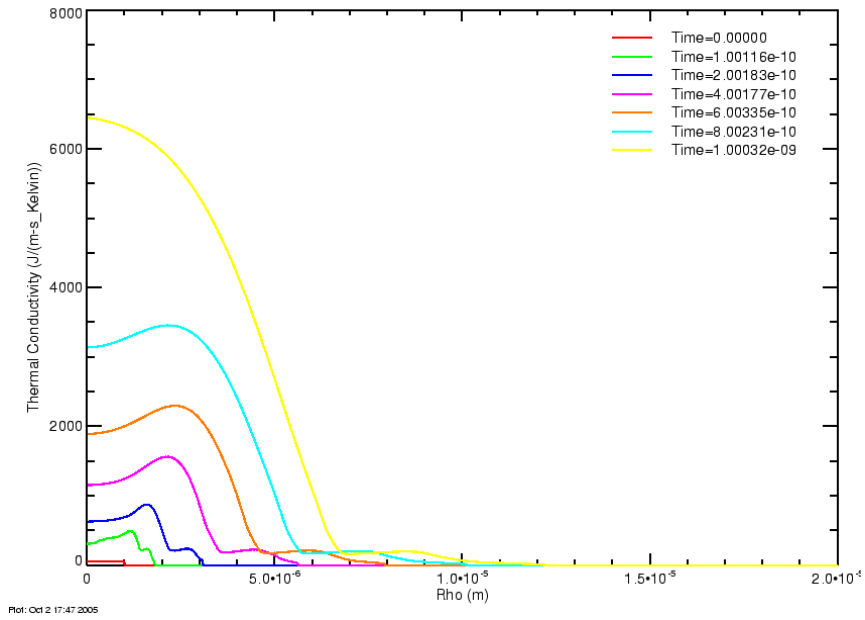
Figure C-16. Early time thermal conductivity profiles for slow ramp current, radiation off
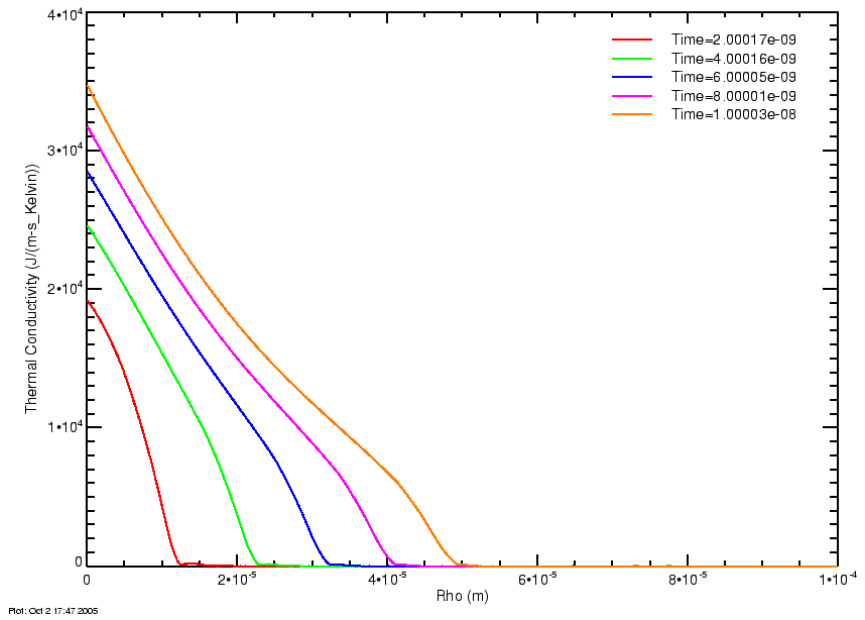
Figure C-17. Intermediate time thermal conductivity profiles for slow ramp current, radiation off

166
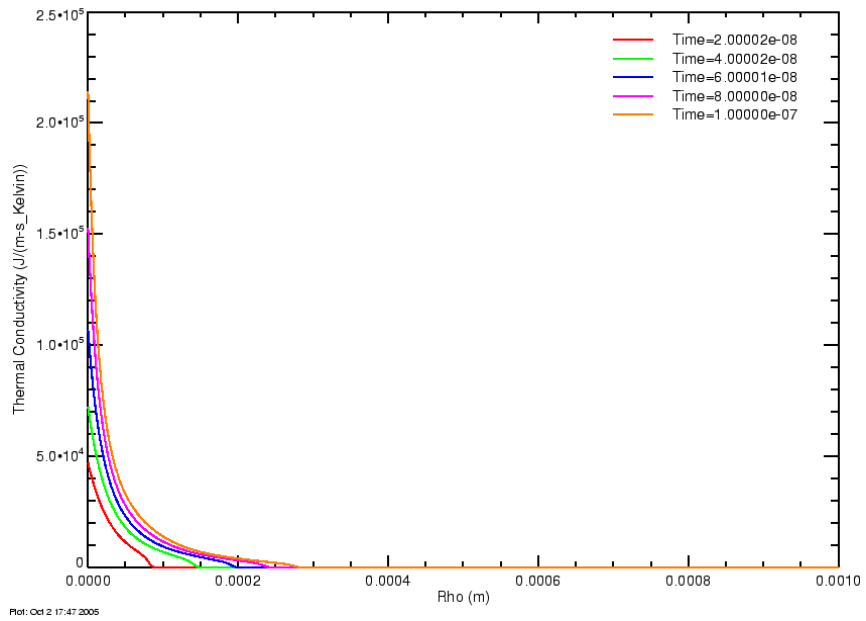
Figure C-18. Late time thermal conductivity profiles for slow ramp current, radiation off
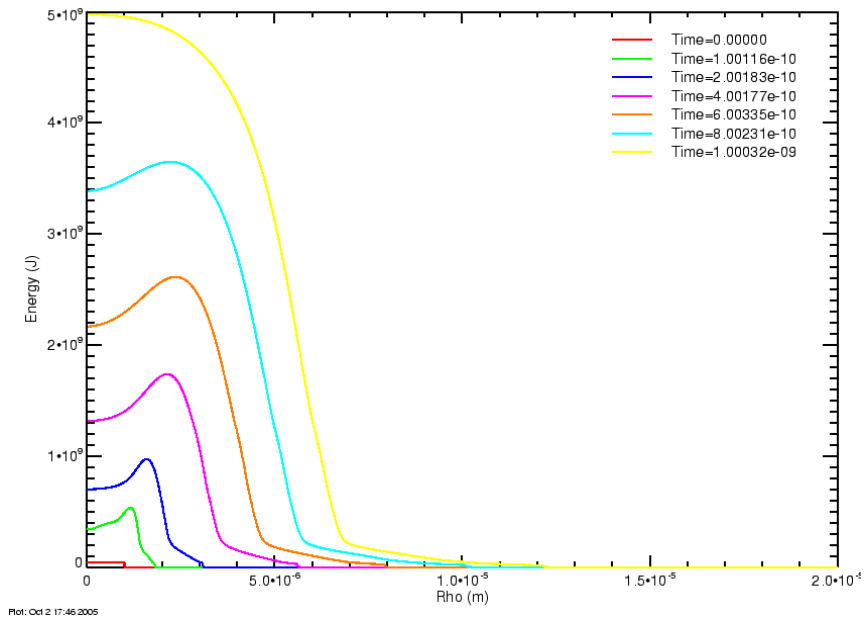
Figure C-19. Early time internal energy profiles for slow ramp current, radiation off
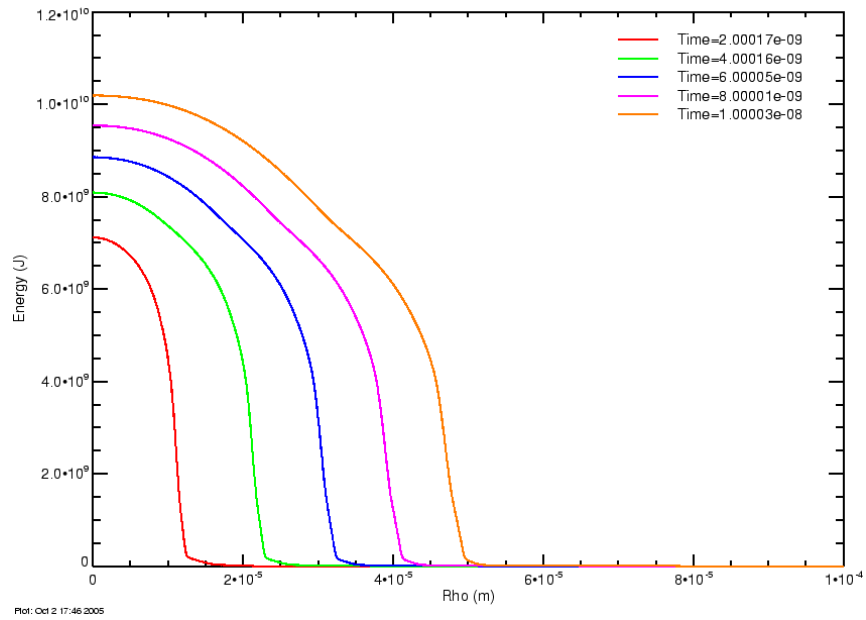
Figure C-20. Intermediate time energy profiles for slow ramp current, radiation off
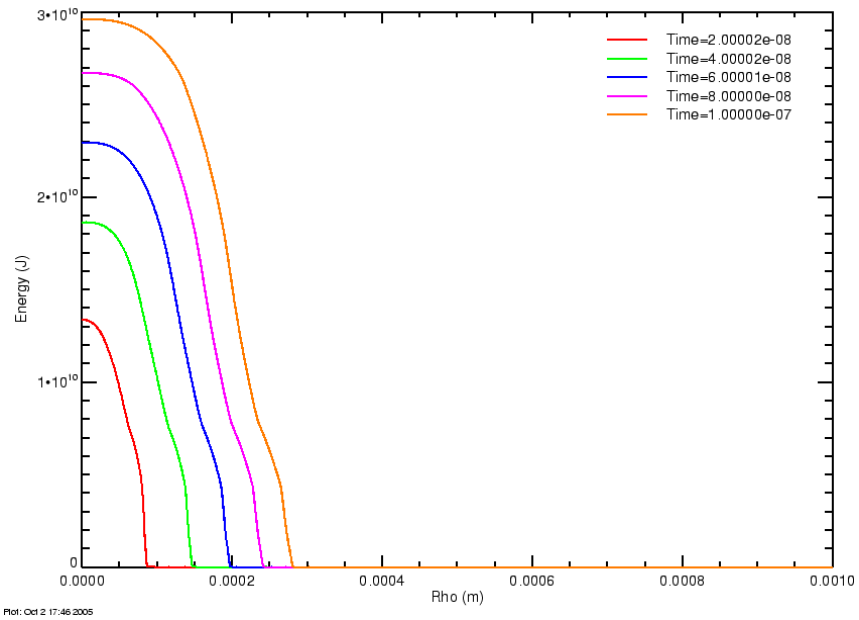
Figure C-21. Late time internal energy profiles for slow ramp current, radiation off
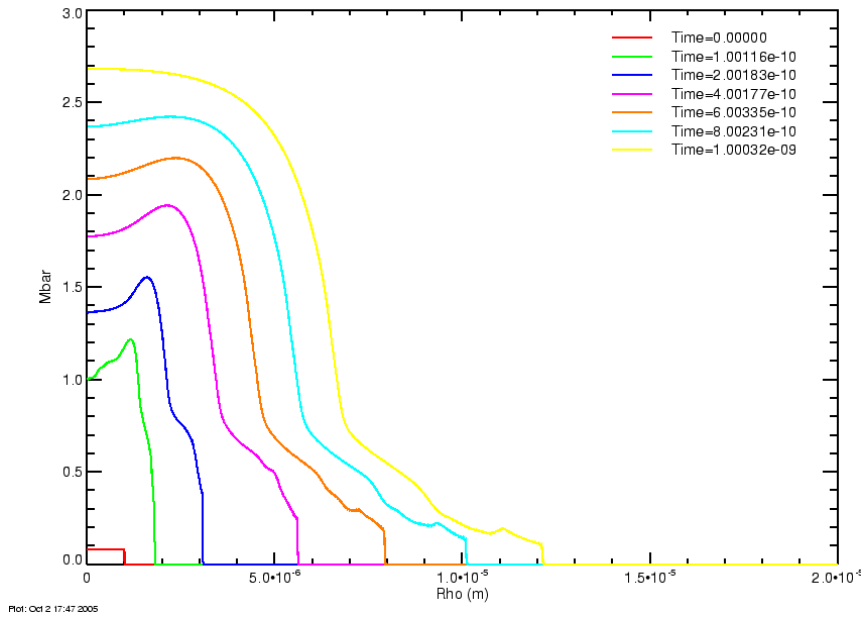
Figure C-22. Early time ionization number profiles for slow ramp current, radiation off
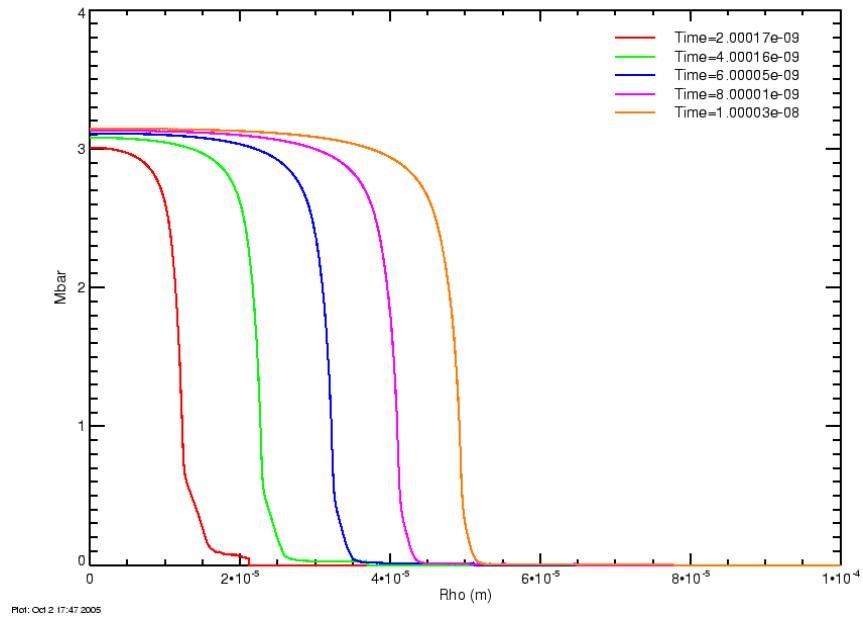
Figure C-23. Intermediate time ionization number profiles for slow ramp current, radiation off
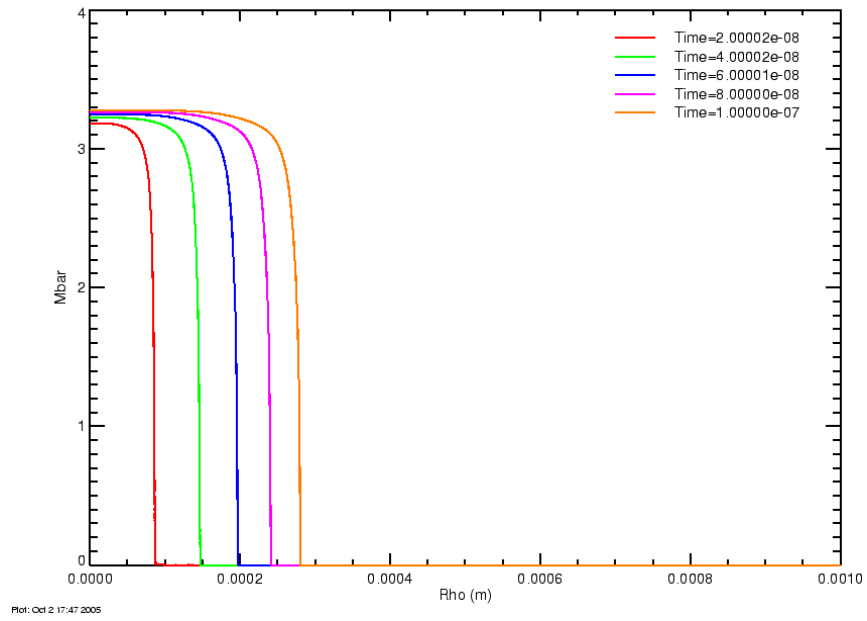
Figure C-24. Late time ionization number profiles for slow ramp current, radiation off

C.2 Larger Initial Channel Radius

The third set has radiation turned on. The current drive is a linear ramp rising to $I_0 = 300$ kA with a risetime of 100 ns. The channel initial conditions are radius of 10 μm, temperature of 1 eV and density of 1000 kg/m^3.
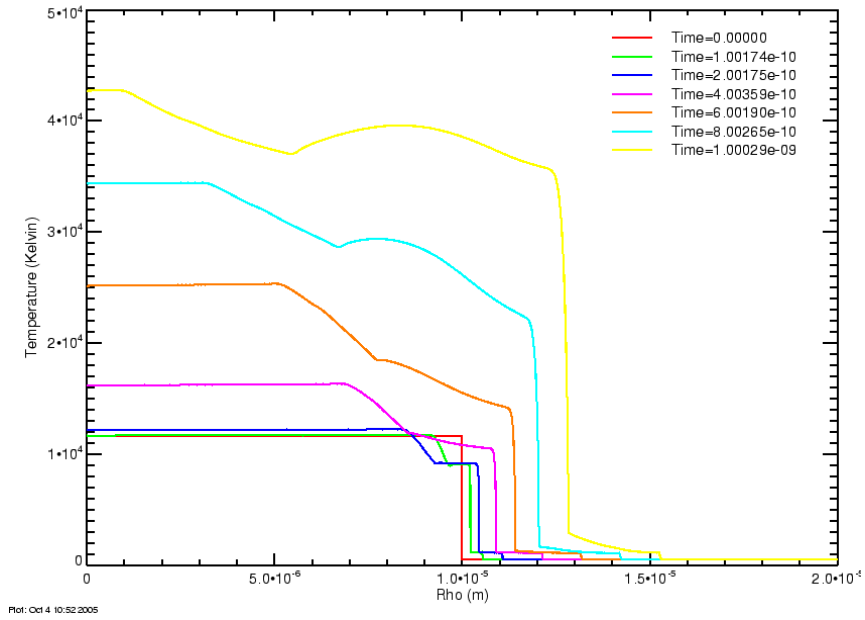
Figure C-25. Early time temperature profiles for slow ramp current, 10 μm initial radius
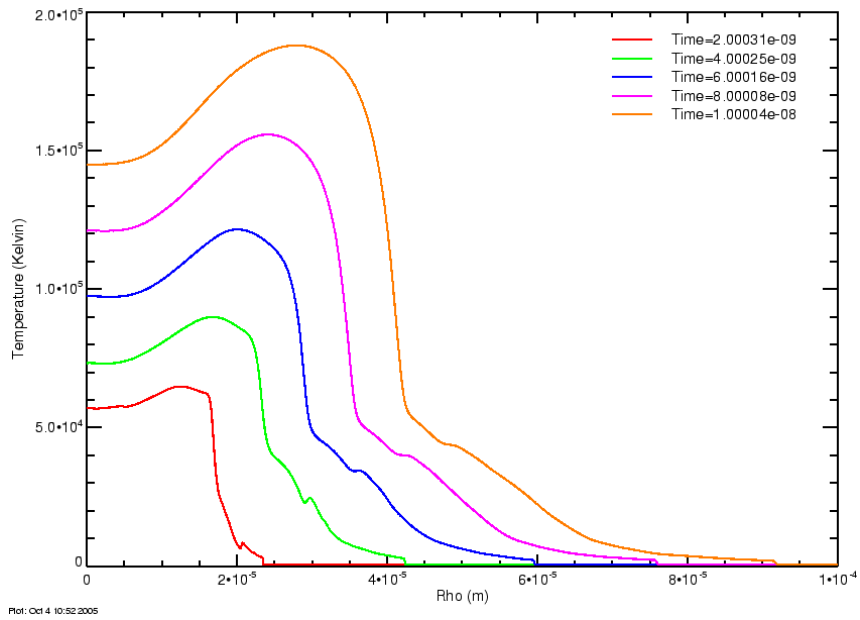
Figure C-26. Intermediate time temperature profiles for slow ramp current, 10 μm initial radius
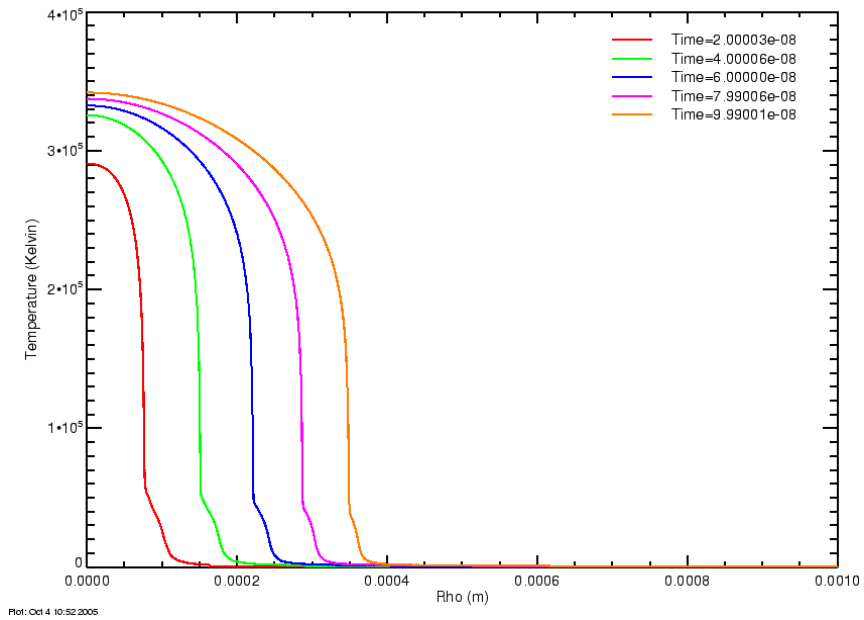
Figure C-27. Late time temperature profiles for slow ramp current, 10 μm initial radius
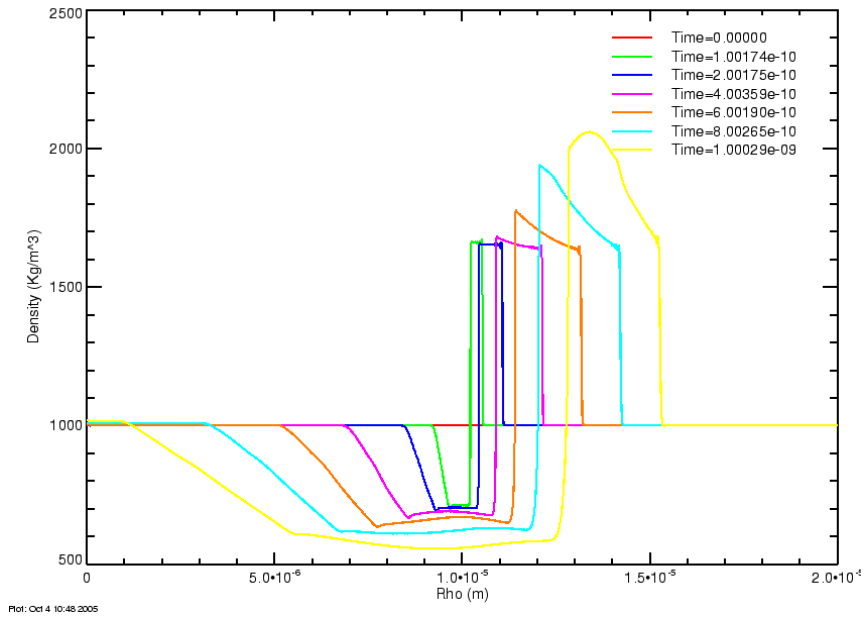
Figure C-28. Early time density profiles for slow ramp current, 10 μm initial radius
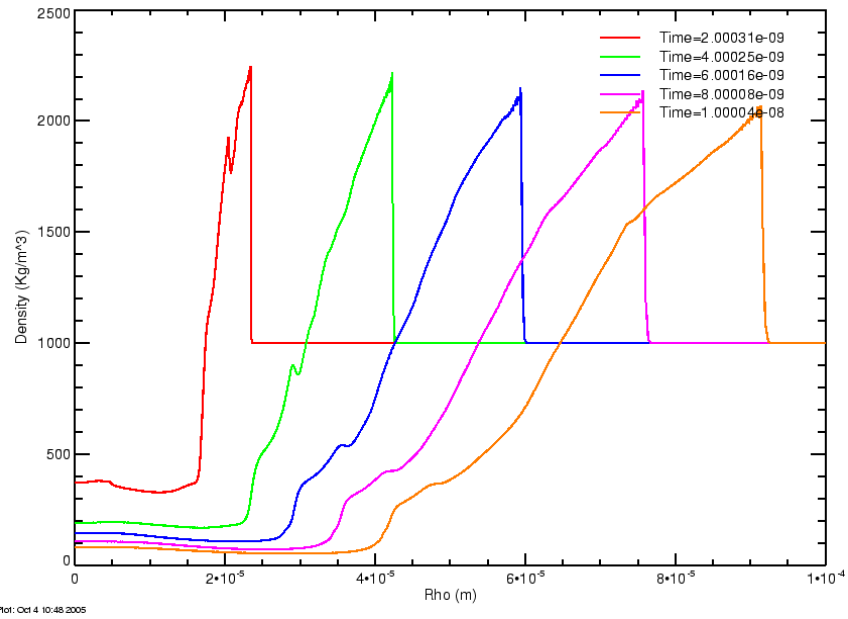
Figure C-29. Intermediate time density profiles for slow ramp current, 10 μm initial radius
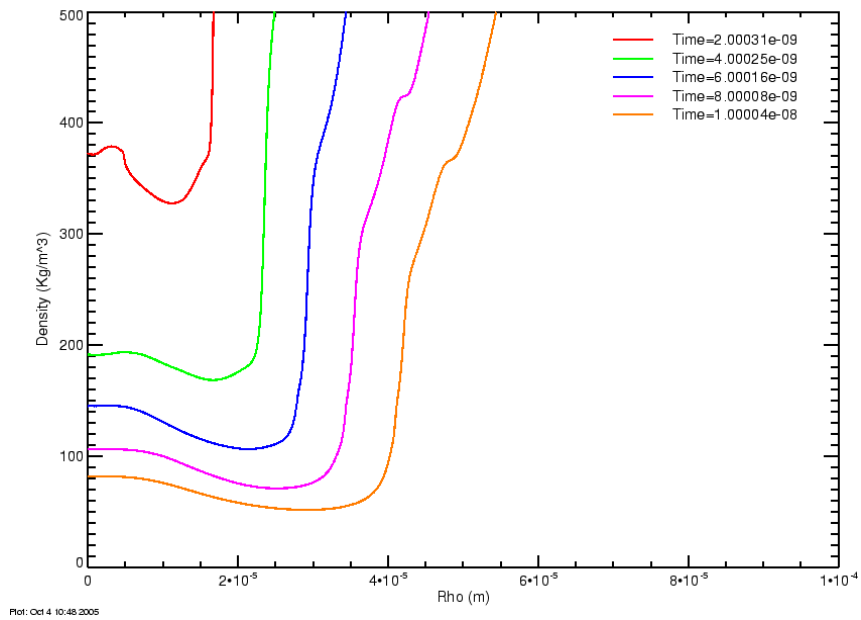
Figure C-30. Detail of intermediate time density profiles for slow ramp current, 10 μm initial radius
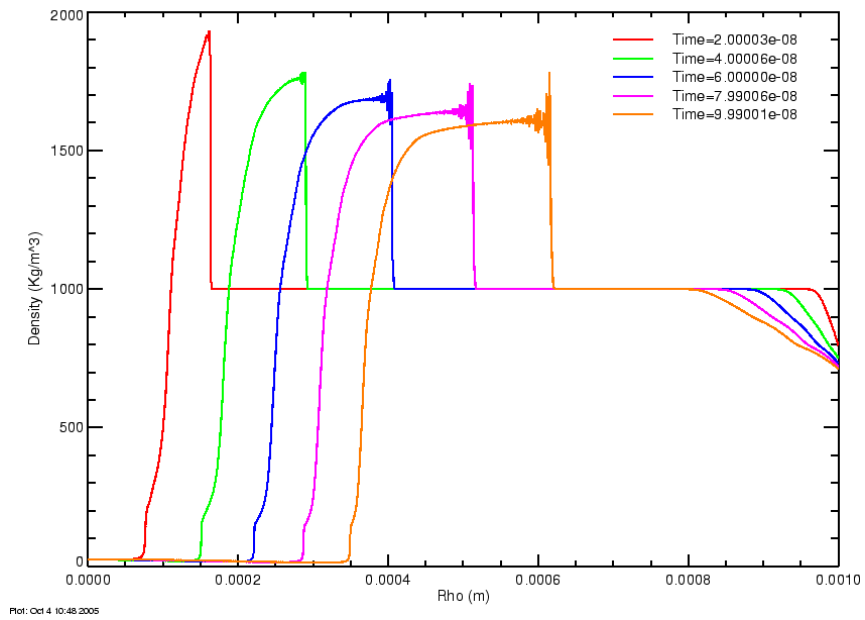
Figure C-31. Late time density profiles for slow ramp current, 10 μm initial radius
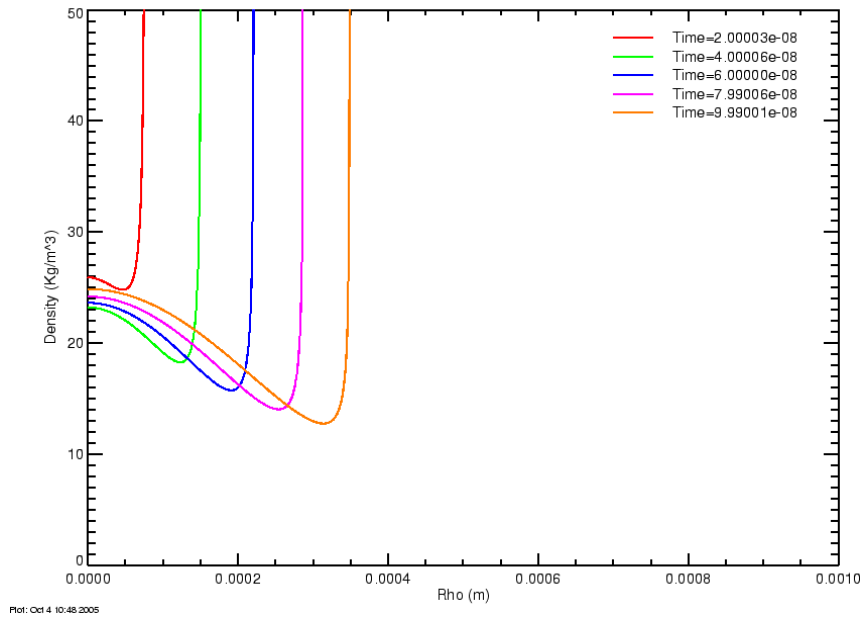
Figure C-32. Detail of late time density profiles for slow ramp current, 10 μm initial radius
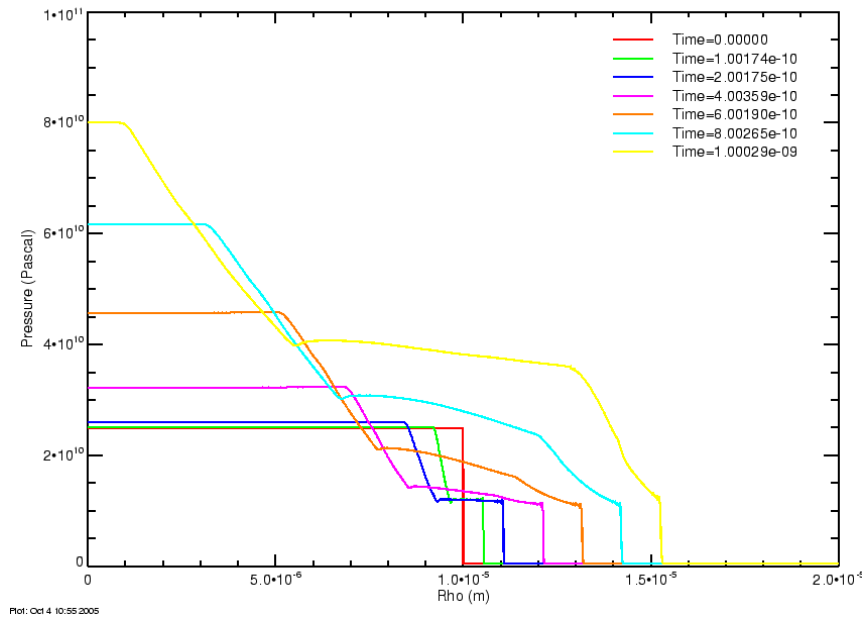
Figure C-33. Early time pressure profiles for slow ramp current, 10 μm initial radius
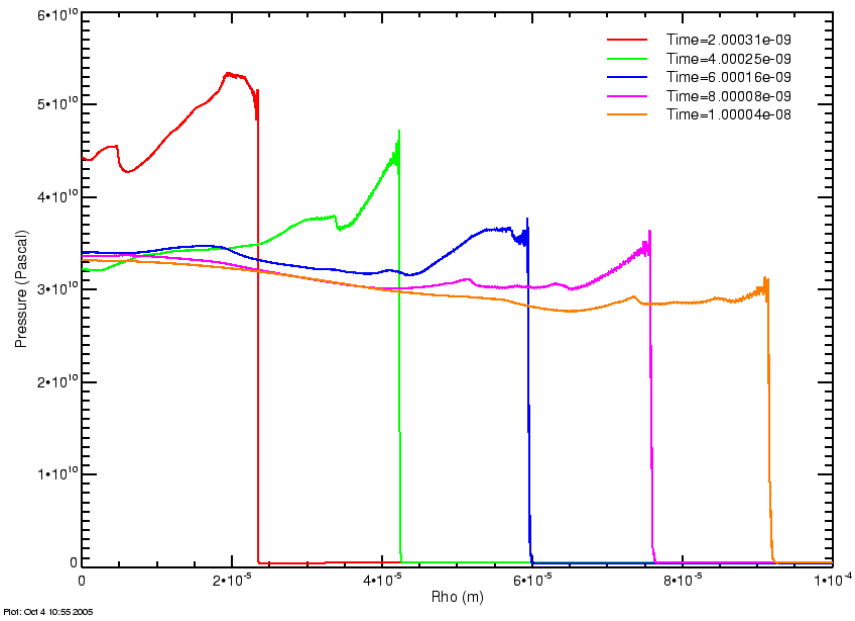
Figure C-34. Intermediate time pressure profiles for slow ramp current, 10 μm initial radius
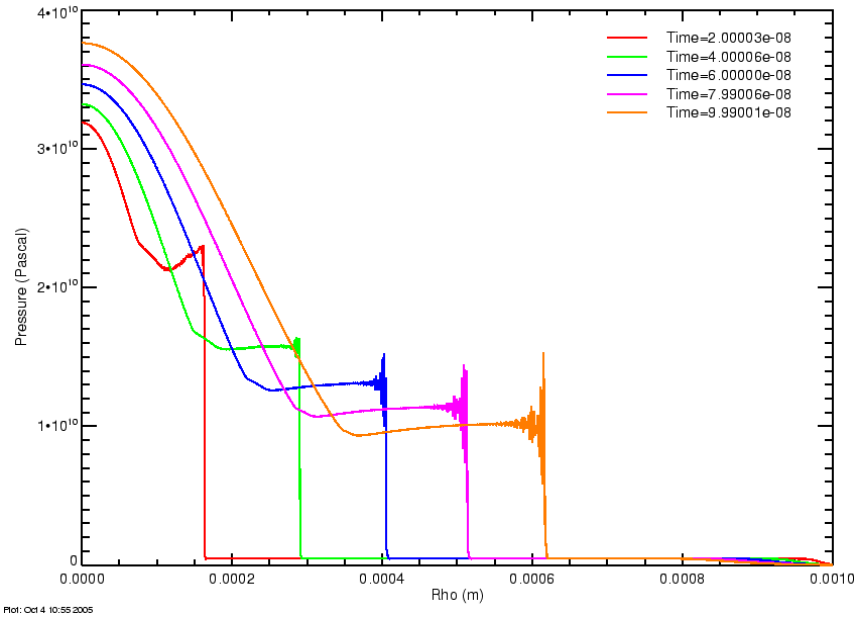
Figure C-35. Late time pressure profiles for slow ramp current, 10 μm initial radius
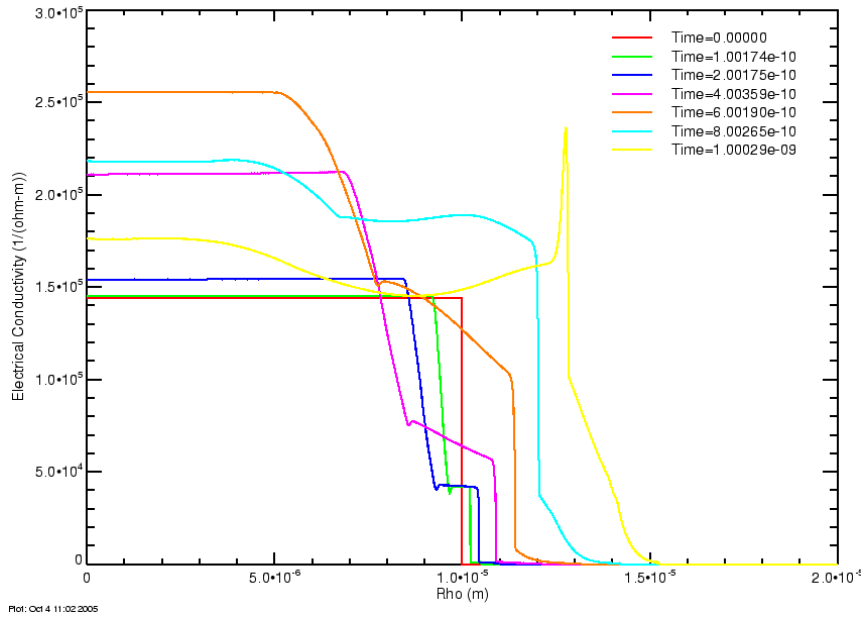
Figure C-36. Early time electrical conductivity profiles for slow ramp current, 10 μm initial radius
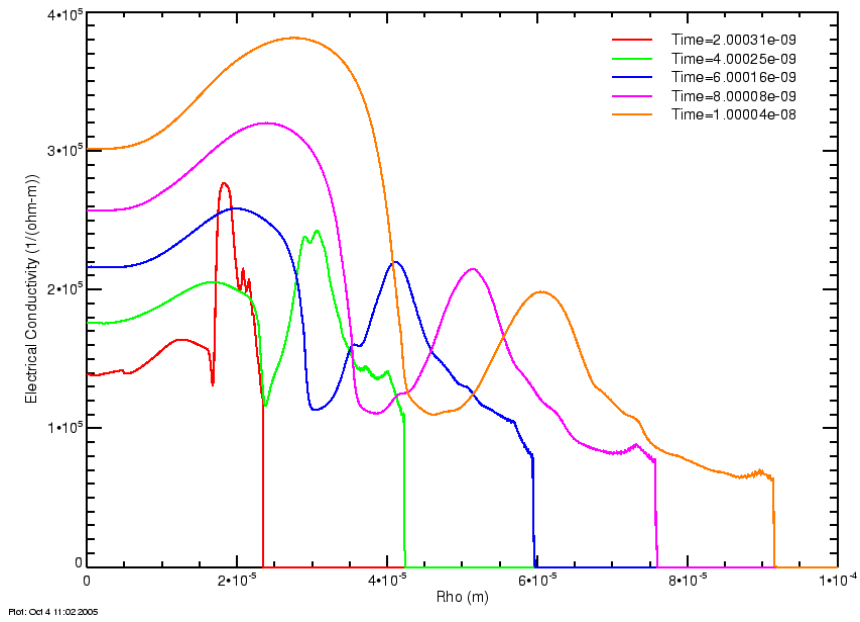
Figure C-37. Intermediate time electrical conductivity profiles for slow ramp current, 10 μm initial radius
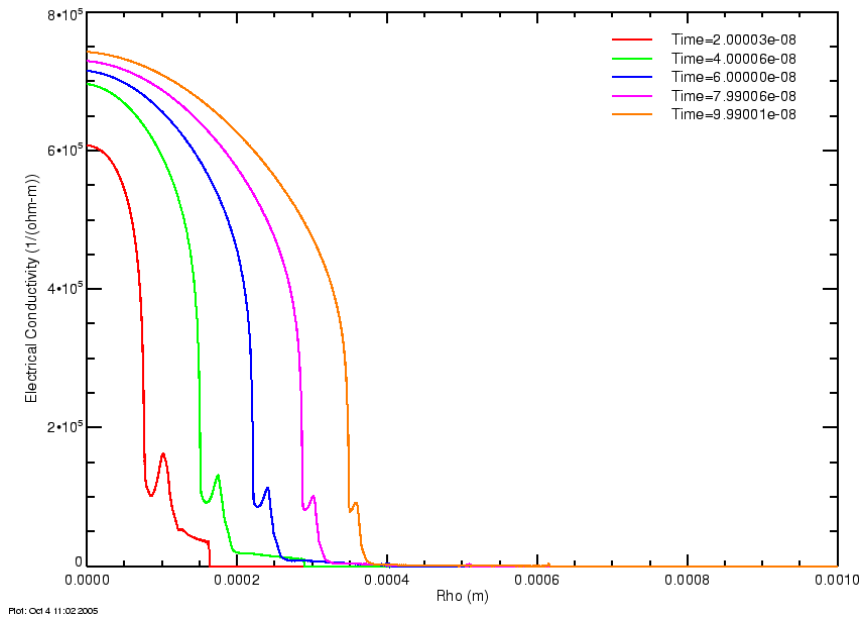
Figure C-38. Late time electrical conductivity profiles for slow ramp current, 10 μm initial radius
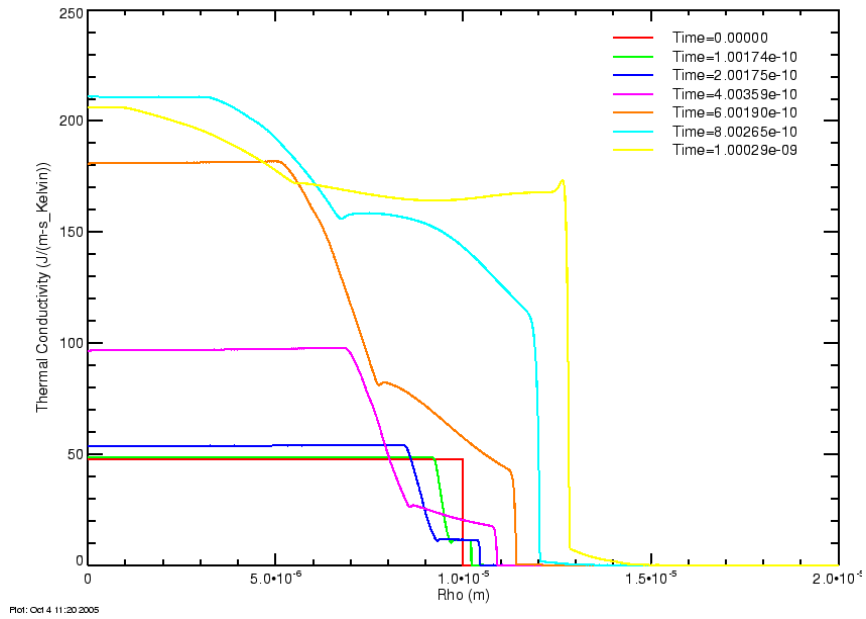
Figure C-39. Early time thermal conductivity profiles for slow ramp current, 10 μm initial radius
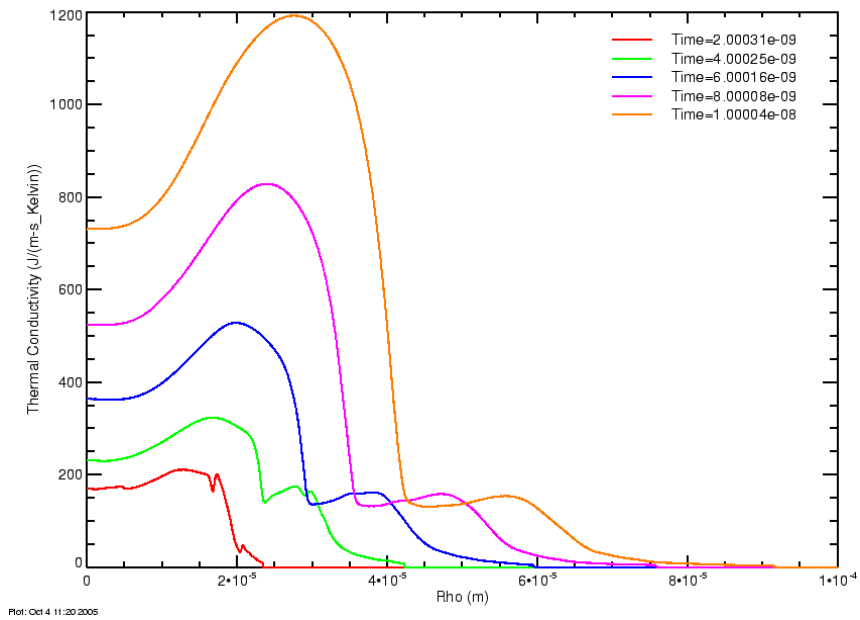
Figure C-40. Intermediate time thermal conductivity profiles for slow ramp current, 10 μm initial radius
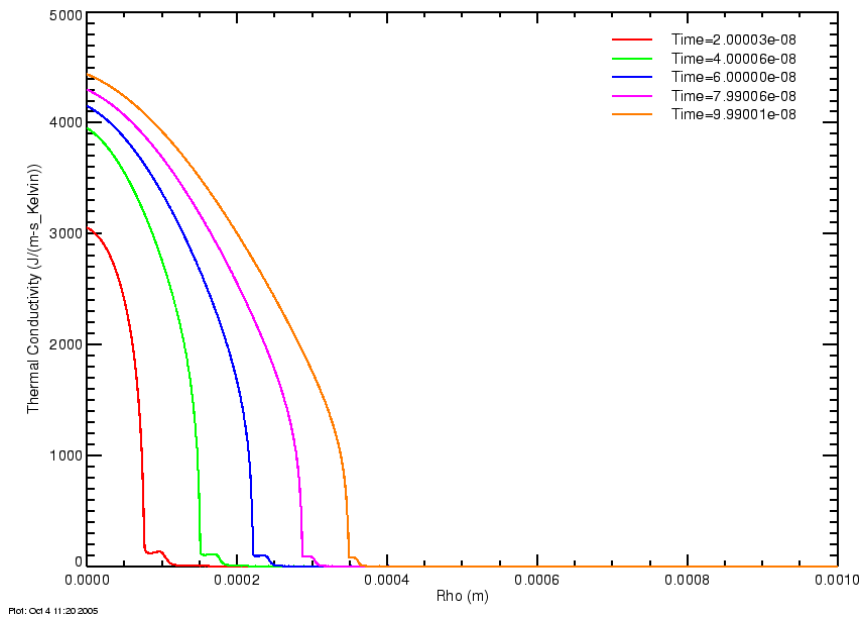
Figure C-41. Late time thermal conductivity profiles for slow ramp current, 10 μm initial radius
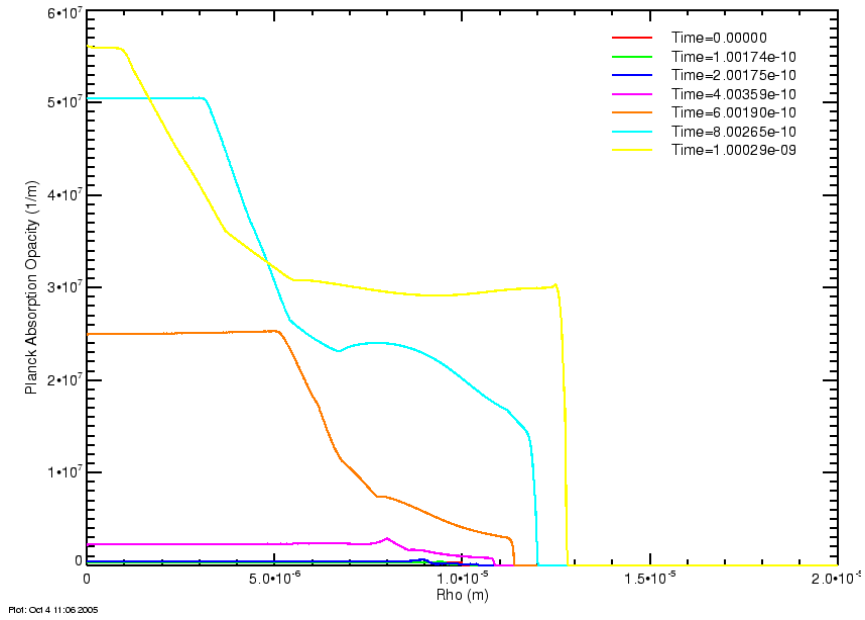
Figure C-42. Early time average opacity profiles for slow ramp current, 10 μm initial radius
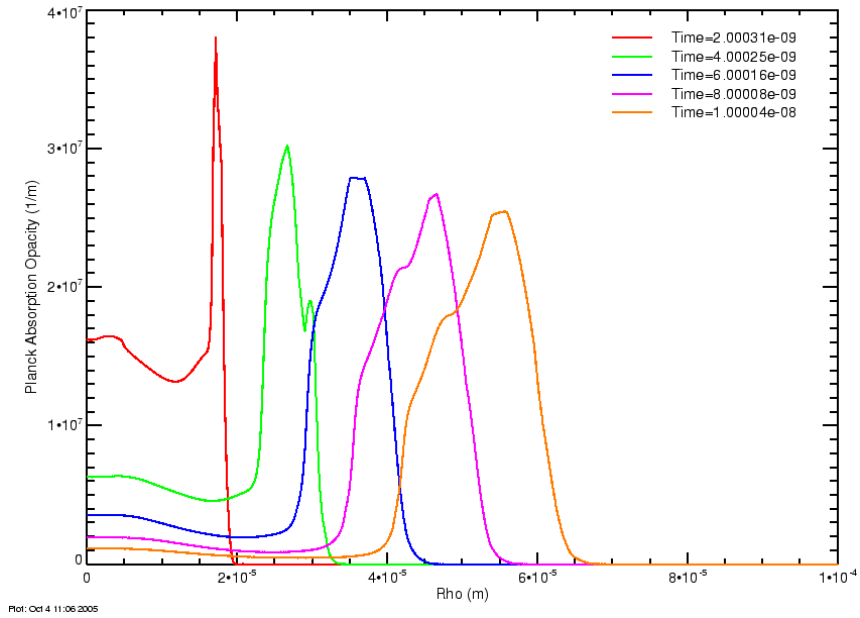
Figure C-43. Intermediate time average opacity profiles for slow ramp current, 10 μm initial radius
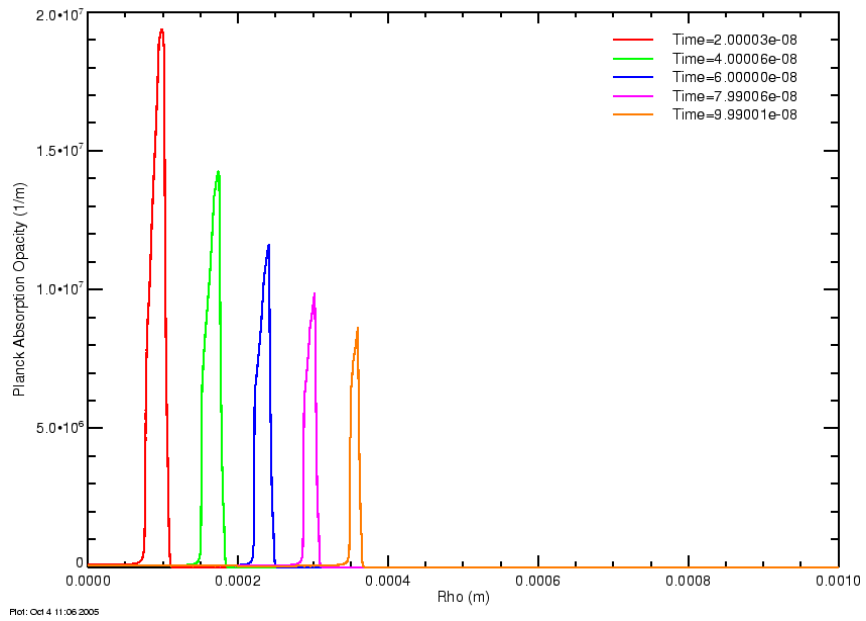
Figure C-44. Late time average opacity profiles for slow ramp current, 10 μm initial radius
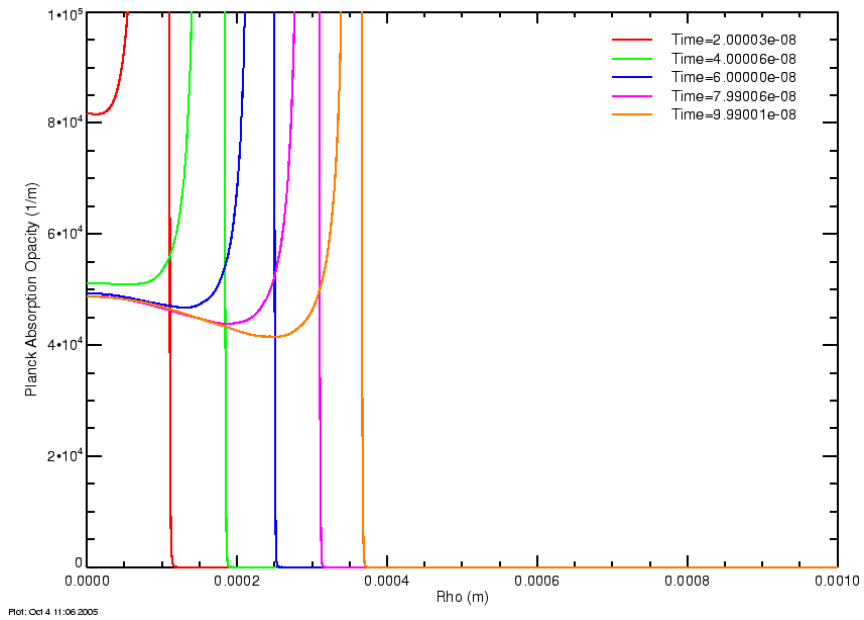
Figure C-45. Detail of late time average opacity profiles for slow ramp current, 10 μm initial radius
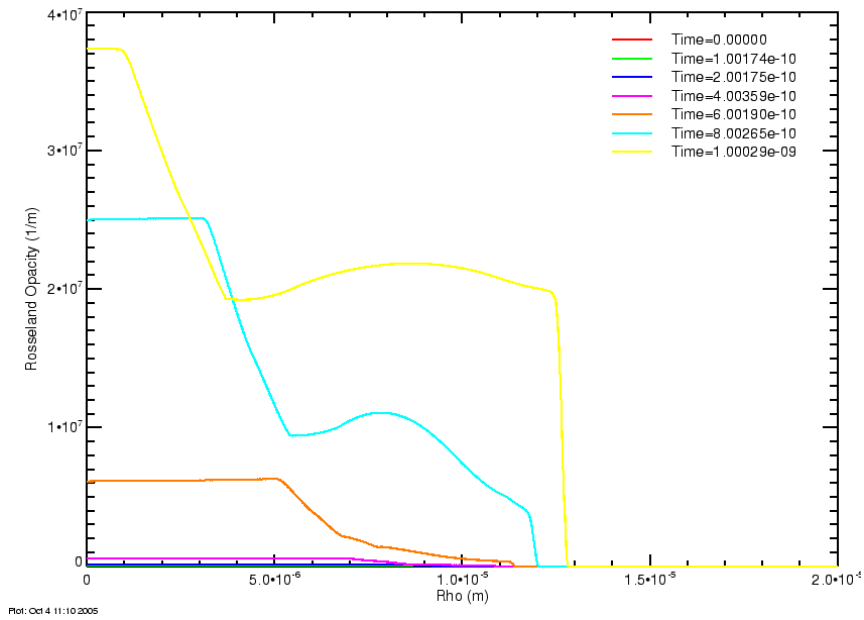
Figure C-46. Early time Rosseland opacity profiles for slow ramp current, 10 μm initial radius

184
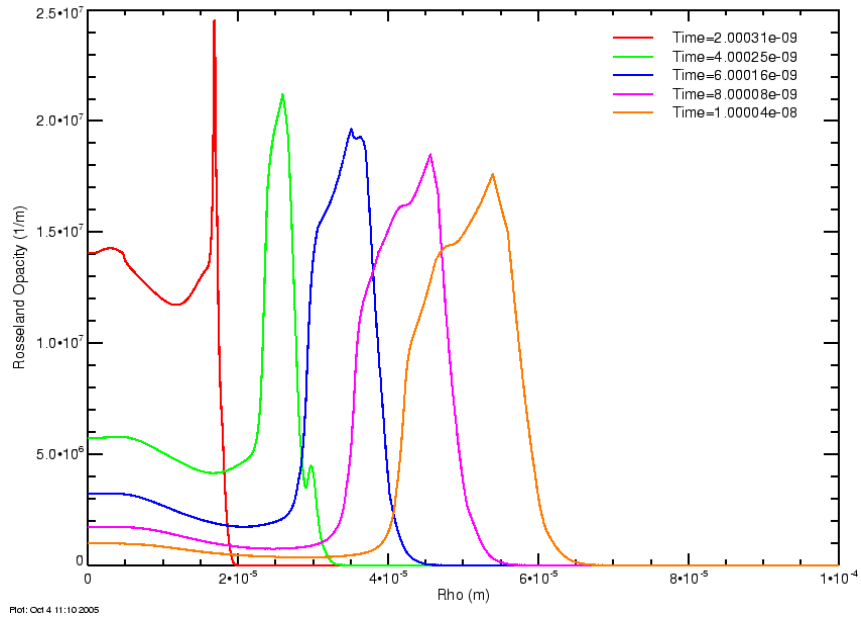
Figure C-47. Intermediate time Rosseland opacity profiles for slow ramp current, 10 μm initial radius
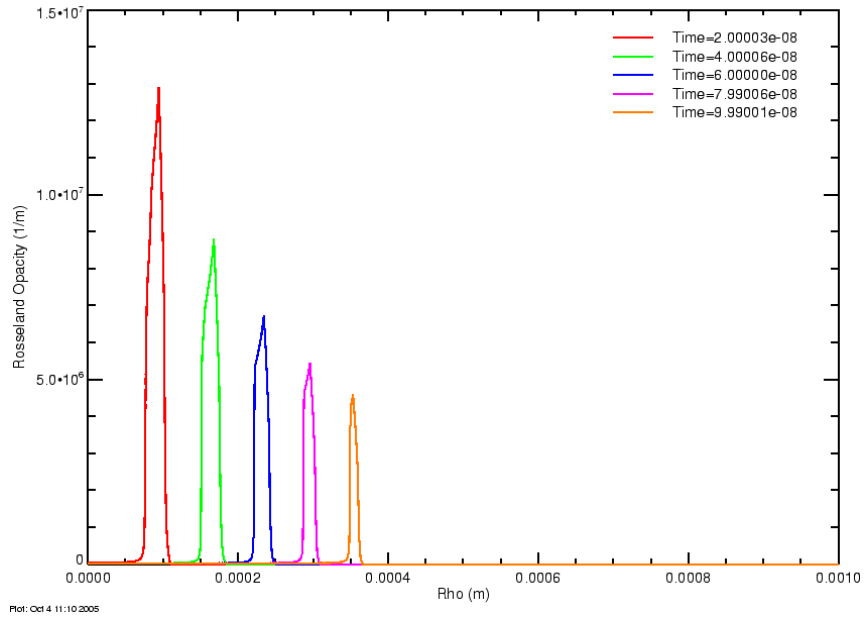
Figure C-48. Late time Rosseland opacity profiles for slow ramp current, 10 μm initial radius
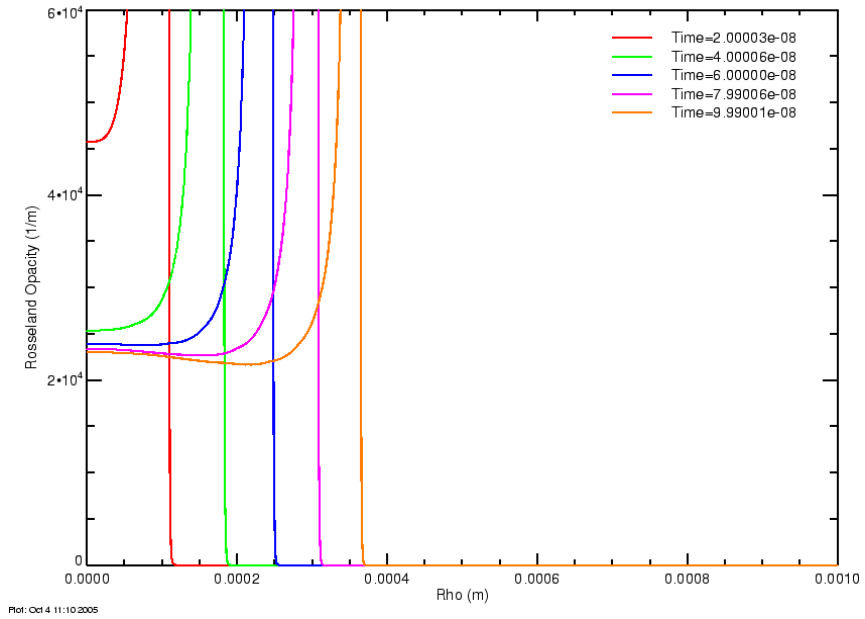
Figure C-49. Detail of late time Rosseland opacity profiles for slow ramp current, 10 μm initial radius
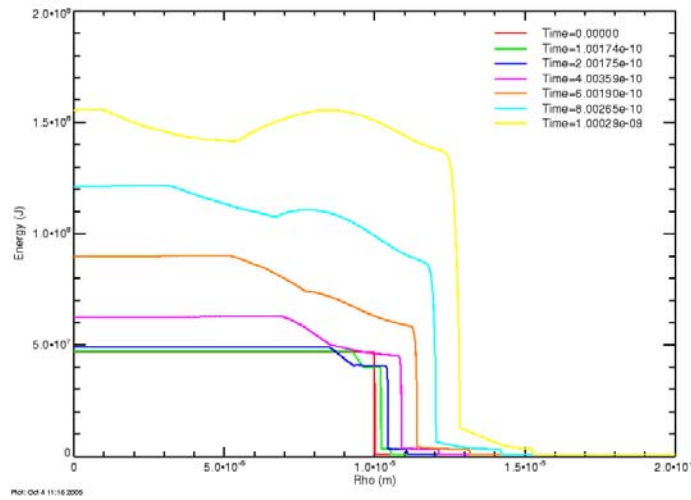
Figure C-50. Early time internal energy profiles for slow ramp current, 10 μm initial radius
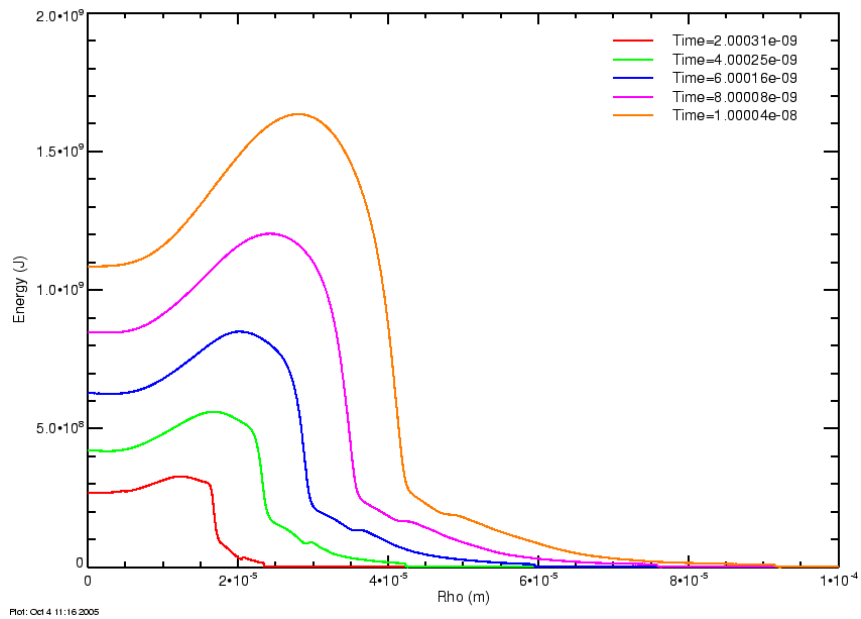
Figure C-51. Intermediate time energy profiles for slow ramp current, 10 μm initial radius
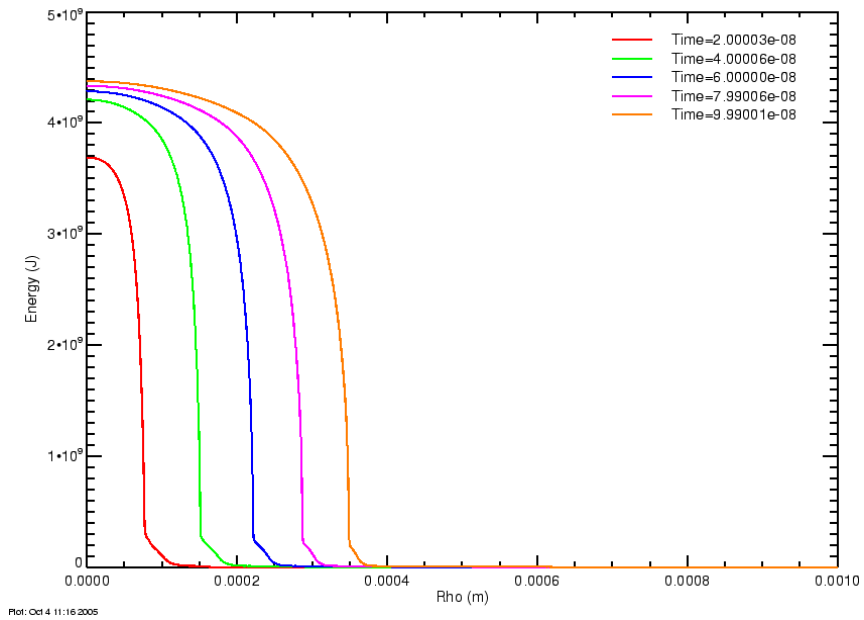
Figure C-52. Late time internal energy profiles for slow ramp current, 10 μm initial radius
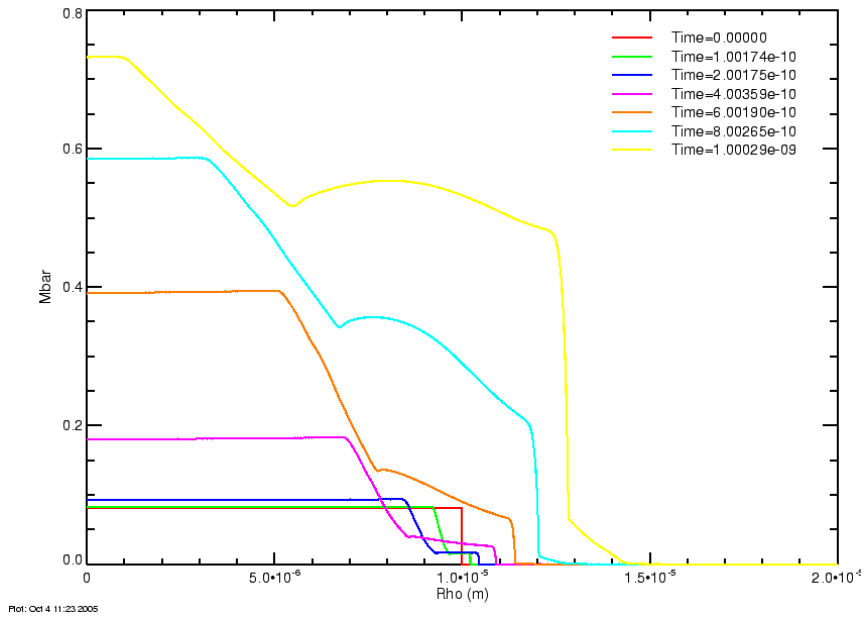
Figure C-53. Early time ionization number profiles for slow ramp current, 10 μm initial radius

188
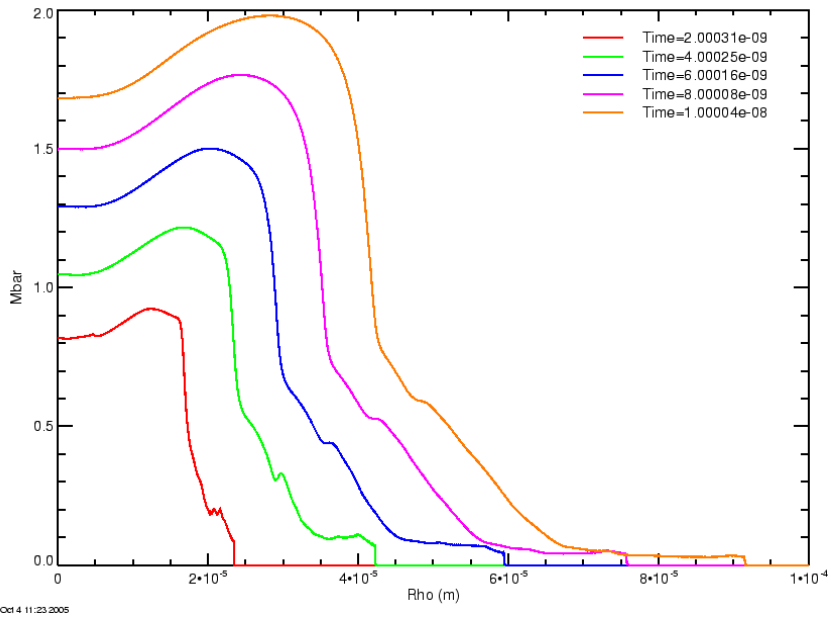
Figure C-54. Intermediate time ionization number profiles for slow ramp current, 10 μm initial radius
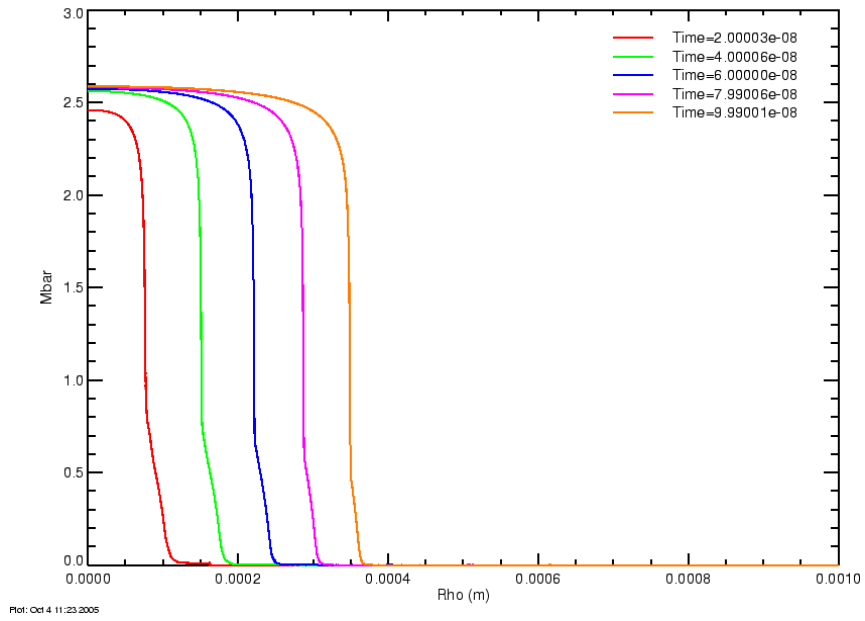
Figure C-55. Late time ionization number profiles for slow ramp current, 10 μm initial radius

C.3 Fast Rise Current Drive

The fourth set has radiation turned on. The current drive is a linear ramp rising to $I_0 = 300$ kA with a risetime of 15 ns. After the current attains the peak it remains at 300 kA until the end of the simulation. The channel initial conditions are radius of 1 μm, temperature of 1 eV and density of 1000 kg/m^3.
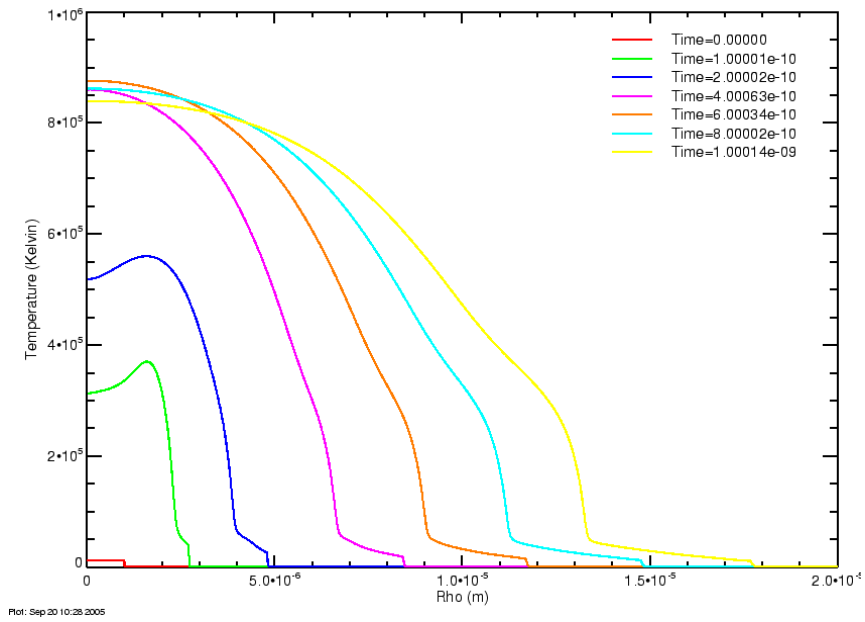
Figure C-56. Early time temperature profiles for 15 ns risetime, 300 kA current
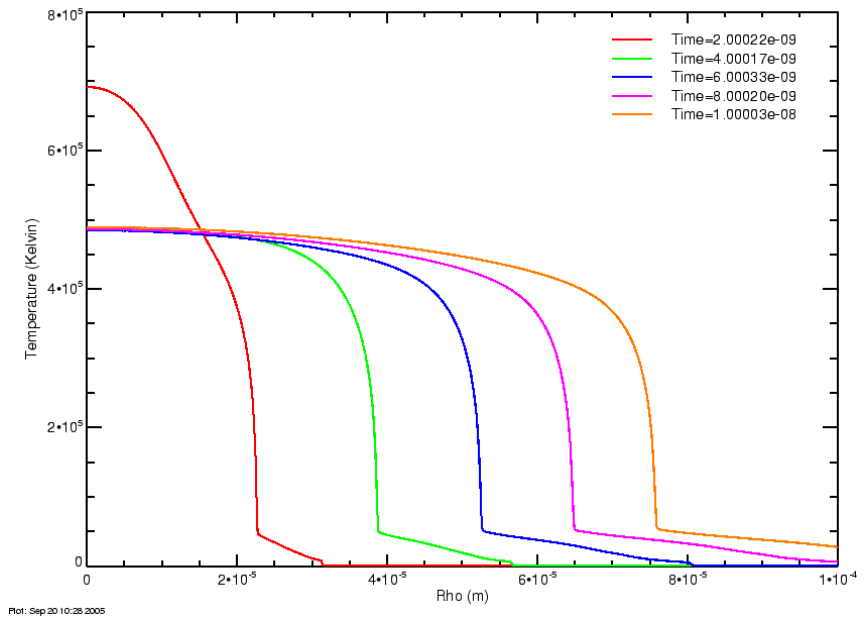
Figure C-57. Intermediate time temperature profiles for 15 ns risetime, 300 kA current
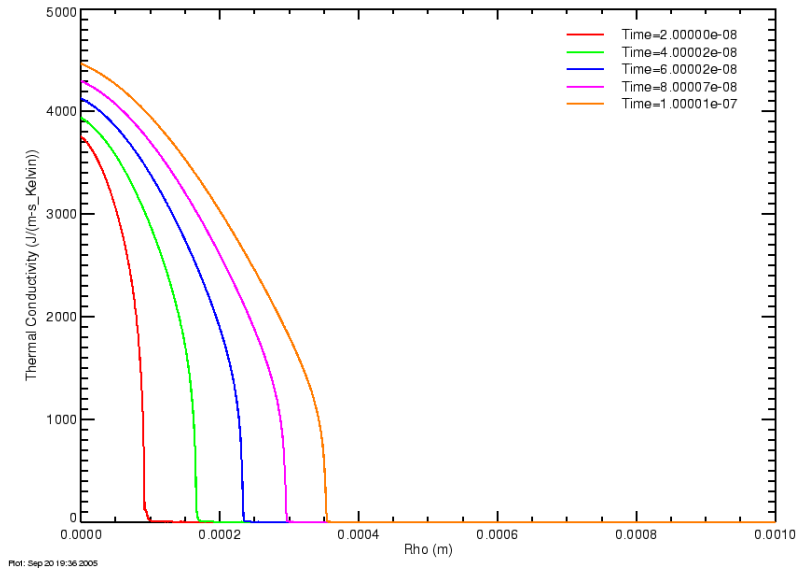
Figure 28. Late time thermal conductivities for slow current drive.
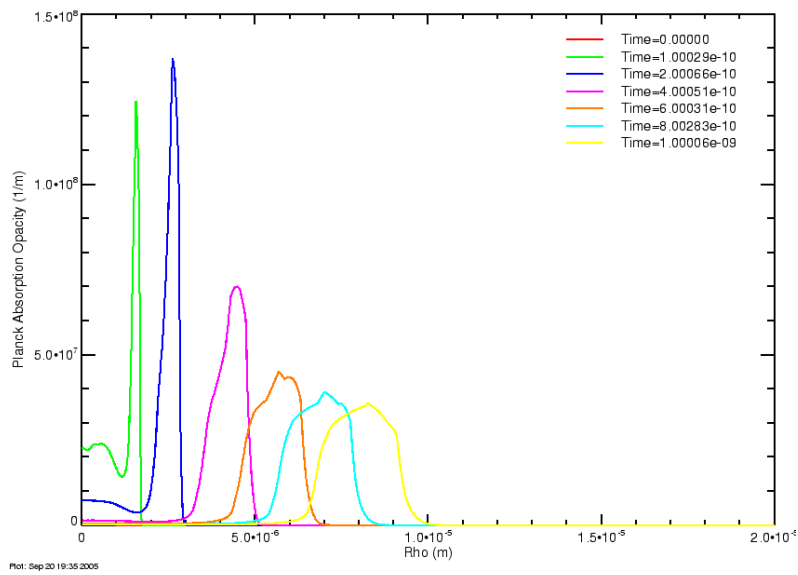
Figure 29. Early time average opacities for slow current drive.
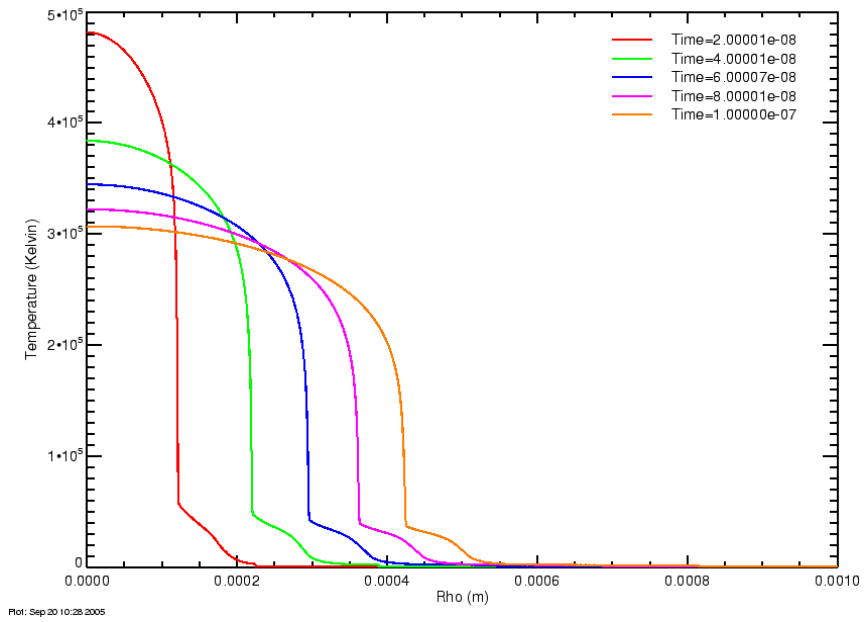
Figure C-58. Late time temperature profiles for 15 ns risetime, 300 kA current
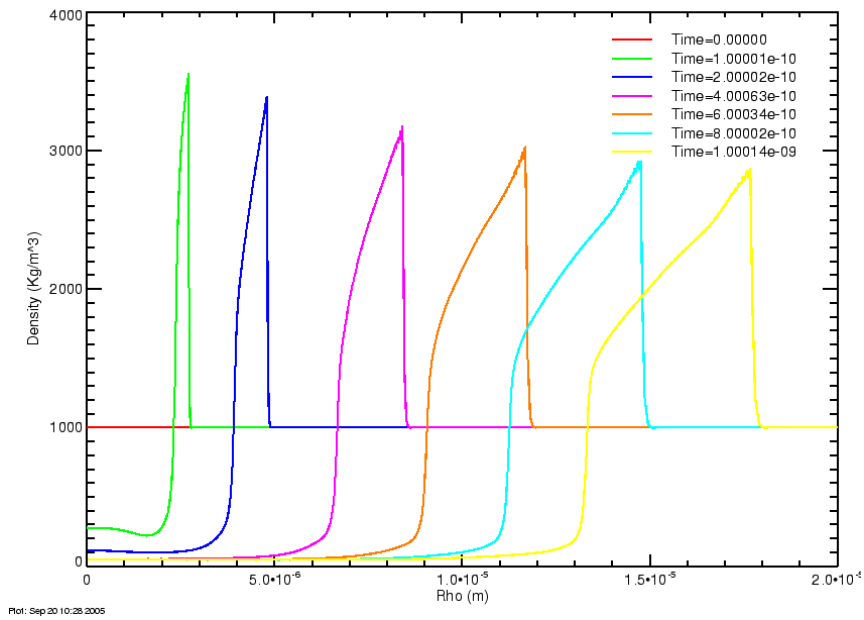
Figure C-59. Early time density profiles for 15 ns risetime, 300 kA current

192
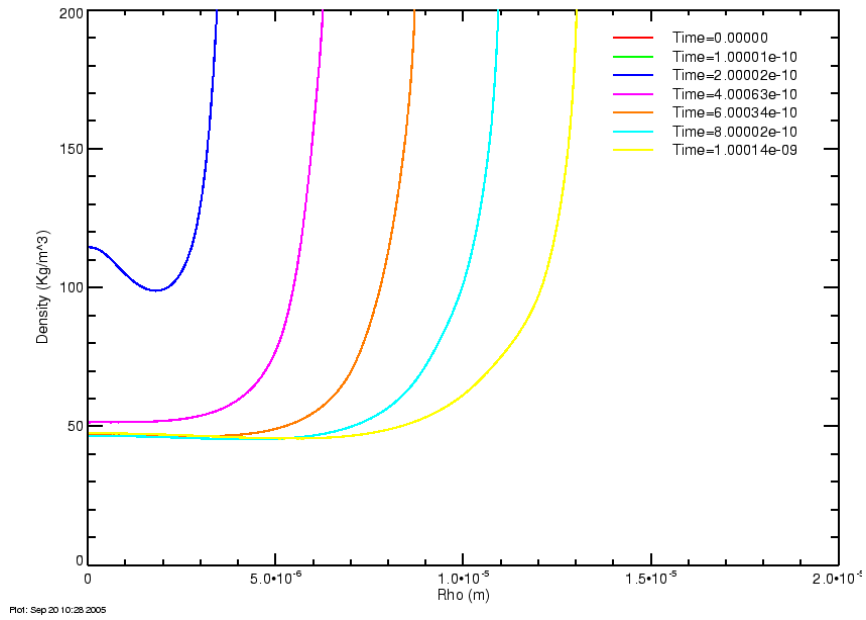
Figure C-60. Detail of early time density profiles for 15 ns risetime, 300 kA current
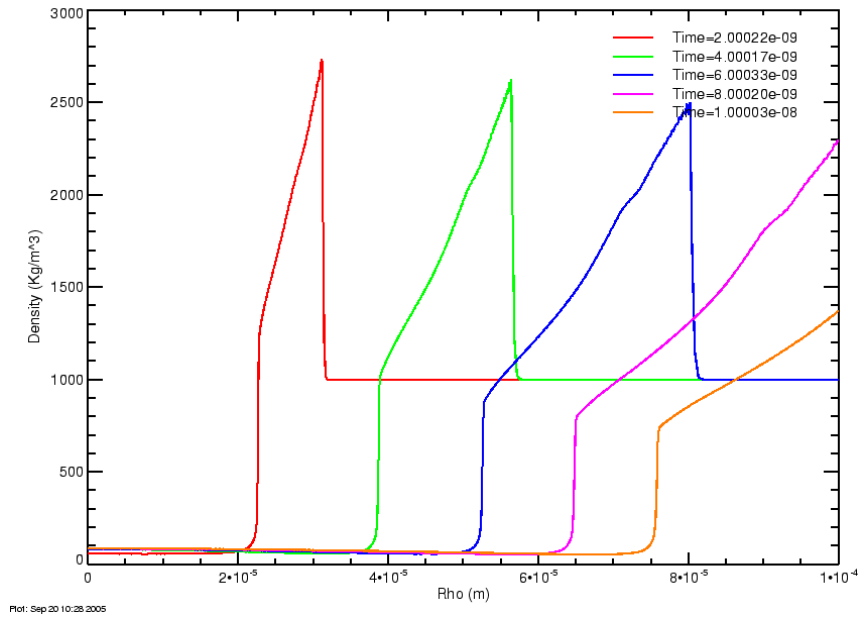
Figure C-61. Intermediate time density profiles for 15 ns risetime, 300 kA current
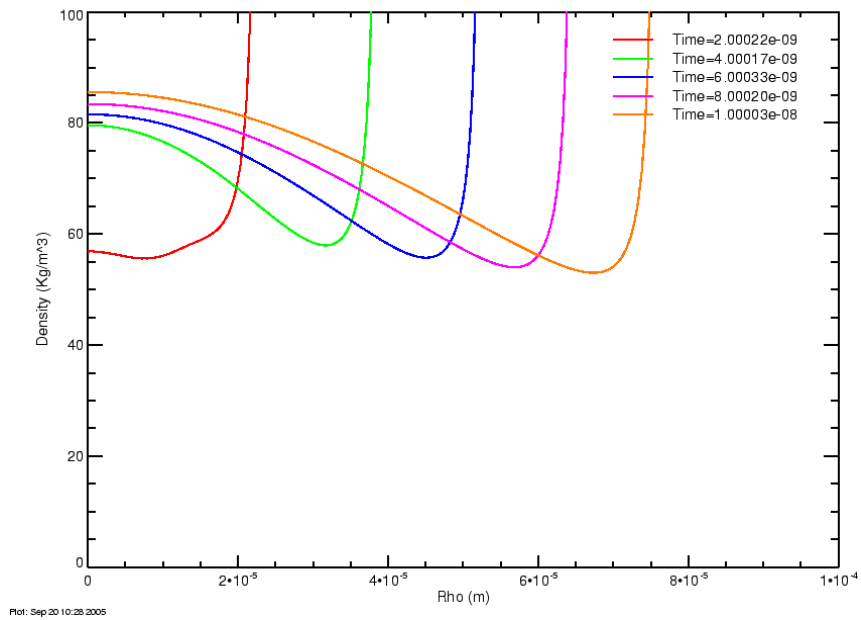
Figure C-62. Detail of intermediate time density profiles for 15 ns risetime, 300 kA current
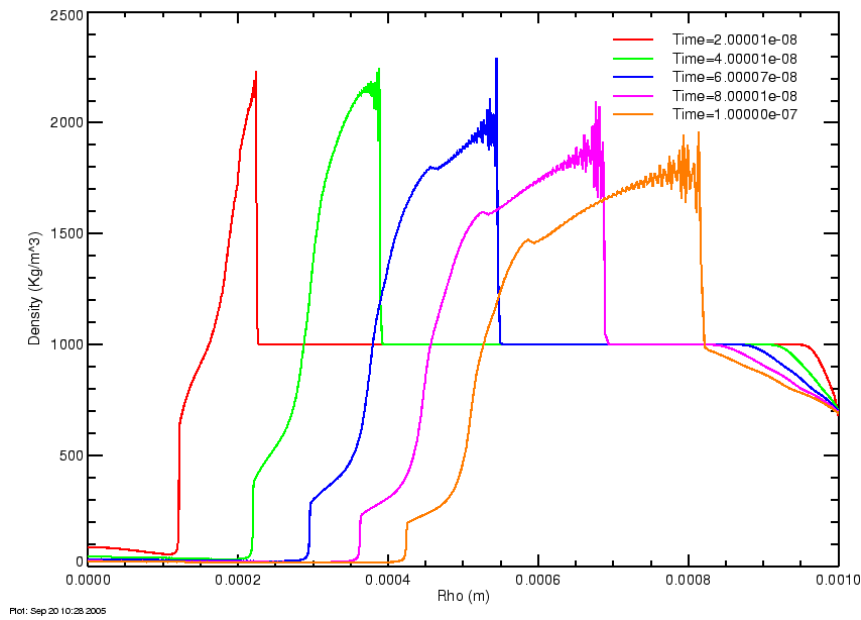
Figure C-63. Late time density profiles for 15 ns risetime, 300 kA current

194
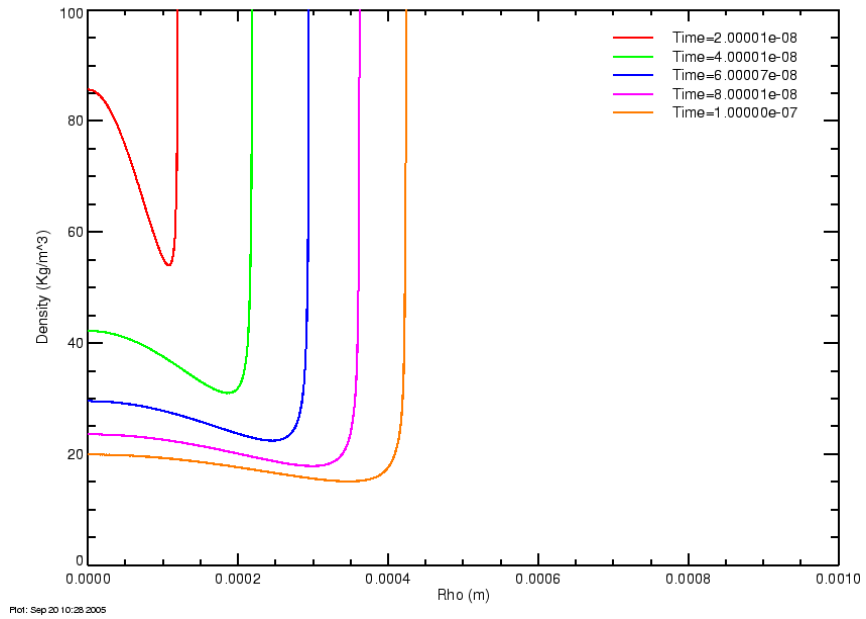
Figure C-64. Detail of late time density profiles for 15 ns risetime, 300 kA current
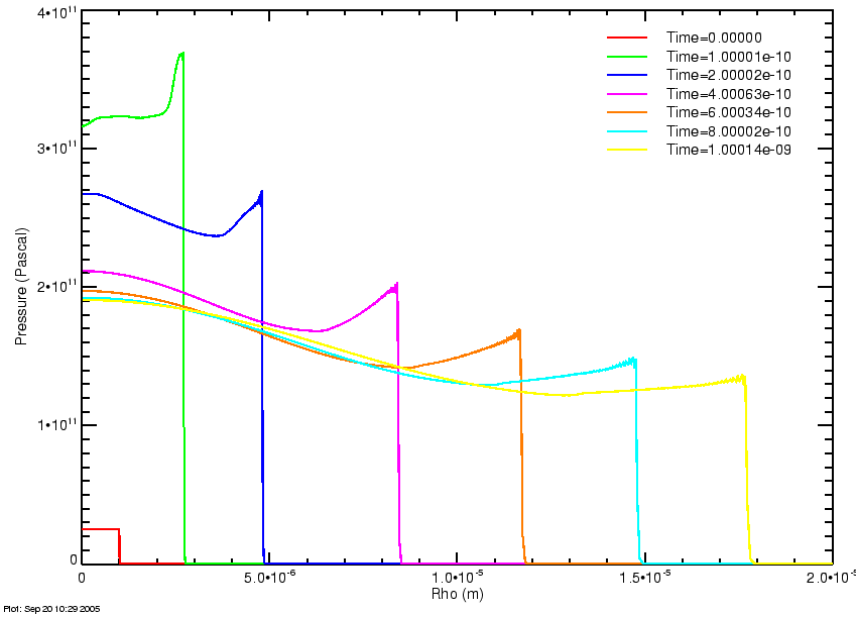
Figure C-65. Early time pressure profiles for 15 ns risetime, 300 kA current
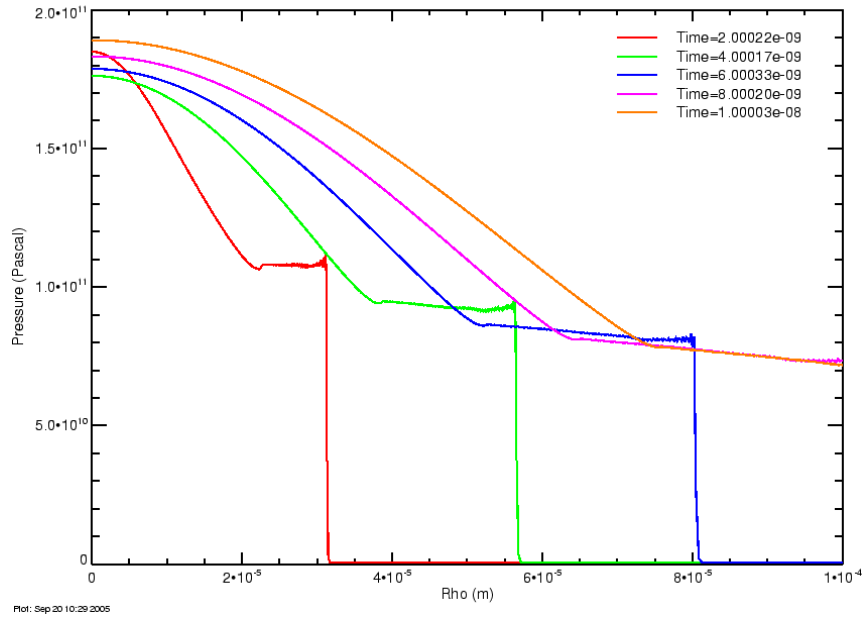
Figure C-66. Intermediate time pressure profiles for 15 ns risetime, 300 kA current
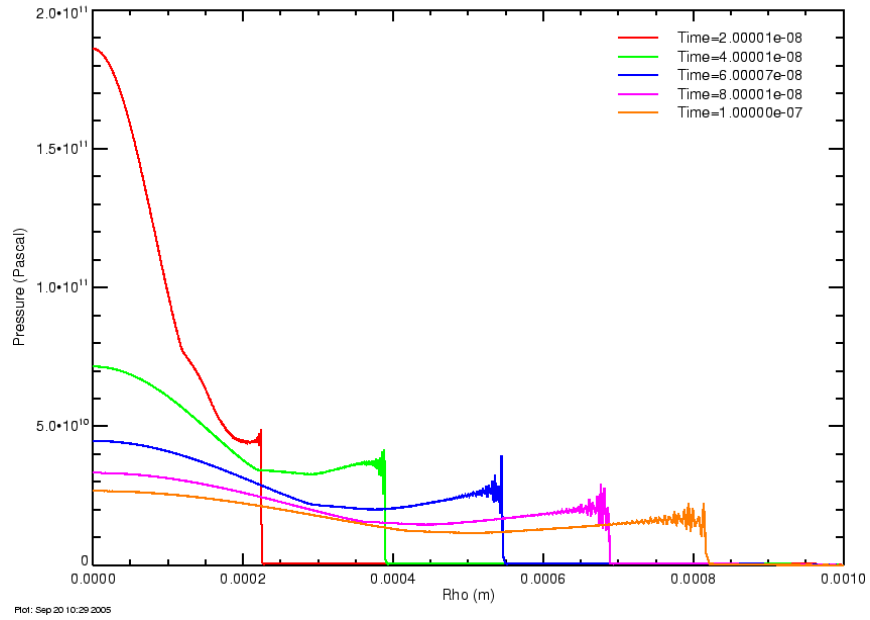
Figure C-67. Late time pressure profiles for 15 ns risetime, 300 kA current
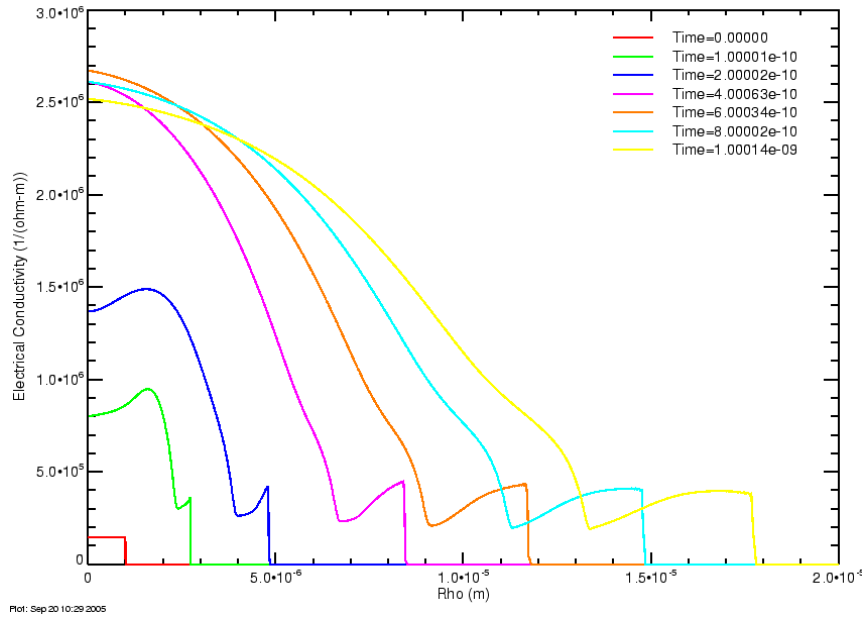
Figure C-68. Early time electrical conductivity profiles for 15 ns risetime, 300 kA current
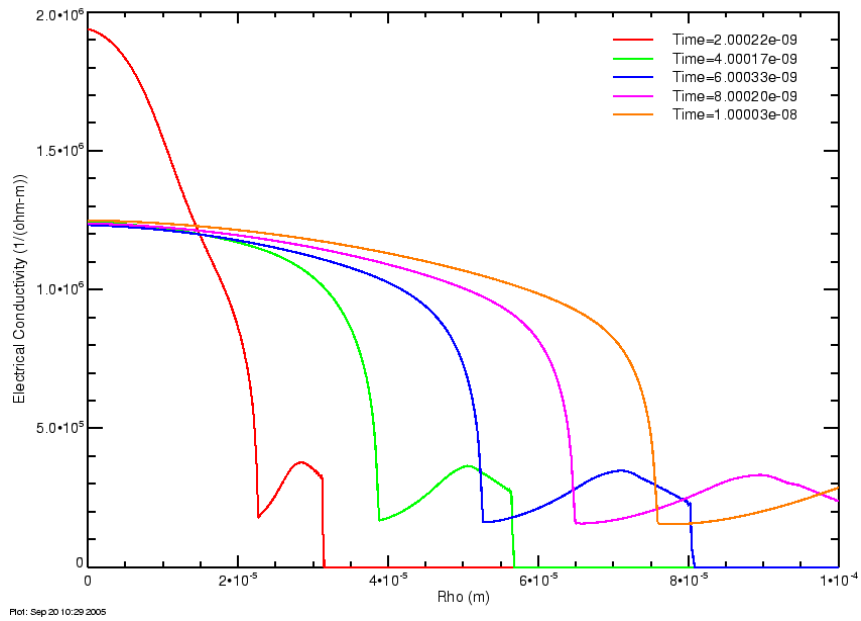
Figure C-69. Intermediate time electrical conductivity profiles for 15 ns risetime, 300 kA current
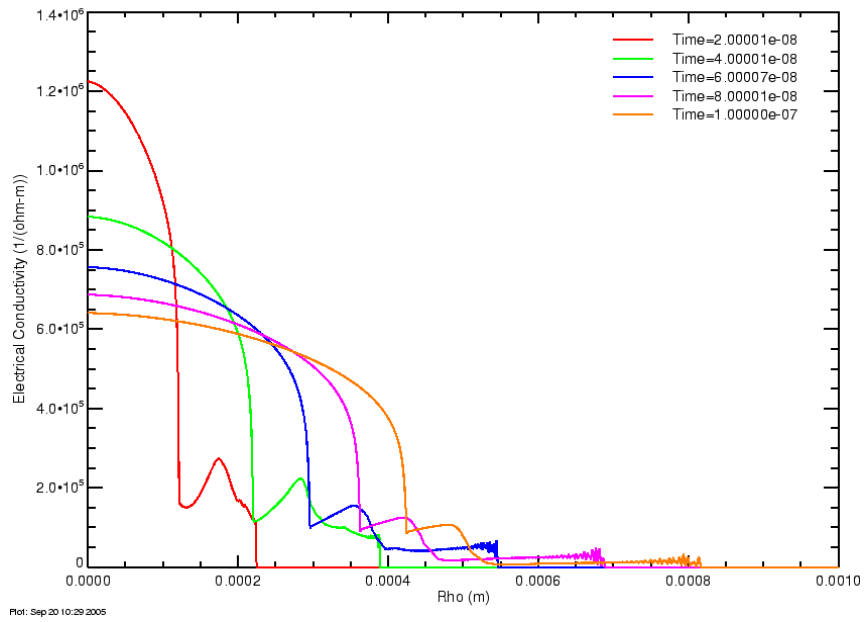
Figure C-70. Late time electrical conductivity profiles for 15 ns risetime, 300 kA current
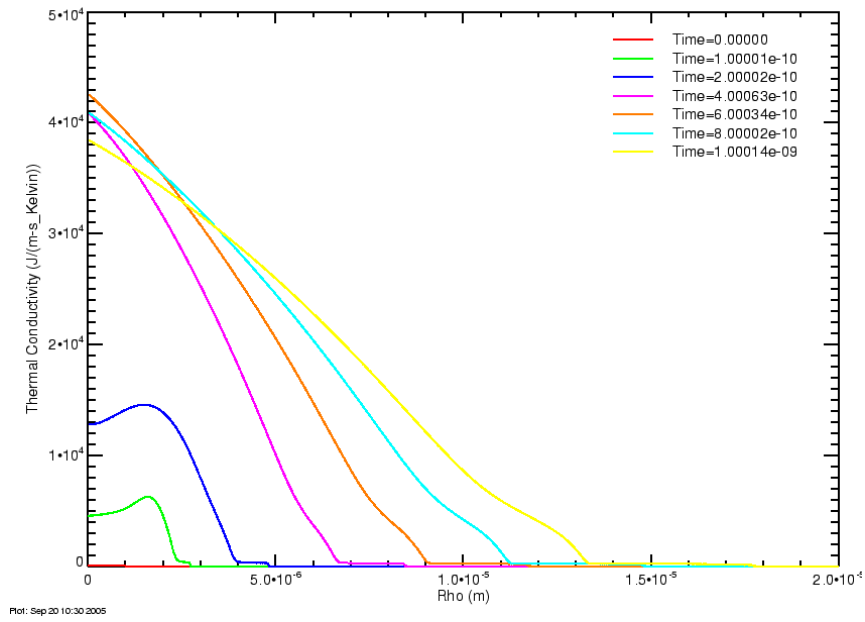
Figure C-71. Early time thermal conductivity profiles for 15 ns risetime, 300 kA current
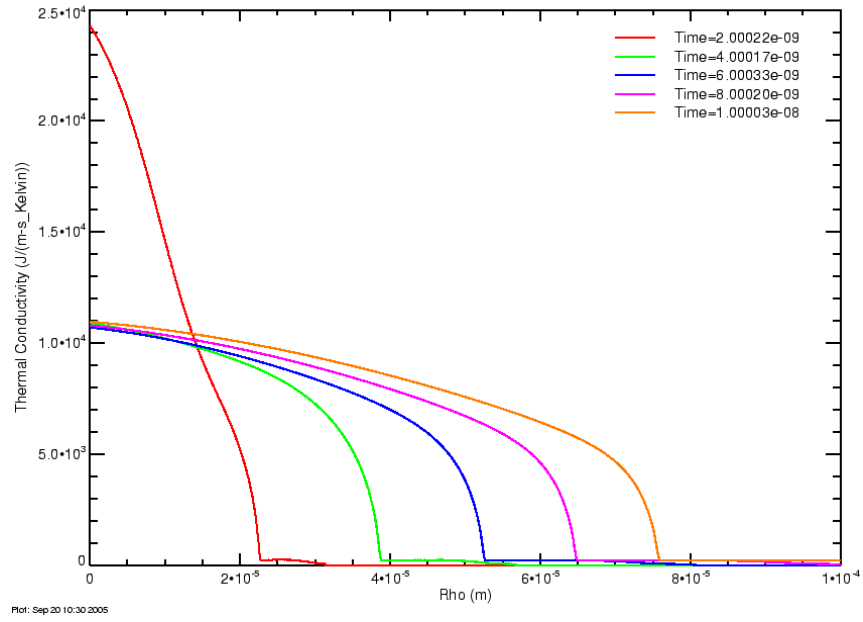
Figure C-72. Intermediate time thermal conductivity profiles for 15 ns risetime, 300 kA current
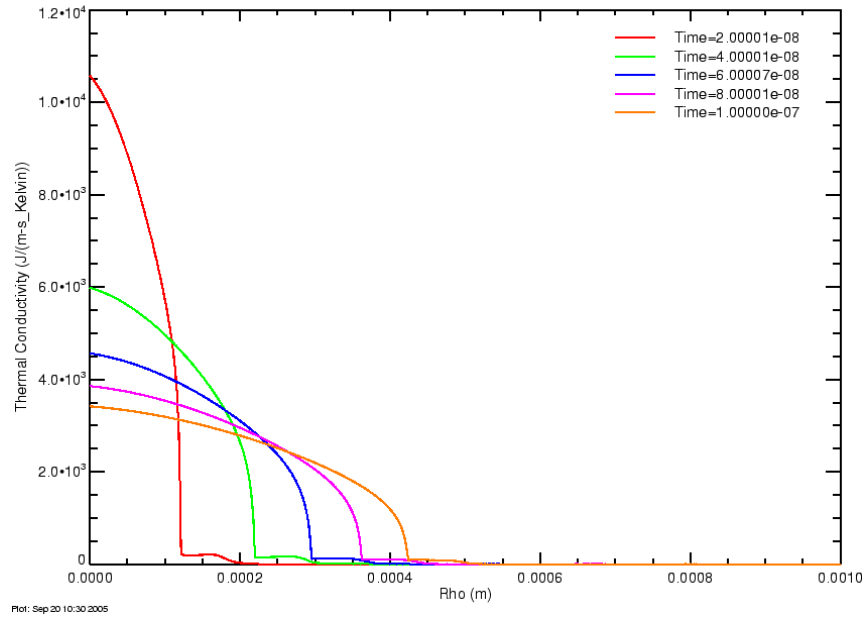
Figure C-73. Late time thermal conductivity profiles for 15 ns risetime, 300 kA current
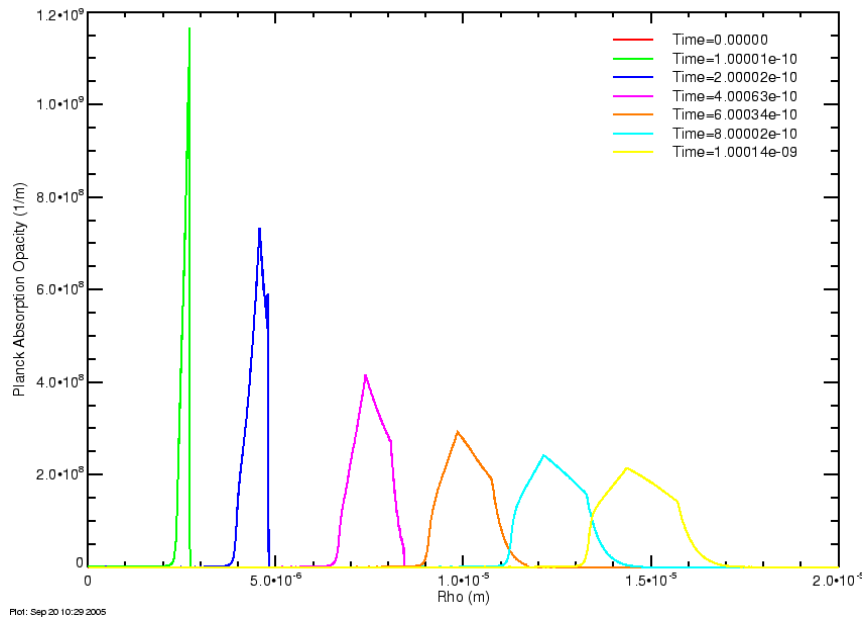
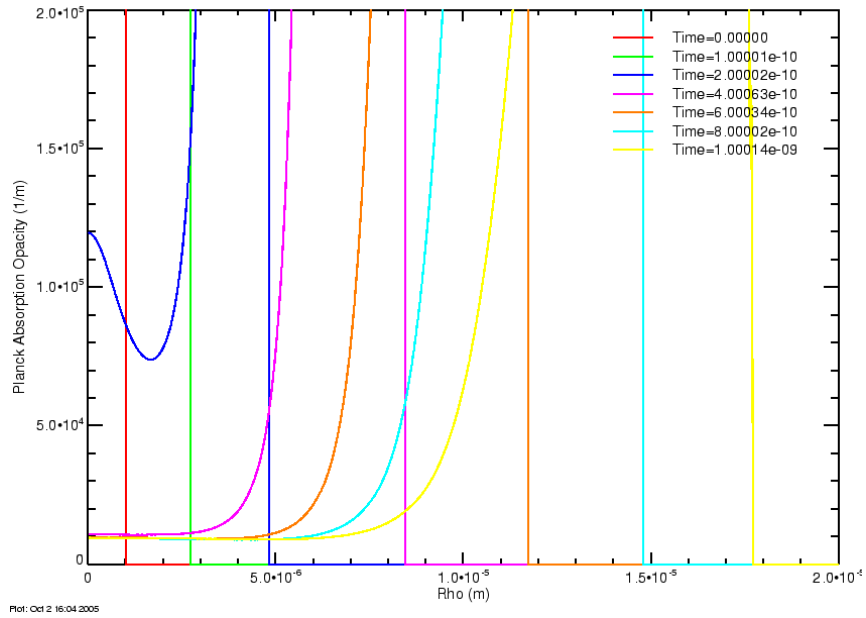Figure C-74. Early time average opacity profiles for 15 ns risetime, 300 kA current
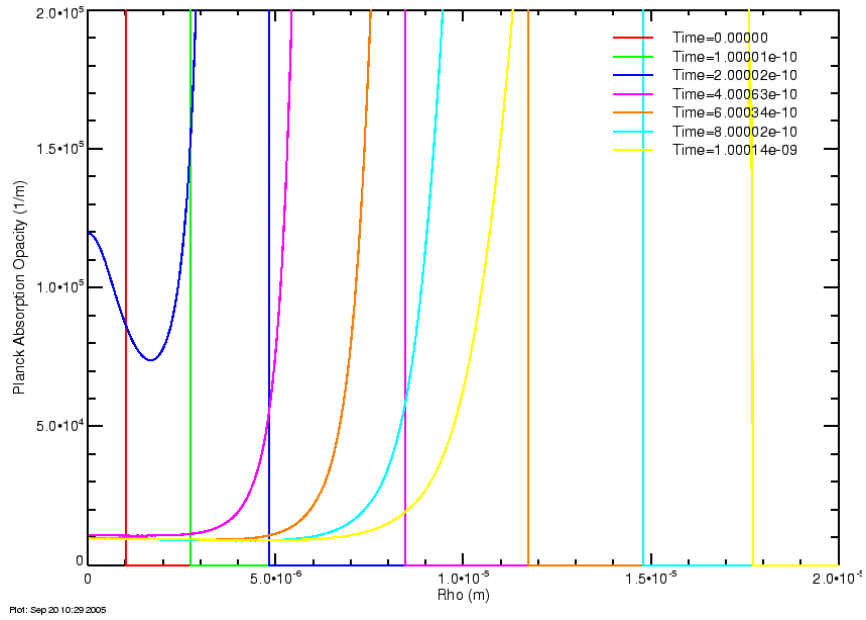
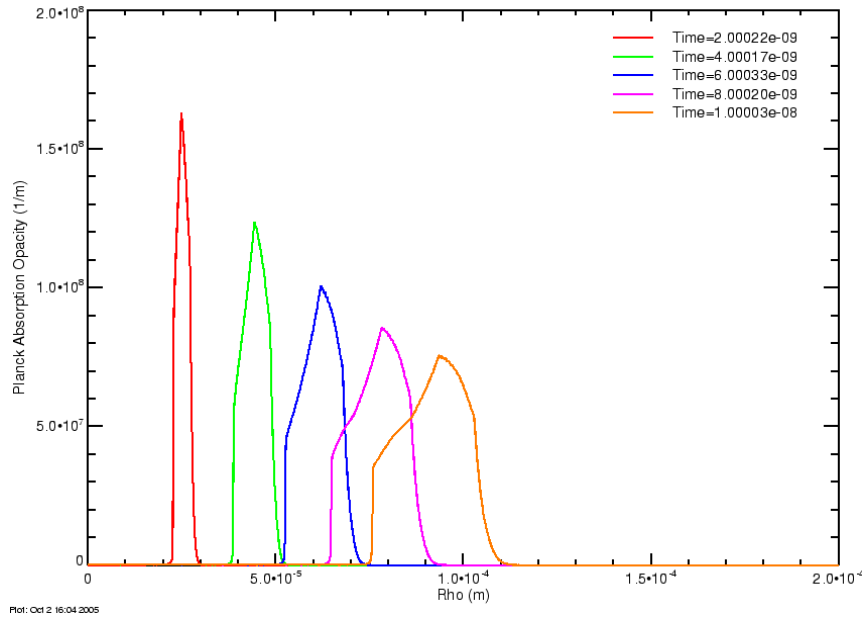Figure C-75. Detail of early time average opacity profiles for 15 ns risetime, 300 kA current
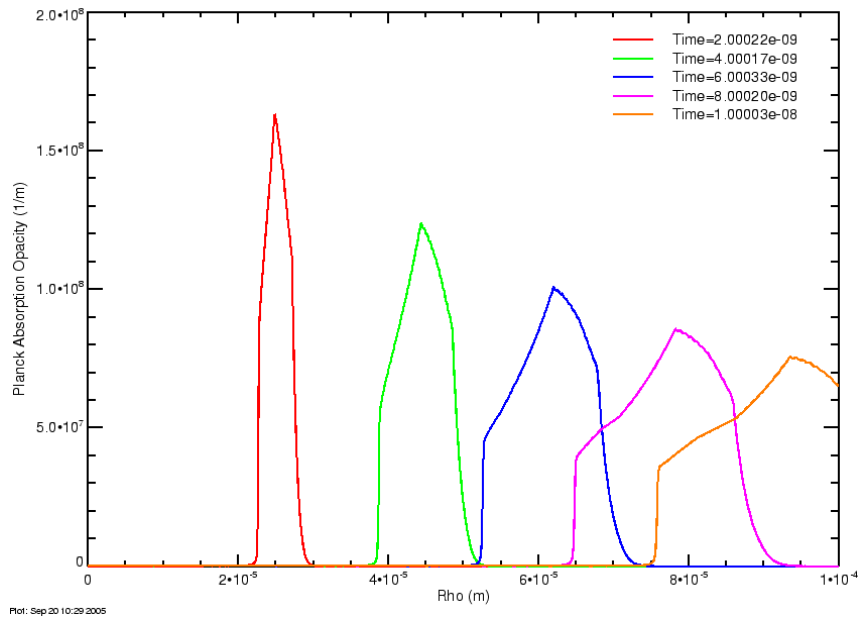
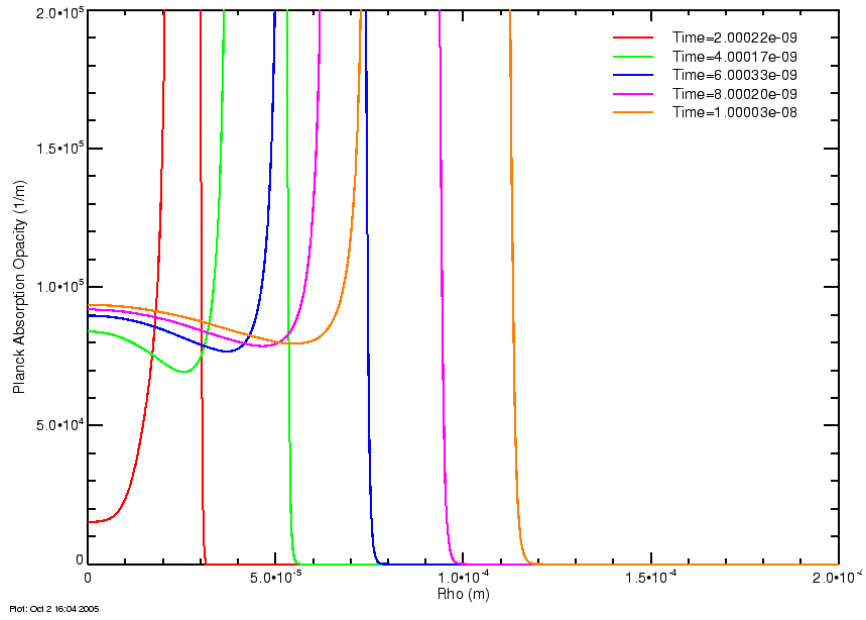Figure C-76. Intermediate time average opacity profiles for 15 ns risetime, 300 kA current
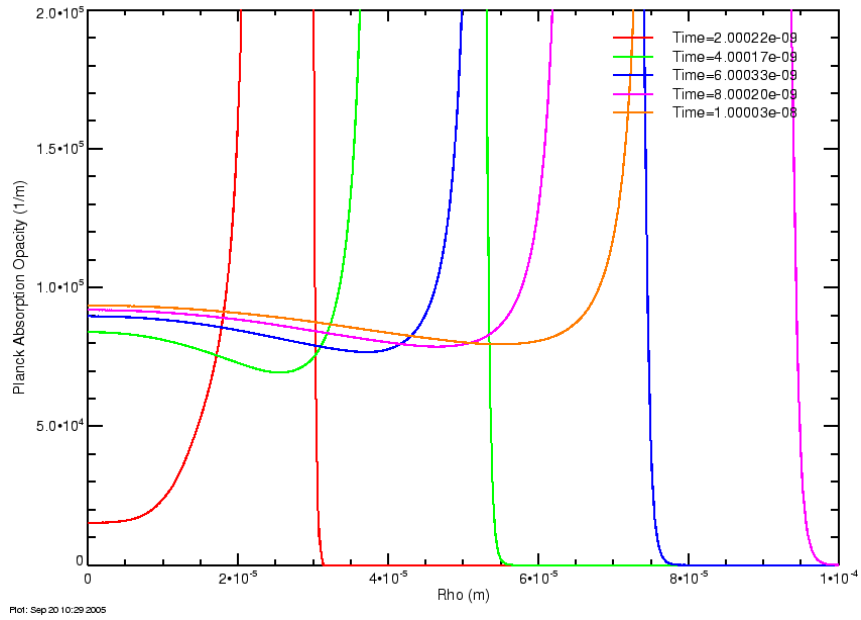
Figure C-77. Detail of intermedicate time average opacity profiles for 15 ns risetime, 300 kA current
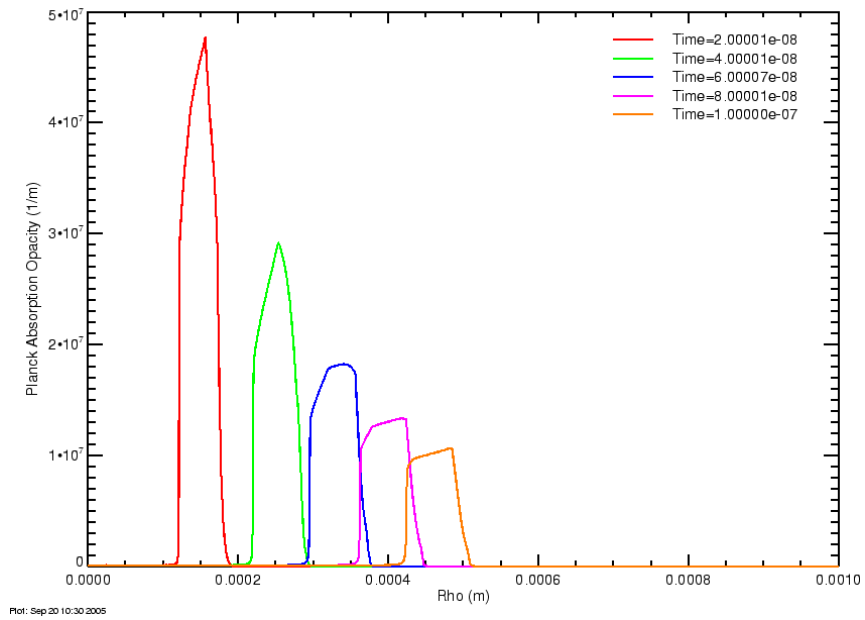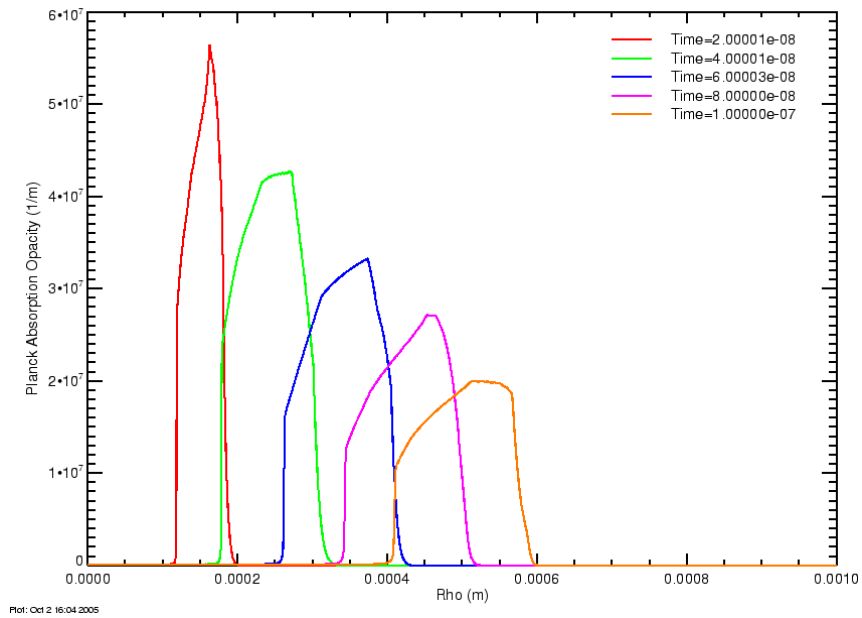

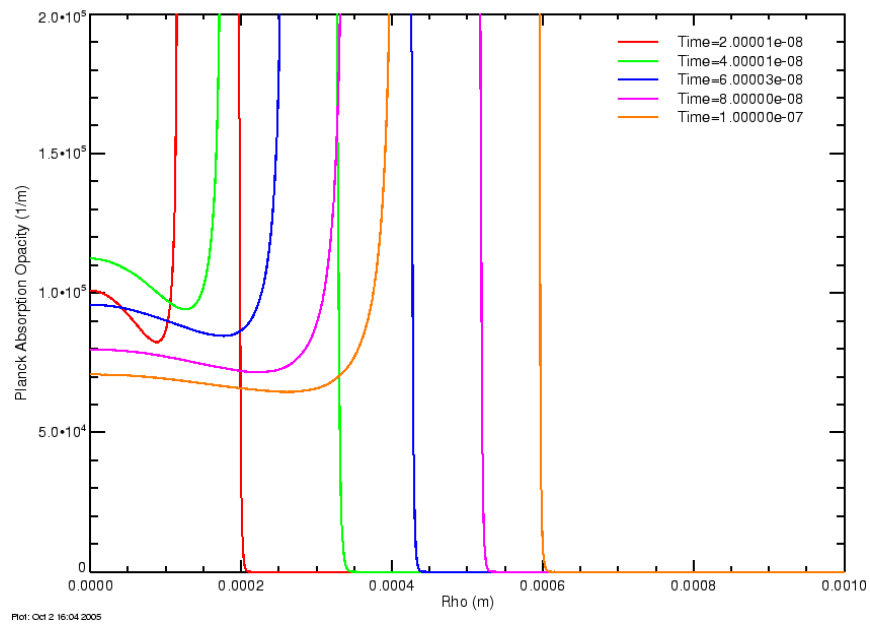Figure C-78. Late time average opacity profiles for 15 ns risetime, 300 kA current
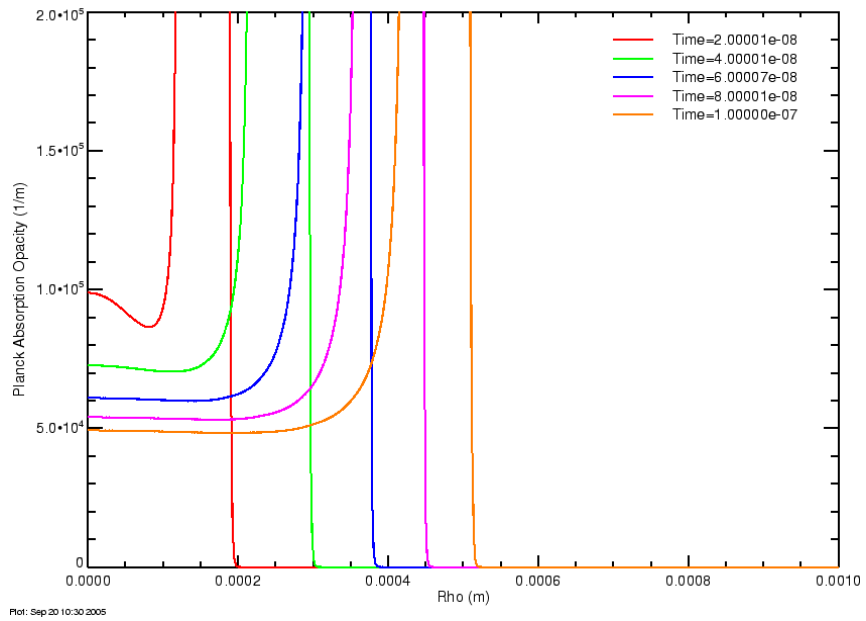
Figure C-79. Detail of late time average opacity profiles for 15 ns risetime, 300 kA current
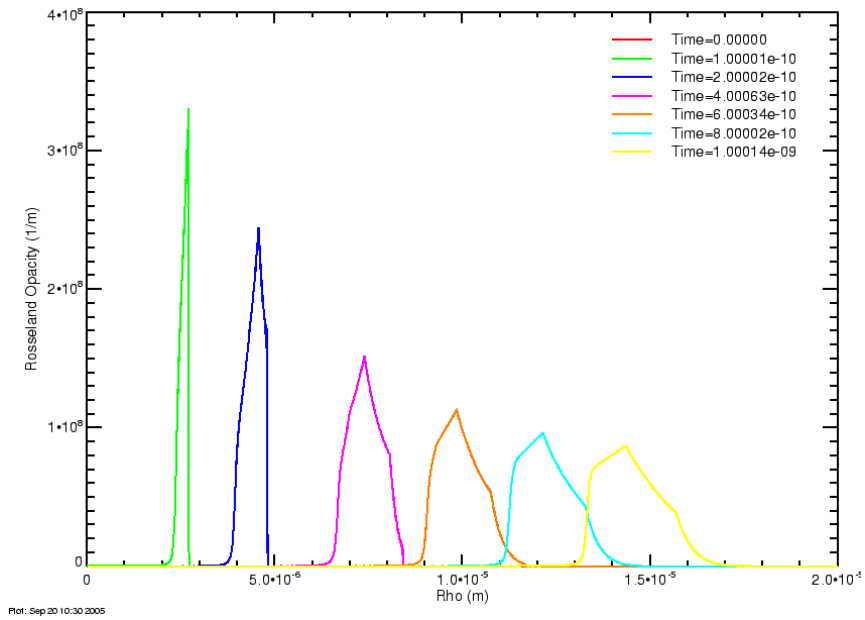
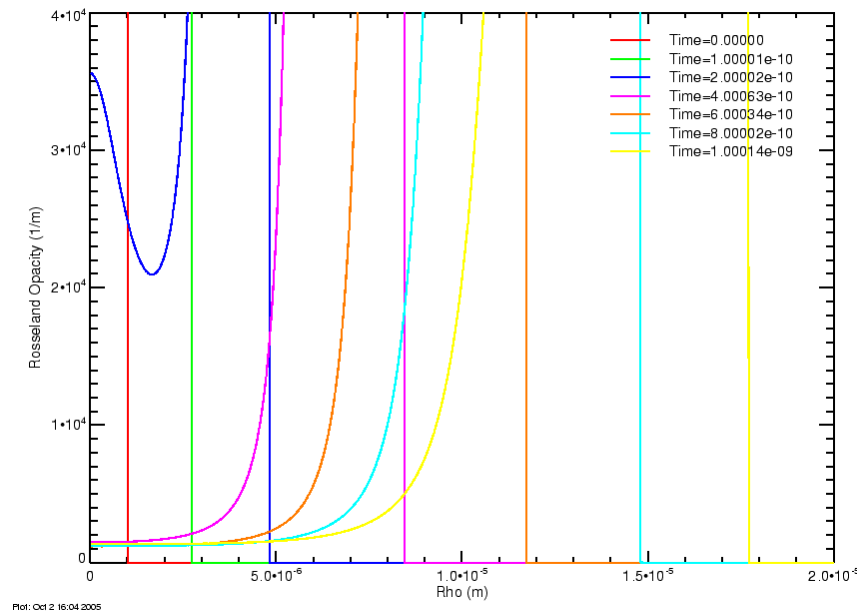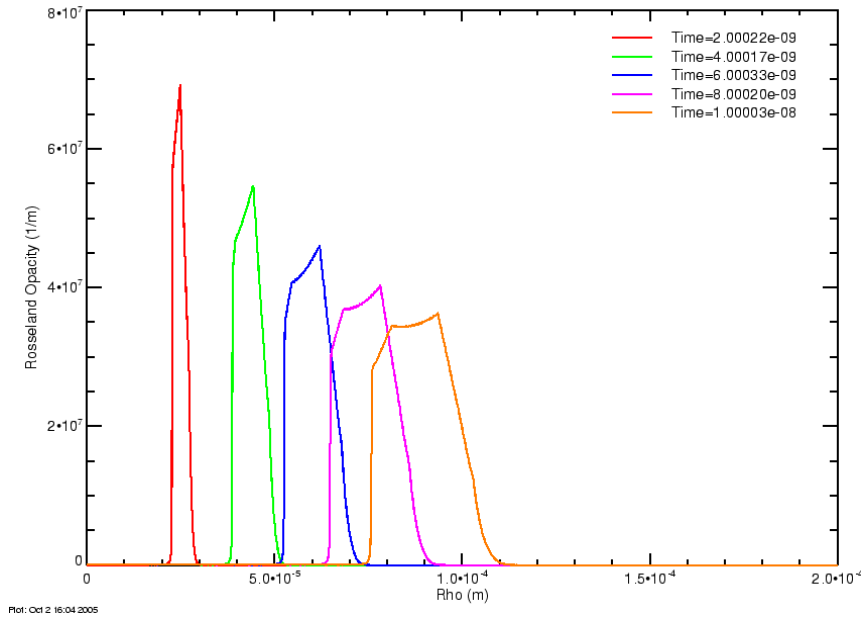Figure C-80. Early time Rosseland opacity profiles for 15 ns risetime, 300 kA current
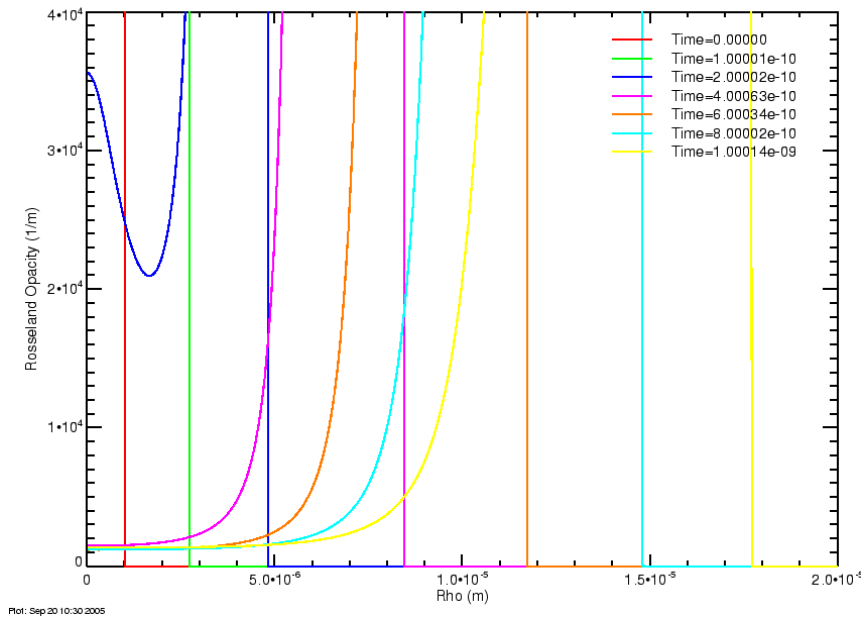
Figure C-81. Detail of early time average opacity profiles for 15 ns risetime, 300 kA current
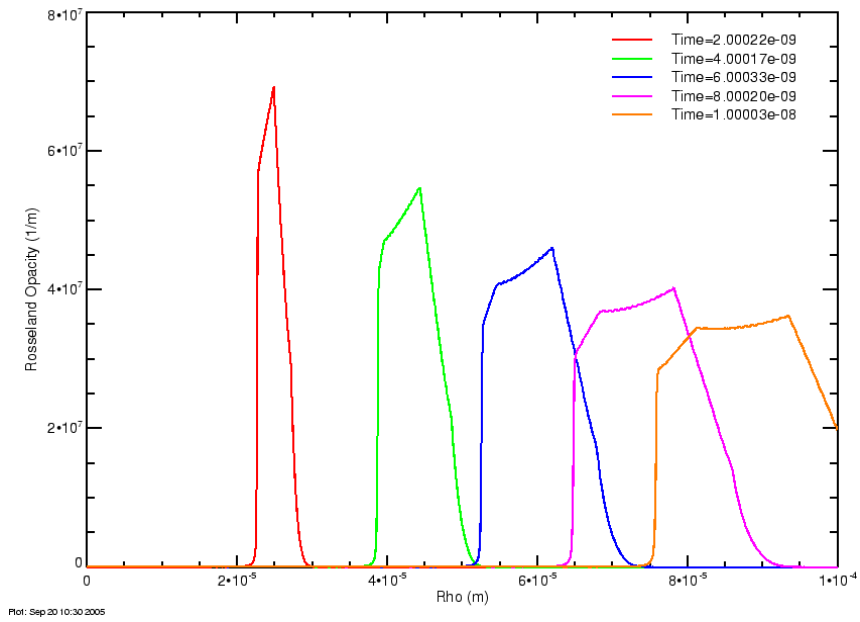
Figure C-82. Intermediate time average opacity profiles for 15 ns risetime, 300 kA current
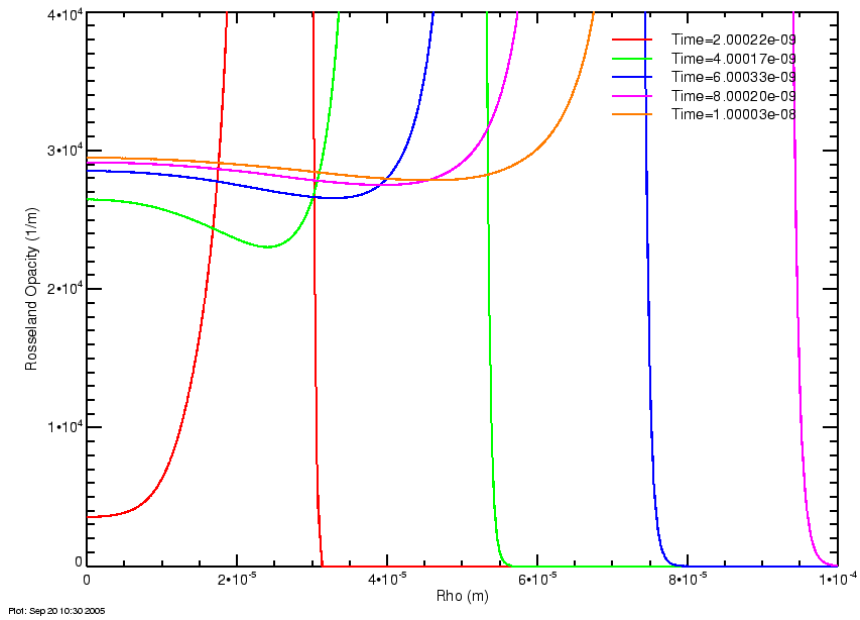
Figure C-83. Detail of intermediate time average opacity profiles for 15 ns risetime, 300 kA current
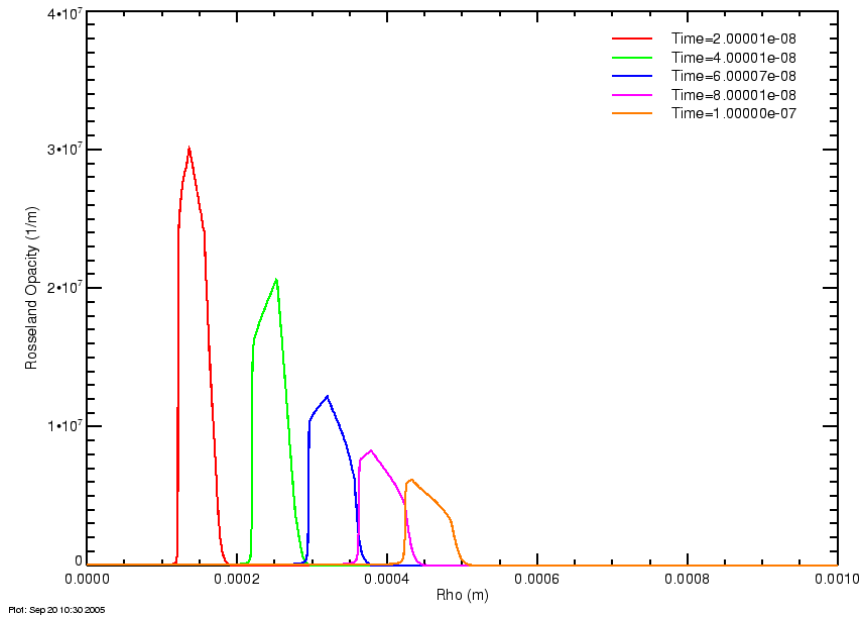
Figure C-84. Late time average opacity profiles for 15 ns risetime, 300 kA current
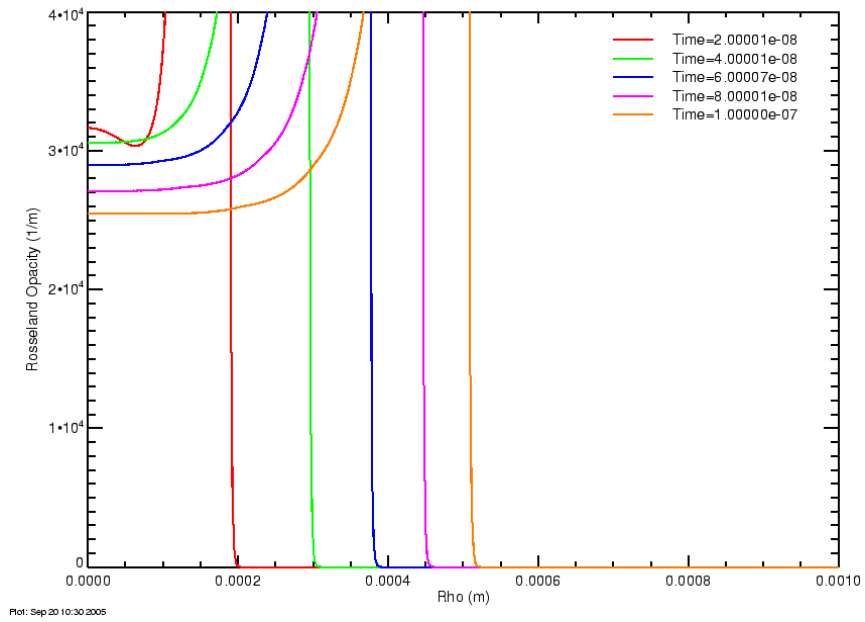
Figure C-85. Detail of late time average opacity profiles for 15 ns risetime, 300 kA current
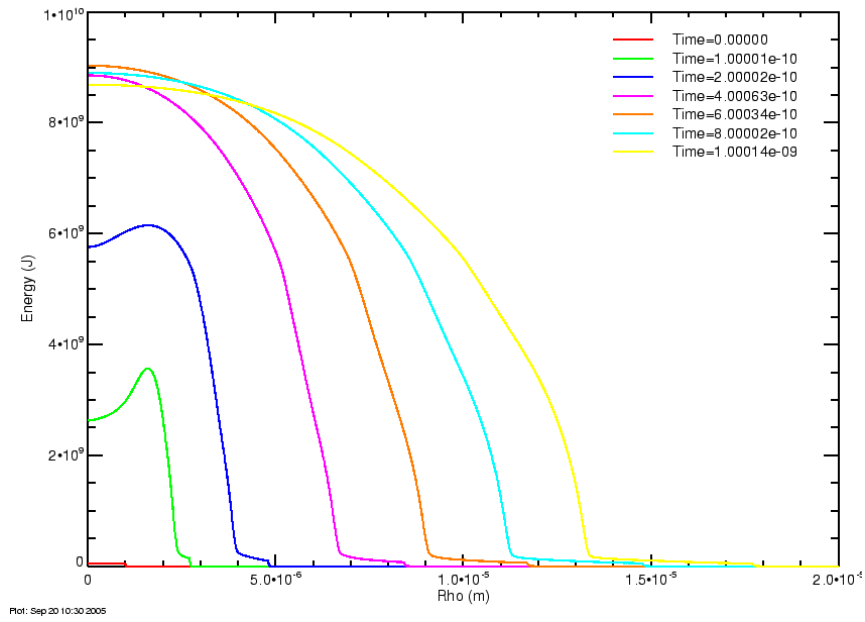
Figure C-86. Early time internal energy profiles for 15 ns risetime, 300 kA current
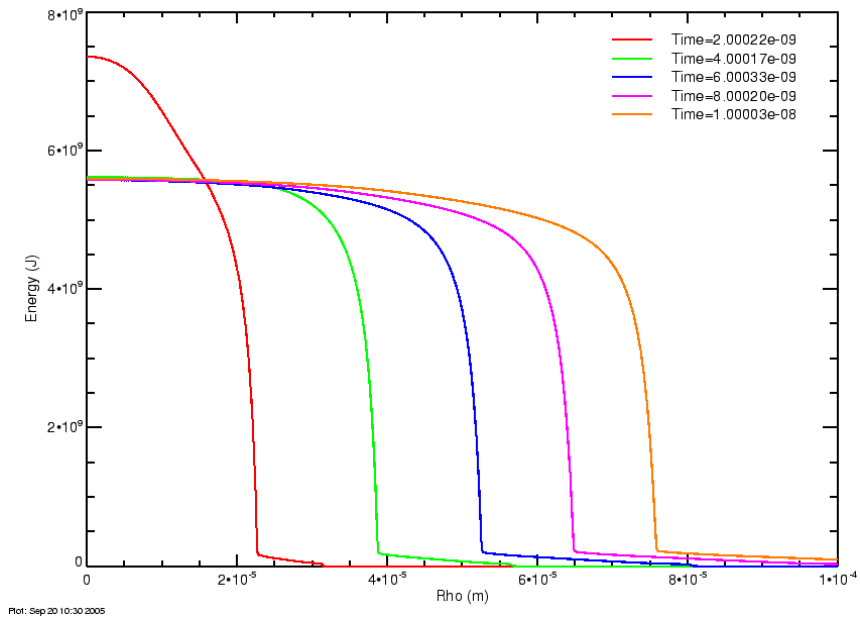
Figure C-87. Intermediate time energy profiles for 15 ns risetime, 300 kA current
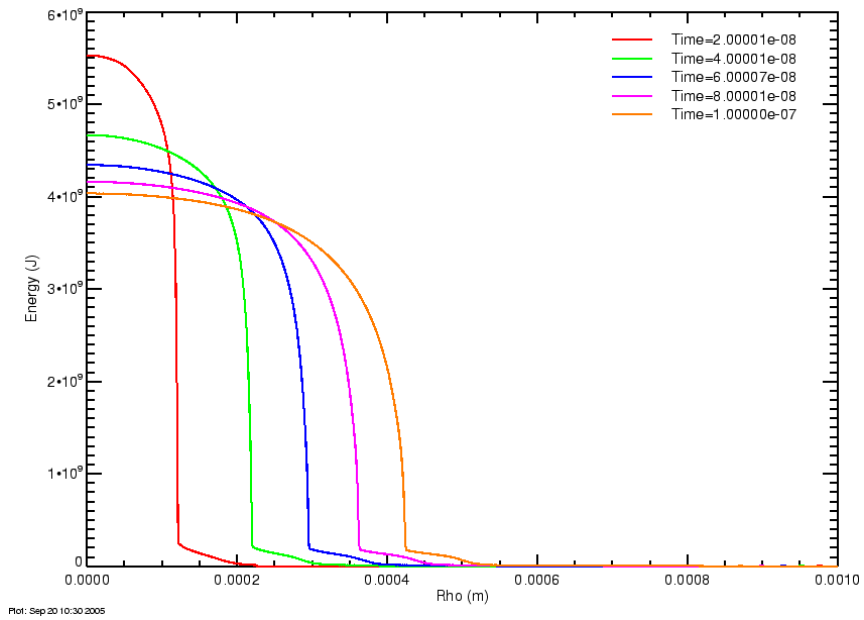
Figure C-88. Late time internal energy profiles for 15 ns risetime, 300 kA current
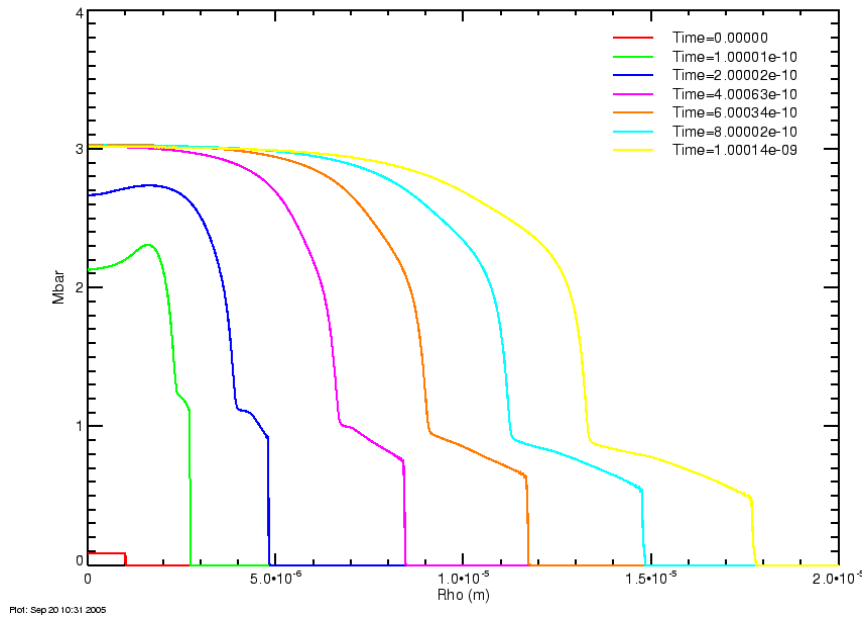
Figure C-89. Early time ionization number profiles for 15 ns risetime, 300 kA current
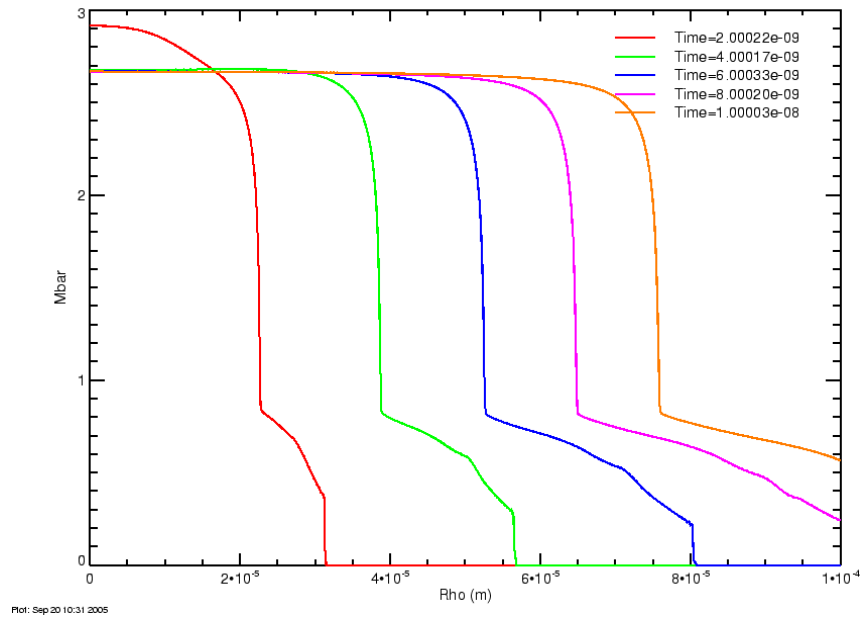
Figure C-90. Intermediate time ionization number profiles for 15 ns risetime, 300 kA current

C.4 Fast Rise High Current Drive

The fifth set has radiation turned on. The current drive is a linear ramp rising to $I_0 = 600$ kA with a risetime of 30 ns. After attaining the peak, the current remains at 600 kA until the end of the simulation. The channel initial conditions are radius of 1 μm, temperature of 1 eV and density of 1000 kg/m^3.
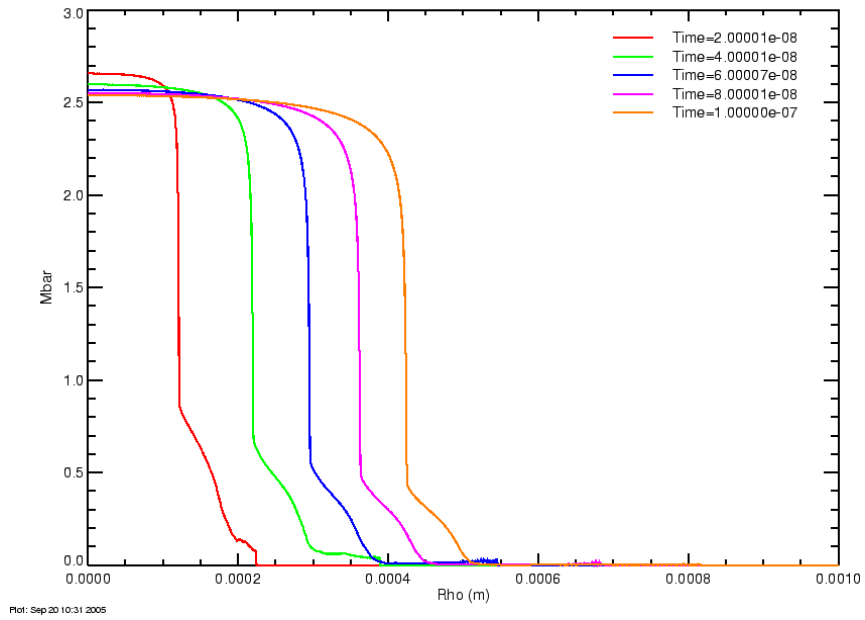
Figure C-91. Late time ionization number profiles for 15 ns risetime, 300 kA current
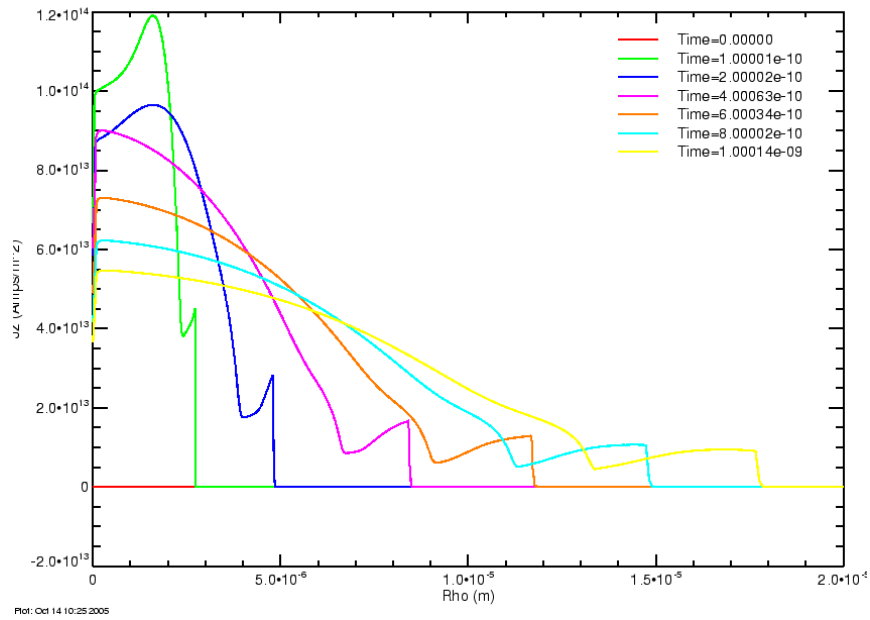
Figure C-92. Early time current density profiles for 15 ns risetime, 300 kA current
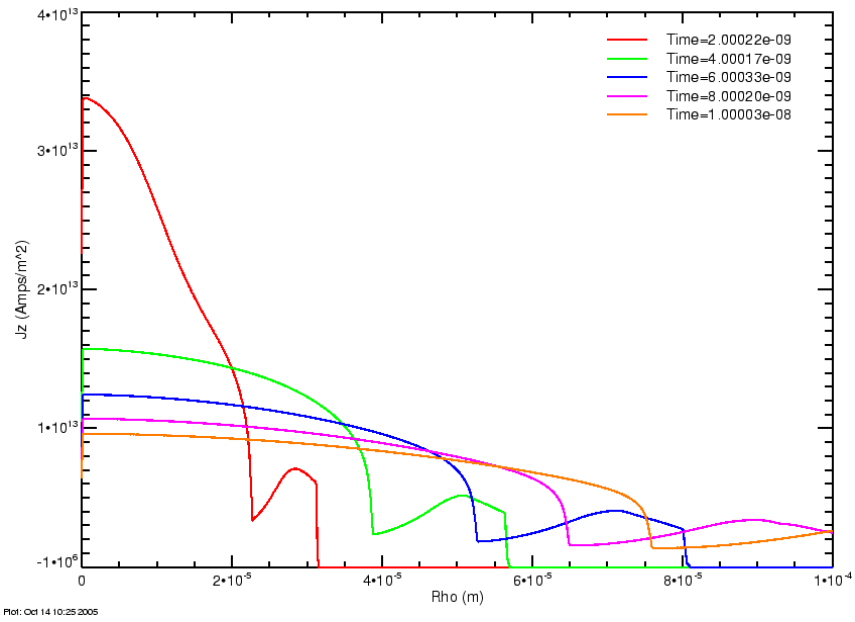
Figure C-93. Intermediate time current density profiles for 15 ns risetime, 300 kA current
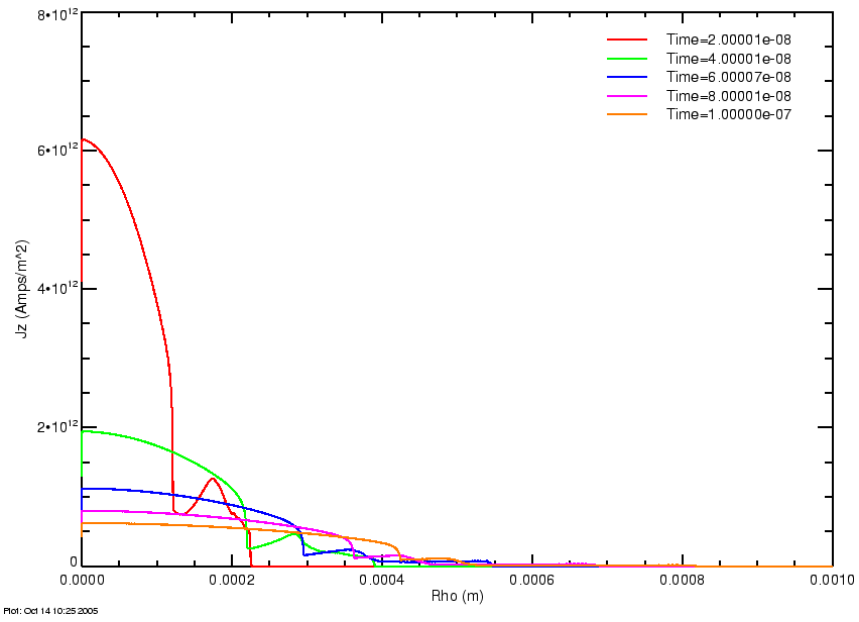
Figure C-94. Late time current density profiles for 15 ns risetime, 300 kA current
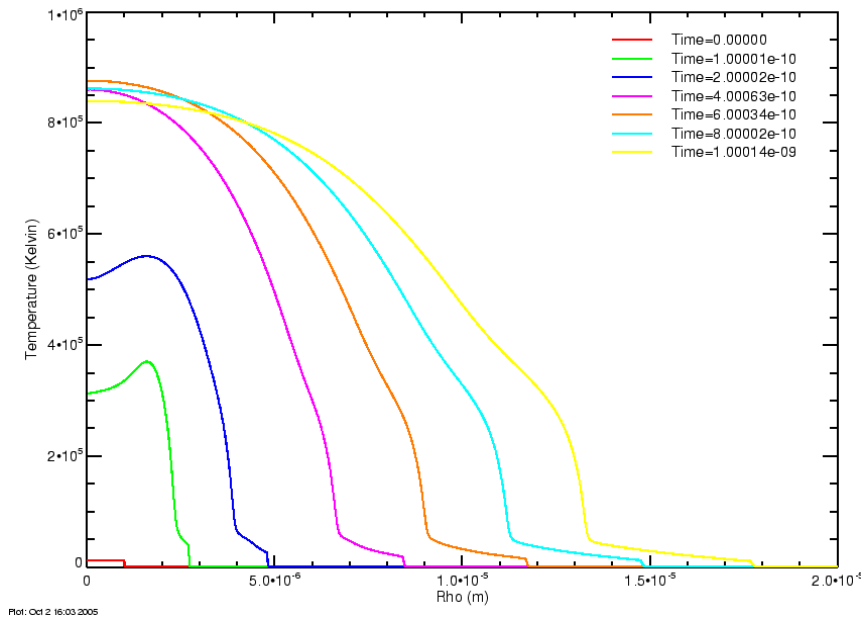
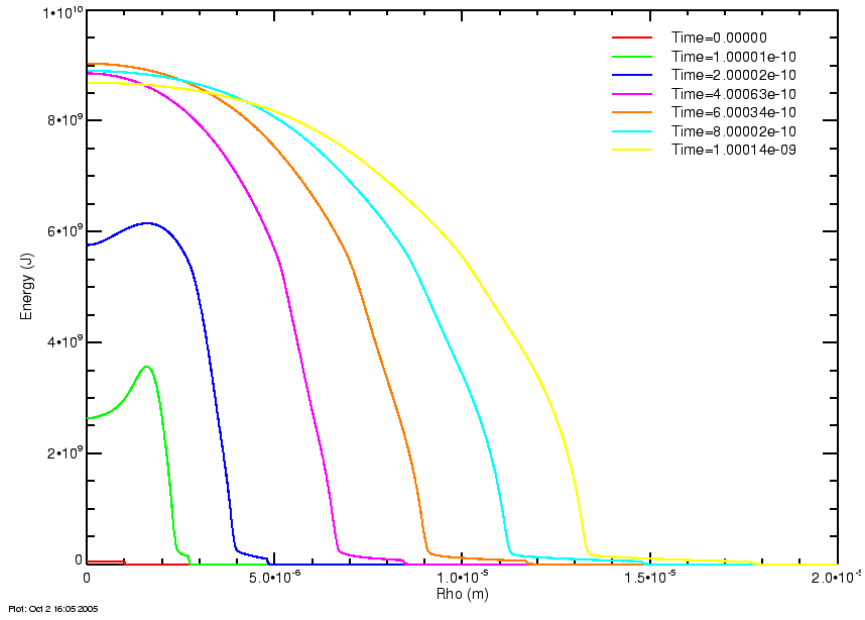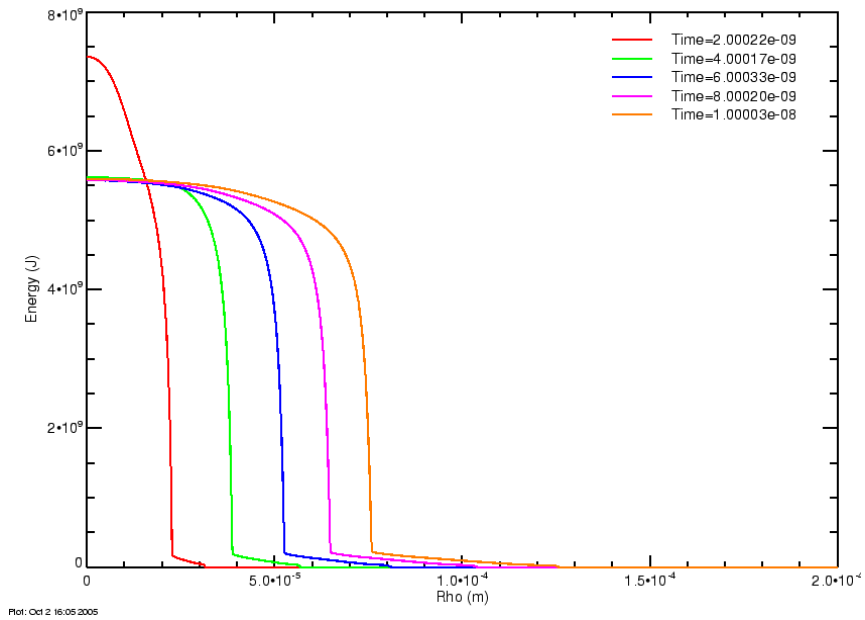Figure C-95. Early time temperature profiles for 30 ns risetime, 600 kA current
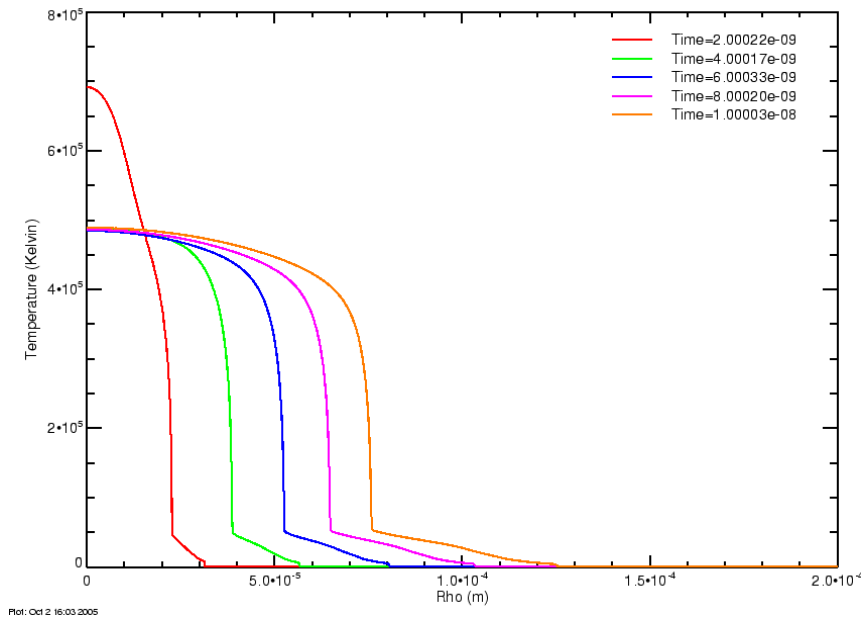
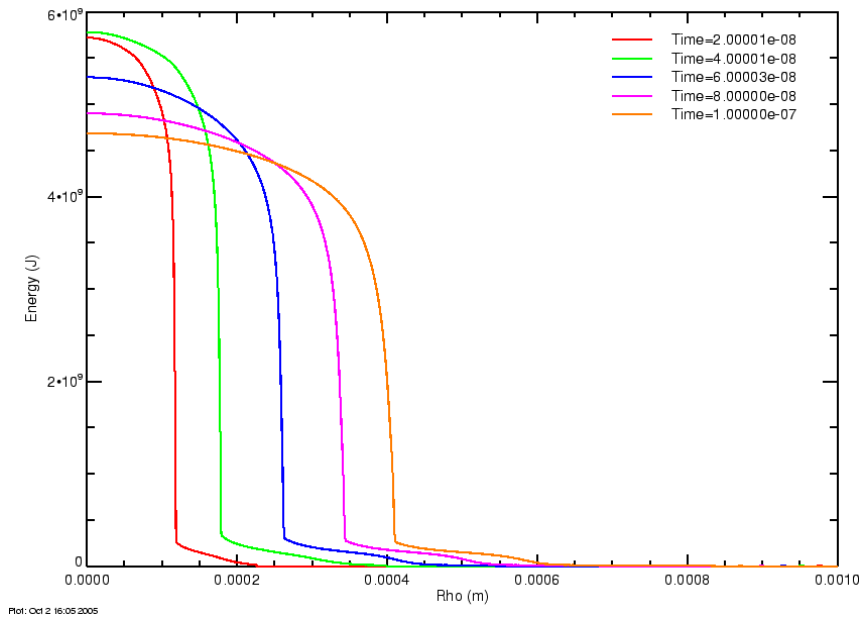Figure C-96. Intermediate time temperature profiles for 30 ns risetime, 600 kA current
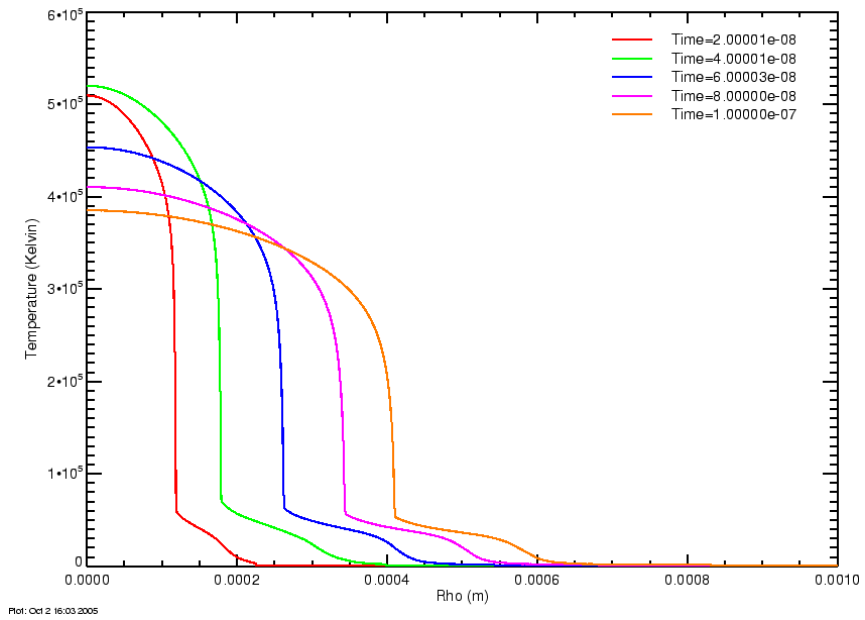
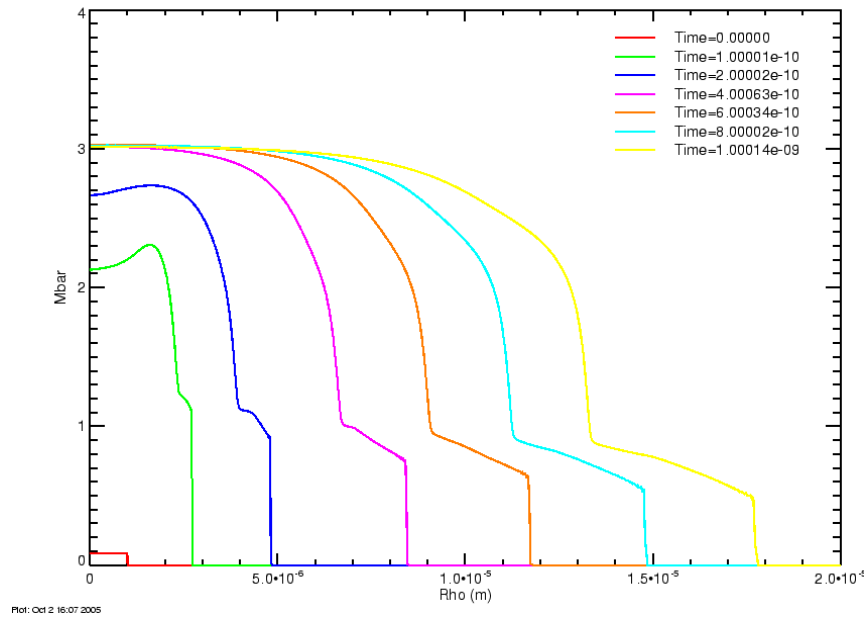Figure C-97. Late time temperature profiles for 30 ns risetime, 600 kA current
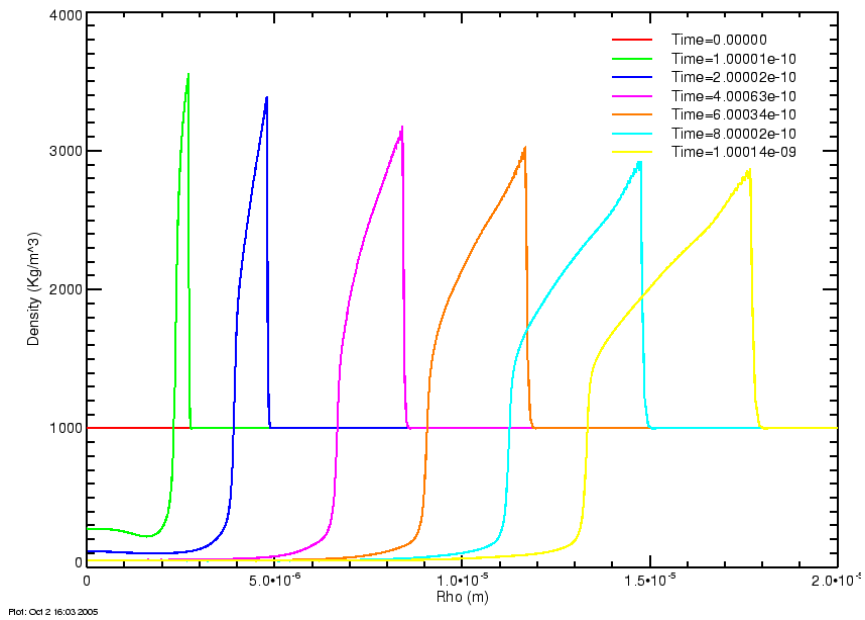
Figure C-98. Early time density profiles for 30 ns risetime, 600 kA current
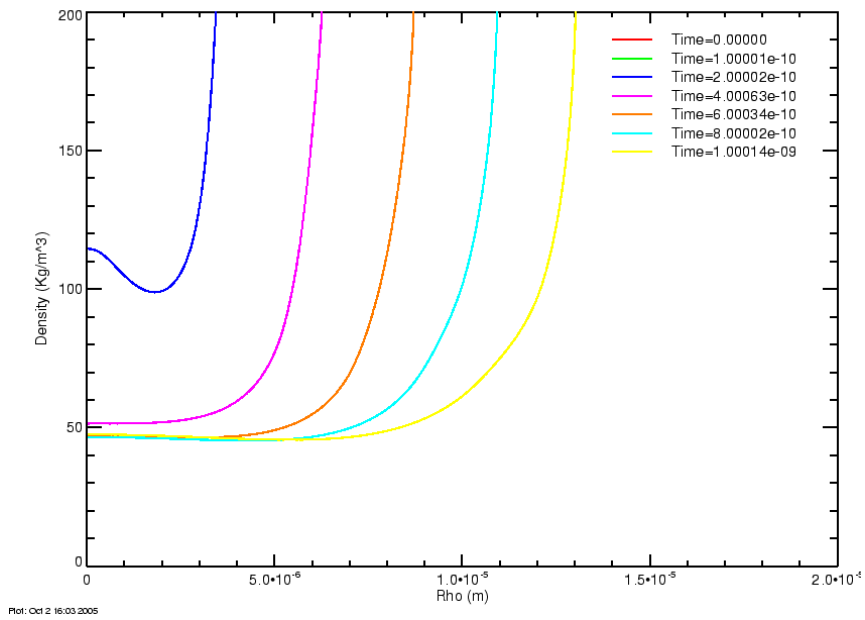
Figure C-99. Detail of early time density profiles for 30 ns risetime, 600 kA current

216
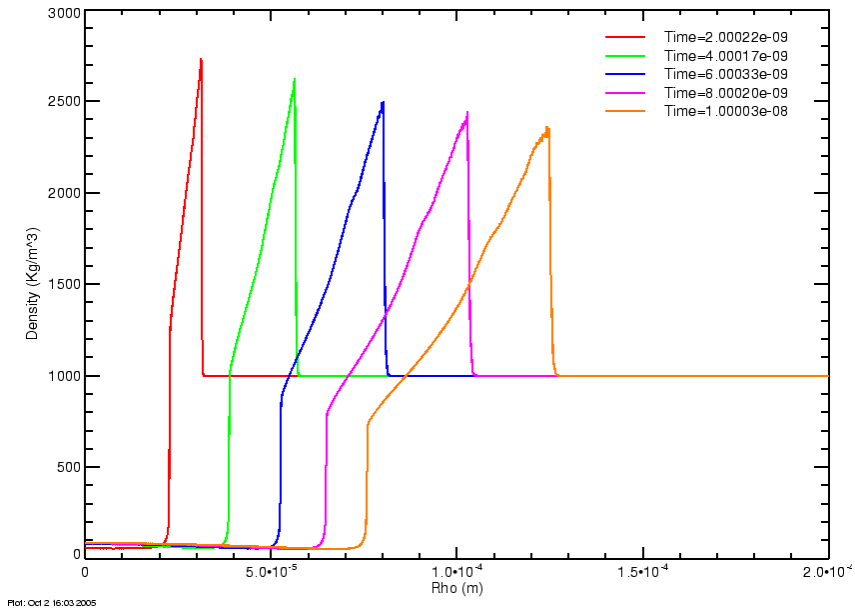
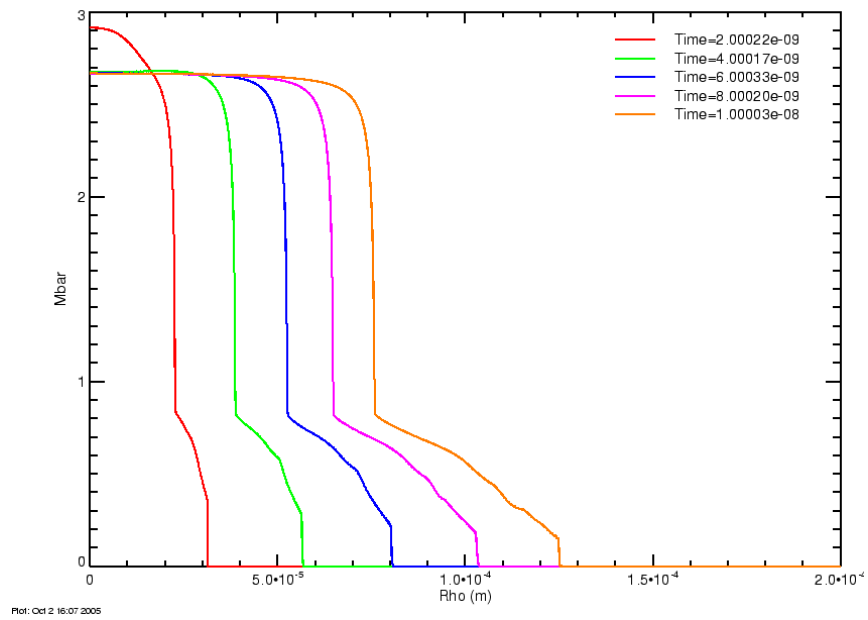Figure C-100. Intermediate time density profiles for 30 ns risetime, 600 kA current
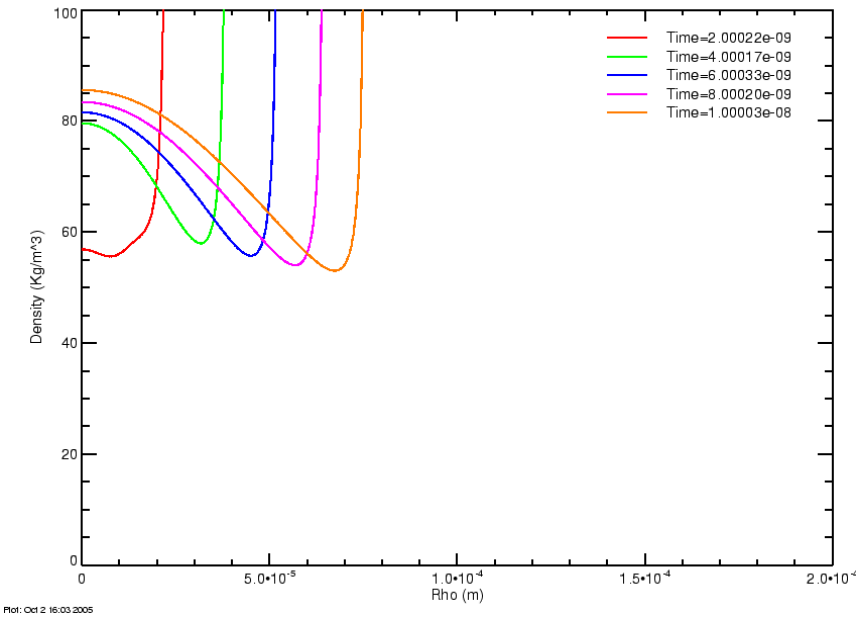
Figure C-101. Detail of intermediate time density profiles for 30 ns risetime, 600 kA current
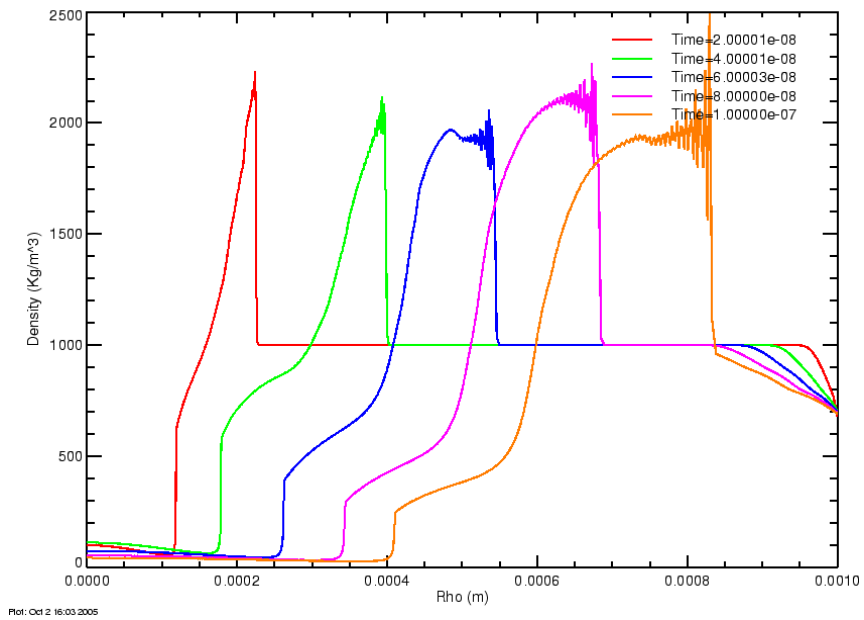
Figure C-102. Late time density profiles for 30 ns risetime, 600 kA current
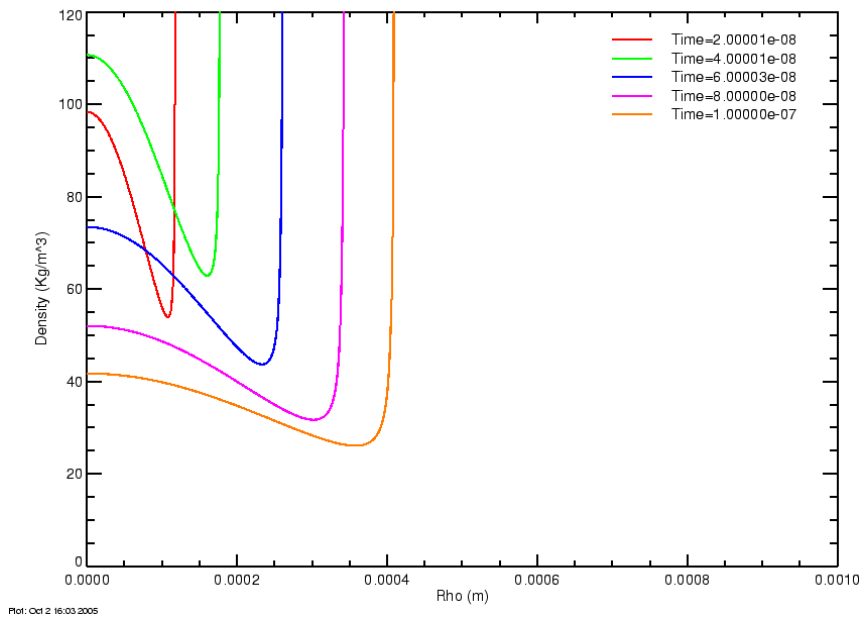
Figure C-103. Detail of late time density profiles for 30 ns risetime, 600 kA current
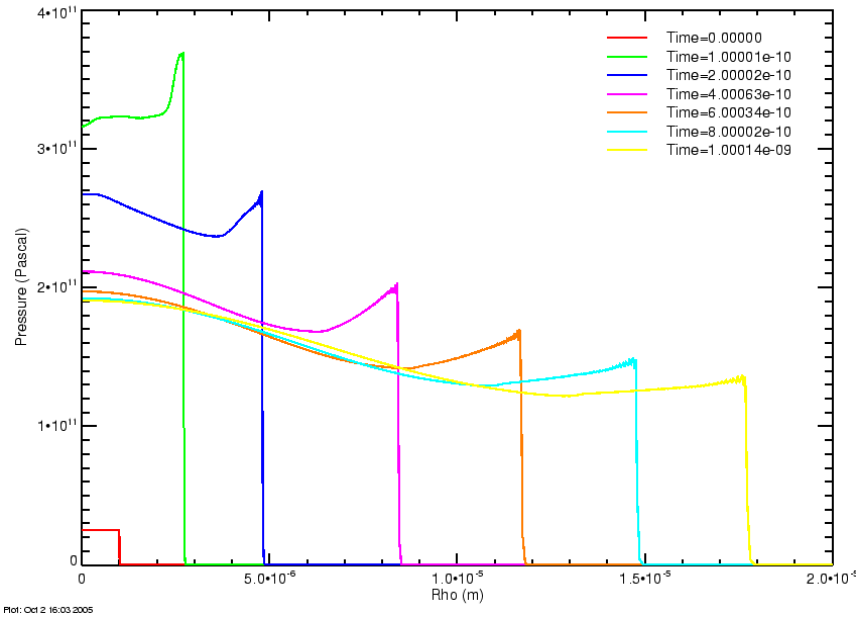
Figure C-104. Early time pressure profiles for 30 ns risetime, 600 kA current
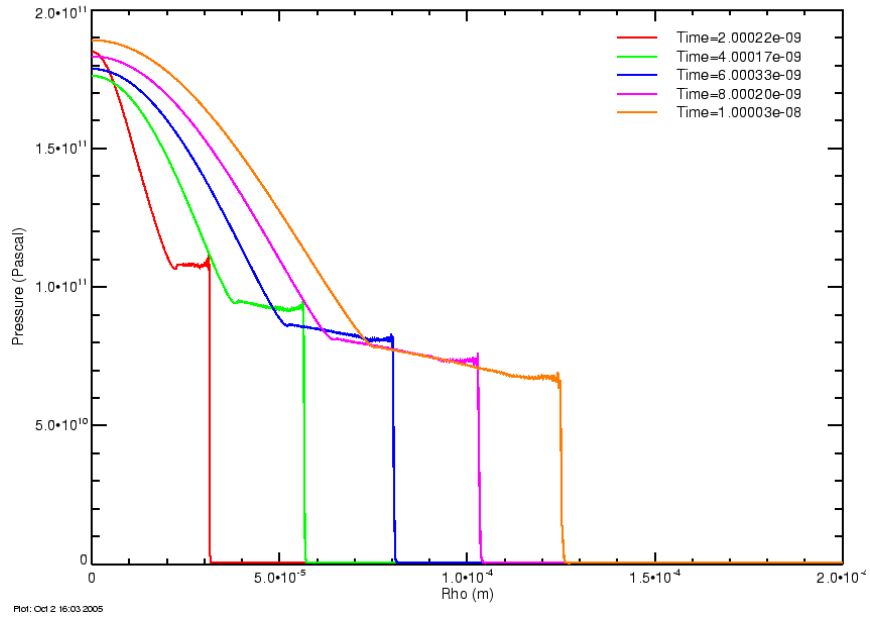
Figure C-105. Intermediate time pressure profiles for 30 ns risetime, 600 kA current
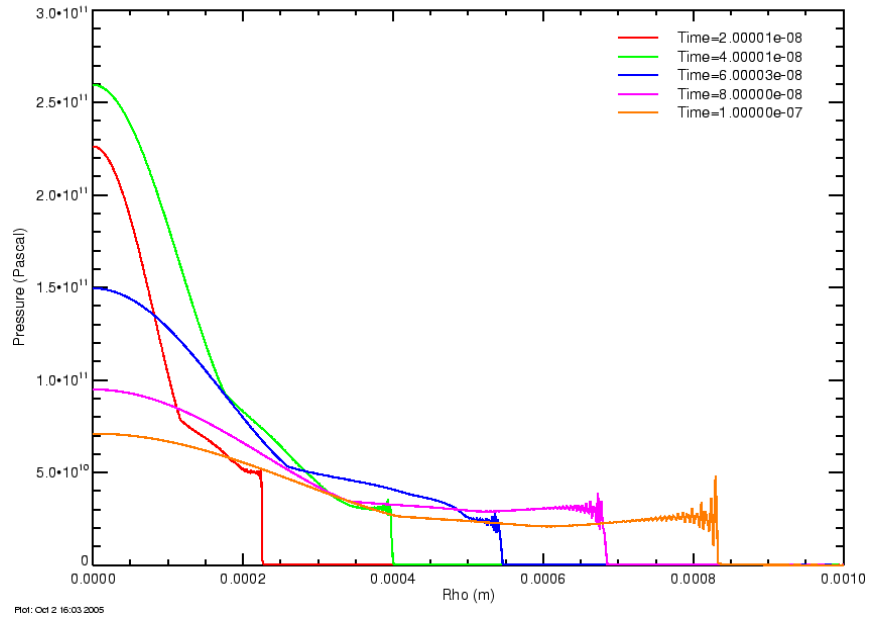
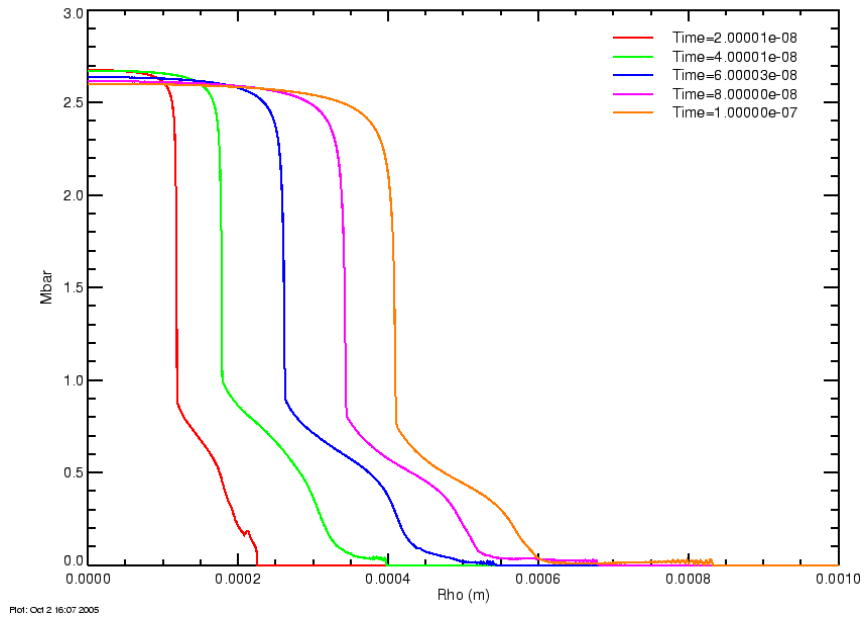Figure C-106. Late time pressure profiles for 30 ns risetime, 600 kA current
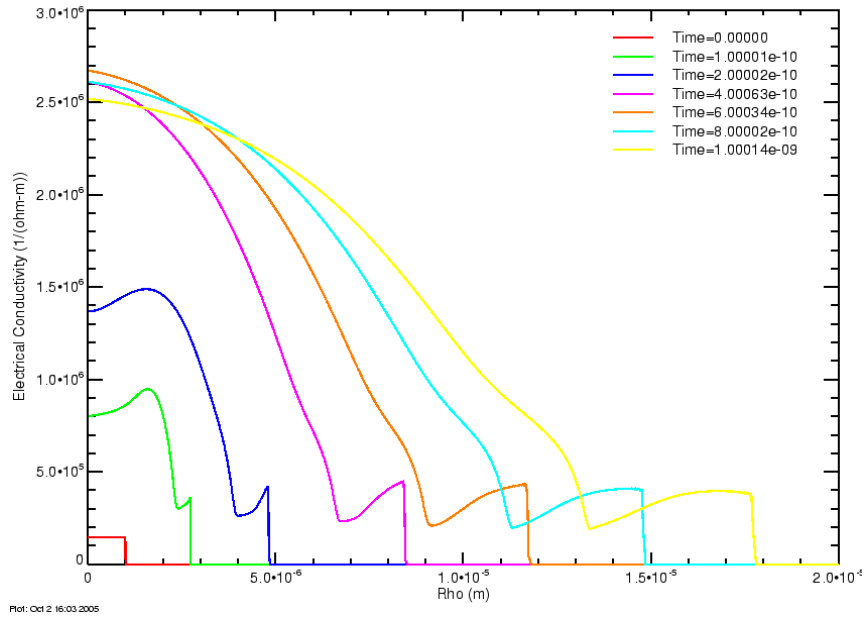
Figure C-107. Early time electrical conductivity profiles for 30 ns risetime, 600 kA current
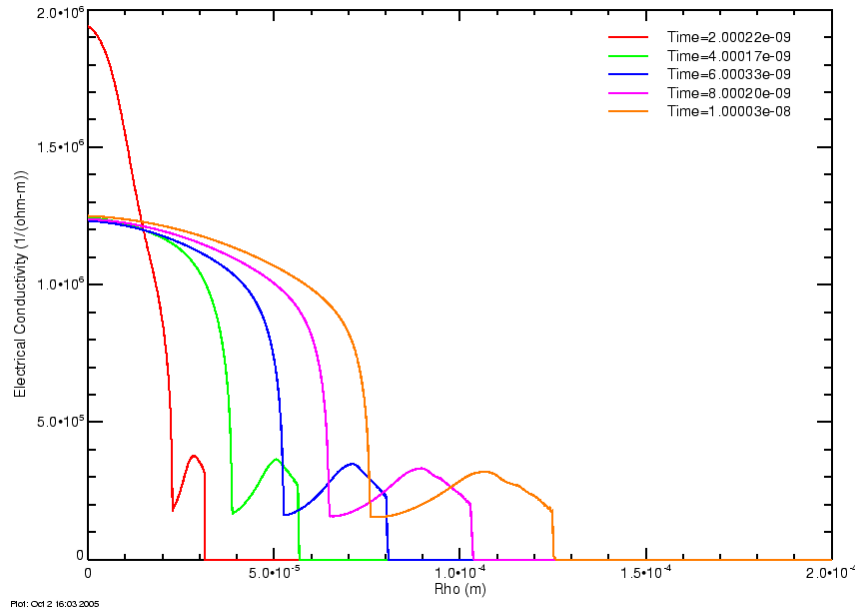
Figure C-108. Intermediate time electrical conductivity profiles for 30 ns risetime, 600 kA current
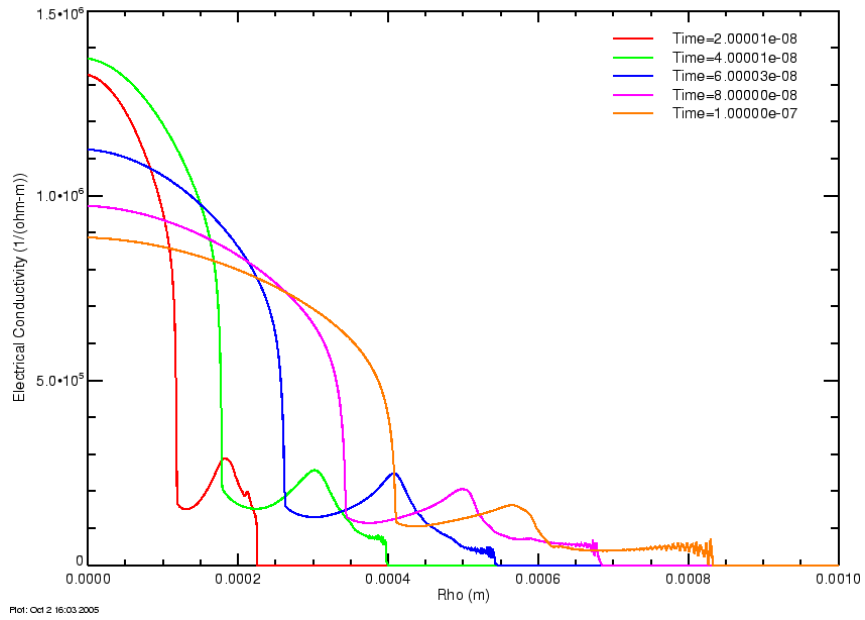
Figure C-109. Late time electrical conductivity profiles for 30 ns risetime, 600 kA current
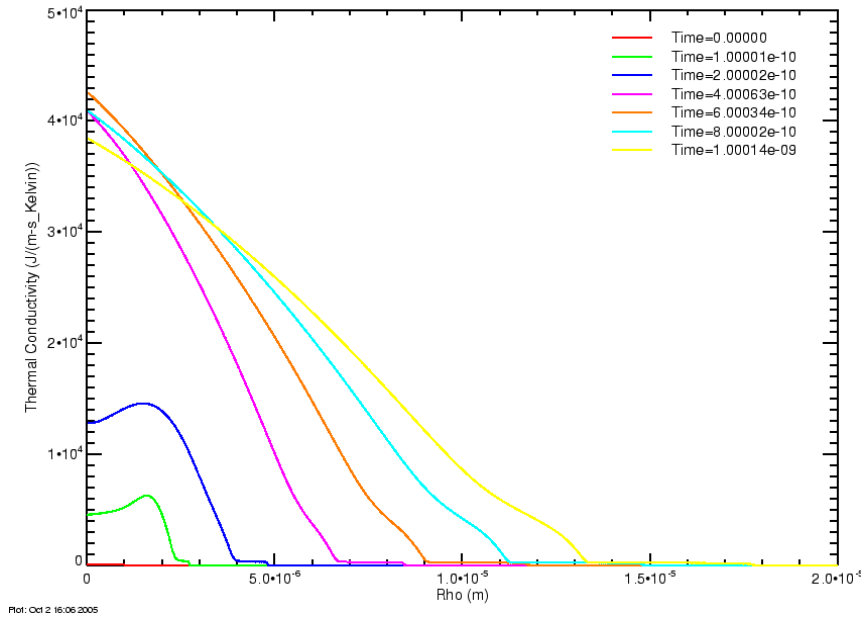
Figure C-110. Early time thermal conductivity profiles for 30 ns risetime, 600 kA current
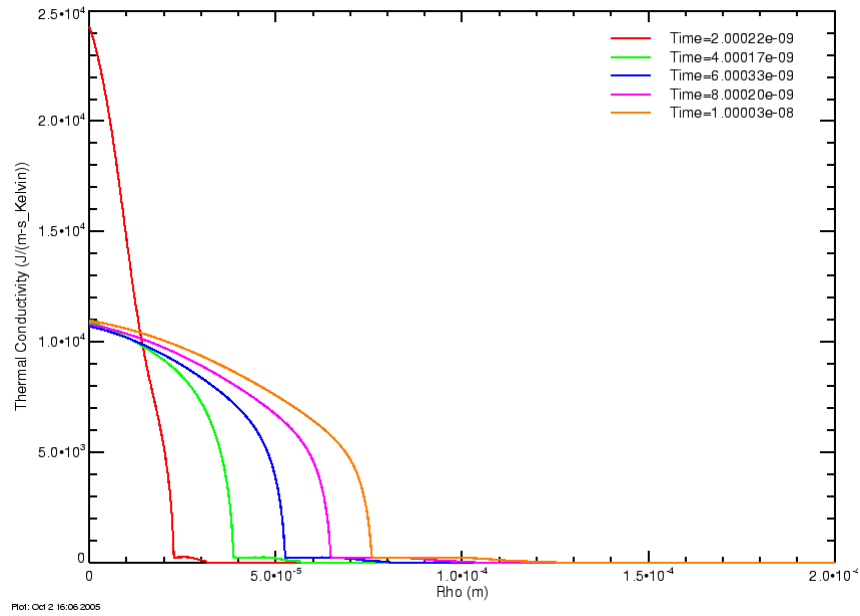
Figure C-111. Intermediate time thermal conductivity profiles for 30 ns risetime, 600 kA current
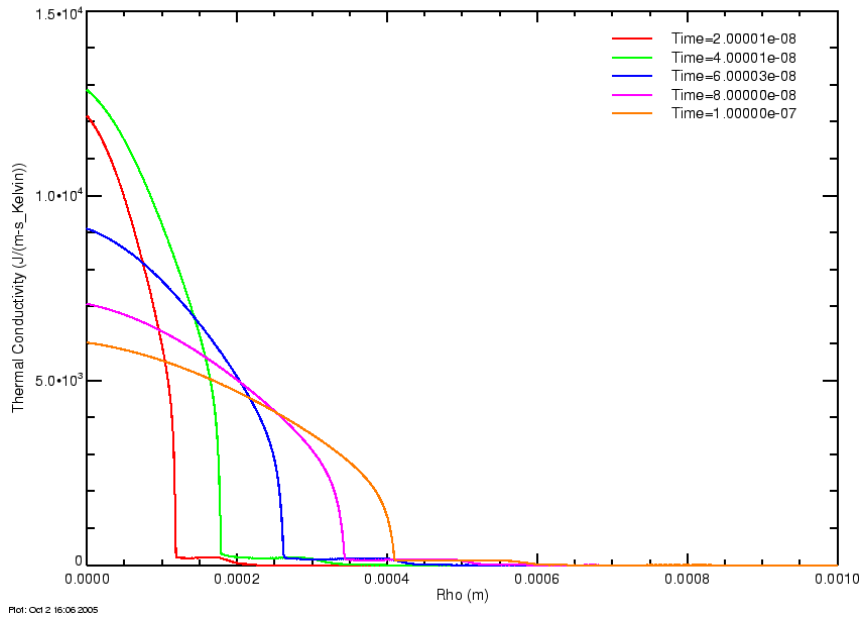
Figure C-112. Late time thermal conductivity profiles for 30 ns risetime, 600 kA current
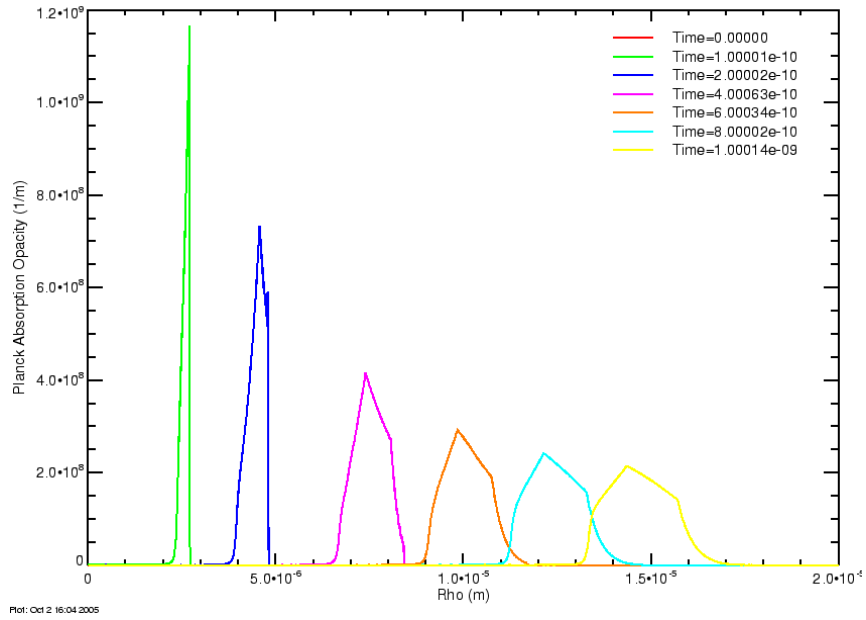
Figure C-113. Early time average opacity profiles for 30 ns risetime, 600 kA current

Figure C-114. Detail of early time average opacity profiles for 30 ns risetime, 600 kA current

224

Figure C-115. Intermediate time average opacity profiles for 30 ns risetime, 600 kA current

Figure C-116. Detail of early time average opacity profiles for 30 ns risetime, 600 kA current

Figure C-117. Late time average opacity profiles for 30 ns risetime, 600 kA current

Figure C-118. Detail of late time average opacity profiles for 30 ns risetime, 600 kA current
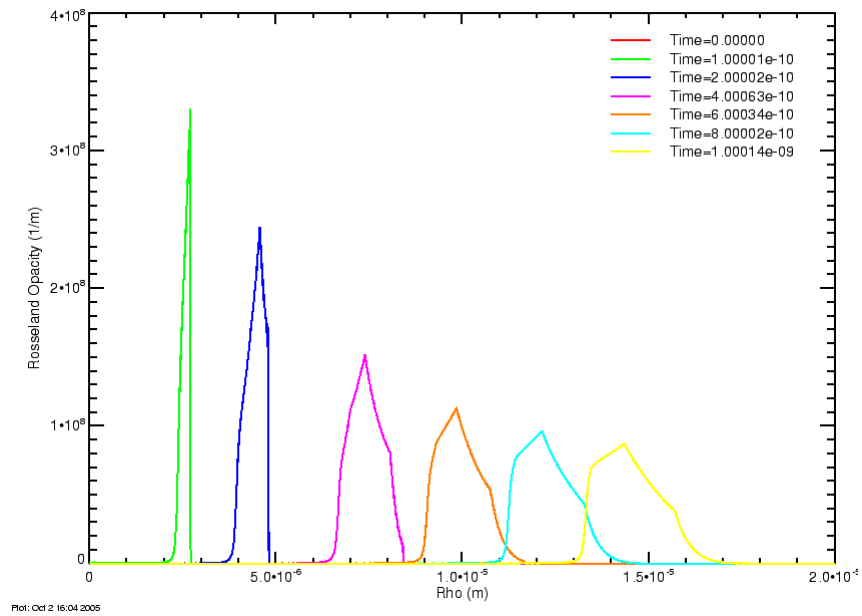
Figure C-119. Early time Rosseland opacity profiles for 30 ns risetime, 600 kA current

Figure C-120. Detail of early time Rosseland opacity profiles for 30 ns risetime, 600 kA current

Figure C-121. Intermediate time Rosseland opacity profiles for 30 ns risetime, 600 kA current
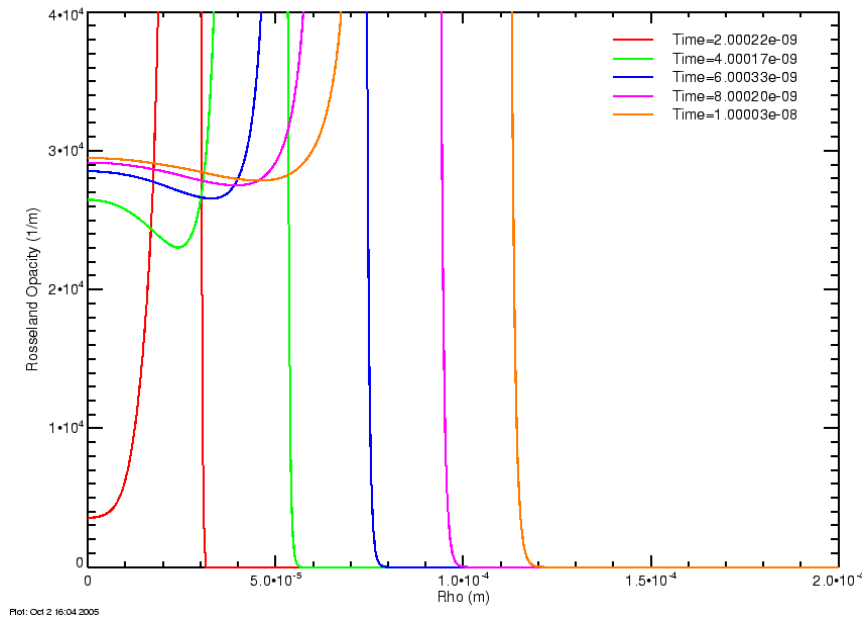
Figure C-122. Detail of intermediate time Rosseland opacity profiles for 30 ns risetime, 600 kA current

C.5   Step Voltage Drive

The sixth set has radiation turned on. The voltage drive is a linear ramp rising to $V_{oc} = 45$ MV with a risetime of 1 ns. The external impedance is 160 Ω to make the peak current 280 kA. The channel initial conditions are radius of 1 μm, temperature of 1 eV and density of 1000 kg/m^3.
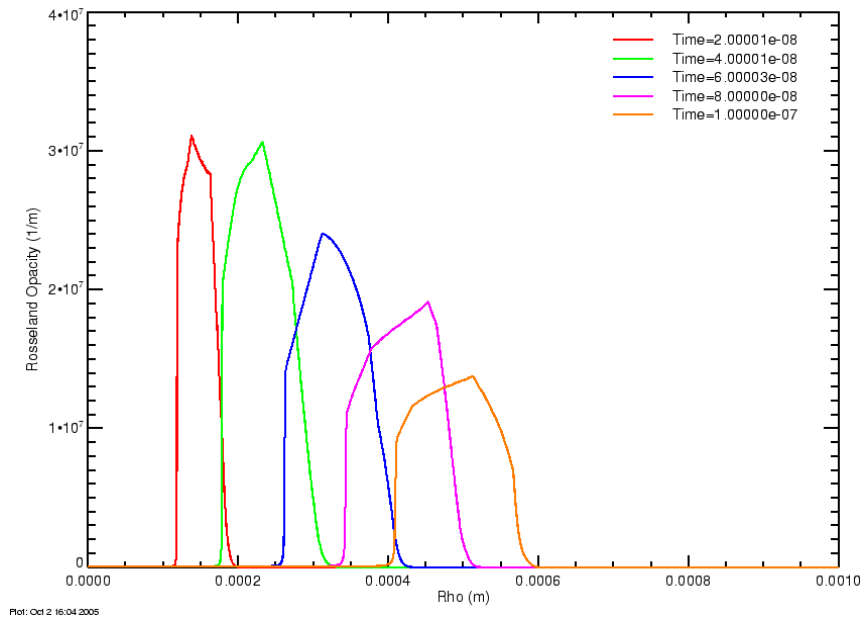
Figure C-123. Late time Rosseland opacity profiles for 30 ns risetime, 600 kA current
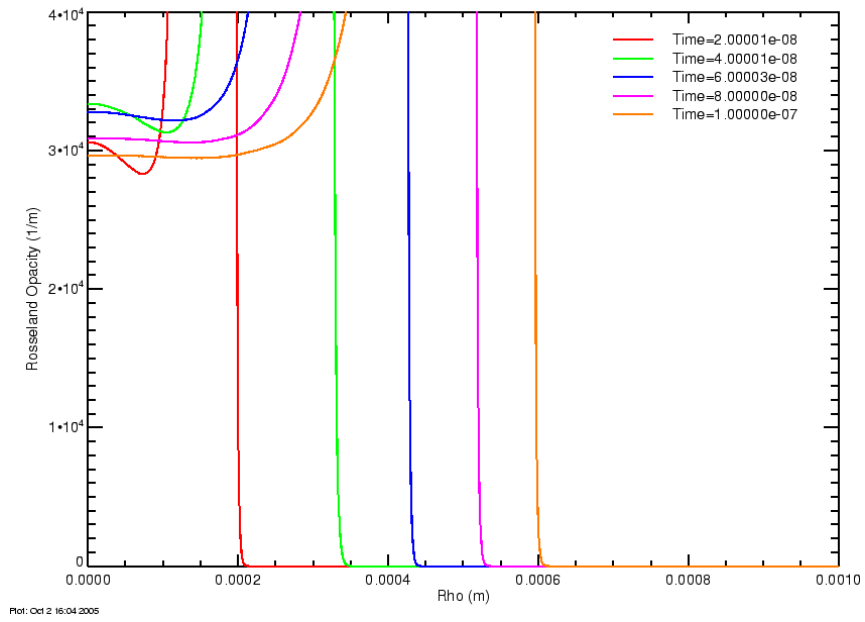
Figure C-124. Detail of late time Rosseland opacity profiles for 30 ns risetime, 600 kA current
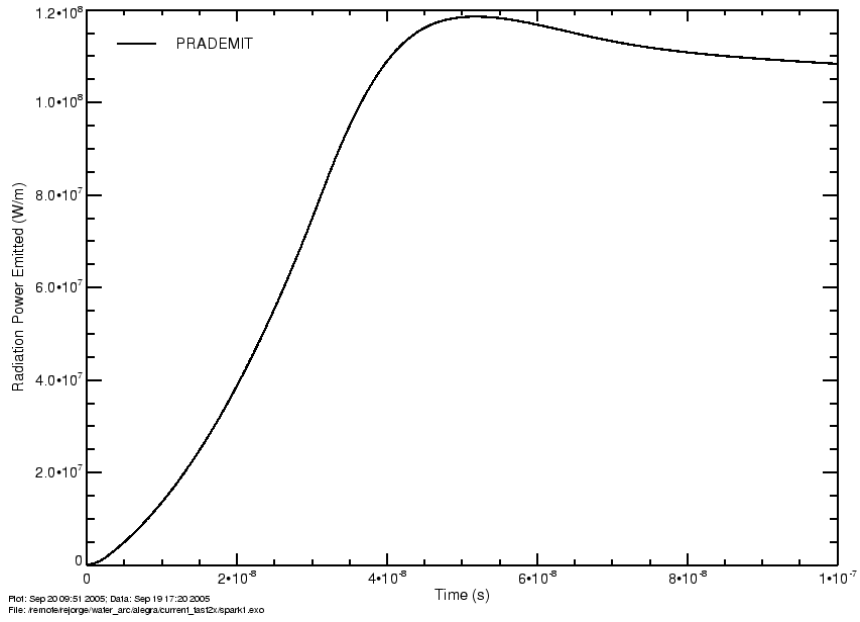
Figure C-125. Total problem radiation for 300 ns risetime, 600 kA current

Figure C-126. Early time internal energy profiles for 30 ns risetime, 600 kA current

Figure C-127. Intermediate time energy profiles for 30 ns risetime, 600 kA current

Figure C-128. Late time internal energy profiles for 30 ns risetime, 600 kA current

Figure C-129. Early time ionization number profiles for 30 ns risetime, 600 kA current

Figure C-130. Intermediate time energy profiles for 30 ns risetime, 600 kA current

233

Figure C-131. Late time internal energy profiles for 30 ns risetime, 600 kA current
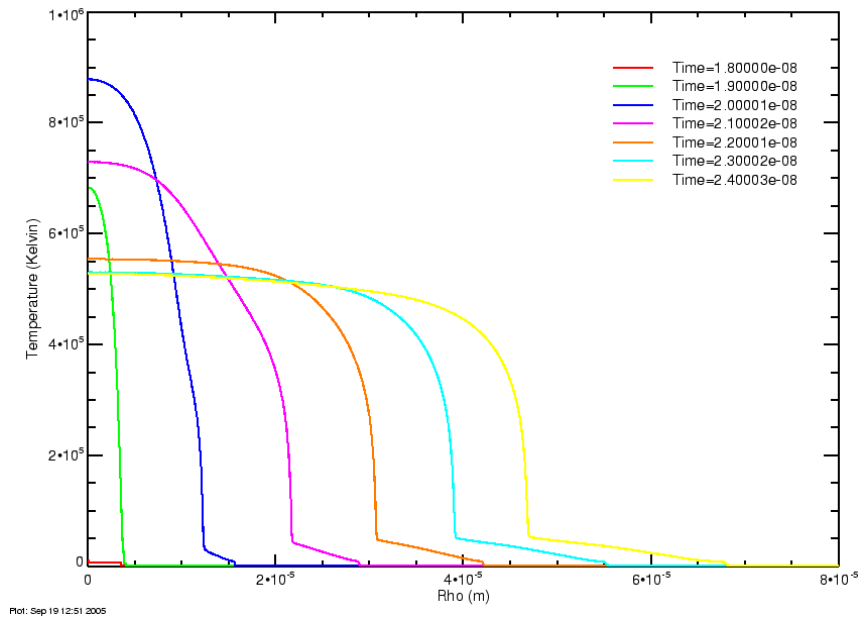
Figure C-132. Early time temperature profiles for a voltage drive with 1 ns risetime, 45 MV peak and $R_0 = 160 \ \Omega$
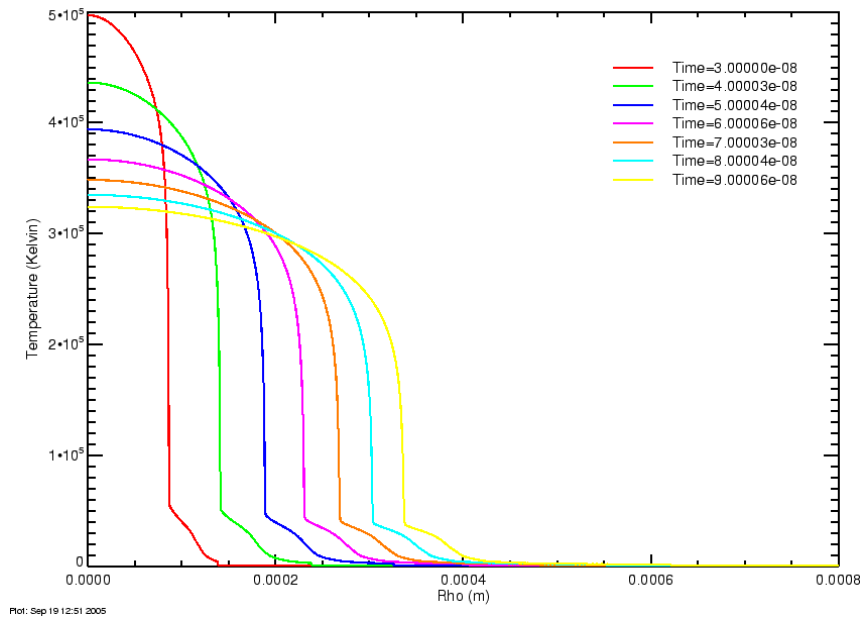
Figure C-133. Late time temperature profiles for a voltage drive with 1 ns risetime, 45 MV peak and $R_0 = 160 \ \Omega$
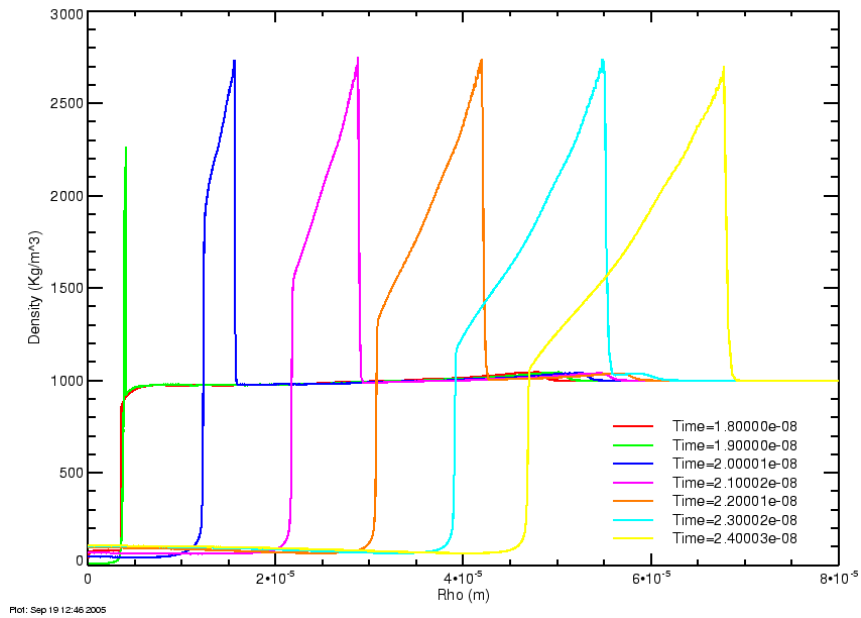
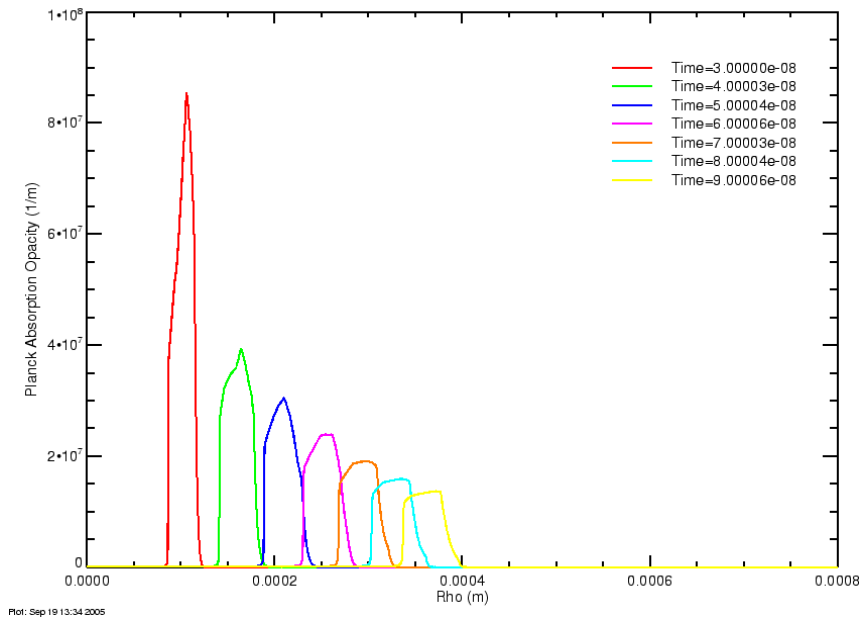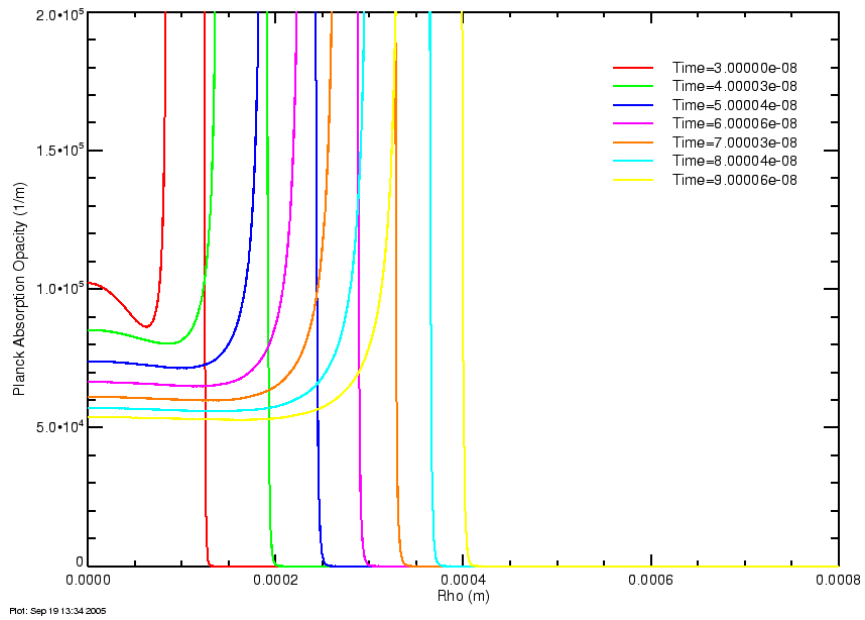Figure C-134. Early time density profiles for a voltage drive with 1 ns risetime, 45 MV peak and $R_0 = 160$ Ω
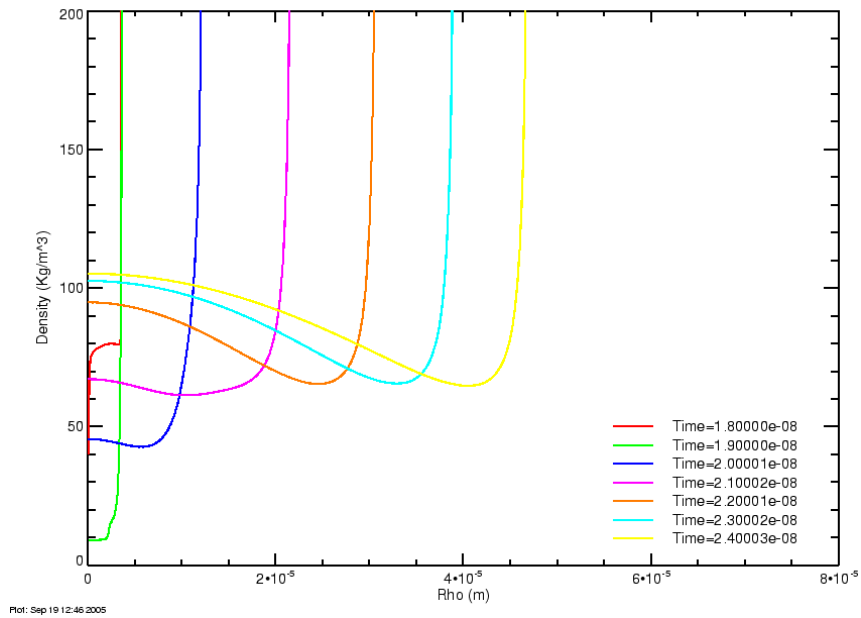
Figure C-135. Detail of early time density profiles for a voltage drive with 1 ns risetime, 45 MV peak and $R_0 = 160$ Ω
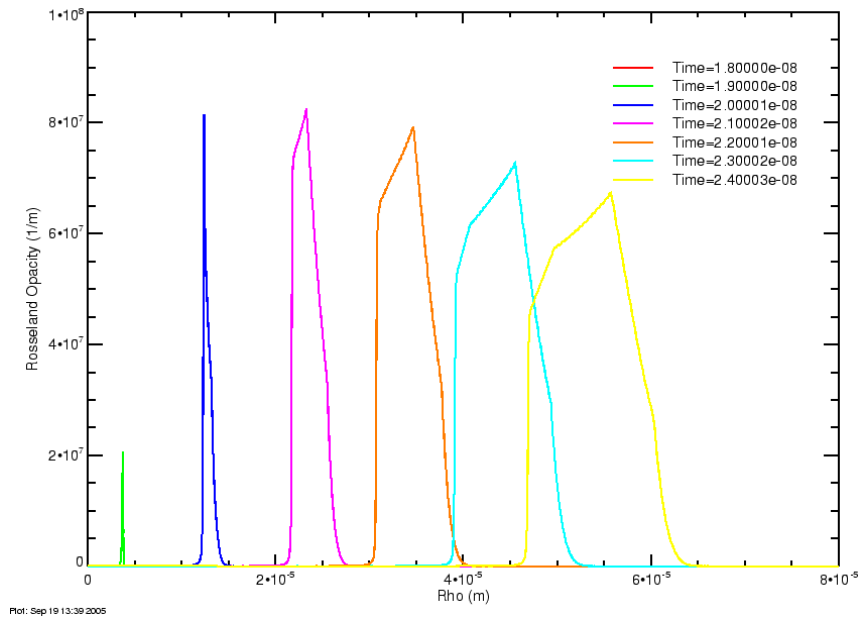
Plot: Sep 19 12:46 2005
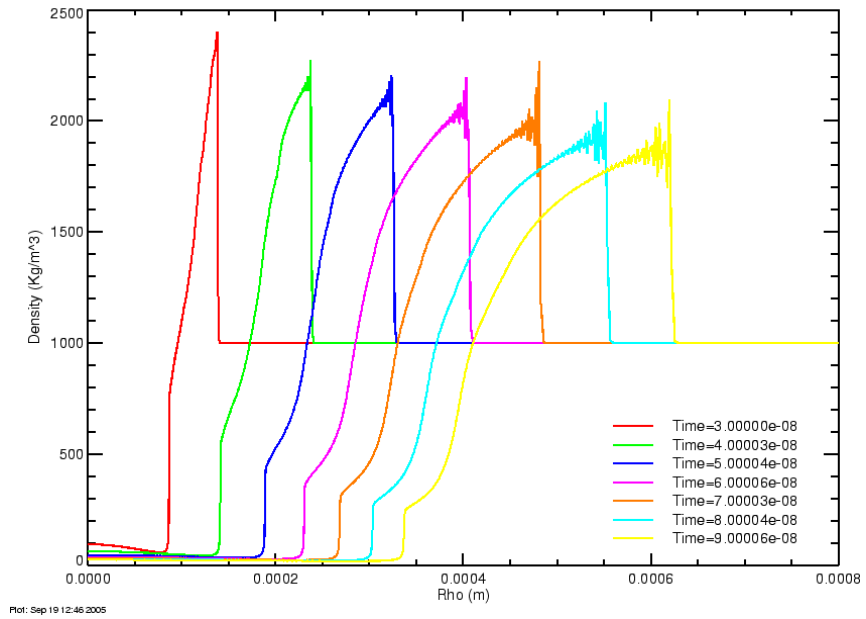
Figure C-136. Late time density profiles for a voltage drive with 1 ns risetime, 45 MV peak and $R_0 = 160\ \Omega$
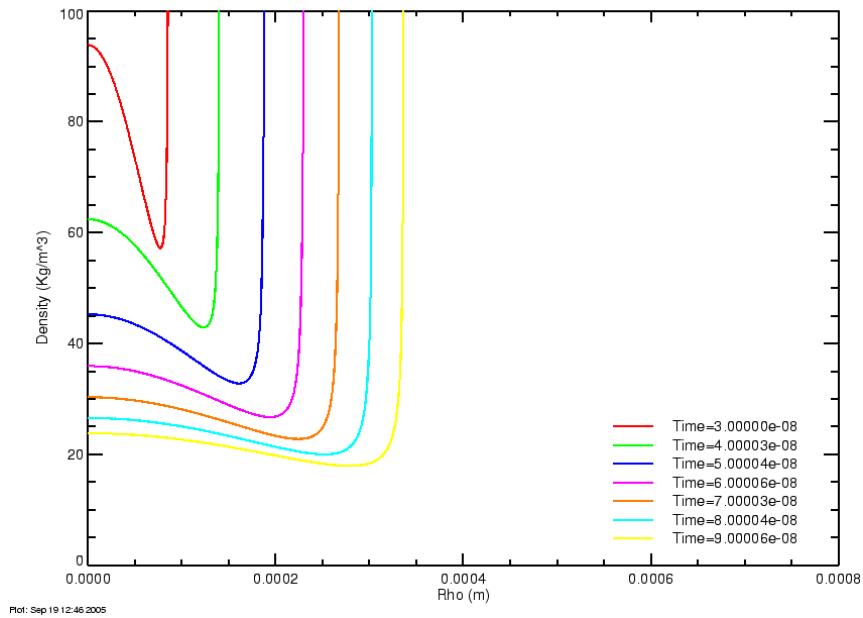
Figure C-137. Detail of late time density profiles for a voltage drive with 1 ns risetime, 45 MV peak and $R_0 = 160\ \Omega$
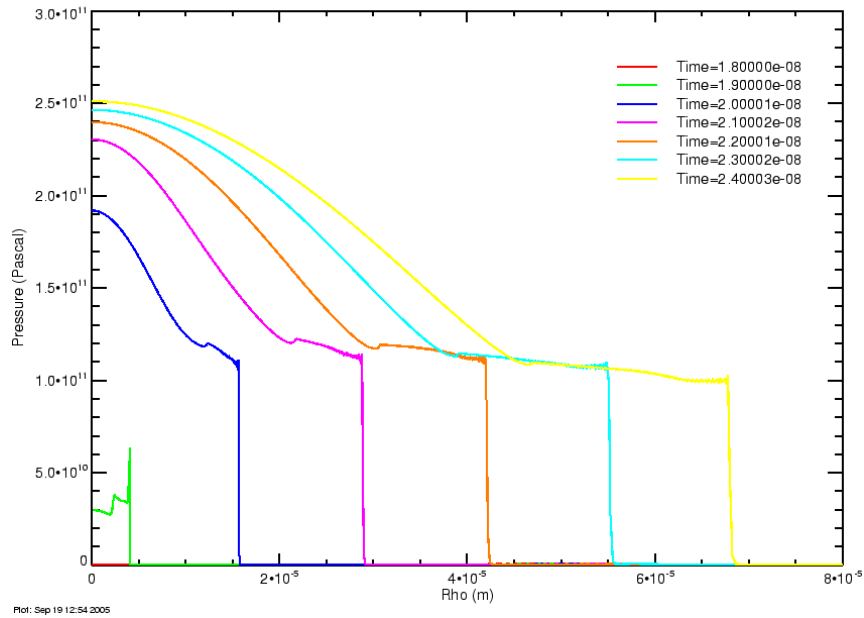
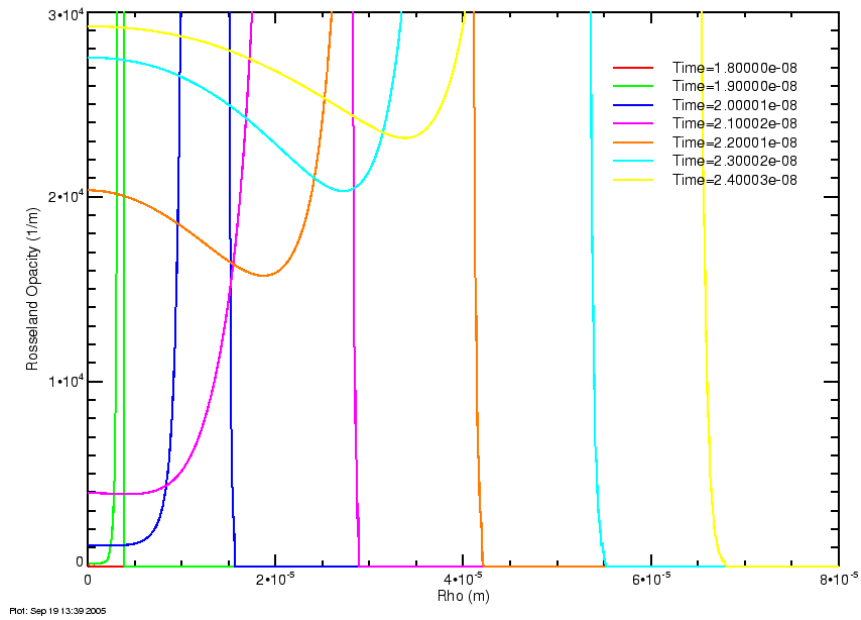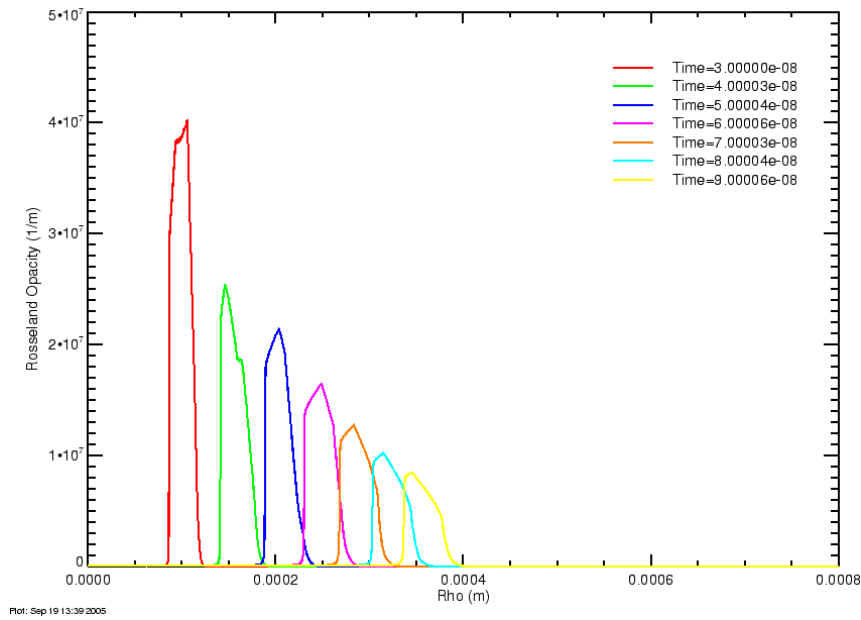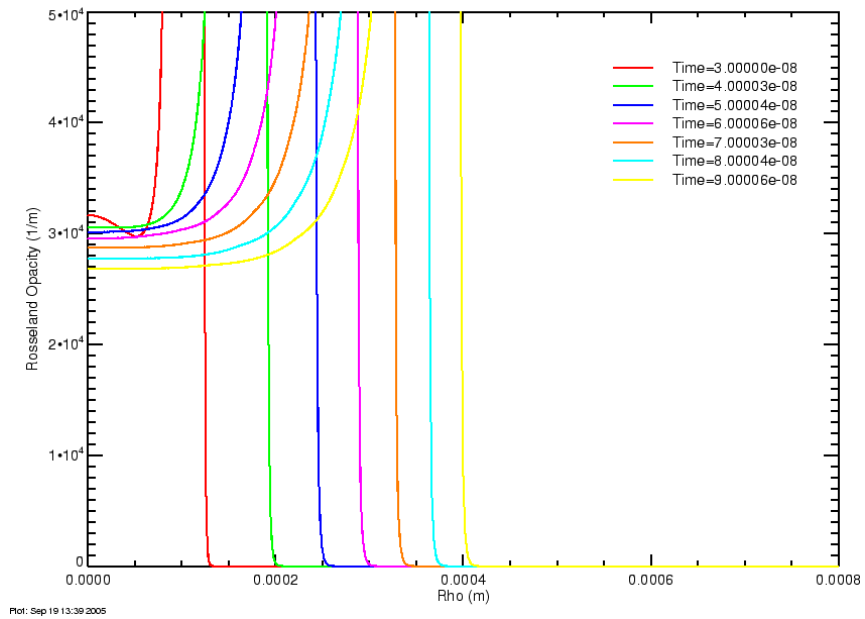Figure C-138. Early time pressure profiles for a voltage drive with 1 ns risetime, 45 MV peak and $R_0 = 160\ \Omega$
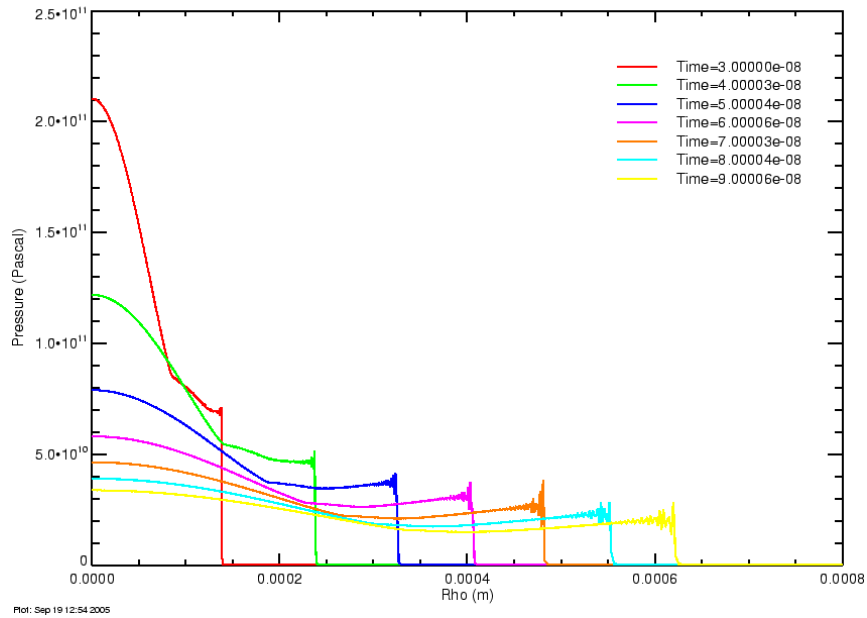
Figure C-139. Late time pressure profiles for a voltage drive with 1 ns risetime, 45 MV peak and $R_0 = 160$ Ω
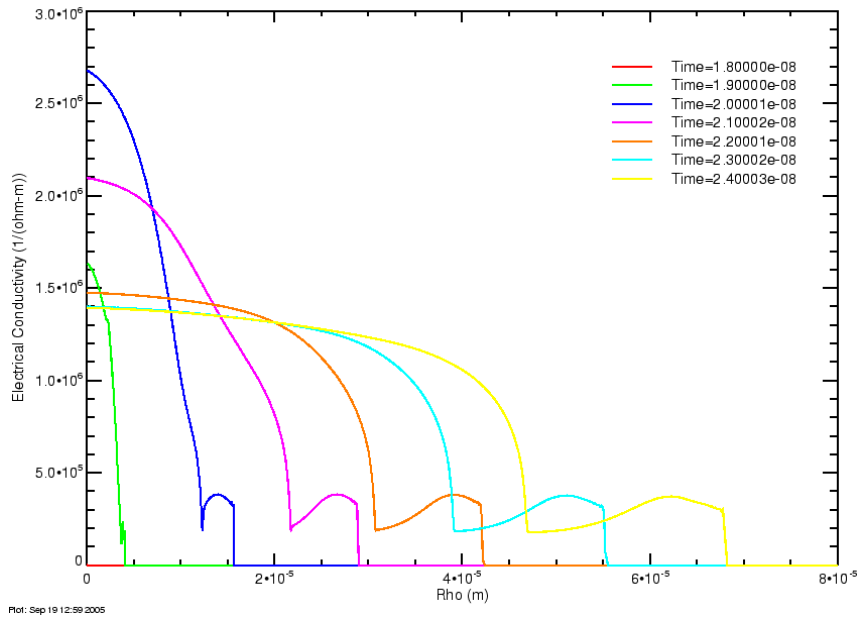
Figure C-140. Early time electrical conductivity profiles for a voltage drive with 1 ns risetime, 45 MV peak and $R_0 = 160$ Ω
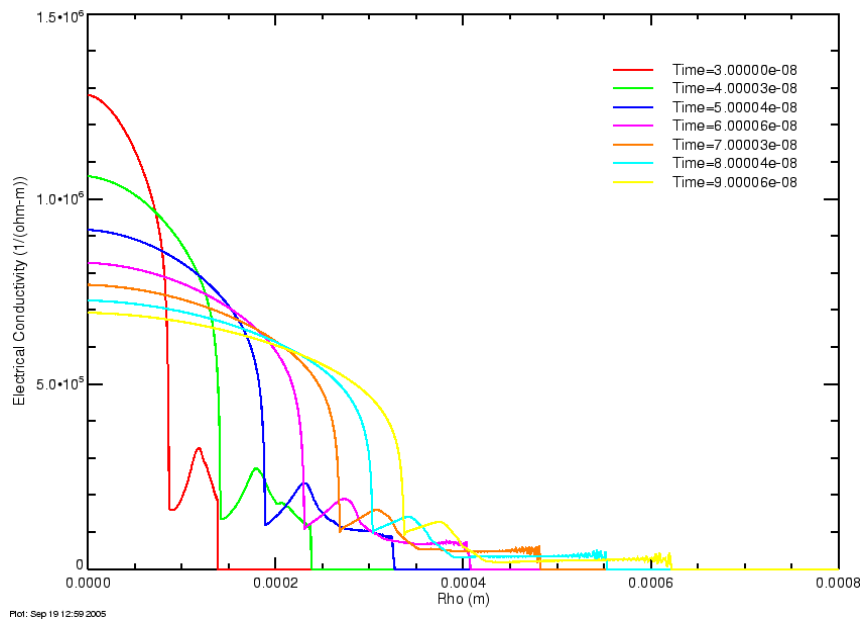
Figure C-141. Late time electrical conductivity profiles for a voltage drive with 1 ns risetime, 45 MV peak and $R_0 = 160 \ \Omega$
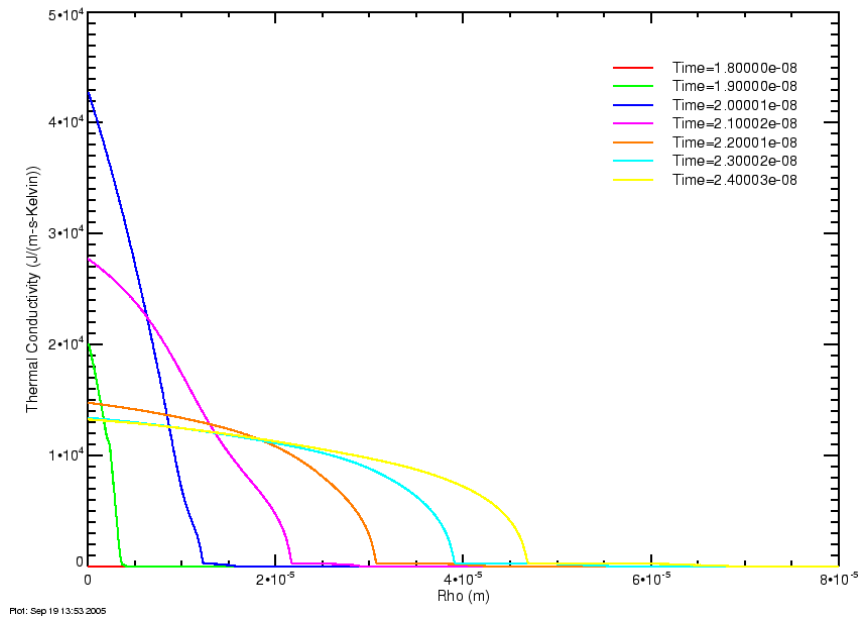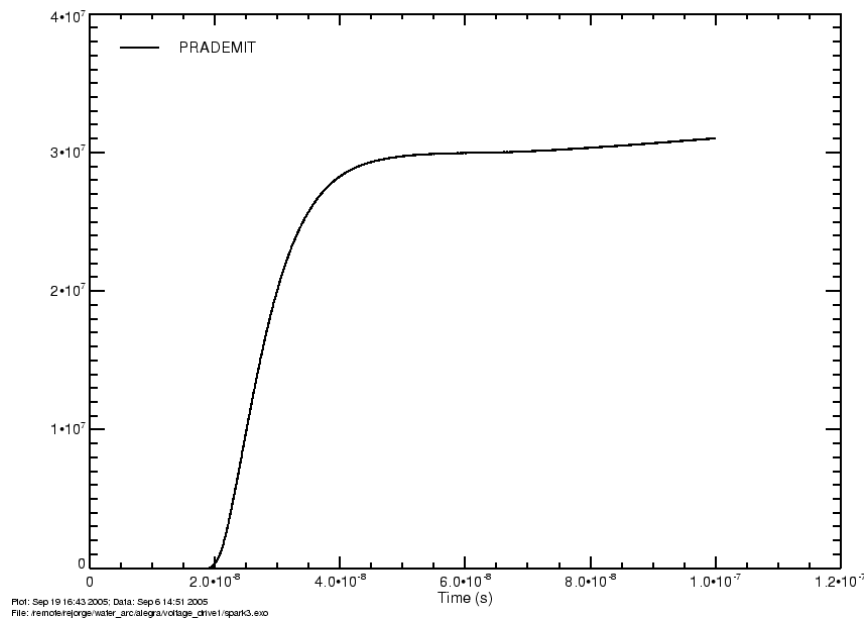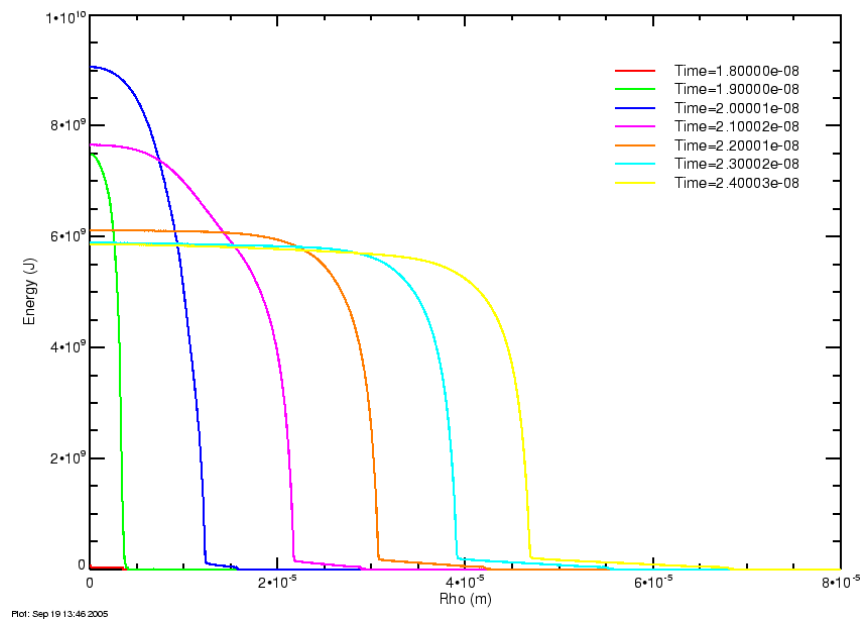
Figure C-142. Early time thermal conductivity profiles for a voltage drive with 1 ns risetime, 45 MV peak and $R_0 = 160\ \Omega$
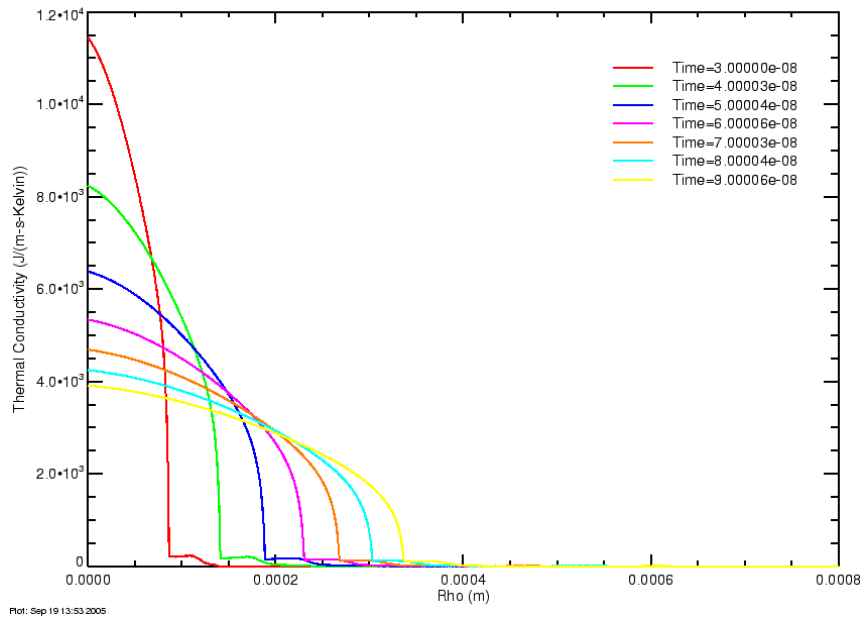
Figure C-143. Late time thermal conductivity profiles for a voltage drive with 1 ns risetime, 45 MV peak and $R_0 = 160\ \Omega$
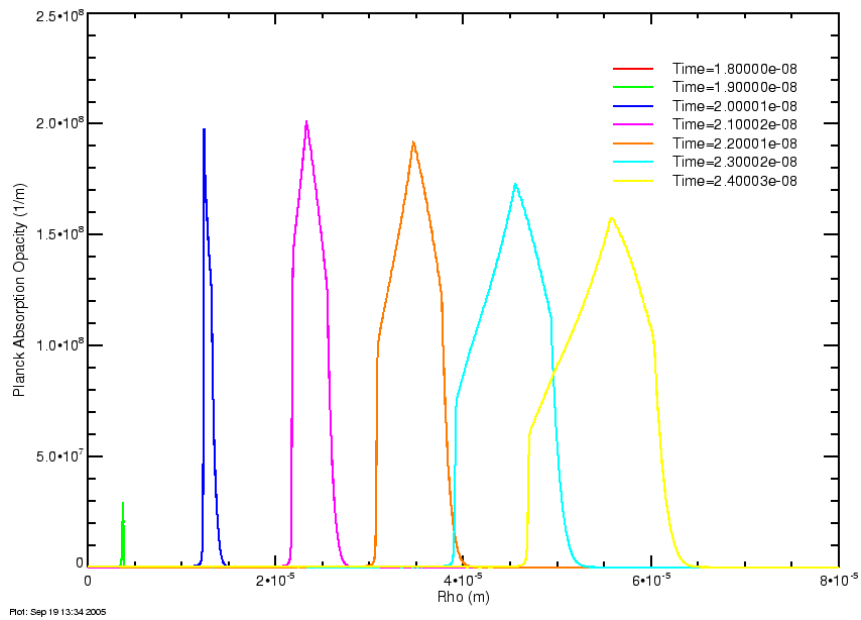
Figure C-144. Early time average opacity profiles for a voltage drive with 1 ns risetime, 45 MV peak and $R_0 = 160 \ \Omega$
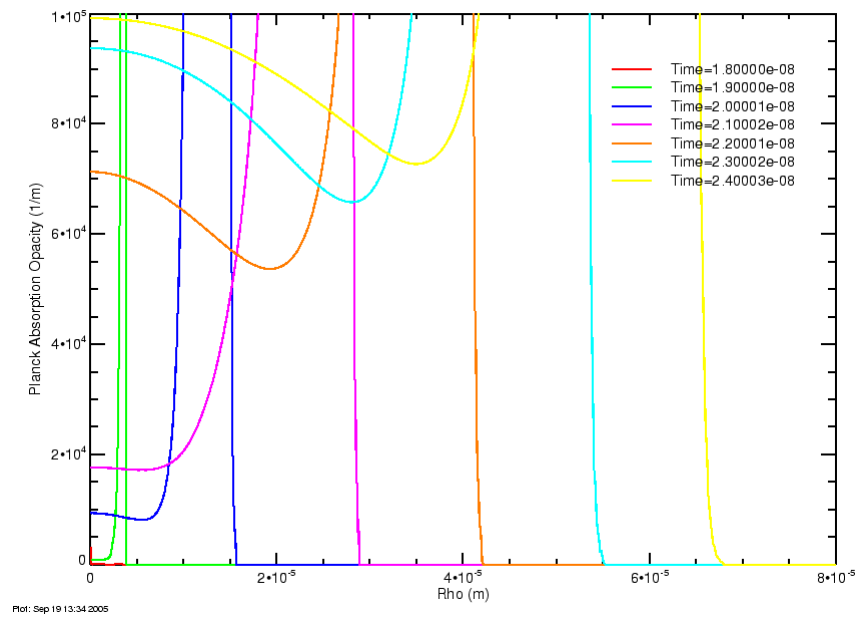

Figure C-145. Detail of early time average opacity profiles for a voltage drive with 1 ns risetime, 45 MV peak and $R_0 = 160 \ \Omega$

242

Figure C-146. Late time average opacity profiles for a voltage drive with 1 ns risetime, 45 MV peak and $R_0 = 160 \ \Omega$
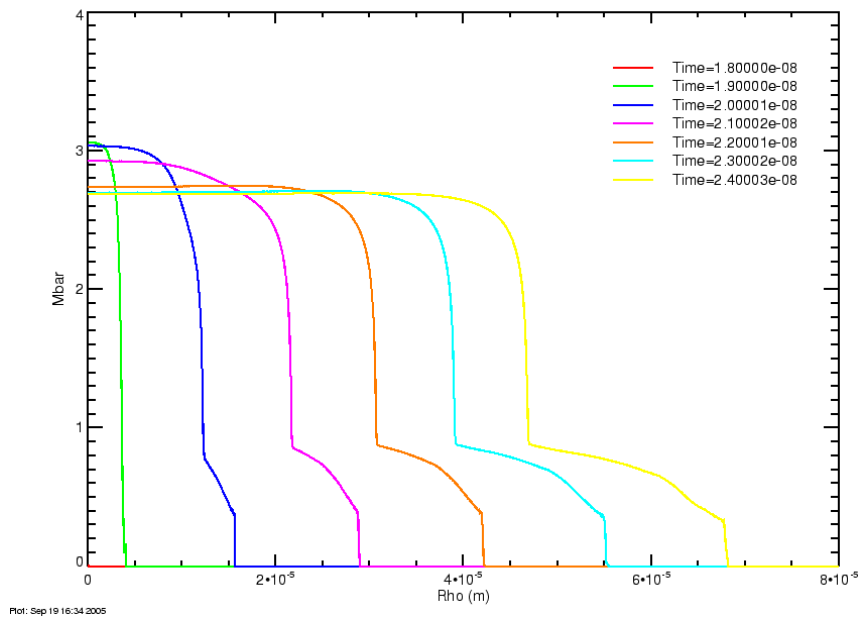
Figure C-147. Detail of late time average opacity profiles for a voltage drive with 1 ns risetime, 45 MV peak and $R_0 = 160 \ \Omega$

Figure C-148. Early time Rosseland opacity profiles for a voltage drive with 1 ns risetime, 45 MV peak and $R_0 = 160 \ \Omega$
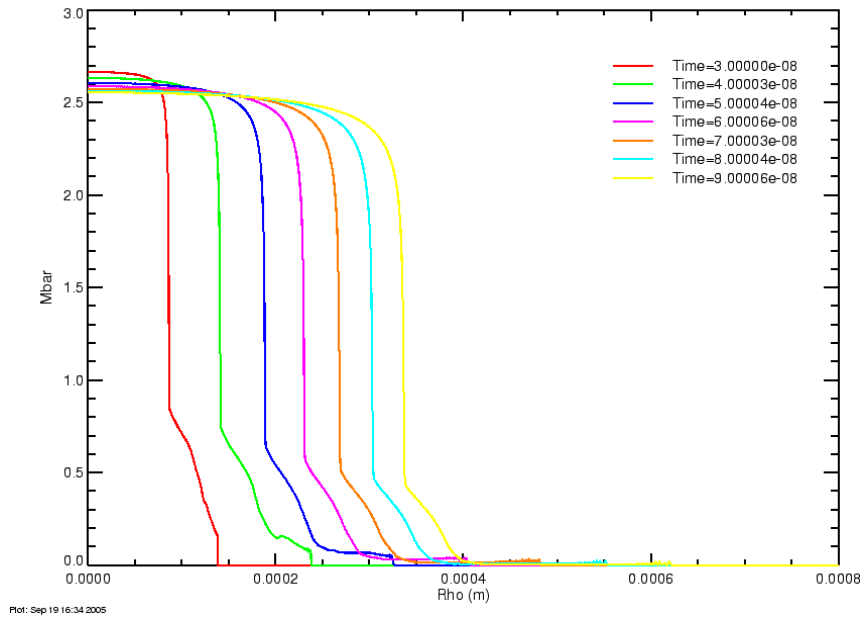
244

Figure C-149. Detail of early time Rosseland opacity profiles for a voltage drive with 1 ns risetime, 45 MV peak and $R_0 = 160 \ \Omega$

Figure C-150. Late time Rosseland opacity profiles for a voltage drive with 1 ns risetime, 45 MV peak and $R_0 = 160 \ \Omega$
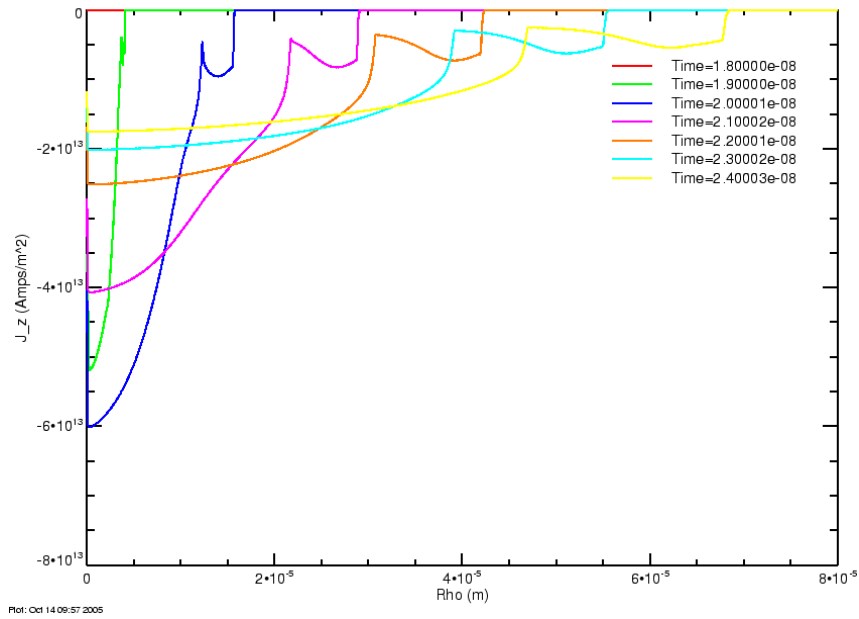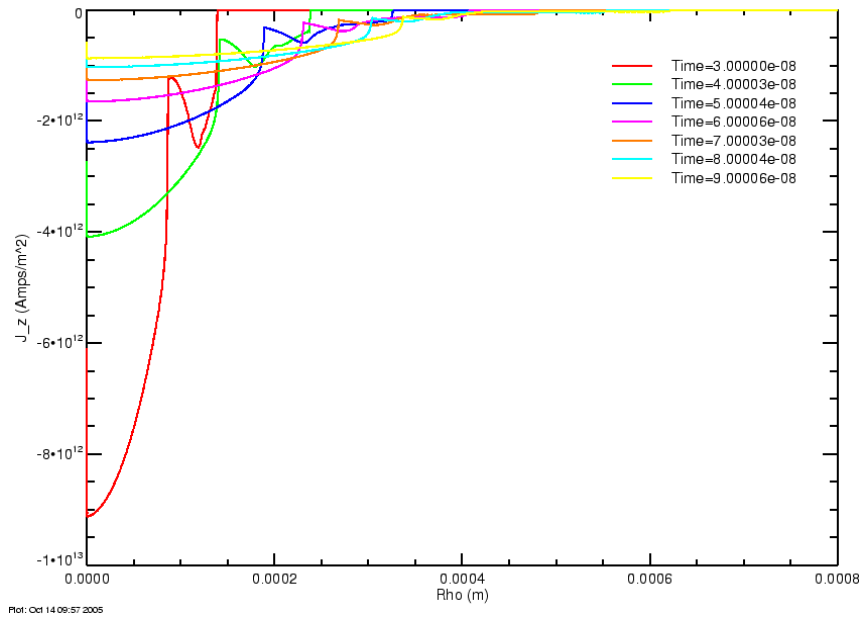
Figure C-151. Detail of late time Rosseland opacity profiles for a voltage drive with 1 ns risetime, 45 MV peak and $R_0 = 160 \; \Omega$

Figure C-152. Total problem radiation for a voltage drive with 1 ns risetime, 45 MV peak and $R_0 = 160\ \Omega$
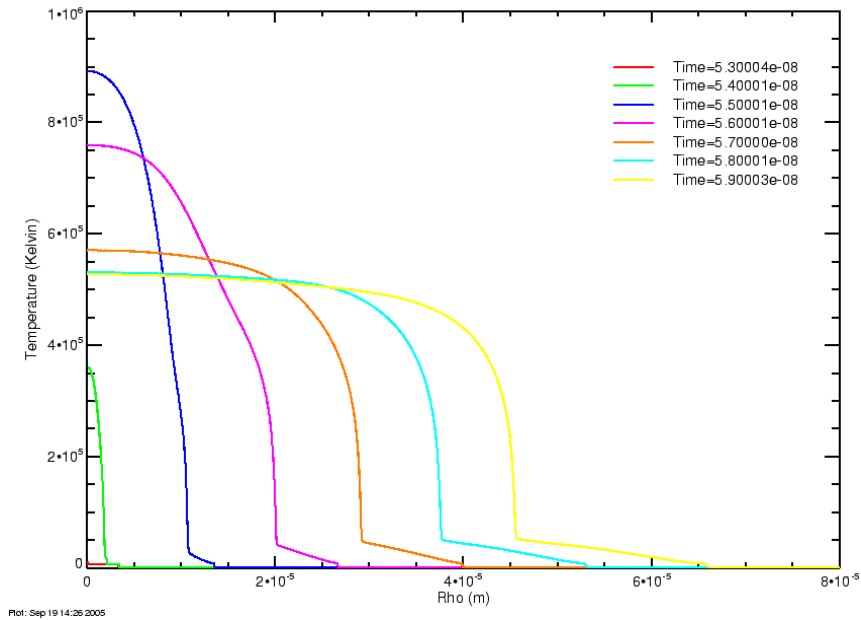

Figure C-153. Early time internal energy profiles for a voltage drive with 1 ns risetime, 45 MV peak and $R_0 = 160\ \Omega$
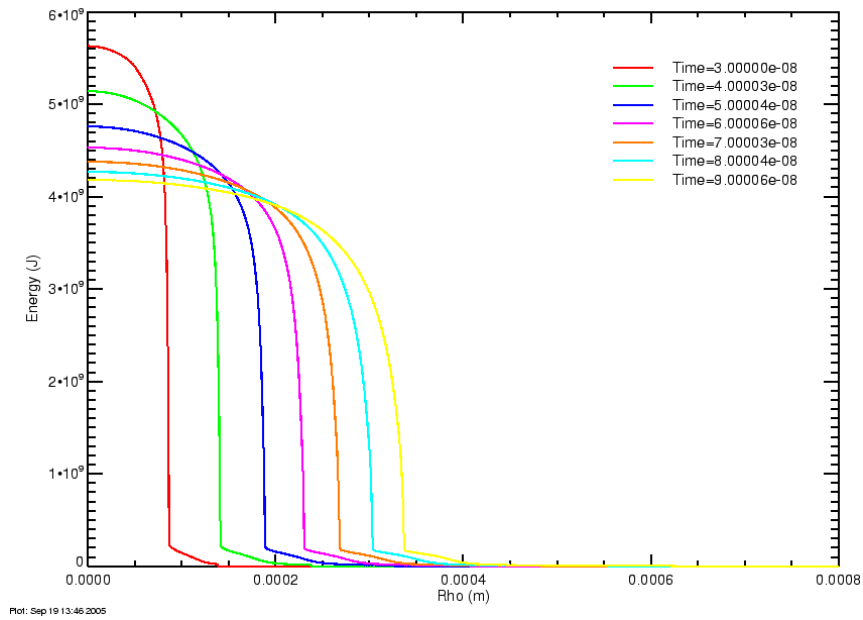
Figure C-154. Late time internal energy profiles for a voltage drive with 1 ns risetime, 45 MV peak and $R_0 = 160\ \Omega$

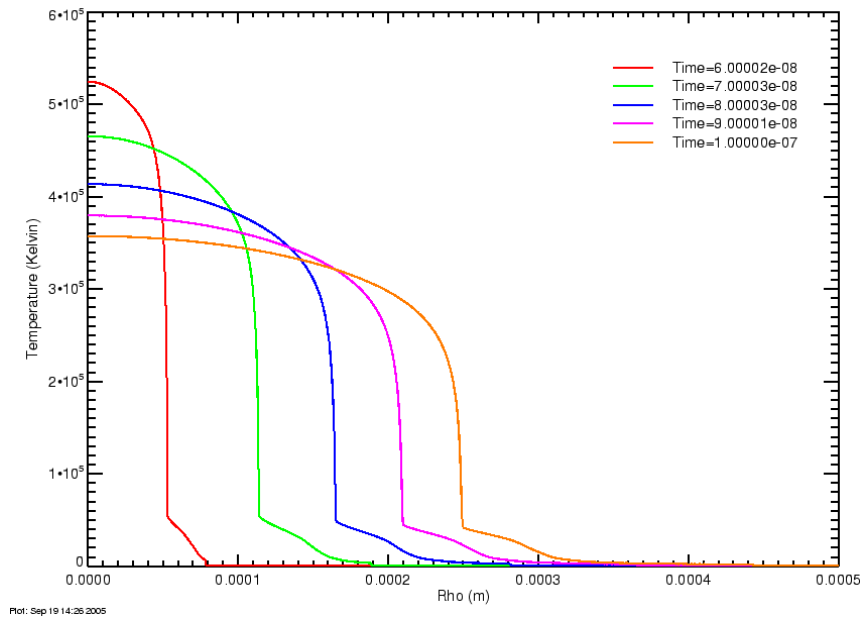Figure C-155. Early time ionization number profiles for a voltage drive with 1 ns risetime, 45 MV peak and $R_0 = 160\ \Omega$

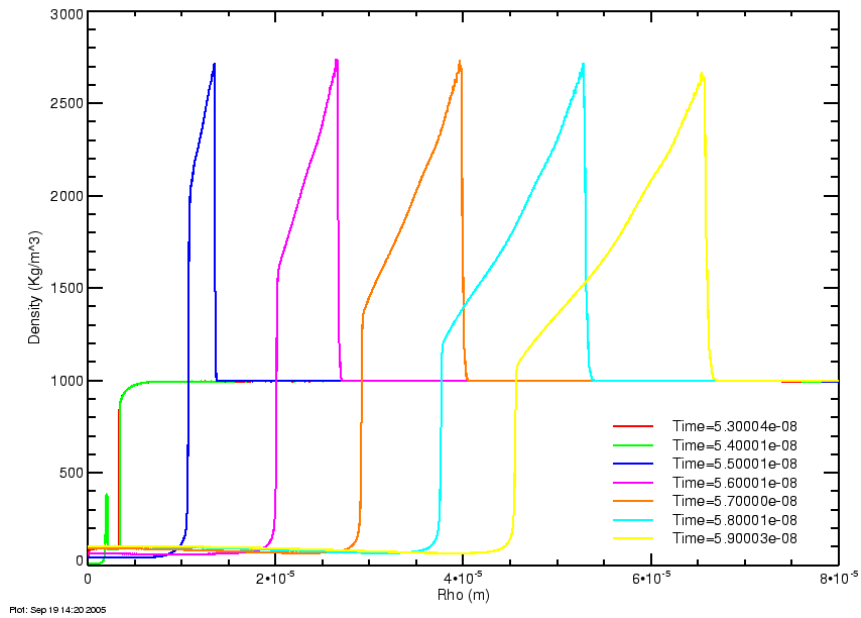Figure C-156. Late time ionization number profiles for a voltage drive with 1 ns risetime, 45 MV peak and $R_0 = 160$ Ω

Figure C-157. Early time current density profiles for a voltage drive with 1 ns risetime, 45 MV peak and $R_0 = 160$ Ω

C.6 Slow Rise Voltage Drive

The seventh and final set has radiation turned on. The voltage drive is a linear ramp rising to $V_{oc} = 45$ MV with a risetime of 50 ns. The external impedance is 160 Ω to make the peak current 280 kA. The channel initial conditions are radius of 1 μm, temperature of 1 eV and density of 1000 kg/m^3.

Figure C-158. Late time current density profiles for a voltage drive with 1 ns risetime, 45 MV peak and $R_0 = 160$ Ω

Figure C-159. Early time temperature profiles for a voltage drive with 50 ns risetime, 45 MV peak and $R_0 = 160 \ \Omega$
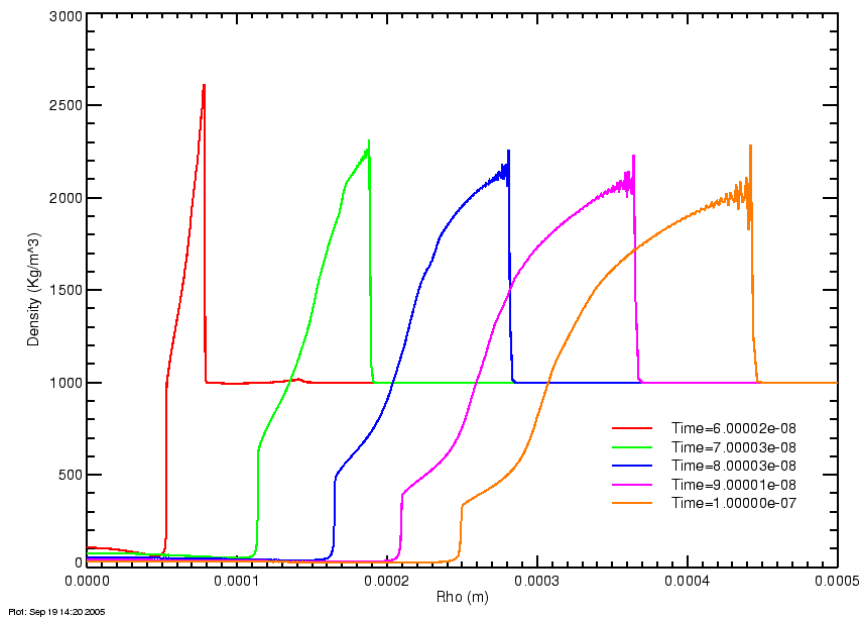

Figure C-160. Late time temperature profiles for a voltage drive with 50 ns risetime, 45 MV peak and $R_0 = 160 \ \Omega$

Figure C-161. Early time density profiles for a voltage drive with 50 ns risetime, 45 MV peak and $R_0 = 160$ Ω
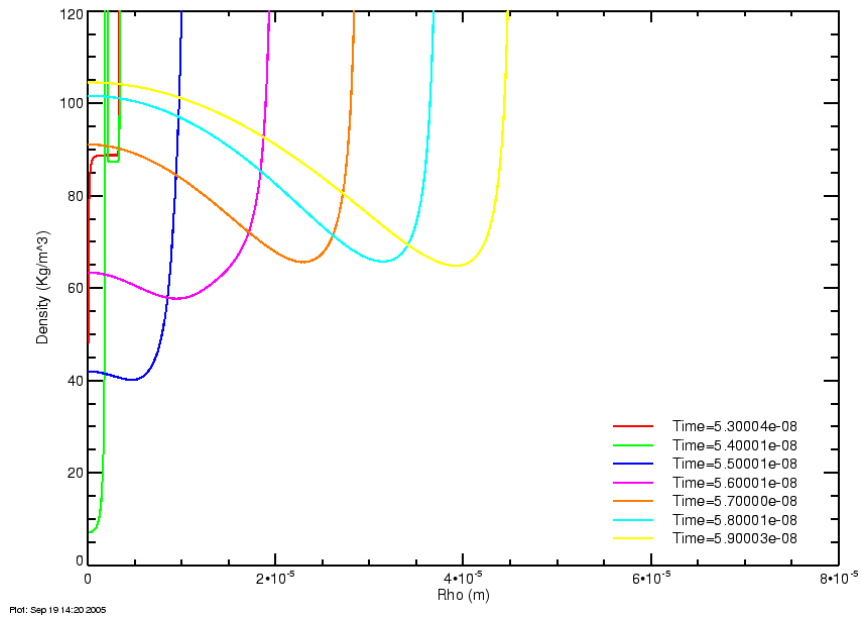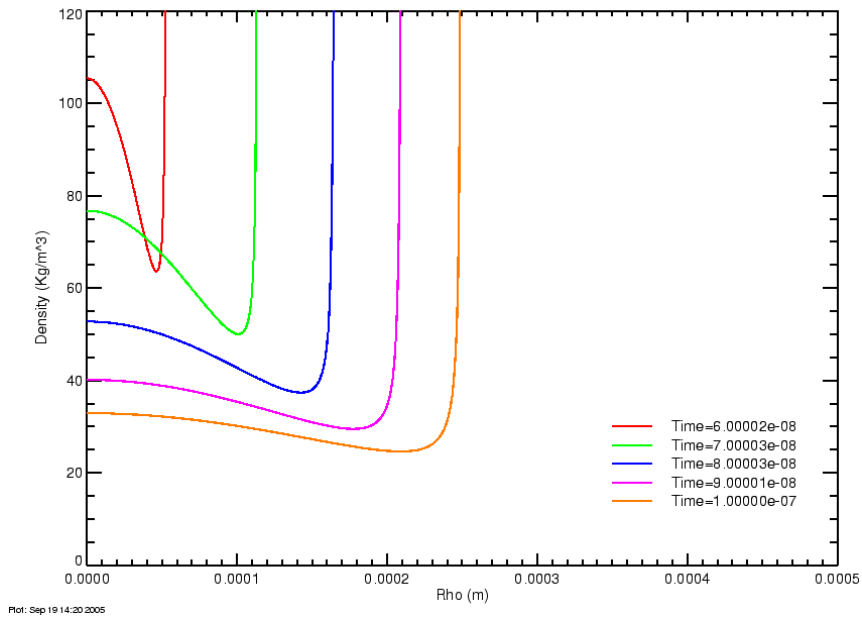

Figure C-162. Detail of early time density profiles for a voltage drive with 50 ns risetime, 45 MV peak and $R_0 = 160$ Ω

Figure C-163. Late time density profiles for a voltage drive with 50 ns risetime, 45 MV peak and $R_0 = 160$ Ω
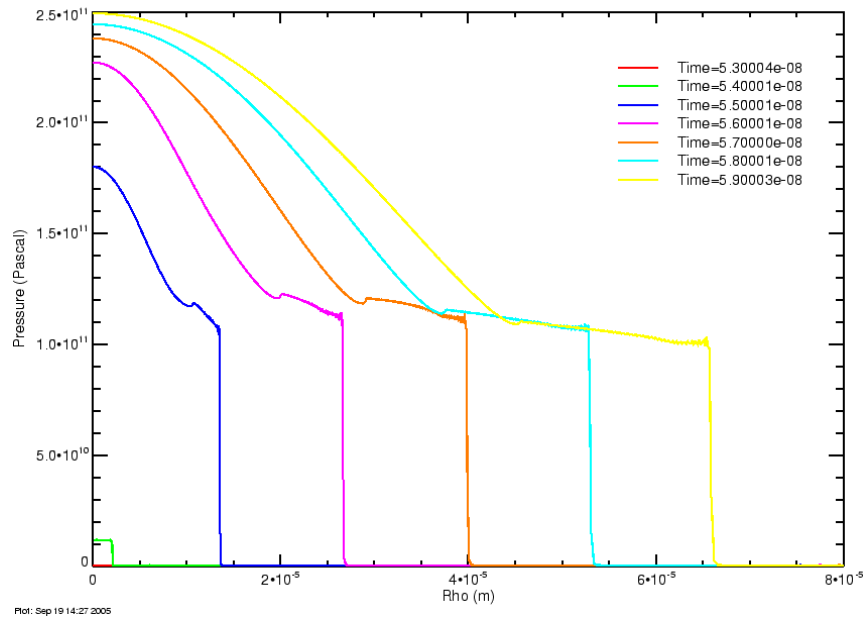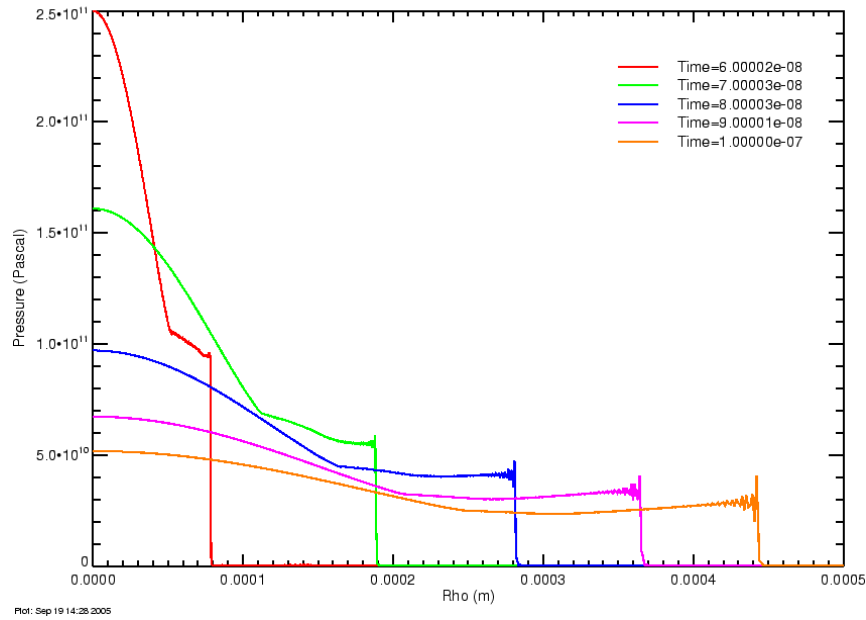

Figure C-164. Detail of late time density profiles for a voltage drive with 50 ns risetime, 45 MV peak and $R_0 = 160$ Ω

254

Figure C-165. Early time pressure profiles for a voltage drive with 50 ns risetime, 45 MV peak and $R_0 = 160$ Ω

Figure C-166. Late time pressure profiles for a voltage drive with 50 ns risetime, 45 MV peak and $R_0 = 160$ Ω
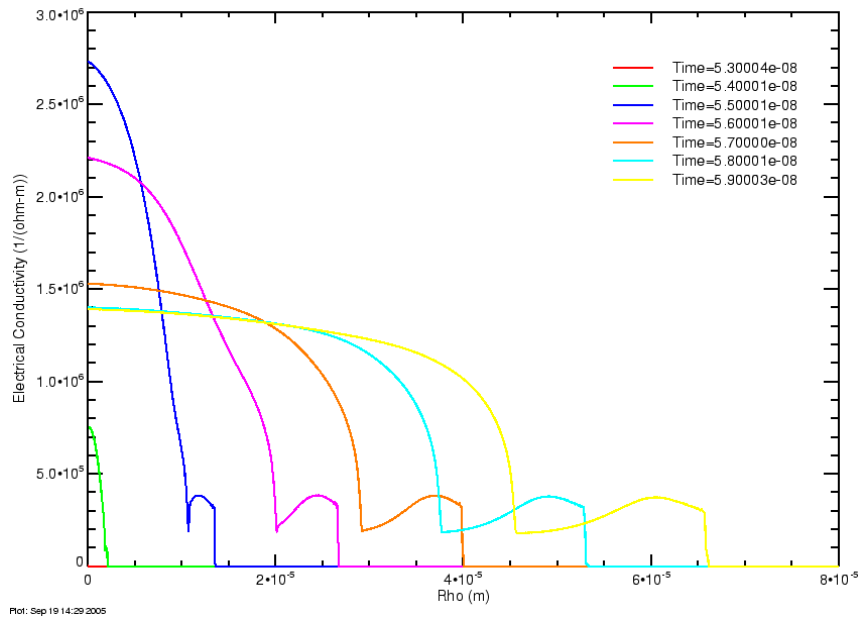
Figure C-167. Early time electrical conductivity profiles for a voltage drive with 50 ns risetime, 45 MV peak and $R_0 = 160\ \Omega$
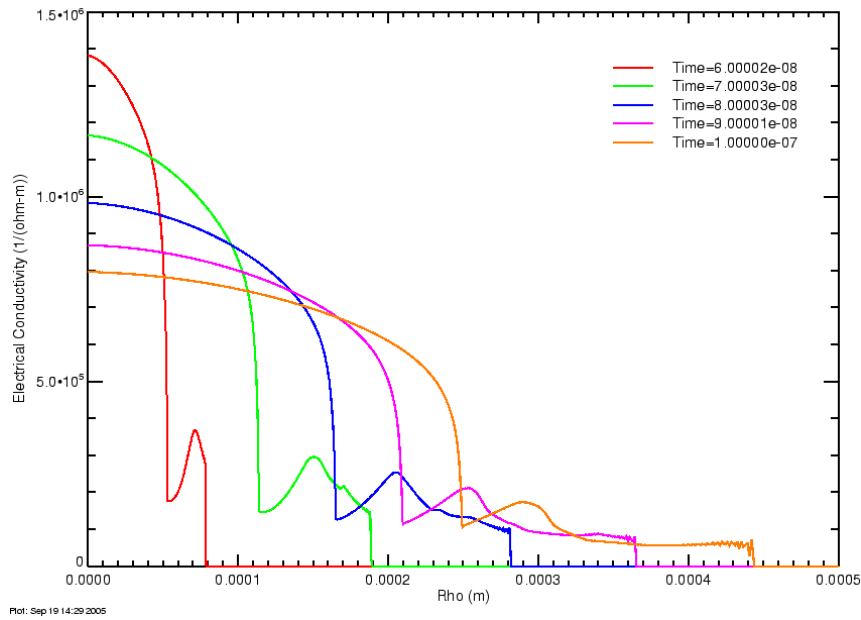

Figure C-168. Late time electrical conductivity profiles for a voltage drive with 50 ns risetime, 45 MV peak and $R_0 = 160\ \Omega$
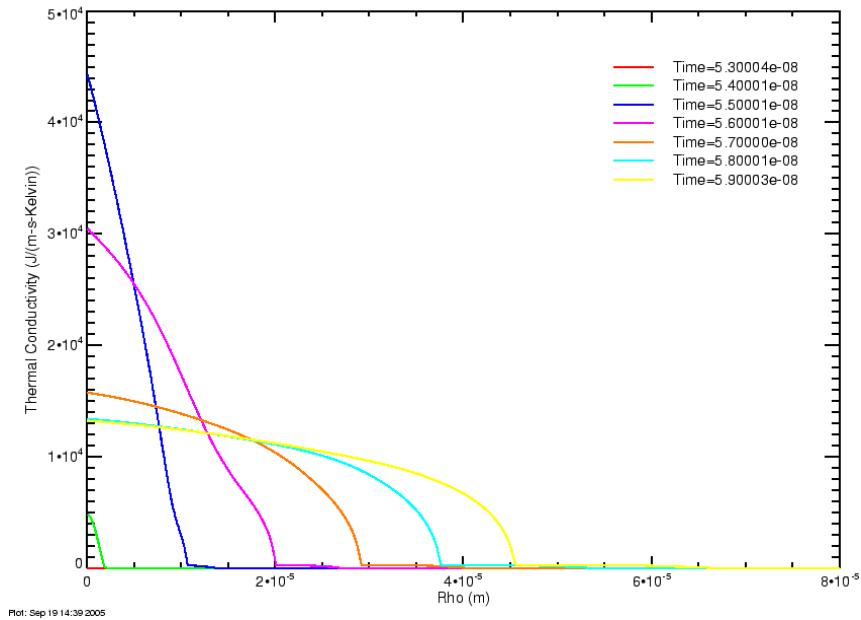
Figure C-169. Early time thermal conductivity profiles for a voltage drive with 50 ns risetime, 45 MV peak and $R_0 = 160\ \Omega$
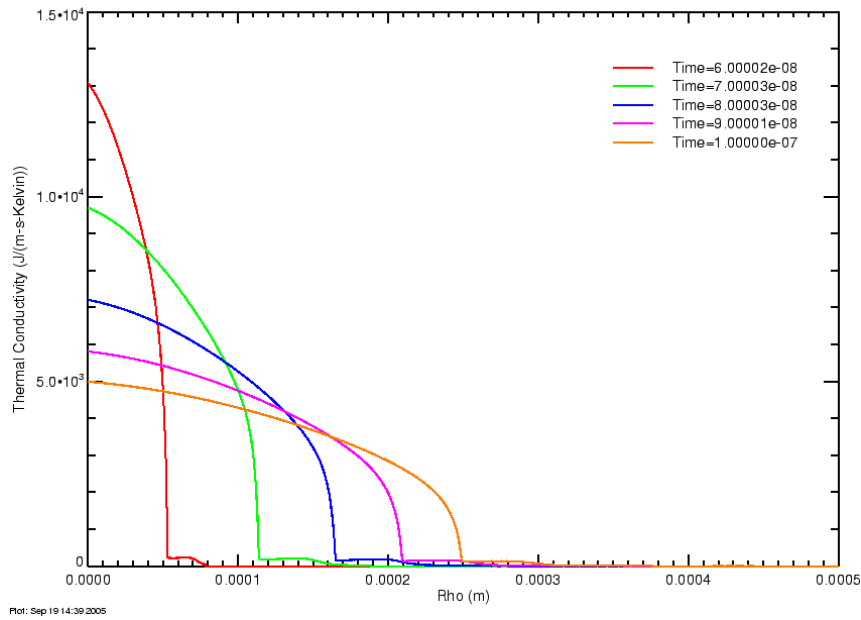

Figure C-170. Late time thermal conductivity profiles for a voltage drive with 50 ns risetime, 45 MV peak and $R_0 = 160\ \Omega$
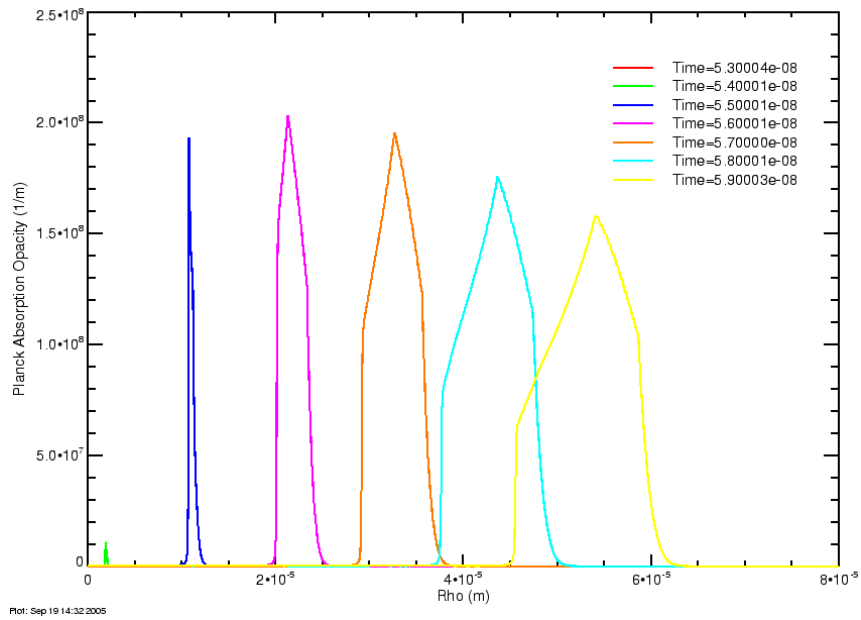
Figure C-171. Early time average opacity profiles for a voltage drive with 50 ns risetime, 45 MV peak and $R_0 = 160 \ \Omega$
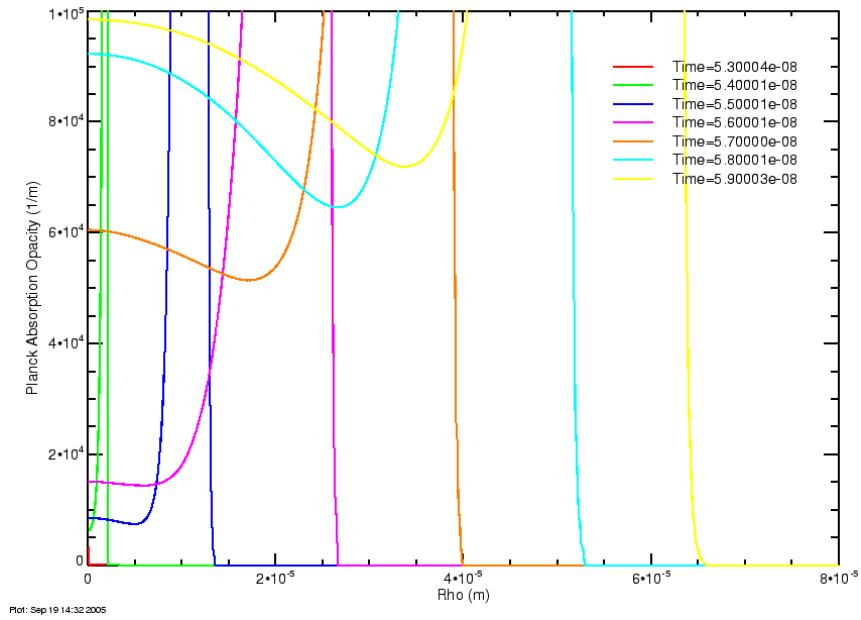

Figure C-172. Detail of early time average opacity profiles for a voltage drive with 50 ns risetime, 45 MV peak and $R_0 = 160 \ \Omega$
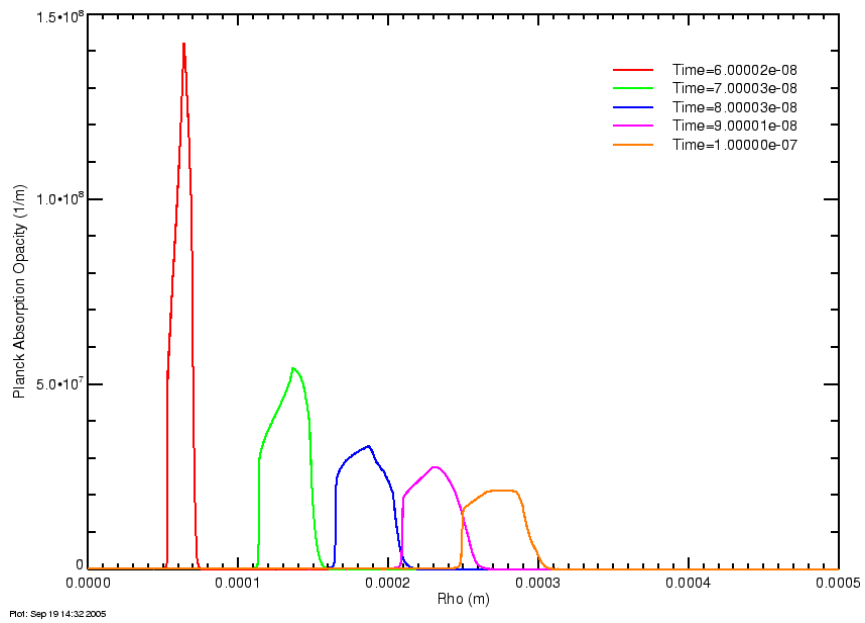
Figure C-173. Late time average opacity profiles for a voltage drive with 50 ns risetime, 45 MV peak and $R_0 = 160 \ \Omega$
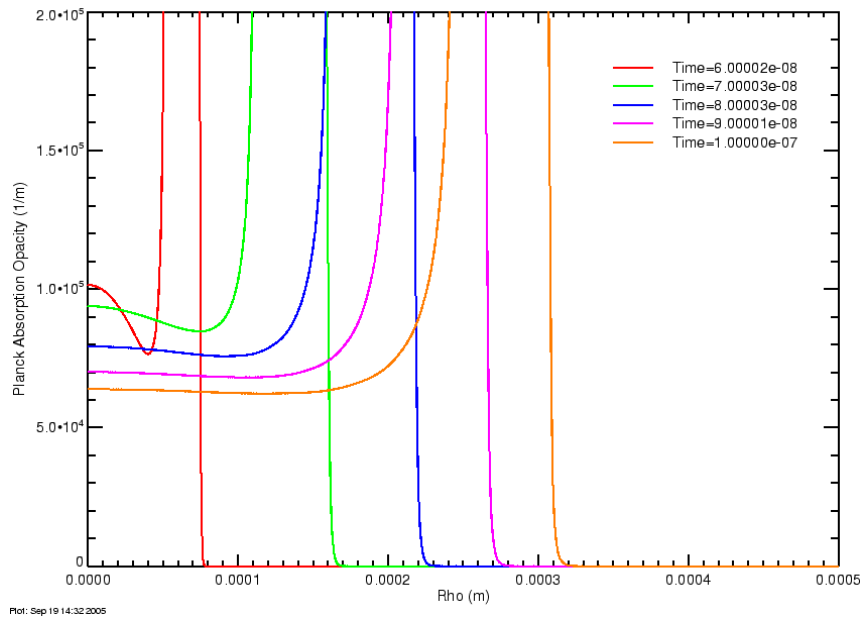
Figure C-174. Detail of late time average opacity profiles for a voltage drive with 50 ns risetime, 45 MV peak and $R_0 = 160$ Ω
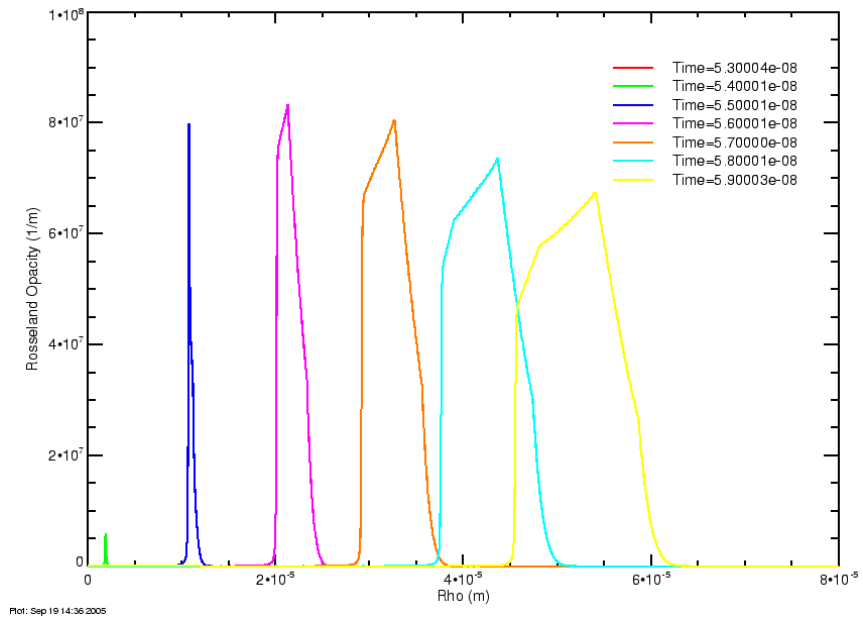

Figure C-175. Early time Rosseland opacity profiles for a voltage drive with 50 ns risetime, 45 MV peak and $R_0 = 160$ Ω

Figure C-176. Detail of early time Rosseland opacity profiles for a voltage drive with 50 ns risetime, 45 MV peak and $R_0 = 160\ \Omega$

Figure C-177. Late time Rosseland opacity profiles for a voltage drive with 50 ns risetime, 45 MV peak and $R_0 = 160\ \Omega$
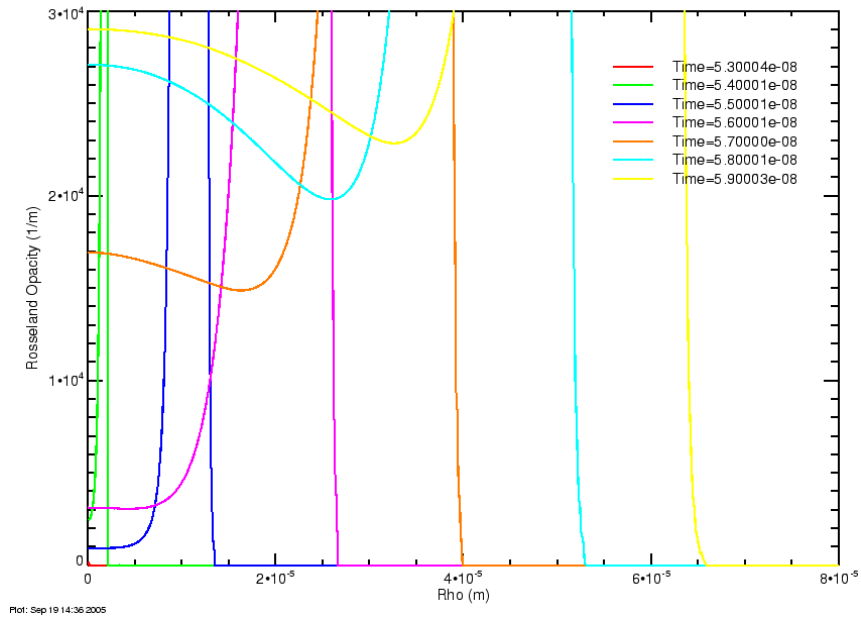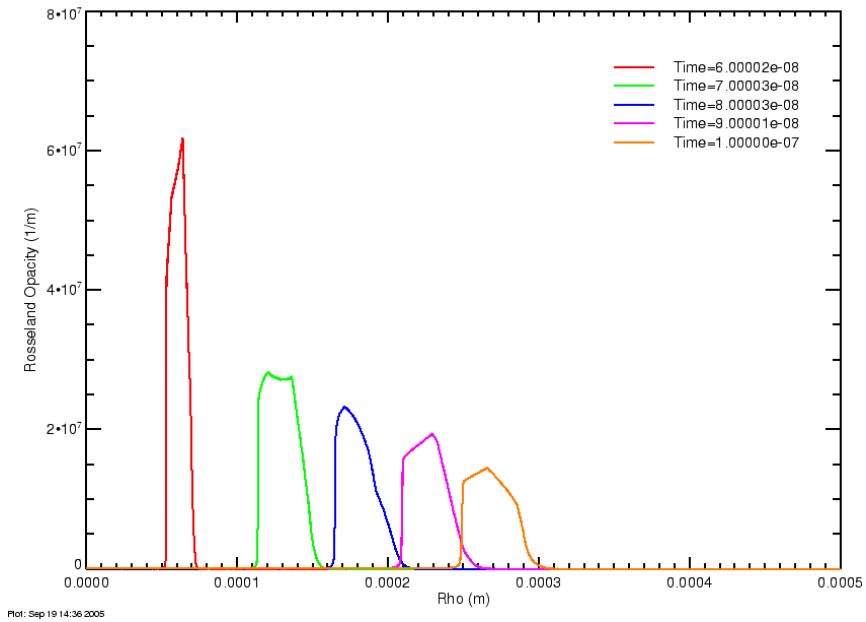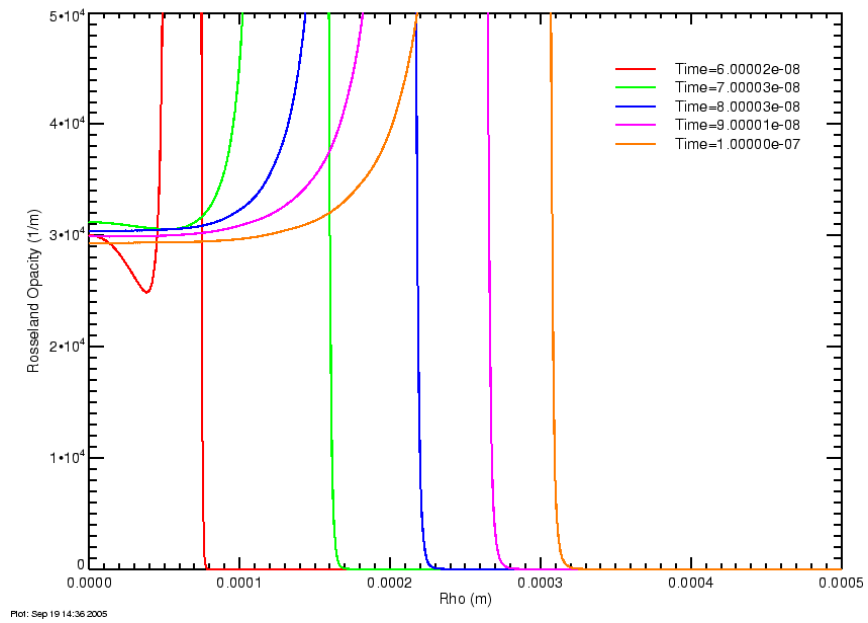
Figure C-178. Detail of late time Rosseland opacity profiles for a voltage drive with 50 ns risetime, 45 MV peak and $R_0 = 160\ \Omega$
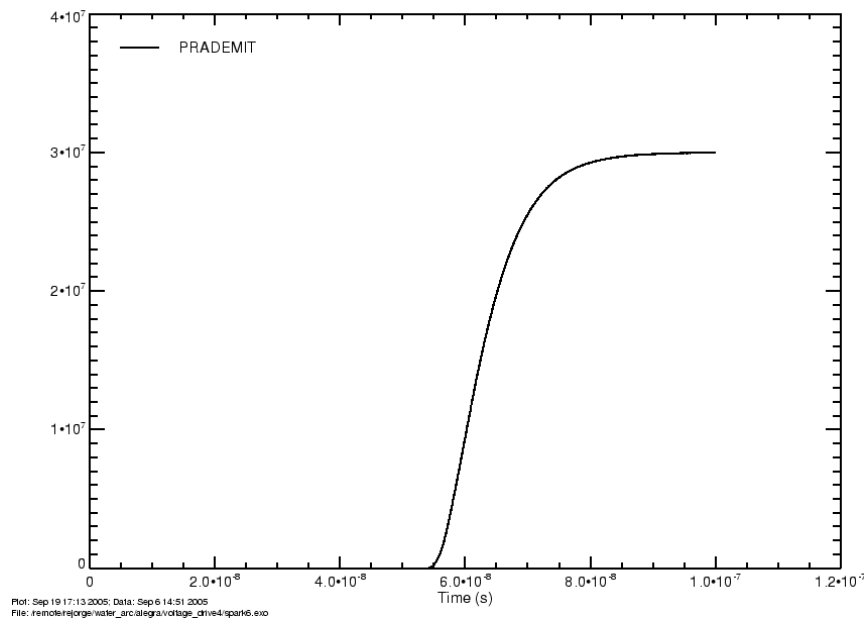
Figure C-179. Total problem radiation for a voltage drive with 50 ns risetime, 45 MV peak and $R_0 = 160 \ \Omega$

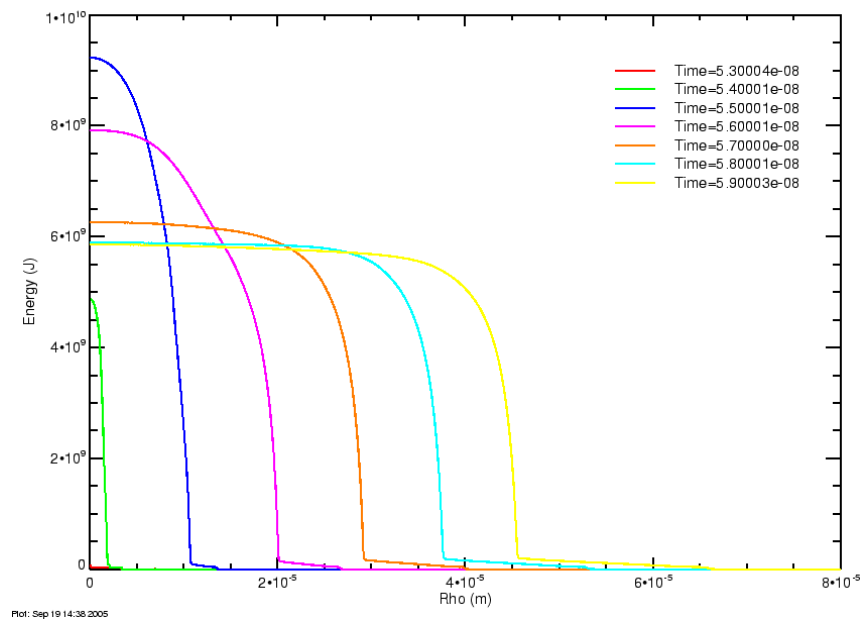

Figure C-180. Early time internal energy profiles for a voltage drive with 50 ns risetime, 45 MV peak and $R_0 = 160 \ \Omega$
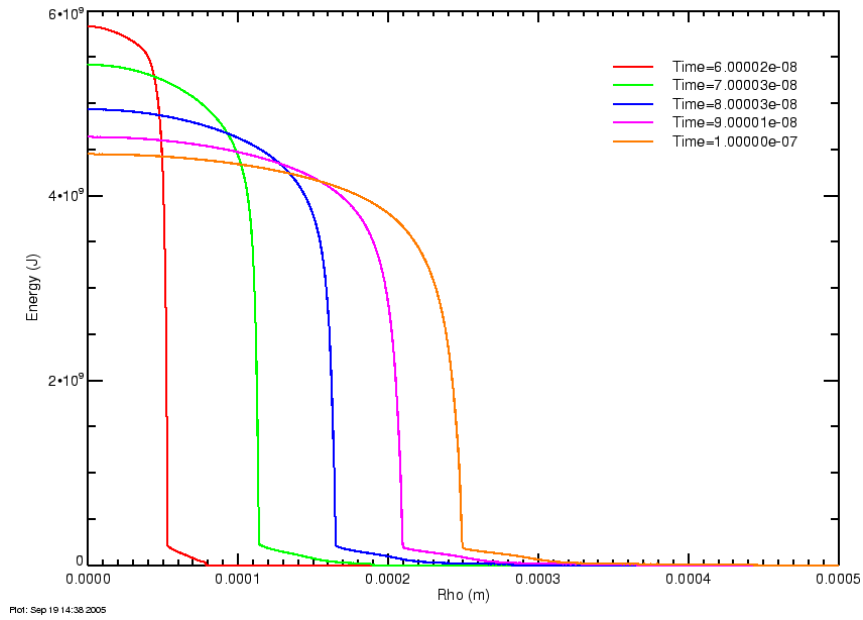
263

Figure C-181. Late time internal energy profiles for a voltage drive with 50 ns risetime, 45 MV peak and $R_0 = 160$ Ω
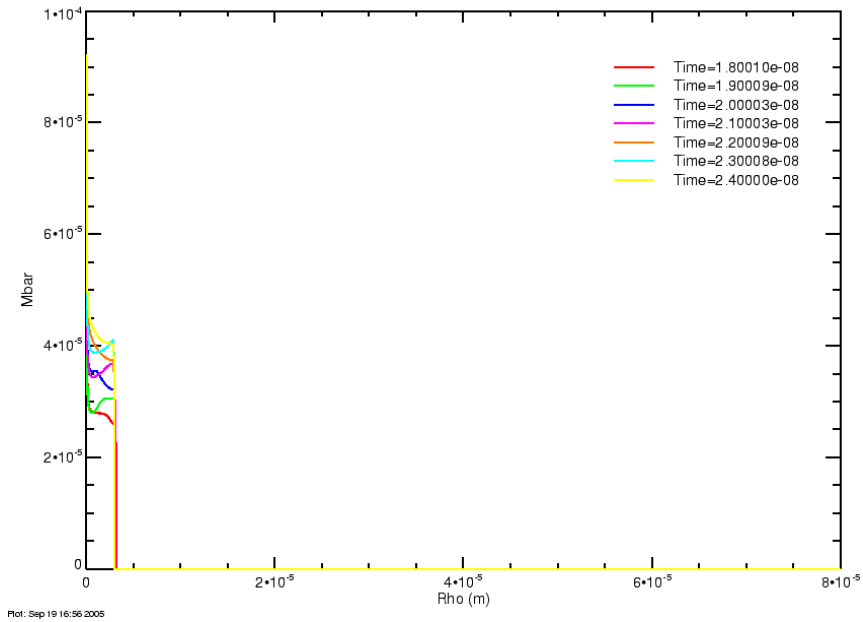

Figure C-182. Early time ionization number profiles for a voltage drive with 50 ns risetime, 45 MV peak and $R_0 = 160$ Ω
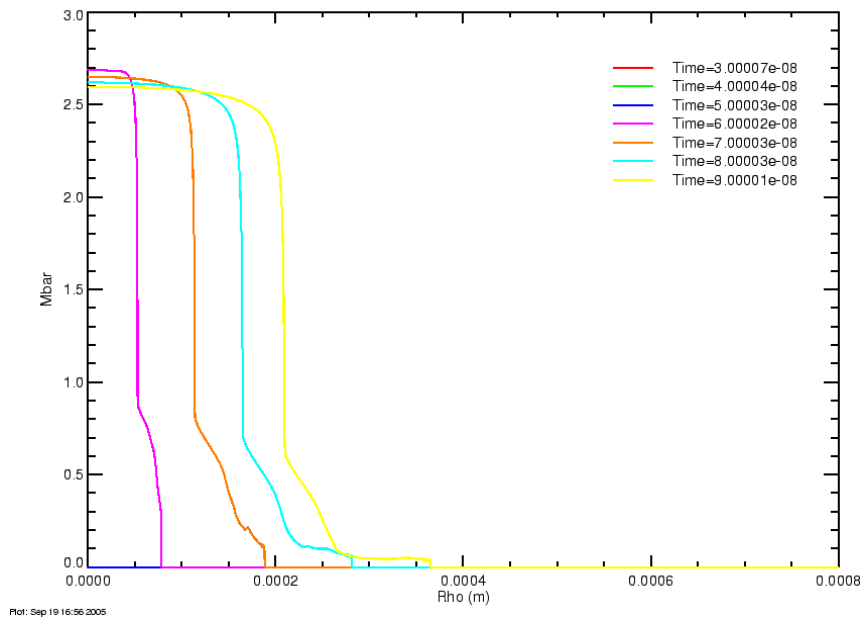
264

Figure C-183. Late time ionization number profiles for a voltage drive with 50 ns risetime, 45 MV peak and $R_0 = 160 \ \Omega$

Distribution

1   Prof. Erich E. Kunhardt
        Stevens Institute of Technology
        Dept. Physics and Engineering
        Castle Point On Hudson
        Hoboken, NJ 07030

1   Dr. Kelvin S. H. Lee
        ITT Industries/AES
        1033 Gayley Avenue
        Suite 215
        Los Angeles, CA 90024

1   Dr. Thomas H. Martin
        1516 Catron Ave. SE
        Albuquerque, NM 87123

1   Prof. Andreas Neuber
        Texas Tech University
        Dept. of Electrical and Computer Engineering
        PO Box 43102
        Lubbock, TX 79409-3102

1   Dr. Ian Smith
        L-3 Titan Pulse Sciences
        2700 Merced Street
        San Leandro, CA 94577

1	**MS0123**	D. C. Chavez, LDRD Office, 01011
1	MS0888	R. A. Anderson, 01821
1	MS1110	H. P. Hjalmarson, 01435
1	MS0492	K. C. Chen, 12332
1	MS0405	K. O. Merewether, 12346
2	MS1193	J. M. Lehr, 01645
1	MS1193	J. E. Maenchen, 01645
1	MS0492	J. R. Woodworth, 01645
2	MS1152	R. E. Jorgenson, 01652
1	MS1152	M. L. Kiefer, 01652
1	MS1152	M. E. Morris, 01652
1	MS1152	T. D. Pointon, 01652
1	MS1152	D. B. Seidel, 01652
5	MS1152	L. K. Warne, 01652

1	MS1186	M. P. Desjarlais, 01674
1	MS1186	T. K. Mattsson, 01674
1	MS1194	D. H. McDaniel, 01600
1	MS1194	K. R. Prestwich, 01640
1	MS0335	J. M. Elizondo-Decanini, 02564
2	MS9018	Central Technical Files, 8945-1
2	MS0899	Technical Library, 04536